Mechanics of inelastic deformation and delamination in paperboard

by

Qingxi Steve Xia

B.S., Aerospace Engineering, Beijing University of Aeronautics and Astronautics, Beijing, China 1994

M.S., Mechanical Engineering, Georgia Institute of Technology, Atlanta, 1998

Submitted to the Department of Mechanical Engineering
in partial fulfillment of the requirements for the degree of

Doctor of Philosophy in Mechanical Engineering

at the

MASSACHUSETTS INSTITUTE OF TECHNOLOGY

Feburary 2002

Author ... .
Department of Mechanical Engineering
January 28, 2002

Certified by. .....
Mary C. Boyce
Professor
Thesis Supervisor

Certified by .....
David M. Parks
Professor
Thesis Supervisor

Accepted by ....
Ain Sonin
Chairman, Department Committee on Graduate Students

Mechanics of inelastic deformation and delamination in paperboard

by

Qingxi Steve Xia

Submitted to the Department of Mechanical Engineering
on January 28, 2002, in partial fulfillment of the
requirements for the degree of
Doctor of Philosophy in Mechanical Engineering

Abstract

Paperboard is one of the most widely used materials. The inelastic deformation of paperboard plays a crucial role during many manufacturing processes (e.g., the converting process whereby paperboard is converted into a product such as a milk carton by punching and subsequent folding) and during in-service applications. There is a scarcity of constitutive models describing inelastic behavior of paperboard under complex loading, despite the paper industry's great need of analytical tools to aid the design and manufacturing of better paperboard products. In this thesis, two constitutive models are developed to model the highly anisotropic, elastic-plastic behavior of paperboard/paper: (1) A three-dimensional elastic-plastic interface constitutive model is developed to model the out-of-plane delamination behavior of paperboard. The onset of interface separation is controlled by a limit surface in the normal-shear traction space. The limit surface is taken to shrink with a monotonically-increasing scalar internal variable reflecting damage associated with the history of inelastic relative interface displacement. (2) A three-dimensional, anisotropic continuum constitutive model is developed to model the in-plane elastic-plastic deformation of paper and paperboard. The proposed initial yield surface is directly constructed from the yield strengths measured in various loading directions and the corresponding ratios of plastic strain components. An associated flow rule is used to model the plastic flow of the material. Anisotropic strain-hardening of yield strengths is introduced to model the evolution of the yield surface with inelastic strain. The two constitutive models are implemented into finite element software to enable the simulation of paperboard mechanical behavior under complex, finite deformation. The models are shown to be capable of accurately capturing both the out-of-plane delamination (via the interface model) and the anisotropic in-plane elastic-plastic (via the continuum in-plane model) behavior of paperboard under complex loading.

The two models are combined to simulate the mechanics of a converting process (creasing and subsequent folding) of paperboard. The simulations agree well with

corresponding experimental observations. In particular, the underlying mechanisms of damage and delamination development during creasing and subsequent folding are predicted well; the macroscopic response of the bending moment vs. bending angle also agrees with experimental data.

This research provides physically based three-dimensional material models of the anisotropic, elastic-plastic deformation of paperboard that enable the computational design of paperboard process and product design.

Thesis Supervisor: Mary C. Boyce
Title: Professor

Thesis Supervisor: David M. Parks
Title: Professor

Acknowledgments

It has been four special years for me at MIT. Looking back today, I would like to express my most sincere thanks to my advisors, Professor Boyce and Professor Parks, for their insightful guidance and constant support during this research work. I will never forget Professor Boyce's dedicaiton to research and Professor Parks's constant drive to pursue perfection. What I learned from them will forever benefit me in my future career no matter what I do. I would also like to thank Prof. Lorna Gibson for serving on my thesis committee and providing thoughtful suggestions. Financial support for my research from STFI, TetraPak, StoraEnso and Assidomän is also gratefully acknowledged.

Niclas Stenberg, Heather Dunn and Alexis Smith provided important experimental data and insights for my research. Stimulating discussions with members of the steering committee, especially Dr. Johan Tryding, helped me to concentrate on solving real engineering problems.

Many thanks to my buddies in the *M&M* lab, Jin, Hang, Prakash, Yu, Franco, Matts, Brian, Chen, Matt, Ethan, Rebecca and the rest of the *M&M* gang. You guys have been great and I really enjoyed being your friend. Ray and Una, they two are the best. I am sure I will miss you all.

I would not be able to accomplish this study without my parents's love and unconditional support for my education. I dedicate this work to them. I owe a great deal to my wife Weihong, for her love, understanding and support during my study.

Contents

1 Introduction **27**

1.1 Description of material 28

1.2 Review of experimental behavior of paperboard 30

1.3 Research motivation and framework of this research 32

1.4 Outline of the thesis 35

2 In-plane Constitutive Model **45**

2.1 Introduction 45

2.2 Experimentally-Observed Behavior 46

2.2.1 Elastic-Plastic Behavior of TRIPLEX^{TM} Paperboard 46

2.3 The In-Plane Constitutive Model 51

2.3.1 Stress-strain relationship 51

2.3.2 Yield Condition 52

2.3.3 Flow rule 56

2.3.4 Strain-hardening functions 58

2.3.5 Discussion 59

2.4 Implementation and verification of the model: Application to model TRIPLEX^{TM} 60

2.4.1 Simulations to determine the model parameters for behavior of the TRIPLEX^{TM} laminate 60

2.4.2 Simulations predicting the off-axis in-plane stress-strain behavior of TRIPLEX^{TM} 62

2.4.3 Simulation of deformation of paperboard under inhomogeneous in-plane loading 62
2.5 Evaluation of material parameters for mechanical and chemical pulp layers 65
2.5.1 Experimental data on individual layers 66
2.5.2 Additional assumptions made 67
2.5.3 Simulations to determine the model parameters for behavior of individual pulp layers inside TRIPLEX^{TM} 68
2.6 Discussion 69

3 Interface Constitutive Model **107**
3.1 EXPERIMENTAL OBSERVATIONS 108
3.1.1 Macroscopic experiments 108
3.1.2 Microscopic experiments 111
3.1.3 Summary 113
3.2 INTERFACE MODELING AND FORMULATION 115
3.2.1 Kinematics 116
3.2.2 Decomposition of Displacement Jump 119
3.2.3 Interface Constitutive Law 119
3.2.4 Interface separation criterion 120
3.2.5 Flow rule 122
3.2.6 Evolution of State Variable 124
3.2.7 Residual shear resistance 125
3.2.8 Finite element implementation 127
3.3 Evaluation of properties of interfaces 129
3.4 Verification of interface model 131
3.5 Simulation of out-of-plane tests on paperboard 134
3.6 Simulation of Buckling of paperboard under In-plane Compression . . 140

3.7 Discussion 141

4 Simulation of an Exemplar Converting Process: Creasing and folding 181

4.1 Simulation of SEM creasing/folding process 182

4.2 Simulation of an industrial creasability test 188

4.3 Discussion 190

5 Summary and Future Work 223

5.1 Summary 223

5.2 Future work 224

A Method to determine the model parameters from experiments 227

A.1 Definition of properties 227

A.2 Methodology for identifying material properties from data 227

A.2.1 Elastic constants 229

A.2.2 Initial yield and subsequent strain hardening 229

List of Figures

1-1 Schematics of paper and paperboard macrostructure and microstructure. 36

1-2 SEM image of MD-CD planar view of the chemical layer of coated TRIPLEX^{TM} at low magnification. 37

1-3 SEM image of MD-CD planar view of the chemical layer of coated TRIPLEX^{TM} at intermediate magnification. 37

1-4 SEM image of MD-CD planar view of the chemical layer of coated TRIPLEX^{TM} at high magnification. 38

1-5 SEM image of MD-CD planar view of the mechanical layer of coated TRIPLEX^{TM} at low magnification. 38

1-6 SEM image of MD-CD planar view of the mechanical layer of coated TRIPLEX^{TM} at intermediate magnification. 39

1-7 SEM image of MD-CD planar view of the mechanical layer of coated TRIPLEX^{TM} at high magnification. 39

1-8 SEM image of ZD-MD side view of the TRIPLEX^{TM} at low magnification. 40

1-9 SEM image of ZD-MD side view of the TRIPLEX^{TM} at high magnification. 40

1-10 SEM image of ZD-CD side view of the TRIPLEX^{TM} at low magnification. 41

1-11 SEM image of ZD-CD side view of the TRIPLEX^{TM} at high magnification. 41

1-12 A schematic of the paperboard converting process. 42

1-13 Example of parameters that can influence the final quality of a crease. 42

1-14 SEM image of a good crease. 43
1-15 SEM image of a bad crease. 43
1-16 Illustration of the framework of modeling the TRIPLEX^{TM} paperboard. 44

2-1 TRIPLEX^{TM} in-plane stress strain curves. (Stenberg [31]) 74
2-2 Lateral strain *vs.* axial strain curve for tensile loading in the MD direction. (Stenberg [31]) 75
2-3 Lateral strain *vs.* axial strain curve for tensile loading in the CD direction. (Stenberg [31]) 75
2-4 Lateral plastic strain *vs.* axial plastic strain curve for tensile loading in the MD and CD directions. (Stenberg [31]) 76
2-5 In-plane compression stress-strain curves for MD and CD directions. (Stenberg, *et al.* [32]) 76
2-6 Illustration of the new Arcan design. [32] 77
2-7 Through-thickness ZD tension stress-strain curve. (Stenberg, *et al.* [32],[33]) 77
2-8 Through-thickness compressive stress-strain curve. 78
2-9 Through-thickness MD-ZD and CD-ZD shear stress-strain curves. (Stenberg, *et al.* [32],[33]) 78
2-10 Biaxial failure surfaces (deRuvo, *et al.* (1980)). Note: here τ_{12} indicates the in-plane shear stress. 79
2-11 Initial yield surface for biaxial normal stress loadings, showing its four sub-surfaces. ($2k = 4$) 79
2-12 Effect of constant $2k$ on the shape of yield surface. 80
2-13 Schematic of yield surface for general in-plane loading, showing six sub-surfaces. 80
2-14 Hardening of yield surface. ($2k = 4$) 81
2-15 Comparison of experimental and simulated stress-strain curves for uniaxial MD, CD and 45° tension. 81

2-16 Comparison of experimental and simulated lateral strain *vs.* axial strain curves for uniaxial MD and CD tension. 82

2-17 Comparison of experimental and simulated stress-strain curves for uniaxial MD and CD compression. 82

2-18 Comparison of experimental and simulated stress-strain curves for tensile loading in off-axis directions 22.5° and 67° from the MD direction. 83

2-19 Mesh of simulation of straining of TRIPLEX^{TM} rectangular board ($40mm$ long; $30mm$ wide) with central hole. 84

2-20 Contour plot of the in-plane normal stress component T_{XX} before any plasticity developed (Stage A on the corresponding macroscopic stress-strain curve) from simulation of straining of TRIPLEX^{TM} rectangular board ($40mm$ long; $30mm$ wide) with central hole. 85

2-21 Contour plot of the normalized in-plane normal stress component T_{XX} before any plasticity developed from simulation of straining of TRIPLEX^{TM} rectangular board ($40mm$ long; $30mm$ wide) with central hole. 86

2-22 Contour plot of the in-plane normal stress component T_{YY} before any plasticity developed from simulation of straining of TRIPLEX^{TM} rectangular board ($40mm$ long; $30mm$ wide) with central hole. 87

2-23 Contour plot of the in-plane normal stress component T_{XX} from simulation of straining of TRIPLEX^{TM} rectangular board ($40mm$ long; $30mm$ wide) with central hole. 88

2-24 Macroscopic nominal stress *vs.* nominal strain curve for normal stress component T_{XX} from simulation of straining of TRIPLEX^{TM} rectangular board ($40mm$ long; $30mm$ wide) with central hole. 89

2-25 Contour plot of the in-plane normal stress component T_{YY} from simulation of straining of TRIPLEX^{TM} rectangular board ($40mm$ long; $30mm$ wide) with central hole. 90

2-26 Contour plot of the equivalent plastic strain, $\bar{\gamma}$, from simulation of straining of TRIPLEX^{TM} rectangular board ($40mm$ long; $30mm$ wide) with central hole at nominal strain of 5%. 91

2-27 Magnified upper right corner (around the hole) of the contour plot of the equivalent plastic strain, $\bar{\gamma}$, shown in Fig. 2-26. 92

2-28 Mesh of simulation of straining of TRIPLEX^{TM} rectangular board ($40mm$ long; $60mm$ wide) with central hole. 93

2-29 Contour plot of the in-plane normal stress component T_{XX} from simulation of straining of TRIPLEX^{TM} rectangular board ($40mm$ long; $60mm$ wide) with central hole. 94

2-30 Contour plot of the in-plane normal stress component T_{YY} from simulation of straining of TRIPLEX^{TM} rectangular board ($40mm$ long; $60mm$ wide) with central hole. 95

2-31 Contour plot of the equivalent plastic strain, $\bar{\gamma}$, from simulation of straining of TRIPLEX^{TM} rectangular board ($40mm$ long; $60mm$ wide) with central hole. 96

2-32 Mesh of simulation of off-axis straining of TRIPLEX^{TM} rectangular board ($40mm$ long; $30mm$ wide) with central hole. 97

2-33 Contour plot of the in-plane normal stress component T_{XY} before any plasticity developed from simulation of off-axis straining of TRIPLEX^{TM} rectangular board ($40mm$ long; $30mm$ wide) with central hole. 98

2-34 Contour plot of the in-plane normal stress component T_{XY} from simulation of off-axis straining of TRIPLEX^{TM} rectangular board ($40mm$ long; $30mm$ wide) with central hole. 99

2-35 Contour plot of the in-plane normal stress component T_{XX} from simulation of off-axis straining of TRIPLEX^{TM} rectangular board ($40mm$ long; $30mm$ wide) with central hole. 100

2-36 Contour plot of the in-plane normal stress component T_{YY} from simulation of off-axis straining of TRIPLEX^{TM} rectangular board ($40mm$ long; $30mm$ wide) with central hole. 101

2-37 Contour plot of the equivalent plastic strain, $\bar{\gamma}$, from simulation of off-axis straining of TRIPLEX^{TM} rectangular board ($40mm$ long; $30mm$ wide) with central hole. 102

2-38 Comparison of MD tensile stress-strain curve for mechanical and chemical pulp layers (Stenberg [31]) 103

2-39 Comparison of MD and CD tensile stress-strain curve for mechanical pulp layer (Stenberg [31]) 103

2-40 Comparison of experimental and simulated stress-strain curves for MD tensile loading for mechanical pulp layer. 104

2-41 Comparison of experimental and simulated stress-strain curves for CD tensile loading for mechanical pulp layer. 104

2-42 Comparison of experimental and simulated stress-strain curves for MD tensile loading for chemical pulp layer. 105

2-43 Mesh used to reproduce the MD tensile stress-strain curve for TRIPLEX^{TM} using fitted parameters for each of the individual layers. 105

2-44 Comparison of model-reproduced and experimental MD tensile stress-strain curve for TRIPLEX^{TM}. 106

3-1 ZD dilation - shear displacement curve under unconstrained ZD-MD shear(Stenberg, *et al.* [32], [33]). 144

3-2 Pressure sensitivity of shear strength: MD-ZD experimental shear stress-strain curves with different fixed normal stress values. 145

3-3 Experimental peak strength locus and theoretical initial separation surfaces. 145

3-4 Micro-level stress ZD normal strain curve curve obtained by Dunn [18] from SEM. 146

3-5 Triplex MD through-thickness SEM tension image correlated with stress-strain data obtained by Dunn [18](Step 1). 146
3-6 Triplex MD through-thickness SEM tension image correlated with stress-strain data obtained by Dunn [18] (Step 2). 147
3-7 Triplex MD through-thickness SEM tension image correlated with stress-strain data obtained by Dunn [18] (Step 3). 147
3-8 Triplex MD through-thickness SEM tension image correlated with stress-strain data obtained by Dunn [18] (Step 4). 148
3-9 Triplex MD through-thickness SEM tension image correlated with stress-strain data obtained by Dunn [18] (Step 5). 148
3-10 Triplex MD through-thickness SEM tension image correlated with stress-strain data obtained by Dunn [18] (Step 6). 149
3-11 Triplex MD through-thickness SEM tension image correlated with stress-strain data obtained by Dunn [18] (Step 7). 149
3-12 Triplex MD through-thickness SEM tension image correlated with stress-strain data obtained by Dunn [18] (Step 8). 150
3-13 Triplex MD through-thickness SEM tension image correlated with stress-strain data obtained by Dunn [18] (Step 9). 150
3-14 Triplex MD through-thickness SEM tension image correlated with stress-strain data obtained by Dunn [18] (Step 10). 151
3-15 Micro-level stress ZD-MD shear strain curve curve obtained by Dunn [18] from SEM. 151
3-16 Triplex MD through-thickness SEM shear image correlated with stress-strain data obtained by Dunn [18] (Step 1). 152
3-17 Triplex MD through-thickness SEM shear image correlated with stress-strain data obtained by Dunn [18] (Step 2). 152
3-18 Triplex MD through-thickness SEM shear image correlated with stress-strain data obtained by Dunn [18] (Step 3). 153

3-19 Triplex MD through-thickness SEM shear image correlated with stress-strain data obtained by Dunn [18] (Step 4). 154
3-20 Triplex MD through-thickness SEM shear image correlated with stress-strain data obtained by Dunn [18] (Step 5). 155
3-21 Triplex MD through-thickness SEM shear image correlated with stress-strain data obtained by Dunn [18] (Step 6). 155
3-22 Illustration of 3-D interface between two solids. 156
3-23 Flow directions on the yield surface. 156
3-24 Kinematics: 2-D interface element. 157
3-25 Comparison of ZD tensile stress-strain curve of the outer interface and the entire composite of TRIPLEX^{TM} 157
3-26 Through-thickness tensile stress-strain curve from one-element FEM simulation 158
3-27 Through-thickness MD-ZD shear stress-strain curve from one-element FEM simulation. 158
3-28 Through-thickness dilation *vs.* shear displacement (MD-ZD) curve from one-element FEM simulation. 159
3-29 Through-thickness normal stress *vs.* shear displacement (MD-ZD) curve from one-element FEM simulation with zero through-thickness normal displacement ($\Delta_n = 0$). 159
3-30 Pressure sensitivity curve of through-thickness shear stress-strain behavior (MD-ZD) from one-element FEM simulations. 160
3-31 Loading/unloading stress-strain curve from one-element FEM simulation 160
3-32 Response of non-softening interface element in the traction space under combined through-thickness loading of monotonically increasing proportional relative separation and sliding. ($d\Delta_t/d\Delta_n = 1.0$) 161
3-33 Response of softening interface element in the traction space under combined through-thickness loading of monotonically increasing proportional relative separation and sliding. ($d\Delta_t/d\Delta_n = 1.0$) 161

3-34 Initial defect distribution 1. 162

3-35 Initial defect distribution 2. 163

3-36 Comparison of ZD tension stress-strain curves from experiment and FEM. 164

3-37 Contour of local normal stress component in ZD from pure tension simulations using defect distribution 1 (Fig. 3-34). A-D, respectively, denote contours at load levels of the correspondingly named points on the stress-strain curves shown in Fig. 3-36 165

3-38 Contour of normal stress component in ZD from pure tension simulations using defect distribution 1 (Fig. 3-34) (continued). E-H, respectively, denote contours at load levels of the correspondingly named points on the stress-strain curves shown in Fig. 3-36 166

3-39 Magnified view of central part of contour of normal stress component in ZD from pure tension simulation using defect distribution 1 (Fig. 3-34). Relative position $0.3 \leq x \leq 0.65$. 167

3-40 Magnified view of central part of contour of normal stress component in ZD from pure tension simulation using defect distribution 1 (Fig. 3-34) (continued). Relative position $0.3 \leq x \leq 0.65$. 168

3-41 Comparison of MD-ZD pure shear stress applied shear displacement curves from experiment and FEM. 169

3-42 Comparison of dilation curves under pure shear from experiment and FEM. 169

3-43 Contour of through-thickness shear stress component from pure shear simulation using defect distribution 1 (Fig. 3-34). A-D, respectively, denote contours at load levels of the correspondingly named points on the stress-strain curves shown in Fig. 3-41. 170

3-44 Contour of through-thickness shear stress component from pure shear simulation using defect distribution 1 (Fig. 3-34) (continued). E-H, respectively, denote contours at load levels of the correspondingly named points on the stress-strain curves shown in Fig. 3-41. 171

3-45 Magnified view of central part of contour of normal stress component in ZD from pure shear simulation using defect distribution 1 (Fig. 3-34). Relative position $0.3 \leq x \leq 0.65$. 172

3-46 Magnified view of central part of contour of normal stress component in ZD from pure shear simulation using defect distribution 1 (Fig. 3-34) (continued). Relative position $0.3 \leq x \leq 0.65$. 173

3-47 Pressure sensitivity of shear strength: Comparison of experimental and numerical results in MD-ZD. 174

3-48 Contour of through-thickness normal stress component from combined through-thickness shear and tension simulation using defect distribution 1 (Fig. 3-34) (MD-ZD). 175

3-49 History of applied boundary conditions for from FEM simulation using defect distribution 1 (Fig. 3-34) 176

3-50 MD-ZD pure shear stress applied shear displacement curves from FEM using defect distribution 1 (Fig. 3-34) (first stage of deformation). . . 176

3-51 ZD normal stress *vs.* applied normal displacement curves from FEM using defect distribution 1 (Fig. 3-34) (second stage of deformation). . 177

3-52 Mesh of the paperboard at different stages of deformation from the in-plane buckling simulation of TRIPLEX^{TM}. 178

3-53 Compressive stress *vs.* applied compressive displacement curve obtained from in-plane buckling simulation of TRIPLEX^{TM}. 179

4-1 Experimental apparatus for conducting the punching test as the first step of the converting process [18] 192

4-2 Experimental apparatus for conducting the folding test as the last step of the converting process [18] 193
4-3 Illustration of the creasing/folding process, part (a), creasing. 193
4-4 Illustration of the converting process, part (b), bending. 194
4-5 SEM image of TRIPLEX^{TM} MD punching process (step 1) [18] . . . 195
4-6 Contour plot of MD normal stress from simulation of SEM TRIPLEX^{TM} MD punching process corresponding to that shown in Fig. 4-5. 195
4-7 SEM image of TRIPLEX^{TM} MD punching process (step 2) [18]. . . . 196
4-8 Contour plot of MD normal stress from simulation of SEM TRIPLEX^{TM} MD punching process corresponding to that shown in Fig. 4-7. 196
4-9 SEM image of TRIPLEX^{TM} MD punching process (step 4) [18]. . . . 197
4-10 Contour plot of MD normal stress from simulation of SEM TRIPLEX^{TM} MD punching process corresponding to that shown in Fig. 4-9. 197
4-11 SEM image of TRIPLEX^{TM} MD punching process (step 6) [18]. . . . 198
4-12 Contour plot of MD normal stress from simulation of SEM TRIPLEX^{TM} MD punching process corresponding to that shown in Fig. 4-11. . . . 198
4-13 SEM image of TRIPLEX^{TM} MD punching process (step 7) [18]. . . . 199
4-14 Contour plot of MD normal stress from simulation of SEM TRIPLEX^{TM} MD punching process corresponding to that shown in Fig. 4-13. . . . 199
4-15 SEM image of TRIPLEX^{TM} MD punching process (step 8) [18]. . . . 200
4-16 Contour plot of MD normal stress from simulation of SEM TRIPLEX^{TM} MD punching process corresponding to that shown in Fig. 4-15. . . . 200
4-17 Punching force *vs.* punching distance curve for the male die obtained from FEM simulation of the punching process as first step of a converting process. 201
4-18 SEM image of TRIPLEX^{TM} MD folding process (step 1) [18]. 202
4-19 Contour plot of initial equivalent plastic strain from simulation of SEM TRIPLEX^{TM} prior to MD folding process corresponding to that shown in Fig. 4-18. 202

4-20 SEM image of TRIPLEX^{TM} MD folding process (step 3) [18]. 203
4-21 Contour plot of MD normal stress from simulation of SEM TRIPLEX^{TM} MD folding process corresponding to that shown in Fig. 4-20. 203
4-22 SEM image of TRIPLEX^{TM} MD folding process (step 6) [18]. 204
4-23 Contour plot of MD normal stress from simulation of SEM TRIPLEX^{TM} MD folding process corresponding to that shown in Fig. 4-22. 204
4-24 Bending moment *vs.* bending angle curve obtained from FEM simulation of the folding process as last step of a converting process. 205
4-25 Illustration of location of a representative interface element used to investigate behavior of the interface during converting process. 205
4-26 Time history of the relative interface normal and tangential separation of the representative interface element shown in Fig. 4-25 during the entire converting process. 206
4-27 Time history of the accumulated damage inside the representative interface element shown in Fig. 4-25 during the entire converting process. 207
4-28 SEM image of TRIPLEX^{TM} MD punching process (step 1, male die width $0.84mm$ and female die width $2.03mm$) [18]. 208
4-29 Contour plot of MD normal stress from simulation of SEM TRIPLEX^{TM} MD punching process corresponding to that shown in Fig. 4-28. . . . 208
4-30 SEM image of TRIPLEX^{TM} MD punching process at the last step (male die width $0.84mm$ and female die width $2.03mm$) [18]. 209
4-31 Contour plot of MD normal stress from simulation of SEM TRIPLEX^{TM} MD punching process corresponding to that shown in Fig. 4-30. . . . 209
4-32 SEM image of TRIPLEX^{TM} MD punching process at the last step of unloading (male die width $0.84mm$ and female die width $2.03mm$) [18]. 210
4-33 Contour plot of MD normal stress from simulation of SEM TRIPLEX^{TM} MD punching process corresponding to that shown in Fig. 4-32. . . . 210
4-34 SEM image of TRIPLEX^{TM} MD punching process at the first step of folding (male die width $0.84mm$ and female die width $2.03mm$) [18]. . 211

4-35 Contour plot of MD normal stress from simulation of SEM TRIPLEX^{TM} MD punching process corresponding to that shown in Fig. 4-34. . . . 211
4-36 SEM image of TRIPLEX^{TM} MD punching process at step 2 of folding (male die width 0.84mm and female die width 2.03mm) [18]. 212
4-37 Contour plot of MD normal stress from simulation of SEM TRIPLEX^{TM} MD punching process corresponding to that shown in Fig. 4-36. . . . 212
4-38 SEM image of TRIPLEX^{TM} MD punching process at step 3 of folding (male die width 0.84mm and female die width 2.03mm) [18]. 213
4-39 Contour plot of MD normal stress from simulation of SEM TRIPLEX^{TM} MD punching process corresponding to that shown in Fig. 4-38. . . . 213
4-40 SEM image of TRIPLEX^{TM} MD punching process at the final step of folding (male die width 0.84mm and female die width 2.03mm) [18]. . 214
4-41 Bending moment *vs.* bending angle curve obtained from FEM simulation of the folding process as last step of a converting process. (male die width 0.84mm and female die width 2.03mm) 214
4-42 Schematics of the creasability test apparatus. 215
4-43 Illustration of the creasability test, part (a), creasing. 216
4-44 Illustration of the creasability test, part (b), folding. 217
4-45 Geometry of the creasability test. 218
4-46 Illustration of parameters whose effect is investigated in the creasability test. 218
4-47 Comparison of numerical and experimental bending moment *vs.* bending angle curve for creasability test 1. 219
4-48 Comparison of numerical and experimental bending moment *vs.* bending angle curve for creasability test 2. 219
4-49 Comparison of numerical and experimental bending moment *vs.* bending angle curve for creasability test 3. 220
4-50 Comparison of numerical and experimental bending moment *vs.* bending angle curve for creasability test 4. 220

4-51 Comparison of numerical and experimental bending moment *vs.* bending angle curve for creasability test 5. 221
4-52 Contour plot of MD normal stress component at the final stage of the FEM creasability test simulation. 221
4-53 Contour plot of the equivalent plastic strain at the final stage of the FEM creasability test simulation. 222

List of Tables

2.1 Experimental results of uniaxial tensile tests. (Stenberg [31]) 71

2.2 Elastic out-of-plane properties. (Stenberg, *et al.* [32, 33]) 71

2.3 Non-zero components of the sub-surface normals used in modeling TRIPLEX^{TM}, expressed in the material coordinates 71

2.4 Elastic constants used by model for the TRIPLEX^{TM} composite laminate. 72

2.5 In-plane yielding and hardening parameters used to model TRIPLEX^{TM}. 72

2.6 Elastic constants used for the chemical pulp material. 72

2.7 Elastic constants used for the mechanical pulp material. 72

2.8 In-plane yielding and hardening parameters used by model for mechanical pulp layers in TRIPLEX^{TM}. 72

2.9 In-plane yielding and hardening parameters used by model for chemical pulp layers in the TRIPLEX^{TM} composite laminate. 73

3.1 Parameters used for the outer interfaces (MD-ZD plane) 135

3.2 Parameters used for the inner interfaces (MD-ZD plane) 136

4.1 Control parameters used for the creasability tests. 189

4.2 Comparison of peak bending moment for the creasability tests. 190

A.1 Definition of properties 228

Chapter 1

Introduction

Paper and paperboard are two of the most commonly utilized materials in nearly every industry. Paper is formed by draining a suspension of fibers in a fluid through a filter screen to form a sheet of pulp fibers. Paperboard is in general composed of several pulp fiber sheets bonded by starch or adhesive material, and is usually a multi-layered structure. Schematics of typical paper and paperboard macrostructure and microstructure are shown in Fig. 1-1, which also depicts the common nomenclature for the three orthogonal directions of paper and paperboard. "MD" refers to the machine (rolling) direction, and "CD" refers to the cross or transverse direction. The machine and cross directions form the plane of the structure, and ZD refers to the out-of-plane (or through-thickness) direction. Due to the continuous nature of the paper-making process, fibers are primarily oriented in the plane; furthermore, within the plane, fibers are more highly oriented in the MD than the CD. In this thesis, to simplify notation, the 1-direction is used to represent the MD, the 2-direction for CD and the 3-direction for ZD.

In contrast to the wide applications of paper material and the existence of paper since ancient times in China, there is a scarcity of constitutive models describing the mechanical behavior of paper and paperboard. In the paper industry, trial and error approaches are still commonly used for the design of paperboard products and manufacturing processes. Although mechanical testing can be conducted to help de-

sign the processes, an experimental database approach is an expensive and laborious approach, given the wide range in material and processing parameters of paper and paperboard, including different mechanical/chemical treatments, surface treatments (e.g., coatings, prints), pulp and layering parameters (thickness, order etc.), loading geometry, and service conditions. Analytical models with the capability to capture the mechanical behavior of paper/paperboard offer the possibility to computationally assess the parameter space and optimize the products and process design. The purpose of this research is to develop such constitutive models, based on experimental observation of stress-strain behavior of paper and paperboard, which can be applied to simulate and predict behavior of paper and paperboard in their manufacturing process or in service.

1.1 Description of material

The basic component of paper and paperboard is wood pulp. Desired properties of paper and paperboard can be achieved by many ways; *e.g.*, using different wood fibers, different fiber density (grammage [grams/area]), applying different chemical and mechanical processing, different structure (*e.g.*, number of pulp layers), *etc.* In the paper-making process, wood pulp is suspended in a dilute aqueous solution before being sprayed onto a moving filter mesh to create one layer of the paper pulp sheet. For paperboard, several of these pulp sheets are bonded together with starch or adhesives. Bond density is lower between layers than within them. Coming off the filtering mesh, the paper sheet or the paperboard laminate is pressed through large cylindrical roller to densify and squeeze out moisture. The sheet or laminate is further dried by pressing it through rollers while subjected to elevated temperatures. Rolling of the sheets results in densification and improves the intra-layer and inter-layer bonding.

Depending on fiber type, fiber density and the chemical/mechanical treatment, the mechanical behavior of different types of paper and paperboard differ in detail. However, general characteristics of the response remain similar. In this contribution,

the anisotropic elastic-plastic behavior of paper and paperboard is illustrated using TRIPLEX^{TM}[1] paperboard as an exemplar material. TRIPLEX^{TM} is a commercial product of STORA-ENSO. It is comprised of five layers: the three-layer core is made of mechanically-processed softwood pulp (commonly termed "mechanical" layers), and the two outer layers (one on each side of the core) are made of bleached kraft pulp (commonly termed "chemical" layers). This is shown schematically in Fig. 1-1. A layer of starch or other adhesive is sprayed between adjacent layers during the lamina consolidation processing stage. The two outer layers of bleached kraft pulp are designed to be stiffer than the core's mechanically-processed softwood pulp. The final thickness of the board is approximately $0.45mm$, and the grammage is about $280g/m^2$.

The microstructure of TRIPLEX^{TM} was studied by Dunn [18] and Smith [5] through SEM (Scanning Electron Microscope) images. Fig. 1-2 to Fig. 1-4 depict an in-plane view of a coated chemical layer with image magnification from low to high. Images of the mechanical layer were also obtained by carefully peeling off the chemical layers from TRIPLEX^{TM}. Fig. 1-5 to Fig. 1-7 show the MD-CD planar view (looking from ZD) of the mechanical layer with increasing magnifications. From these pictures, we can observe that the majority of fibers are along or within a small angle of the machine direction. It is also obvious that the fibers are densely interconnected with each other. Because the chemical layer experiences the pressing from the roller in the machine direction more directly than does the mechanical layer, this "preferred" fiber orientation effect is slightly more pronounced in the chemical layer. By comparing the planar views of the chemical and mechanical layers, we can also observe that the fiber density of the chemical layer is higher than that of the mechanical layer. By looking at these images and the corresponding length scale, we note that the fiber length is of the order of $1-5mm$ and the fibers possess the shape of a flattened tube, with fiber width/diameter approximately of the order of 10 - $50\mu m$.

Micrographs of sample TRIPLEX^{TM} paperboard were also taken edge-on. Fig. 1-

[1]TRIPLEX^{TM} is a trademark of STORA-ENSO, Sweden.

8 and Fig. 1-9 depict a cross-section view of the paperboard in the MD-ZD plane (looking from the CD). Those from the CD-ZD plane (looking from the MD) are shown in Fig. 1-10 and Fig. 1-11. Again, from these images we can see the flattened tube shape of the fiber (flat because of the rolling and pressing). From the MD-ZD view images, we primarily see the fibers that have been cut longitudinally along its axial direction because the majority of the tubes are oriented in the Machine Direction. In contrast, from the CD-ZD plane view pictures, we observe the oval shape of the cross-sections of the fibers pointing out of the plane.

1.2 Review of experimental behavior of paperboard

The preferential fiber orientation in paper and paperboard results in highly anisotropic mechanical behavior, including anisotropic elasticity, initial yielding, strain-hardening and tensile failure strength:

- Anisotropic elastic constants for paper and paperboard have been measured by several investigators (e.g., Mann, *et al.*[23], Castegnade, *et al.*[11], Persson[28], Koubaa and Koran [4]). Their data show that the through-thickness moduli are at least two orders of magnitude less than the in-plane moduli. In-plane data of Persson [28] and Stenberg, *et al.*[31] show that moduli in the MD are 2-4 times greater than those of the CD.

- The Persson [28] data on paperboard also shows that the initial tensile yield strength ($\sim$ proportional limit) in the through-thickness direction is two orders of magnitude lower than the in-plane initial yield strength values. The Stenberg, *et al.* [31] data on multi-layer paperboard and single-layer pulp shows similar results. Within the plane, these data show that the initial tensile yield strength of paper and paperboard in the MD is typically greater than that in the CD by a factor of $2-4$. The Stenberg, *et al.* [31] data also show an asymmetry in the initial yield strength for in-plane tension and compression in both the machine

and cross directions.

- The in-plane tensile stress-strain curves of Persson [28] and Stenberg, *et al.* [31] on paperboard show substantial strain-hardening in which the yield strength increased by more than a factor of two after a strain of less than 5%. The in-plane strain-hardening is also highly anisotropic. The percentage strain hardening achieved in MD tension is greater than that obtained in CD tension.

- The Persson [28] and Stenberg, *et al.* [31] data also show that the in-plane tensile failure strength in the MD is greater than that of the CD by a factor of $2 - 4$.

- Stenberg, *et al.* [31] data indicate that initial yield strengths as well as failure strengths for paperboard are different for tension and compression in the same direction.

- Biaxial-stress failure loci (Gunderson, *et al.* [16],[17], deRuvo, *et al.* [13] and Fellers, *et al.* [15]) show substantially different failure strengths in machine and cross directions. These data also show that failure tends to be dominated by one or the other of these two directions when subjected to combined loading in both directions. Data by Gunderson, *et al.* [16],[17], and Fellers, *et al.* [15] also show that the failure strength for paper is different in tension and compression in the same direction.

Most experimental investigations on mechanical behavior of paper and paperboard have been concentrated on the in-plane behavior. However, during manufacturing and in-service applications, paperboard is often subjected to combined loadings which include out-of-plane deformations. The out-of-plane loadings can cause interfacial delamination to separate the paperboard layers. In some instances delamination is desirable, as in the case of creasing, whereby a punching process locally damages the interface in a controlled manner to enable accurate formation of corners during the subsequent folding of paperboard. In other instances, however, delamination is

undesirable, such as during in-service loading, where, for example, a box may be dropped or subjected to bending (*e.g.*, Carlsson, *et al.* [21] and Donner and Backer [10]). In either situation, the out-of-plane behavior is crucial to the final outcome of the process.

In work by Dunn [18] and Smith [5], the deformation mechanisms operative during through-thickness loading of paperboard are experimentally investigated. Scanning electron microscopy is used to monitor the evolution in microstructure during through-thickness tensile and shear loading. Results show that the initiation, interaction and propagation of delamination along interfaces between paperboard laminae play a crucial role in the damage and failure of the laminated structure under out-of-plane loading. In work by Stenberg, *et al.* [32], [33], a series of modified ARCAN [6] testing systems are used to obtain nominal stress-strain curves of paperboard under various combined out-of-plane loading conditions.

In addition to the out-of-plane tests, Stenberg [31] and Dunn [18] also conducted extensive testing on the in-plane behavior of TRIPLEX^{TM} to facilitate the development of constitutive models to capture the in-plane behavior. These results will be reviewed in more detail later in this thesis.

1.3 Research motivation and framework of this research

Besides the general purpose of developing constitutive models to simulate and predict mechanical behavior of paper and paperboard, this research was also partly motivated by the need of the paper and pulp industry to have an analytical design tool to simulate and predict the behavior of the paperboard during two of the key processes of producing paperboard packages: creasing and subsequent folding. These two processes are part of the paperboard converting process, which converts paper/paperboard into specific end products.

Creasing/folding can be divided into three steps: (1) The creasing or punching of the paperboard into a female die by a male die. (2) Unloading of the the board by removing the male die. (3) Folding of the creased board to form corners with the desired shape as parts of the paperboard package. The entire process is schematically illustrated in Fig. 1-12.

In the first step, as shown in part (b) of Fig. 1-12, the paperboard is punched between a narrow male and female die. The purpose of this process is to create interlaminar damage inside the creased region primarily by out-of-plane shearing. After the punching process, the paperboard is taken out and folded in the direction that would make the punched area bulge out to form the interior of the corner of a paperboard box. Micromechanically, the crease is formed because the in-plane compressive stress and out-of-plane shear stress introduced by the bending cause the paperboard layers to separate along the pre-damaged surfaces created by the punching process. This converting process involves complicated, history-dependent behavior of the paperboard under both in-plane and out-of-plane loadings. For the paper and pulp industry, it is very important to be able to obtain a good quality crease, such that the overall designed shape can be obtained for the final paperboard products, while securing the capability of the boxes to sustain loads during service.

The final quality of the crease can be influenced by many different factors in addition to the structure and the material properties of the paperboard, such as the geometry of the male and female die during the punching process, the depth of the punching, the way the creased paperboard is folded, *etc.* (some of these processing parameters are illustrated in Fig. 1-13) Fig. 1-14 shows the SEM picture of a good crease and Fig. 1-15 shows that of a bad one. If there is insufficient bulging out of the crease in the form of delamination at the outside of the crease, the outside layer of material may tear or fracture, which will result in a bad crease and a loss of end product function. A crease is also considered of poor quality if delamination occurs preferentially toward one side of the bend rather than in the middle, because this weakens the crease's capability to take loads along its axis, which can result

in undesirable wandering of the package edge. Considering the complexity of the creasing/folding process, it is obvious that analytical models capable of simulating the process are very desirable because going through the traditional trial-and-error approach for designing this process can be very expensive and time-consuming. One of the end-goals of this research is to develop such an analytical tool.

Based on the experimental results and motivations discussed above, in this research we propose two constitutive laws to model the three-dimensional mechanical behavior of paperboard under combined (both in-plane and out-of-plane) loading conditions. First, a three-dimensional, anisotropic constitutive law is introduced to model the elastic-plastic in-plane behavior of paperboard layers (or paper sheets). The initial yield surface of the model is directly constructed from internal state variables comprising the yield strengths measured in various loading directions and the corresponding ratios of plastic strain components. An associated flow rule is used to model the plastic flow of the material. Anisotropic strain-hardening of yield strengths is introduced to model the evolution in the yield surface with strain. With the inelastic out-of-plane behavior captured by an interface model, this constitutive law will take the out-of-plane behavior as elastic. Second, due to the importance of inelastic out-of-plane behavior of paperboard in processes such as converting, we propose a three-dimensional interface traction *vs.* relative-displacement separation model where a limiting separation surface (analogous to a yield surface) in the normal-shear traction space evolves with the inelastic component of the relative interface displacement following an internal state variable approach. The interface model is capable of simulating the delamination of paperboard along its interfaces, which is the main source of paperboard inelastic out-of-plane deformation as shown by experiments (*e.g.*, Dunn [18] and Carlsson [21]). Schematics of how these two constitutive laws work together to model the behavior of the TRIPLEX^{TM} paperboard are illustrated in Fig. 1-16.

Details of literature review on the constitutive models for paper and paperboard will be reviewed in the next two chapters before the proposed models are introduced.

1.4 Outline of the thesis

The three-dimensional elastic-plastic constitutive law for modeling the behavior of the pulp layers will be introduced first in chapter 2. Related literature will be reviewed before presenting the model developed in this research. The model will then be implemented into the commercial Finite Element Method (FEM) software package ABAQUS, and simulations will be conducted to test the capability and robustness of the implementation.

The interface constitutive model will be presented in Chapter 3. The implemented model will then be used to simulate behavior of paperboard under various through-thickness or combined in-plane and out-of-plane loadings. Numerical results obtained will be compared with experimental data, demonstrating the capability of the model to capture inelastic out-of-plane behavior of paperboard and, potentially, of other laminated composite materials.

Armed with the in-plane and interface constitutive models, the creasing/folding process will be simulated in Chapter 4. First, the numerical results from simulation of SEM creasing and folding tests conducted by Dunn[18] will be compared to the experiments. Second, simulation results of the standard creasibility tests used in the industry will be introduced and compared with experimental data.

In Chapter 5, the entire modeling framework is reviewed and future possible improvements of the models are discussed.

A procedure for identifying the needed material properties from experiments is provided in the appendix.

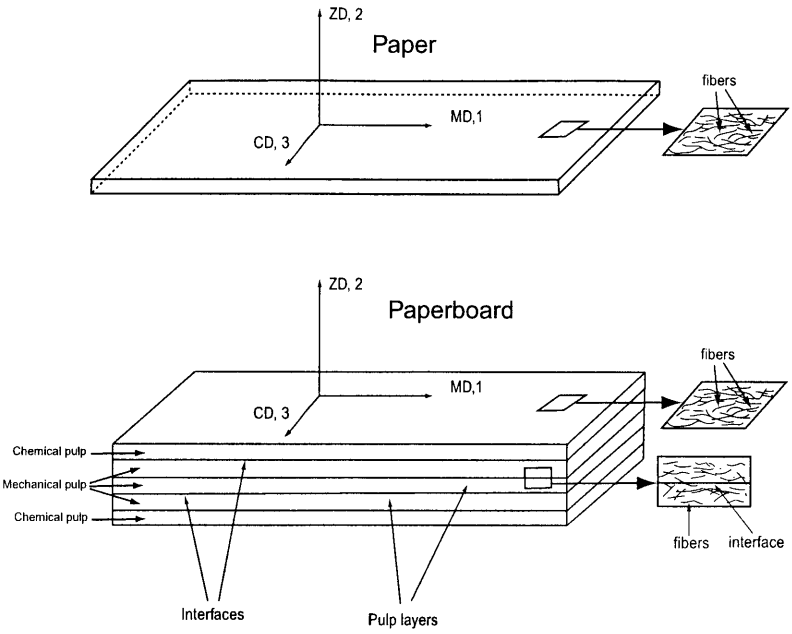

Figure 1-1: Schematics of paper and paperboard macrostructure and microstructure.

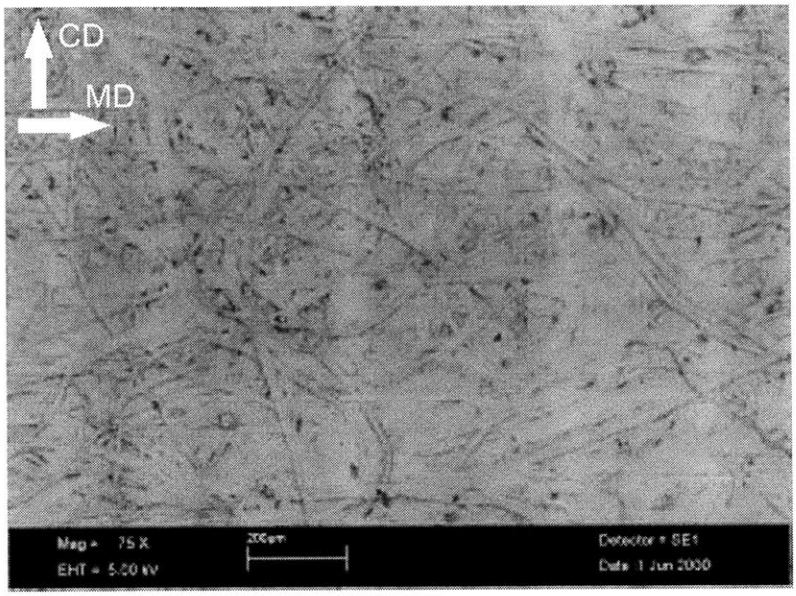

Figure 1-2: SEM image of MD-CD planar view of the chemical layer of coated TRIPLEX^{TM} at low magnification. (Dunn[18])

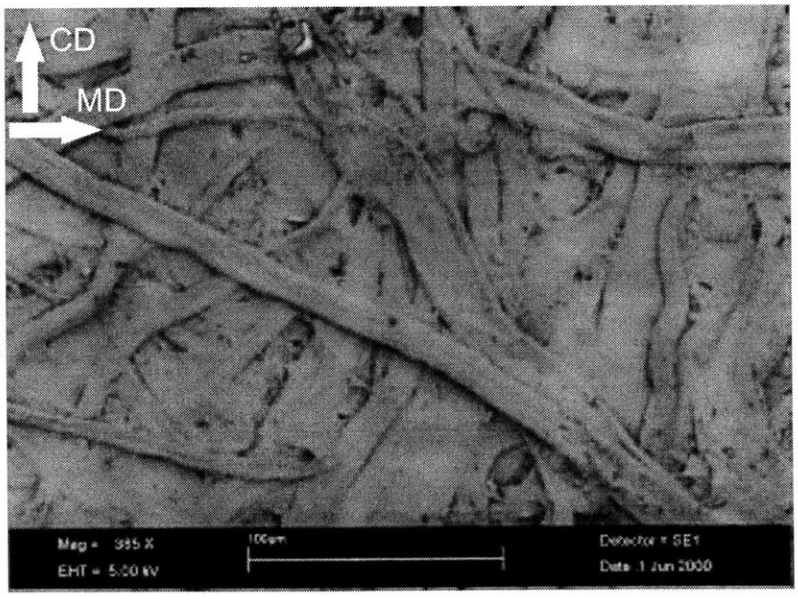

Figure 1-3: SEM image of MD-CD planar view of the chemical layer of coated TRIPLEX^{TM} at intermediate magnification. (Dunn[18])

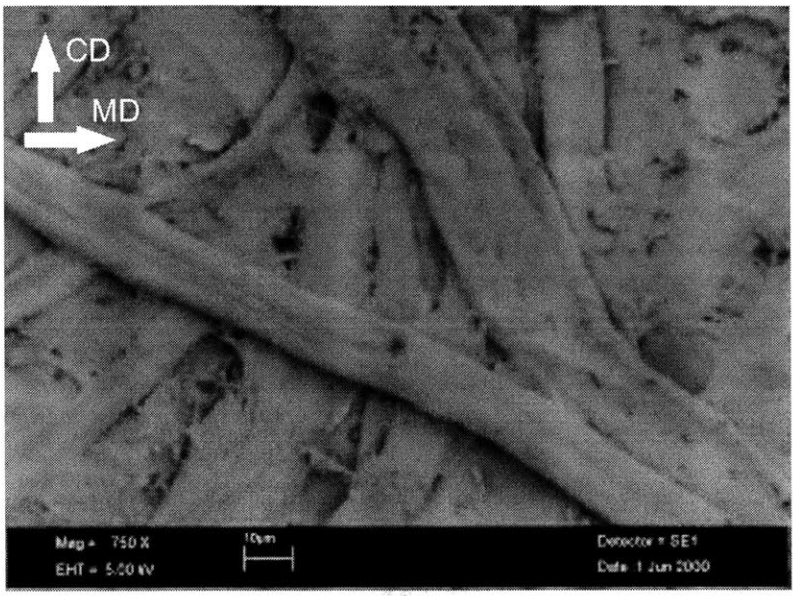

Figure 1-4: SEM image of MD-CD planar view of the chemical layer of coated TRIPLEX^{TM} at high magnification. (Dunn[18])

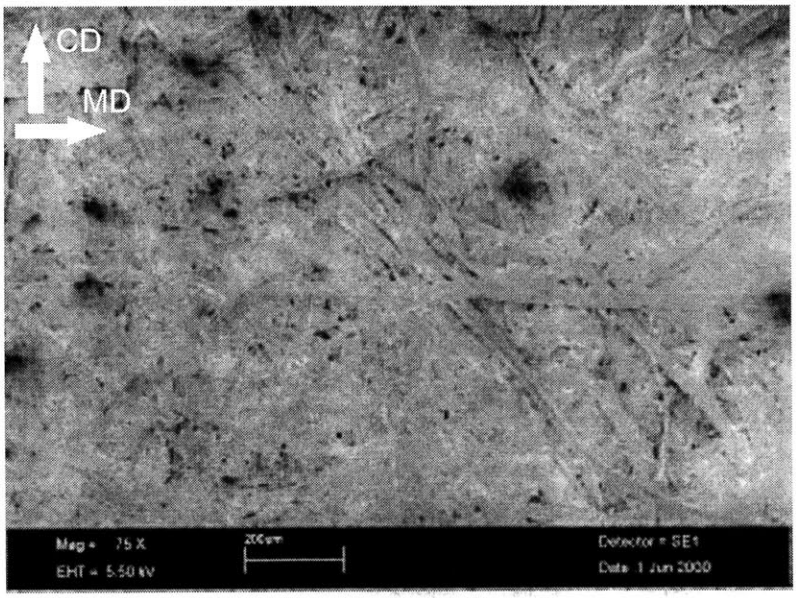

Figure 1-5: SEM image of MD-CD planar view of the mechanical layer of coated TRIPLEX^{TM} at low magnification. (Dunn[18])

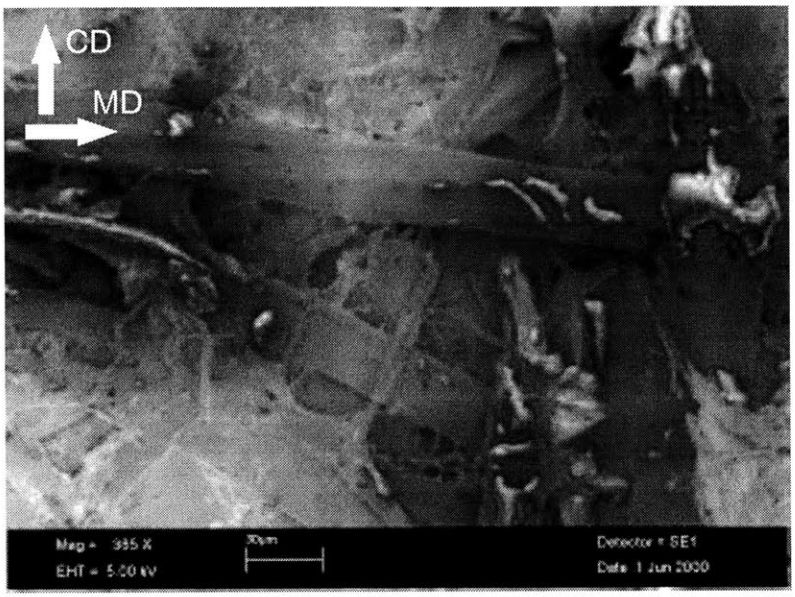

Figure 1-6: SEM image of MD-CD planar view of the mechanical layer of coated TRIPLEX^{TM} at intermediate magnification. (Dunn[18])

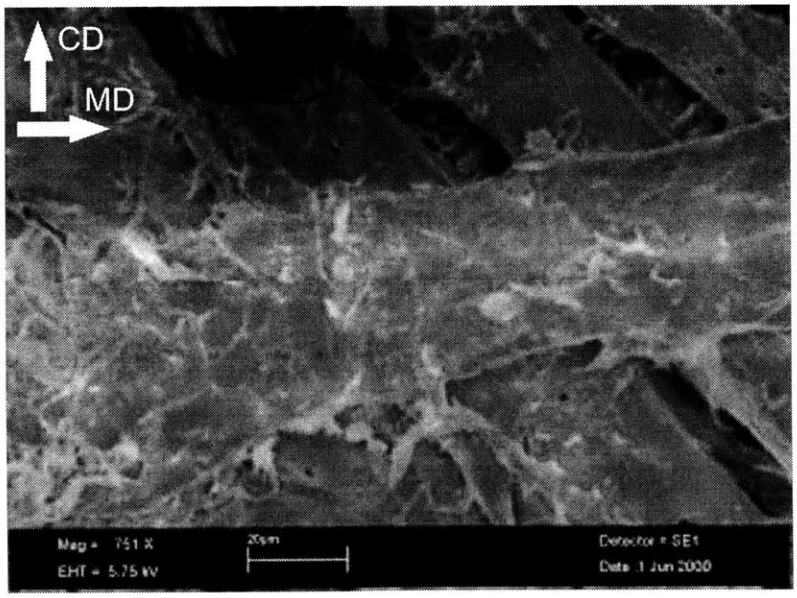

Figure 1-7: SEM image of MD-CD planar view of the mechanical layer of coated TRIPLEX^{TM} at high magnification. (Dunn[18])

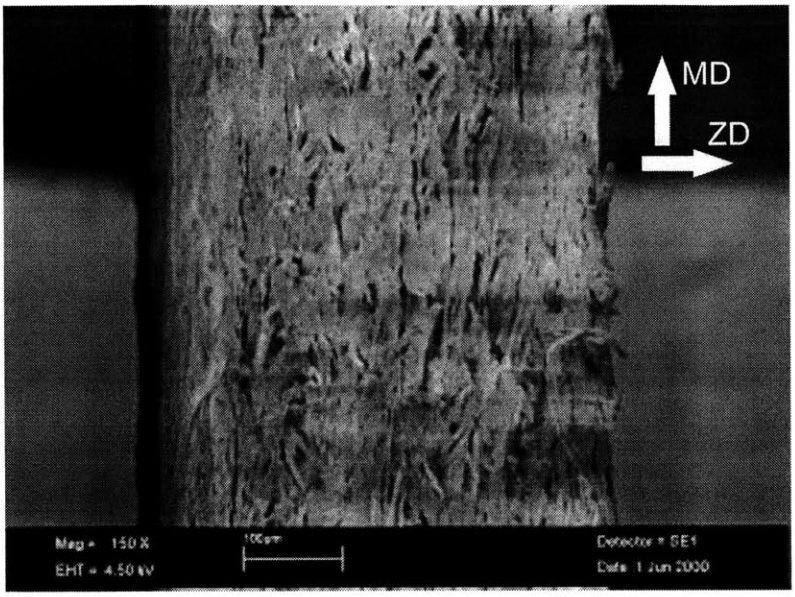

Figure 1-8: SEM image of ZD-MD side view of the TRIPLEX^{TM} at low magnification. (Dunn[18])

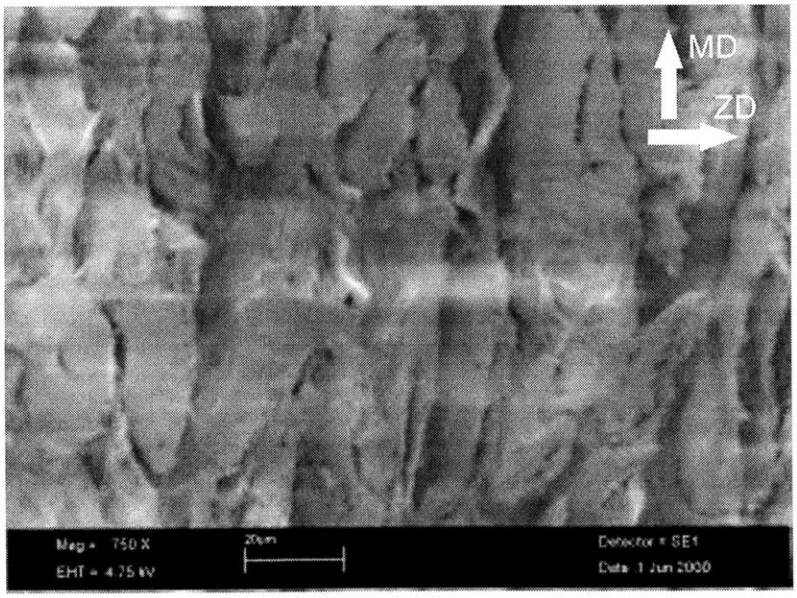

Figure 1-9: SEM image of ZD-MD side view of the TRIPLEX^{TM} at high magnification. (Dunn[18])

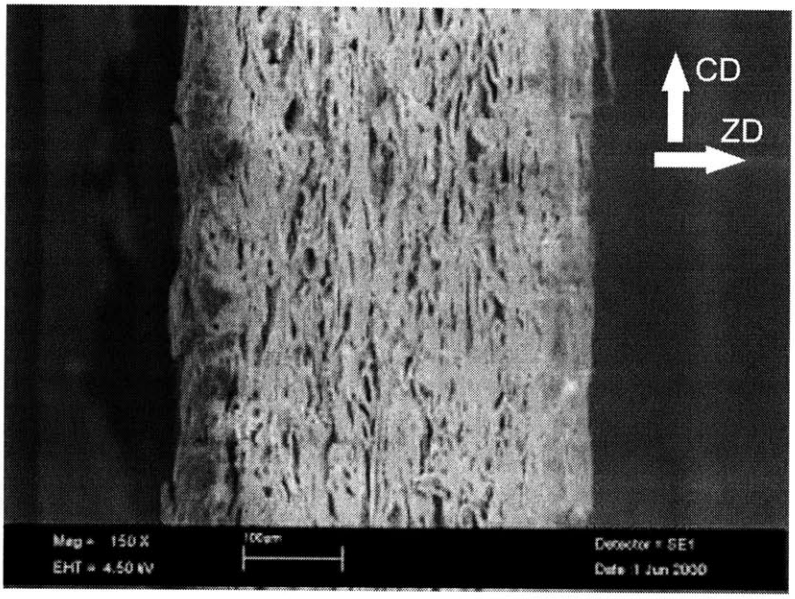

Figure 1-10: SEM image of ZD-CD side view of the TRIPLEX^{TM} at low magnification. (Dunn[18])

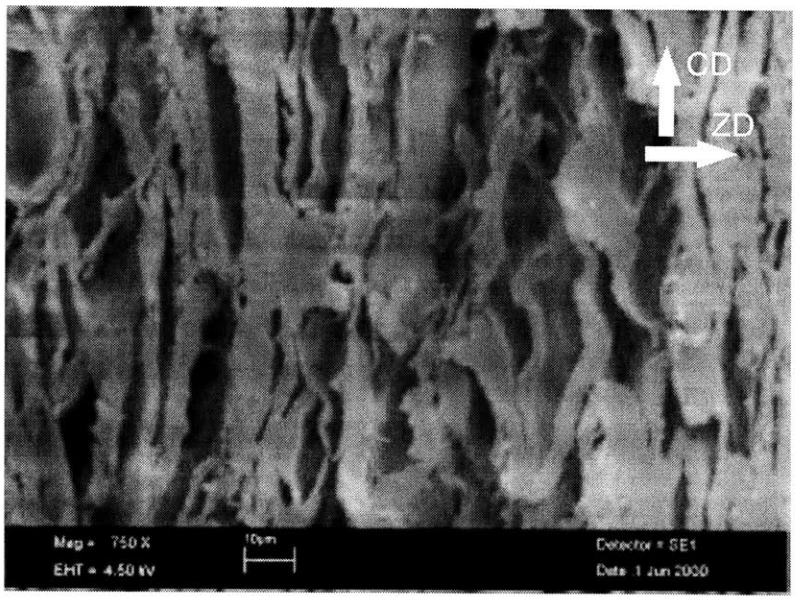

Figure 1-11: SEM image of ZD-CD side view of the TRIPLEX^{TM} at high magnification. (Dunn[18])

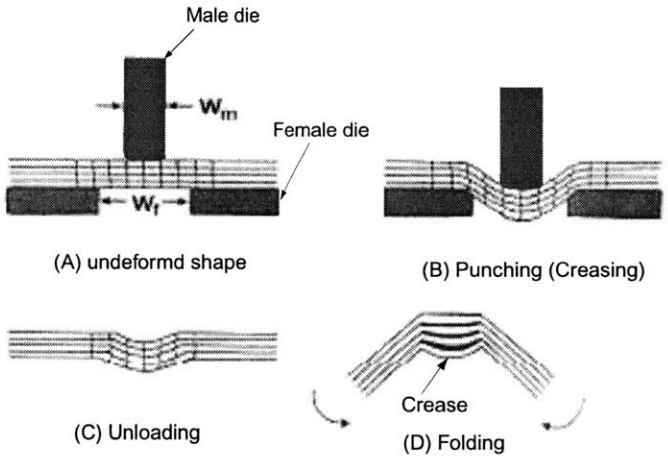

Figure 1-12: A schematic of the paperboard converting process.

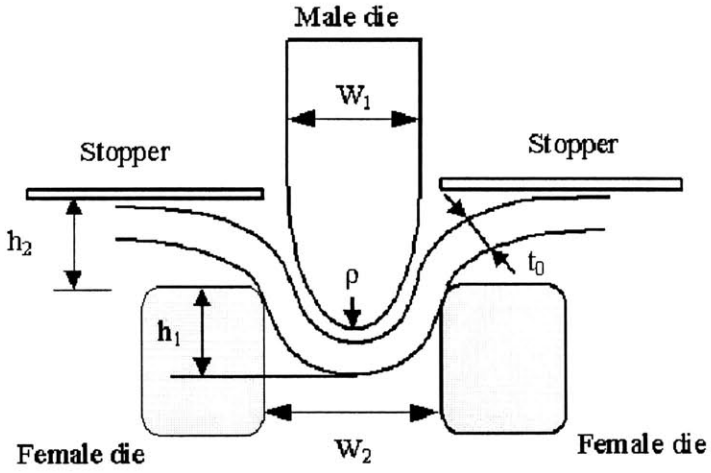

Figure 1-13: Example of parameters that can influence the final quality of a crease.

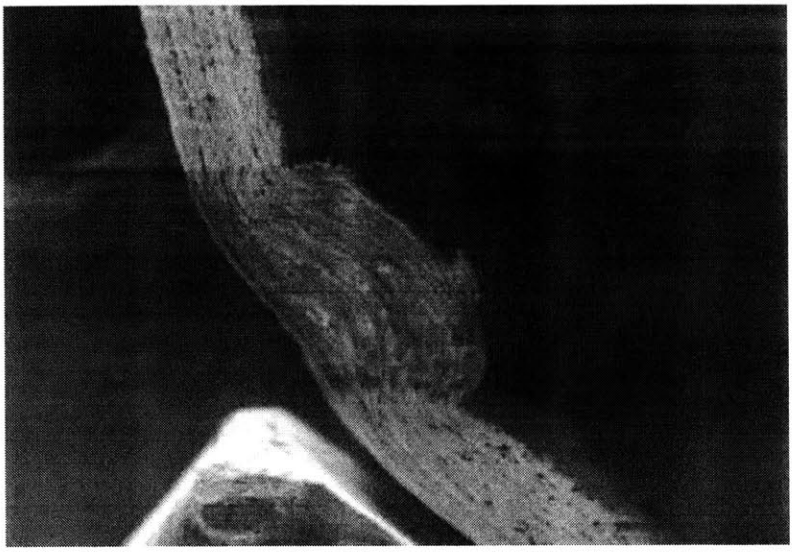

Figure 1-14: SEM image of a good crease. (Tetra Pak)

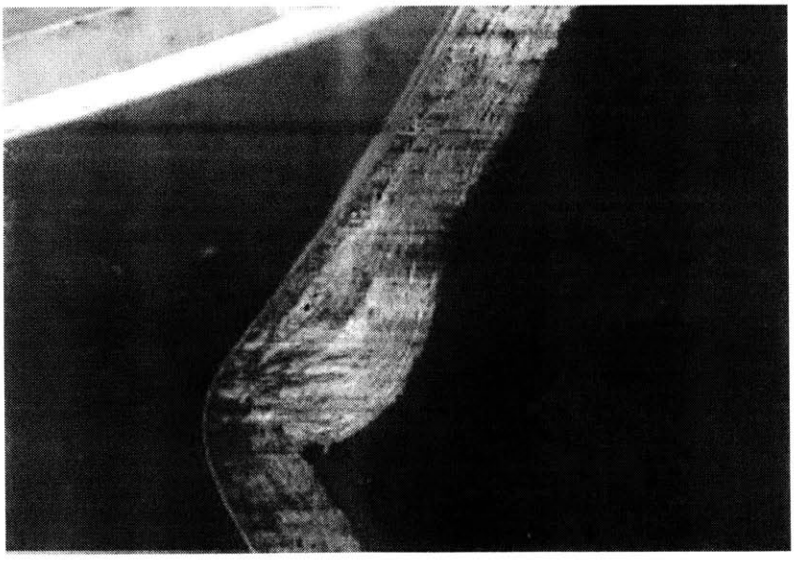

Figure 1-15: SEM image of a bad crease. (Tetra Pak)

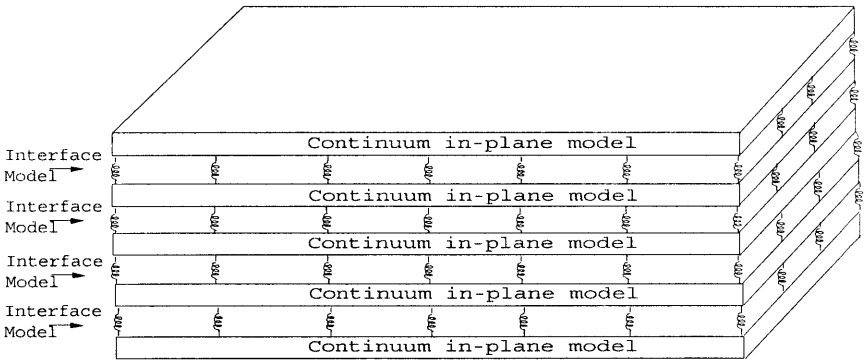

Figure 1-16: Illustration of the framework of modeling the TRIPLEX^{TM} paperboard.

Chapter 2

In-plane Constitutive Model

2.1 Introduction

Many material models have been proposed to describe the mechanical behavior of paperboard. These models fall into roughly three categories: network models, laminate models, and anisotropic models of the yield surface and/or the failure surface.

Perkins, *et al.* [1] and Sinha, *et al.* [3] described a micromechanically-based network model for the in-plane constitutive behavior of paper. A meso-element was constructed to represent the microstructure of the fibrous paper network. The mechanical response of the meso-element depends on the fiber properties and properties of the inter-fiber bonds. They found the inelastic behavior of the inter-fiber bonds to play a crucial role in the overall in-plane inelastic behavior of paper. Stahl and Cramer [30] also developed a network model for low-density fibrous composites. Network models can incorporate micro-level mechanisms, such as inter-fiber interaction and bonding. While these models begin to elucidate the underlying mechanisms of deformation, they do not provide a continuum-level description of paper or paperboard.

Page and Schulgasser [2] developed models of paperboard based on classical laminate theory. While this type of model can predict the elastic response well, it was not extended to capture the anisotropic yielding and subsequent strain hardening

response.

Gunderson, *et al.* [16],[17], deRuvo, *et al.* [13] and Fellers, *et al.* [15] each used the Tsai-Wu quadratic yield condition to model the failure loci they obtained experimentally. The quadratic nature of this type of model has many shortcomings when applied to paper and paperboard. Experimental data showed the biaxial failure locus to be distinctly non-quadratic. Arramon, *et al.* [7] developed a multidimensional anisotropic strength criterion based on isotropic deformation modes (Kelvin modes) that captures the nonquadratic failure envelope. They applied the model to form a strength envelope for paperboard by constructing tensile and compressive modal bounds. However, these efforts only acted to study final failure and did not attempt to study initiation of yield or subsequent strain hardening.

In this research, a general three-dimensional constitutive model of the anisotropic elastic-plastic behavior of paper and paperboard is proposed. The initial elastic behavior is modelled to be linear and orthotropic. The onset of plastic flow is captured by a non-quadratic yield surface. The yield surface is taken to evolve anisotropically with a scalar measure of plastic strain, with plastic flow modelled using an associated flow rule. The model is detailed in the following sections, and numerical results are compared to experimental data.

2.2 Experimentally-Observed Behavior

2.2.1 Elastic-Plastic Behavior of TRIPLEX^{TM} Paperboard

As discussed in the introduction, five-layered TRIPLEX^{TM} Paperboard was used in this research project as an exemplar material. Stenberg, *et al.* [32],[33],[31] conducted an extensive experimental investigation documenting the stress-strain behavior of TRIPLEX^{TM}. Note that the outer chemical pulp layers are typically stiffer and stronger than the inner mechanical layers; however, these layers cannot be separately produced for individual evaluation because their final structure and chemical com-

position are dependent on the processing history. Therefore, Stenberg concentrated most of his effort on obtaining the behavior of TRIPLEX^{TM} material in terms of its effective composite behavior. However, by carefully grinding off other layers of the TRIPLEX^{TM} composite, Stenberg [31] was able to conduct a limited number of tests on the individual mechanical and chemical layers. The experimental results of Stenberg, *et al.* [32],[33],[31] are reviewed below.

In-plane behavior

The TRIPLEX^{TM} composite in-plane uniaxial tensile stress-strain curves for the MD, the CD, and an orientation 45° from the MD are plotted together in Fig. 2-1. These stress-strain curves clearly depict the anisotropic in-plane elastic, initial yield and strain-hardening behavior. There is a factor of 2 to 3 difference in the modulus and initial yield strength between MD and CD. Hardening achieved in MD (flow strength increases by 300% over a strain of 2%) is higher than that in CD (flow strength increases by 200% over a strain of 5%). MD-CD shear properties are deduced from the 45° test result.

Fig. 2-2 shows the in-plane lateral strain (CD) versus axial strain curve for MD-tension, together with the corresponding axial stress-strain curve from Fig. 2-1. Similar data is shown for CD-tension in Fig. 2-3. The elastic in-plane Poisson's ratios ($\nu_{ij} = -\epsilon_j/\epsilon_i$), ν_{13} and ν_{31}, can be calculated from these curves as $\nu_{13} = 0.37$ and $\nu_{31} = 0.12$. Upon subtracting the respective elastic strain components, the lateral plastic strains for both the MD and CD tension cases are computed and shown versus the respective axial plastic strains in Fig. 2-4. These two curves indicate that for both test orientations, the ratio between lateral plastic strain and axial plastic strain is nearly constant until final fracture. This data provides information for later construction of the plastic flow rule.

Tensile loading/unloading/reloading data (Persson [28] and Stenberg, *et al.*[31]) show that after various amounts of plastic strain, upon unloading, the elastic tensile modulus is nearly unaffected by plastic strain, consistent with traditional elasto-

plasticity.

Fig. 2-5 shows the in-plane compression stress-strain curves for the machine and cross directions. Note that global specimen buckling was constrained in these tests. These data show that compressive yield is anisotropic. Furthermore, a comparison of Fig. 2-1 and Fig. 2-5 shows a yield strength difference between tension and compression, with the compressive yield strengths being smaller than those in tension by 65% and 25%, for MD and CD, respectively.

The anisotropic in-plane elastic-plastic properties obtained from these tests are summarized in Table 2.1.

Out-of-plane behavior

The out-of-plane stress-strain behavior of paperboard was experimentally obtained using a modified ARCAN [6] design by Stenberg, *et al.*[32],[33]. Fig. 2-6 shows the schematic of the design. Nominal stress-strain curves were obtained for TRIPLEX^{TM} under various through-thickness loading conditions.

A representative ZD tensile stress-strain curve obtained by Stenberg, *et al.*[32],[33] is shown in Fig. 2-7. The stress measure is force per unit initial cross-sectional area; the x-axis is the nominal strain, defined as the relative normal separation of the top and bottom surfaces of the laminate, divided by the initial laminate thickness. At the earliest stage of deformation, the stress increases linearly with strain, exhibiting a composite modulus of $E_2 = 20\,MPa$. The stress-strain relation shows a small amount of pre-peak nonlinearity before reaching a peak stress of $0.4MPa$. After the peak, the stress-strain curve exhibits pronounced softening. Tensile testing conducted within a scanning electron microscope (Dunn [18], Smith [5]) on the same material reveals the nucleation of multiple inter-laminar microcracks near the peak stress, followed by their growth and coalescence, resulting in the observed softening. Similar results have been obtained for tests involving combined through-thickness tension and shear (Stenberg, *et al.*[32],[33]; Dunn [18]). Therefore, the observed peak stress and subsequent softening for through-thickness loading are due to delamination of the

paperboard and will not be further considered here. This inelastic through-thickness behavior is modelled through an interface model, as will be described in detail in the next chapter. It is also observed that the amount of lateral (in-plane) strain in the plane generated during the through-thickness tensile loading is negligible, indicating that Poisson's ratios ν_{21} and ν_{23} are close to zero.

Fig. 2-8 shows the through-thickness compression stress-strain curve obtained by Stenberg, *et al.*[31]. Up to a nominal compressive strain of 3%, the compressive stress increases linearly with strain. With larger strains, the stress starts to increase exponentially with strain. The data also show that only a small amount of permanent deformation remains after unloading from a peak strain level of more than 20%, indicating nonlinear elastic ZD compressive behavior up to moderately large strains. These observations of the through-thickness compressive behavior will be incorporated into the modeling work.

Representative through-thickness shear stress-strain curves (ZD-MD shear and ZD-CD shear) obtained by Stenberg, *et al.* [32],[33] are shown in Fig. 2-9. Features similar to those of the through-thickness tensile curve are observed. The composite transverse shear moduli are observed to be $G_{12} = 34MPa$ for ZD-MD and $G_{12} = 26MPa$ for ZD-CD, and the peak shear stress is $1.1MPa$ for ZD-MD and $0.9MPa$ for ZD-CD. *In situ* shear testing within a SEM (Dunn, *et al.* [18]) reveals the peak stress and subsequent softening to be governed by microcracking and delamination, similar to that observed during the tensile loading. The through-thickness ZD-CD shear stress-strain curve shows similar features.

When conducting through-thickness tensile and shear experiments, specimens are glued to the loading fixture. For the ZD compression tests, however, no glue is used. The application of glue to the specimen has some influence on the properties of the paperboard due to the penetration of glue into the specimen. Stenberg, *et al.*[32],[33] discussed this issue and proposed a method to account for the effect of glue on the measured properties.

The anisotropic linear elastic out-of-plane properties are summarized in Table 2.2.

The out-of-plane behavior will be discussed in much more detail in the following interface constitutive model chapter.

2.3 The In-Plane Constitutive Model

In this chapter, a three-dimensional, finite deformation constitutive model for paper and paperboard pulp layers is proposed. As discussed in the introduction chapter, from experimental results, the inelastic out-of-plane behavior is predominantly controlled by the delamination of the paperboard along its interface; thus the inelastic out-of-plane behavior will be modeled in this research in the form of an interface element model. Based on this, the model for the continuum pulp layers will take the in-plane behavior to be elastic-plastic and the out-of-plane behavior to be elastic. Due to the assumption of elastic out-of-plane behavior, the application of the in-plane model alone will be limited to predominant in-plane loading. However, when the model is combined with interlaminar decohesion models, as will be described in the next chapter, a general-purpose tool is achieved for modeling behavior under significant out-of-plane loading, such as occurs during converting processes and the in-service behavior of a broad class of paper and paperboard products.

2.3.1 Stress-strain relationship

First, the total deformation gradient $\boldsymbol{F}$ at a material point within a lamina is multiplicatively decomposed into an elastic part and a plastic part:

$$\boldsymbol{F} = \boldsymbol{F}^e \boldsymbol{F}^p, \tag{2.1}$$

where $\boldsymbol{F}^p$ represents the accumulation of inelastic deformation. Although the maximum in-plane strain level in traditional applications of paper sheets is small, we adopt the present finite deformation formulation so that the model can be easily applied to applications such as paperboard converting processes, which generally involve finite rotations of paperboard layers and may exhibit moderately large, but highly localized in-plane strains. The evolution of $\boldsymbol{F}^p$ is given by

$$\dot{\boldsymbol{F}}^p = \boldsymbol{L}^p \boldsymbol{F}^p, \tag{2.2}$$

where $\boldsymbol{L}^p$ is the plastic velocity gradient, which will be defined by the flow rule. The elastic strain is obtained by using the elastic Green strain measure:

$$\boldsymbol{E}^e = \frac{1}{2}[\boldsymbol{F}^{eT}\boldsymbol{F}^e - \boldsymbol{I}], \tag{2.3}$$

where $\boldsymbol{I}$ is the second-order identity tensor. The second Piola-Kirchoff stress measure, $\bar{\boldsymbol{T}}$, relative to the plastically deformed configuration $\boldsymbol{F}^p$, is then calculated using the linear relationship:

$$\bar{\boldsymbol{T}} = \boldsymbol{C}[\boldsymbol{E}^e], \tag{2.4}$$

where $\boldsymbol{C}$ is the fourth-order stiffness tensor, which is taken to be orthotropic. Values of the components of $\boldsymbol{C}$ are defined by the orthotropic elastic moduli. To model the through-thickness nonlinear elastic compressive stress-strain relationship, the through-thickness engineering elastic constant, E_{ZD}, is taken to be an exponential function of the ZD strain under compression as follows:

$$E_{ZD} = E^0_{ZD} e^{(-aE^e_{22})}, \tag{2.5}$$

where E^0_{ZD} is the initial elastic modulus in ZD, E^e_{22} is the ZD elastic Green strain component, and a is a constant determined by fitting the compressive through-thickness stress-strain curve; its value is listed in Table 2.2. The stiffness tensor $\boldsymbol{C}$ under ZD compression is in turn determined assuming constant Poisson's ratios. (i.e., ν_{ij} still correlate to ν_{ji} through original E^0_{ZD} value) The Cauchy stress, $\boldsymbol{T}$, is calculated from its relation to the second Piola-Kirchoff stress by

$$\bar{\boldsymbol{T}} = (det\boldsymbol{F}^e)\boldsymbol{F}^{e-1}\boldsymbol{T}\boldsymbol{F}^{e-T} \tag{2.6}$$

2.3.2 Yield Condition

The through-thickness strengths (tensile and shear) of paper and paperboard materials are typically two orders of magnitude lower than those observed in the plane.

Therefore, the through-thickness stress components play little role in the inelastic deformation and failure of paperboard under in-plane loading.[1] Furthermore, from investigation of the mechanisms of deformation and failure of paperboard under through-thickness loading, it is clear that the majority of through-thickness inelastic deformation occurs in the form of interlaminar microcracking and delamination of the discrete pulp layers, as opposed to inelastic through-thickness deformation distributed quasi-homogeneously within laminae. Thus we can assume that only the in-plane stress components will drive the in-plane inelastic deformation of the pulp layers. Additionally, in classical metal plasticity and in plasticity-based models of yielding in polymers, the deviatoric stress is taken to drive yield because the underlying deformation mechanisms are governed by shear (for example, dislocation glide in crystalline metals). However, in the case of paper, there is no evidence that yield and subsequent plastic flow are driven by deviatoric stress. The porous nature of paper also suggests that mean stress plays a role. Micro-mechanically, yielding is governed by various forms of inter-fiber interactions and nonlinear behavior of wood fibers. Based on these considerations, the total stress will be taken to drive the yield condition described in this research.

In order to experimentally define an in-plane yield surface for paper, multi-axial data is required. Although the anisotropy of the yield surface is well-recognized, due to numerous studies of the uniaxial behavior in different directions, such as that reported in Fig. 2-1, a literature search reveals virtually no data on the initial and evolving multi-axial yield surfaces of paper and paperboard. However, several researchers have obtained biaxial failure surfaces of paperboard under combinations of MD and CD normal stress. Fig. 2-10 shows a representative biaxial failure locus (deRuvo, *et al.* [13]). Similar data have been reported in work by Fellers, *et al.* [15] and Gunderson, *et al.* [16]. In Fig. 2-10, the left plot shows the biaxial strength data of envelope grade paper, and the right one shows those of sack paper. The authors tried to fit

[1]Under significant in-plane compression or very large through-thickness compressive strain, this may not be strictly true. However, for the present, these scenarios will not be considered further.

the failure loci using the Tsai-Wu criterion as shown the solid lines in the figures. However, due to the quadratic nature of the criterion, the fitting is not good in some regions. Meanwhile, one common feature observed in these failure loci is that the data points tend to form prominent "subgroups", with each subgroup lying on a nearly straight line. For example, for low, but non-zero values of MD stress, failure occurs at nearly the CD uniaxial tensile failure strength; similarly, for low, but non-zero values of CD stress, failure occurs at roughly the MD uniaxial tensile failure strength. This observation suggests that the experimental biaxial failure locus can be well-captured by a set of straight lines in a 2-dimensional biaxial stress space, and can be generalized to planes in 3-dimensional space. This is better illustrated in Fig. 2-10, where dashed lines were drawn (not the maximum stress lines). It is obvious that these lines can better represent the failure stress loci. (Karafillis, *et al.* [20] and Arramon, *et al.* [7] developed yield surface and failure surface models, respectively, which capture this nonquadratic feature.) In stress space, these lines or planes can be defined by their minimum distance to the origin, together with their corresponding normal directions. Given that a comprehensive set of experimental data is generally unavailable (and indeed, is a challenging task to obtain) to determine the full surface, we hereby assume that the yield surface exhibits the same characteristic features observed in the failure surface. Therefore, the yield surface is taken to be constructed of N sub-surfaces, where $\boldsymbol{N}^K$ is the normal to the K_{th} such surface, defined in the material coordinates formed by MD, CD and ZD. S^K is the equivalent strength of the K_{th} sub-surface, defined by the distance from the origin to each sub-surface, following its normal direction. Thus, the following form of yield criterion is proposed:

$$f(\bar{\boldsymbol{T}}, S^K) = \sum_{K=1}^{N} [\frac{\chi_K \ \bar{\boldsymbol{T}} \cdot \boldsymbol{N}^K}{S^K}]^{2k} - 1 \ , \tag{2.7}$$

where χ_K is the switching controller with

$$\chi_K = \begin{cases} 1; & \text{if } \bar{\boldsymbol{T}} \cdot \boldsymbol{N}^K > 0 \\ 0; & \text{otherwise} \end{cases} \tag{2.8}$$

$\bar{\boldsymbol{T}}$ is the $2nd$ Piola-Kirchoff stress measure relative to the $\boldsymbol{F}^p$ configuration, and $2k$ is an even integer. $\boldsymbol{N}^K$ is the outward normal of the K_{th} sub-surface, defined relative to the material coordinates.

A schematic of a four sub-surface system ($N = 4$) for biaxial loading, with zero in-plane shear stress, is shown in Fig. 2-11. The normals and corresponding sub-surface strengths are illustrated. The parameter $2k$ is taken to be equal to or larger than 4, indicating a non-quadratic yield surface. Figure 2-12 shows the effect of different $2k$ values in controlling the shape of the yield surface in the biaxial stress plane for this simplified four sub-surface system. Higher $2k$-values give rise to sharper corners between adjacent sub-surfaces and reduce the curvature over increasing central portions of each-subsurface. A schematic of a six sub-surface yield surface, with non-zero in-plane shear stress $\bar{T}_{13}$, is shown in Fig. 2-13. This figure graphically illustrates the normals and corresponding equivalent strengths of the sub-surfaces. For this yield surface, the six normals are taken to be of the following form:

$$\boldsymbol{N}^K = \sum_{i,j=1}^{3} N_{ij}^K \, \boldsymbol{e}_i \otimes \boldsymbol{e}_j, \quad K = I...VI \tag{2.9}$$

and

$$N_{ji}^K = N_{ij}^K, \quad K = I, ...VI \tag{2.10}$$

where $\boldsymbol{e}_i$, $i = 1, 2, 3$ are the basis vectors for the material coordinates formed by the MD, ZD and CD, respectively. Here, the subsurface normal index K ranges over the six Roman numerals $I, ..., VI$.

Because out-of-plane stress components are assumed to have no effect on the plastic deformation within a lamina, components of $\boldsymbol{N}^K$ involving the 2-direction

(*i.e.*, the ZD direction) are set to be zero. This results in elastic through-thickness behavior, as proposed. Determination of each non-zero entry of these matrices will be discussed in the next section.

2.3.3 Flow rule

The plastic flow rule is defined as

$$\boldsymbol{L}^p = \boldsymbol{D}^p = \dot{\bar{\gamma}}\boldsymbol{K} \tag{2.11}$$

where $\boldsymbol{L}^p$ is the plastic flow rate, and $\boldsymbol{D}^p$ is the symmetric part of $\boldsymbol{L}^p$. For paper and paperboard, the in-plane plastic strains (even at failure) are small; therefore we take the skew part of $\boldsymbol{L}^p$ to vanish, or $\boldsymbol{W}^p = 0$, as a simplification. $\boldsymbol{K}$ is the flow direction, and $\dot{\bar{\gamma}}$ is the magnitude of the plastic stretching rate. $\boldsymbol{K}$ is a second-order tensor with unit magnitude:

$$\boldsymbol{K} = \hat{\boldsymbol{K}} / \parallel \hat{\boldsymbol{K}} \parallel, \tag{2.12}$$

where

$$\parallel \hat{\boldsymbol{K}} \parallel = \sqrt{\hat{\boldsymbol{K}} \cdot \hat{\boldsymbol{K}}}. \tag{2.13}$$

In Fig. 2-4, the in-plane lateral plastic strain versus axial plastic strain data showed that the ratio between these two plastic strain components is nearly constant for both the MD and CD simple tension cases. These ratios are taken to define the normal directions of the two respective sub-surfaces of the tensile quadrant of the biaxial yield surface, in the absence of shear stress. Thus, the plastic flow of the material is taken to follow an associated flow rule:

$$\hat{\boldsymbol{K}} = \frac{\partial f}{\partial \bar{\boldsymbol{T}}}. \tag{2.14}$$

With the yield condition defined in Equation 2.7, $\hat{\boldsymbol{K}}$ can be further calculated as

$$\hat{\boldsymbol{K}} = \frac{\partial f}{\partial \bar{\boldsymbol{T}}} = \sum_{K=1}^{N} 2k \; {\Lambda_K}^{2k-1} \; \frac{\chi_K \, \boldsymbol{N}^K}{S^K}, \tag{2.15}$$

where

$$\Lambda_K = \frac{\bar{\boldsymbol{T}} \cdot \boldsymbol{N}^K}{S^K}. \tag{2.16}$$

For the six sub-surface yield surface shown in Fig. 2-13, assuming an associated flow rule, the sub-surface normals $\boldsymbol{N}^K, K = I, II, ...VI$ are defined using the corresponding plastic strain ratios. For example, for sub-surface I(one) in Fig. 2-13, the plastic strain ratio from the MD simple tension test is nearly constant at -0.5. The two nonzero components of $\boldsymbol{N}^I$ are then determined by solving the following two equations:

$$\frac{{N^I}_{33}}{{N^I}_{11}} = -0.5 \tag{2.17}$$

and (to make a unit normal)

$$\left({N^I}_{11}\right)^2 + \left({N^I}_{33}\right)^2 = 1, \tag{2.18}$$

which gives ${N^I}_{11} = 2/\sqrt{5}$ and ${N^I}_{33} = -1/\sqrt{5}$. Similarly, the plastic strain ratio from the CD simple tension test is nearly constant at $-2/15$, giving ${N^{II}}_{11} = -2/\sqrt{229}$ and ${N^{II}}_{33} = 15/\sqrt{229}$. With appropriate experimental data, similar calculations can determine the normals of each of the sub-surfaces. However, currently, there is no experimental data for the plastic strain ratios for compression in either the machine or cross directions. For the four sub-surface biaxial yield surface shown in Fig. 2-11, the normals for the two sub-surfaces in the compressive quadrants, IV and V, are assumed to have normal directions antiparallel to those of corresponding tensile sub-surfaces I and II, respectively, as seen in the figure, but with generally differing strength levels. For the normal of sub-surface III, representing yielding under positive pure shear stress ($\bar{T}_{13} = \bar{T}_{31} \neq 0$; $\bar{T}_{ij} = 0$ otherwise), the two non-zero components are ${N^{III}}_{13}$

and ${N^{III}}_{31}$. Due to the symmetry of shear stress,

$$ {N^{III}}_{13} = {N^{III}}_{31}, \tag{2.19} $$

and

$$ ({N^{III}}_{13})^2 + ({N^{III}}_{31})^2 = 1, \tag{2.20} $$

Thus we have ${N^{III}}_{13} = {N^{III}}_{31} = \sqrt{2}/2$, and the normal of the other sub-surface representing yielding under negative pure shear stresses is taken to be $\boldsymbol{N}^{VI} = -\boldsymbol{N}^{III}$. In summary, the components of the normals in the material coordinates for the six sub-surfaces determined are given in Table 2.3

2.3.4 Strain-hardening functions

To capture the anisotropic strain-hardening observed for the in-plane behavior, the equivalent strengths, S^K, of each sub-surface are taken to evolve with the accumulated equivalent plastic strain, *i.e.*

$$ S^K = S^K(\bar{\gamma}), \tag{2.21} $$

where $\bar{\gamma} = \int \dot{\bar{\gamma}} dt$ is the equivalent plastic strain. Fig. 2-14 shows schematically how the shape of a biaxial yield surface evolves with increasing equivalent plastic strain for the case of zero in-plane shear stress. For the yield surface, the S^K-values, $K = I, II, IV$ and V, are directly related to the uniaxial yield strength of the material for MD/CD tension and compression and the corresponding plastic strain ratios (see appendix). The equivalent yield strengths for the two pure-shear sub-surfaces are taken to be equal, $S^{III} = S^{VI}$, and are related to the in-plane MD-CD shear strength.

In this research, anisotropic strain hardening is modelled by taking the S^K to depend on the amount of accumulated plastic strain as follows:

$$ S^i = S_0^i + A_i tanh(B_i \bar{\gamma}) + C_i \bar{\gamma}, \quad i = I...VI \tag{2.22} $$

where

S_0^i:	Initial equivalent yield strength for sub-surface i
A_i, B_i, C_i:	hardening constants

The constants are determined by fitting the experimental stress-strain curves, as discussed further in the appendix.

2.3.5 Discussion

The proposed constitutive model can be applied to different paperboards as a whole, to any individual pulp layers inside the paperboard, as well as to paper sheets. One of the advantages of the proposed model is its flexibility to incorporate new experimental information. With more experimental information (*e.g.*, off-axis stress-strain curves with corresponding lateral strain *vs.* axial strain curves), the yield surface, and in turn the flow rule, can be easily refined to provide even more accurate modeling of the behavior of paper or paperboard layer by incorporating more sub-surfaces. If a large enough $2k$ value is used, the yield surface will have sharp corners, and the added extra information will not change the previous match between model and data.

2.4 Implementation and verification of the model: Application to model TRIPLEX^{TM}

The constitutive model described above was numerically integrated using a Newton-Raphson procedure. The commercial FEM software package ABAQUS's user-defined material behavior capability (UMAT) was used to implement the model. Several homogeneous and inhomogeneous deformations were simulated to test the model. First, simulations were conducted to determine the model parameters for description of the averaged behavior of TRIPLEX^{TM} by fitting the material properties to experimental data. Uniaxial tension data on TRIPLEX^{TM} paperboard in the MD, CD and 45° direction were used to fit the material properties as were compression data in the MD and CD. A method for fitting model properties to data is given in the appendix. After the model properties were calibrated with the MD, CD and 45° data, these parameters were used to predict the stress-strain behavior during tensile loading in directions 22.5° and 67° off-axis of the MD and were compared to experimental data. Then, the material model was further tested through simulation of the behavior of TRIPLEX^{TM} plates with a central hole, subject to in-plane tensile loading.

2.4.1 Simulations to determine the model parameters for behavior of the TRIPLEX^{TM} laminate

The implemented constitutive model can be applied to the entire composite TRIPLEX^{TM} paperboard laminate, as well as to the individual pulp layers inside the board. In this section, simulations are conducted to determine the model parameters for behavior of the TRIPLEX^{TM} laminate.

Comparisons of the experimental and the simulated stress-strain curves for uniaxial MD, CD and 45° tension are shown in Fig. 2-15. Fig. 2-16 shows the corresponding comparison of experimental and simulated lateral strain *vs.* axial strain curves for the MD and CD. These results demonstrate that the proposed constitutive relationship

can model the elastic-plastic behavior of the paperboard over the full range of strain. It is also seen that an associated flow rule with a simple constant normal direction for the sub-surface captures the lateral strain *vs.* axial strain curves well. If second-order accuracy is needed to capture the lateral strain *vs.* axial strain curve, the sub-surface normals, $\boldsymbol{N}^K$, could be taken to evolve with plastic strain. The CD result, together with the MD result, demonstrates the anisotropic capability of the proposed model.

Compression simulations are also conducted. Fig. 2-17 shows the comparison of the experimental and the simulated stress-strain curves for uniaxial MD and CD compression. These results show that the constitutive law is capable of modeling the asymmetric tension and compression yielding and hardening behavior. Comparison of experimental and simulated stress-strain curves for uniaxial ZD compression is shown earlier in Fig. 2-8. The curves show that the stiffening of through-thickness ZD elastic modulus can be modeled well by setting the modulus to evolve exponentially with the ZD compressive strain.

It should be noted that specimen failure takes the form of fiber fracture or fiber pull-out at the end of the in-plane tensile testing. In this research, in-plane tensile failure is not considered. (Under in-plane compression, paperboard fails in the form of delamination and local buckling, as will be shown later in this thesis)

By fitting these experimental curves, the properties needed in the model were determined. The nine orthotropic elastic constants used for in the simulations in this research for the averaged behavior of TRIPLEX^{TM} are summarized in Table 2.4. (The constant a for exponential stiffening of ZD engineering elastic constant is listed previously in Table 2.2) The yielding and hardening parameters are listed in Table 2.5. The yield surface normals used for TRIPLEX^{TM} have been listed previously in Table 2.3. The details about how to obtain this information from experimental data are discussed in the appendix. The final set of parameters describing the initial yield surface and the hardening of the yield surface used in the simulations was shown in Fig. 2-11 and Fig. 2-14. Because these properties are obtained from experimental results on TRIPLEX^{TM}, which is a five-layered composite, they are averaged values

for the whole composite. If the same set of experiments can be conducted for each individual layer, the properties can be modified to fit each layer. It is also worth noting that the specimen failed under less than 0.4% of total compressive MD strain. Thus the compressive quadrants of the hardened yield surfaces shown in Fig. 2-14 are of less practical meaning when plastic strain is larger than the strain at which the specimen failed by delamination and local buckling [31].

2.4.2 Simulations predicting the off-axis in-plane stress-strain behavior of TRIPLEX^{TM}

With the full suite of material properties obtained from fitting the MD, CD and 45° data on TRIPLEX^{TM}, two simulations were then conducted to test the predictive capability of the model. The stress-strain behavior subjected to tensile loading in two off-axis directions, 22.5° from the MD and 67° from the MD, is simulated. Fig. 2-18 compares the experimental and the simulated stress-strain curves in these two loading directions. The stress-strain curves predicted by the model are in good agreement with the corresponding experimental curves, showing that the model is capable of providing good predictions to the in-plane stress-strain behavior.

2.4.3 Simulation of deformation of paperboard under inhomogeneous in-plane loading

To further test the robustness of the numerical implementation of the constitutive model, simulations of paperboard under inhomogeneous in-plane loading were conducted. In particular, the constitutive model was used to simulate the behavior of a rectangular TRIPLEX^{TM} board with a central hole under in-plane loading. Because of the existence of the central hole, inhomogeneous in-plane straining is going to result when the board is loaded uniformly along its boundary. The averaged values of the material properties of the TRIPLEX^{TM} as a whole, as summarized in Table 2.2 to Table 2.5, were used in these simulations.

First, a $40mm$ long by $30mm$ wide board with a central hole radius of $4mm$ was subjected to uniformly-applied displacement boundary conditions in the MD along opposite sides. The behavior of the board in the elastic regime is first studied. Fig. 2-19 shows the mesh used for this simulation and boundary conditions applied. Due to the symmetry of this problem, only one quarter of the board is simulated. In particular, boundary 1, which includes all nodes on that surface, as marked in the figure, was fixed in the global X direction (same as MD in this case). Boundary 2 was fixed in the global Y direction (same as CD in this case). Boundary 3 was fixed in the global Z (same as ZD in this case) direction to prevent out-of-plane deformation. It is also along boundary 3 where uniform tensile displacement is applied along global X direction. Fig. 2-20 shows the contour of the in-plane normal Cauchy stress component, T_{XX}, in the global X direction as indicated in the figure, before any plastic deformation is developed inside the board. The typical stress concentration distribution is shown around the hole. The stress distribution was also normalized by the corresponding macroscopic nominal stress, (calculated as the reaction force at boundary 3 divided by the initial surface area) and the corresponding contour is shown in Fig. 2-21. This contour plot indicates that the stress concentration factor in this simulation is 3.34, larger than the conventional 3.0 value for an infinite body of isotropic elastic material. A contour plot of the stress component T_{YY} in the elastic regime is also shown in Fig. 2-22, where maximum compressive stress and zero stress are seen at the material points on the circumference of hole, as expected.

After plasticity started to develop inside the board, overall features of the stress distribution remain the same. The macroscopic nominal stress *vs.* nominal strain (calculated as applied displacement divided by the initial length of specimen) curve for this simulation is also plotted in Fig. 2-24. Point A in this figure indicates the elastic stage corresponds to the contour plots just shown. All the following are contours at the final stage of deformation indicated by point B in Fig. 2-24. (With a macroscopic nominal stress of $33MPa$ and nominal strain of 5%.) Fig. 2-23 again shows contours of the in-plane normal Cauchy stress component, T_{XX}, at end of simulation. Plastic

deformation has occured at the equator and then the stress concentration factor has decreased. A contour plot of the Cauchy stress component T_{YY} in global Y direction at end of the loading is shown in Fig. 2-25, where again maximum compressive stress and zero stress are seen at vertices located at the intersection of the global X and Y axes with the circumference of the hole. Fig. 2-26 shows the contour of the equivalent plastic strain, $\bar{\gamma}$. Not surprisingly, the highest plastic strain is observed near the two points around the hole where stress concentration is located. A magnified quarter of region around the hole in this contour is also shown in Fig. 2-27.

Because the board is essentially under compression in the CD in the previous simulation, nodes located on boundary 3, as indicated in Fig. 2-19, were fixed in ZD to prevent warping of the board out of the loading plane. To reduce the influence of this boundary condition, another simulation was run with everything else the same, except the width of the board increased from $30mm$ to $100mm$. The mesh and the contours of the stress components T_{XX} and T_{YY}, as well as the equivalent plastic strain for this geometry are shown in Fig. 2-28 to Fig. 2-31. These figures present the same features of those shown in the previous simulation.

To test the robustness of the numerical implementation of the model to off-axis loading, simulation was conducted with the MD oriented 45° to the global X direction. Due to the asymmetry property of this problem, one half of the board is simulated with appropriate boundary conditions to capture the asymmetric nature of the structure, as shown in Fig. 2-32 with applied boundary conditions indicated. As in the previous simulation, the response of the board in the elastic regime is first investigated. Fig. 2-33 shows the contour of Cauchy stress component T_{XY} (in global coordinates as indicated in the figure.) before any plasticity is developed inside the board. As expected, zero shear stress is shown in vertices located at the intersection of the global X and Y axes with the circumference of the hole. The maximum shear stress is achieved on off-axis points on the circumference of the hole. Fig. 2-34 shows the contour of the same stress component T_{XY} after a nominal strain of 5% applied at the boundary. General features observed in Fig. 2-33 remains at this deformation

stage except that the zone of stress concentration has propagated out. The contours of stress component T_{XX} and T_{YY} are also plotted in Fig. 2-35 and Fig. 2-36. Fig. 2-37 shows the contour of the equivalent plastic strain. The maximum equivalent plastic strain is achieved near the points of stress concentration.

These three simulations verified that the numerical implementation of the constitutive model into UMAT subroutine is robust under inhomogeneous straining conditions.

2.5 Evaluation of material parameters for mechanical and chemical pulp layers

As discussed in the previous sections, there is a scarcity of experimental data on the in-plane yielding and plastic flow of paper or paperboard. So far, the most intensive tests available were conducted by Stenberg [31], and most of his tests were conducted on TRIPLEX^{TM} paperboard, which is composed of a three-layered core formed by three inner mechanical pulp layers and two outer chemical pulp layers. In other words, the in-plane test results shown previously are all based on the five-layered composite and represent an averaged behavior of the three mechanical and two chemical layers. To facilitate the distinction of mechanical and chemical layers in the FEM simulations, the same experimental data obtained for the entire composite is needed for each of these two different types of pulp layers. Unfortunately, because the TRIPLEX^{TM} is a commercial product and is made continuously in its manufacturing process on the paper mill, it is very difficult to reproduce the same type of individual chemical and mechanical pulp layers under lab conditions. Up to this point, only limited further tests were conducted by Stenberg [31] to provide needed additional information. The representative test specimens for each layer were obtained by grinding off the other layers from the TRIPLEX^{TM}. In this section we show results from these tests and discuss how we deduce the material parameters needed to describe the mechanical

and the chemical pulp layers, using the proposed model, based on this experimental information and additional assumptions.

2.5.1 Experimental data on individual layers

Three types of tests were conducted by Stenberg [31] to provide extra information to determine the material parameters needed to describe the in-plane behavior of the chemical and mechanical pulp layers: uniaxial MD tension stress-strain tests on the mechanical pulp layer; uniaxial CD tension stress-strain tests on the mechanical pulp layer; and uniaxial MD tension tests on the chemical pulp layer. The length of the test pieces is $100mm$ and width is $15mm$.

Fig. 2-38 shows the MD tensile stress-strain curves for mechanical and chemical layers. From these two curves, we can obtain the modulus, the initial yield strength and the failure strength for the mechanical and the chemical layers in the MD. One step further, we can calculate the ratio between MD modulus of chemical and mechanical layers to be approximately 2.5 : 1 ($8.9GPa$ *vs.* $3.4GPa$). As a verification, according to elementary composite mechanics, the modulus of the TRIPLEX^{TM} composite can be calculated as $E_c = 0.6E_{mech} + 0.4E_{chem} = 5.6GPa$, where E_{chem} and E_{mech} are the MD modulus of each of the two layers. This value is exactly the same as that observed experimentally from Stenberg's test on TRIPLEX^{TM}. The ratio between the MD tensile initial yield strength of the chemical and mechanical layers is about 2 : 1 ($24MPa$ *vs.* $12MPa$); the ratio between the MD tensile failure strength of the chemical and mechanical layers is about 2.7 : 1 ($80MPa$ *vs.* $30MPa$).

Fig. 2-39 shows the MD and CD tensile stress-strain curves for the mechanical layer. From the CD curve, we can obtain the modulus, the initial yield strength and the failure strength for the mechanical layer in the CD. Furthermore, we can calculate the ratio between MD and CD modulus of the mechanical layer to be approximately 3 : 1 ($3GPa$ *vs.* $1GPa$); the ratio between the MD and CD tensile initial yield strength of the mechanical layer is about 2 : 1 ($12MPa$ *vs.* $6MPa$); the ratio between the MD and CD tensile failure strength of the mechanical layer is about 2 : 1 ($30MPa$

vs. $15MPa$).

2.5.2 Additional assumptions made

Since these curves are all of the experimental data available at this point to distinguish the behavior of the mechanical and chemical layers, we have to make assumptions about the rest of the material parameters needed to describe each of the pulp layers. In this research, the following assumptions are made:

- The ratios between other corresponding elastic moduli of the two pulp layers are the same as those between the MD moduli of the two layers. The poisson's ratios of each individual layer are the same with those of the composite. With these assumptions and the known elastic modulus values of the entire TRIPLEX^{TM}, the elastic moduli of each of the individual layers can be determined by using basic composite mechanics principles. The constant a for exponential stiffening of ZD engineering elastic constant for the two layers are taken to be the same as that of the composite TRIPLEX^{TM}. (listed previously in Table 2.2)

- The ratio between the two pulp layers' initial tensile yield strengths on the yield surface, *i.e.*, the ${S^K}_0$'s ($K = I, II$ and III), is $2:1$, the same as that between the MD initial yield strength of the two layers.

- For the value of the initial compressive yield strength on the subsurface, S_{K0}, ($K = IV$ and V), both layers are assumed to take the same value as those of the TRIPLEX^{TM}. (The mechanisms of in-plane compression yielding and failure in the form of buckling involves the interfaces, not just the pulp layers, and will be further discussed in the interface model chapter.)

- The ratios between the values of the constant A_1, A_2 and A_3 of Equation 2.22 in the two pulp layers is assumed to be $2.7:1$, the same as that between the MD tensile failure strengths of the two layers.

- The values of A_4 and A_5 for both layers are assumed to be the same as those of the composite TRIPLEX^{TM}.

- The B_i and C_i ($i = 1..5$)values in Equation 2.22 for the chemical and mechanical layers are assumed to be the same as those for the entire TRIPLEX^{TM}.

- The yield surface normals for the chemical and mechanical layer are assumed to be the same as those for the entire TRIPLEX^{TM}, given in Table 2.3 .

Further tests will be necessary if more accurate calibration of the model is needed. The numbers used in this research for all the parameters for the two layers are summarized later in this chapter.

2.5.3 Simulations to determine the model parameters for behavior of individual pulp layers inside TRIPLEX^{TM}

Simulations were also conducted to determine model parameters for the chemical and mechanical pulp layers inside TRIPLEX^{TM} by matching the limited experimental data on the individual layers as described previously.

Fig. 2-40 shows the comparison of simulated and experimental results for MD tensile stress-strain for the mechanical layer. Results for CD tensile stress-strain curves for the mechanical layer are shown in Fig. 2-41. Fig. 2-42 shows the comparison of simulated and experimental results for MD tensile stress-strain behavior for the chemical layer. Part of the model parameters for each layer such as the modulus, initial yield strength and failure strength, can be directly determined by matching the experimental data available on these two layers. The remaining parameters are determined by following the assumptions discussed in the previous section. Further verification simulation can be conducted based on these assumptions. For example, after parameters for each layer are determined following the available data and the additional assumptions, they are used to conduct simulations to reproduce behavior of the entire TRIPLEX^{TM} observed experimentally. One of the simulations conducted is

to reproduce the MD tensile composite stress-strain curve for TRIPLEX^{TM}. Fig. 2-43 shows the mesh used to model the TRIPLEX^{TM} composite, with each individual layer modeled using its own set of parameters. Fig. 2-44 then plots the comparison of the model-reproduced MD stress-strain curve of the TRIPLEX^{TM} with the experimental data. The experimental and model-fitted MD stress-strain curves for each of the layer are also plotted in this figure. It can be seen with the set of parameters fitted for each of the layer, the stress-strain behavior of TRIPLEX^{TM} is reasonably reproduced, indicating that the parameters for each layer involving the MD tensile behavior are well deduced. Furthermore, the initial yielding point on the stress-strain curve for chemical and mechanical layers are marked in the figure, with corresponding points (same strain) on the composite stress-strain curve marked as well. It can be seen that because displacement boundary condition was applied, the composite starts to show nonlinear behavior when the chemical layer starts to yield, as marked by point "C" in the figure. With larger strain applied, the mechanical layer starts to yield as well, giving extra nonlinearity to the composite stress-strain curve.

The nine orthotropic elastic constants used in the simulations in this research for the chemical pulp layers are summarized in Table 2.6, and those used for the mechanical pulp layers are in Table 2.7. The yielding and hardening parameters for the two pulp layers are listed in Table 2.8 and Table 2.9. The yield surface normals for the two pulp layers are the same as those used for TRIPLEX^{TM}, listed in Table 2.3.

2.6 Discussion

This chapter presented a finite deformation elastic-plastic constitutive model for in-plane behavior of paper and paperboard. The anisotropic elasticity is modelled using orthotropic linear elasticity, albeit generalized to connect the work-conjugate stress and strain measures $\bar{\boldsymbol{T}}$ and $\boldsymbol{E}^e$. The initial anisotropic yield behavior is modelled by an initial yield surface constructed from sub-surfaces defined by the measured initial yield strengths and plastic strain ratios in various loading conditions. The strength of

each sub-surface is taken to harden with respect to the equivalent plastic strain, thus providing anisotropic strain hardening of the yield surface. The material parameters needed by the model are obtained by fitting uniaxial stress-strain and lateral strain vs. axial strain data. With the fitted parameters, the model was shown to be predictive of other in-plane stress-strain behavior.

The proposed model can be applied to simulate a wide range of in-plane problems for paper and paperboard such as the behavior under inhomogeneous, multiaxial in-plane loading or bending. Furthermore, the proposed constitutive model, together with the interface constitutive law modeling the through-thickness tensile and shear behavior, enables the simulation of complex loading conditions such as those that occur during various converting processes as well as drop-loading conditions of paperboard products.

	Elastic modulus (GPa)	Poisson's Ratio	Tensile yield strength (MPa)	Plastic strain ratio, $d\epsilon^p_\perp / d\epsilon^p_\parallel$	Compressive yield strength (MPa)
MD	5.6	0.37	12.0	-0.5	7.3
CD	2.0	0.12	6.5	-0.133	5.0
45°	4.1		8.0		

Table 2.1: Experimental results of uniaxial tensile tests. (Stenberg [31])

Elastic modulus $E_{ZD}(MPa)$	Poisson's Ratio ν_{21}	Poisson's Ratio ν_{23}	Shear modulus $G_{12}(MPa)$	Shear modulus $G_{23}(MPa)$	Stiffening constant a
18.0	-0.0055	-0.0035	34.0	26.0	5.4

Table 2.2: Elastic out-of-plane properties. (Stenberg, *et al.* [32, 33])

K	N^K_{11}	N^K_{33}	N^K_{13}
I	$2/\sqrt{5}$	$-1/\sqrt{5}$	0
II	$-2/\sqrt{229}$	$15/\sqrt{229}$	0
III	0	0	$\sqrt{2}/2$
IV	$-2/\sqrt{5}$	$1/\sqrt{5}$	0
V	$2/\sqrt{229}$	$-15/\sqrt{229}$	0
VI	0	0	$-\sqrt{2}/2$

Table 2.3: Non-zero components of the sub-surface normals used in modeling TRIPLEX^{TM}, expressed in the material coordinates

E_1 (MPa)	E_2 (MPa)	E_3 (MPa)	G_{12} (MPa)	G_{13} (MPa)	G_{23} (MPa)	ν_{12}	ν_{13}	ν_{23}
5600.0	18.0	2000.0	34.0	1300.0	26.0	-0.005	0.37	-0.004

Table 2.4: Elastic constants used by model for the TRIPLEX^{TM} composite laminate.

$S_0^I(MPa)$	$S_0^{II}(MPa)$	$S_0^{III}(MPa)$	$S_0^{IV}(MPa)$	$S_0^V(MPa)$
10.7	6.5	6.0	6.5	6.3
$A_1(MPa)$	$A_2(MPa)$	$A_3(MPa)$	$A_4(MPa)$	$A_5(MPa)$
19.0	40.0	8.0	6.0	9.0
B_1	B_2	B_3	B_4	B_5
260.0	160.0	375.0	160.0	310.0
$C_1(MPa)$	$C_2(MPa)$	$C_3(MPa)$	$C_4(MPa)$	$C_5(MPa)$
800.0	250.0	200.0	300.0	225.0

Table 2.5: In-plane yielding and hardening parameters used to model TRIPLEX^{TM}.

E_1 (MPa)	E_2 (MPa)	E_3 (MPa)	G_{12} (MPa)	G_{13} (MPa)	G_{23} (MPa)	ν_{12}	ν_{13}	ν_{23}
8900.0	25.0	3400.0	58.0	2400.0	38.0	-0.005	0.37	-0.004

Table 2.6: Elastic constants used for the chemical pulp material.

E_1 (MPa)	E_2 (MPa)	E_3 (MPa)	G_{12} (MPa)	G_{13} (MPa)	G_{23} (MPa)	ν_{12}	ν_{13}	ν_{23}
3400.0	16.0	960.0	20.0	800.0	15.0	-0.005	0.37	-0.004

Table 2.7: Elastic constants used for the mechanical pulp material.

$S_0^I(MPa)$	$S_0^{II}(MPa)$	$S_0^{III}(MPa)$	$S_0^{IV}(MPa)$	$S_0^V(MPa)$
10.7	6.5	6.0	6.3	6.3
$A_1(MPa)$	$A_2(MPa)$	$A_3(MPa)$	$A_4(MPa)$	$A_5(MPa)$
19.0	20.0	7.5	6.0	9.0
B_1	B_2	B_3	B_4	B_5
260.0	160.0	375.0	160.0	310.0
$C_1(MPa)$	$C_2(MPa)$	$C_3(MPa)$	$C_4(MPa)$	$C_5(MPa)$
800.0	250.0	200.0	300.0	225.0

Table 2.8: In-plane yielding and hardening parameters used by model for mechanical pulp layers in TRIPLEX^{TM}.

$S_0^I(MPa)$	$S_0^{II}(MPa)$	$S_0^{III}(MPa)$	$S_0^{IV}(MPa)$	$S_0^V(MPa)$
22.0	16.5	8.0	6.3	6.3
$A_1(MPa)$	$A_2(MPa)$	$A_3(MPa)$	$A_4(MPa)$	$A_5(MPa)$
44.0	20.0	18.0	12.0	12.5
B_1	B_2	B_3	B_4	B_5
260.0	160.0	375.0	160.0	310.0
$C_1(MPa)$	$C_2(MPa)$	$C_3(MPa)$	$C_4(MPa)$	$C_5(MPa)$
800.0	250.0	200.0	300.0	225.0

Table 2.9: In-plane yielding and hardening parameters used by model for chemical pulp layers in the TRIPLEX^{TM} composite laminate.

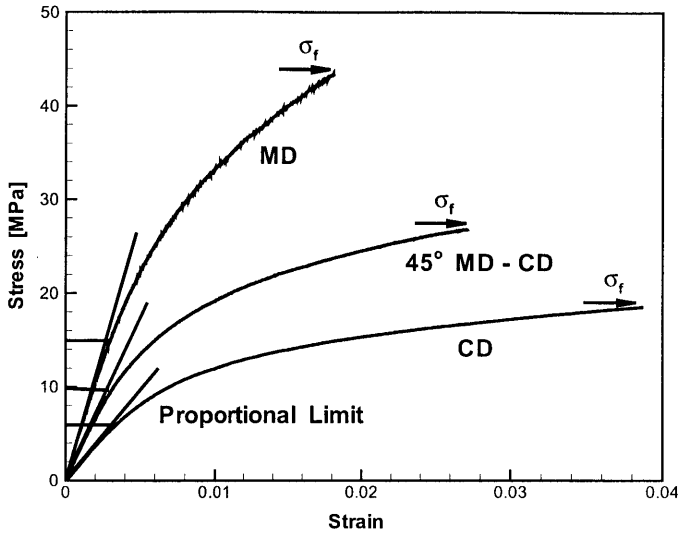

Figure 2-1: TRIPLEX^{TM} in-plane stress strain curves. (Stenberg [31])

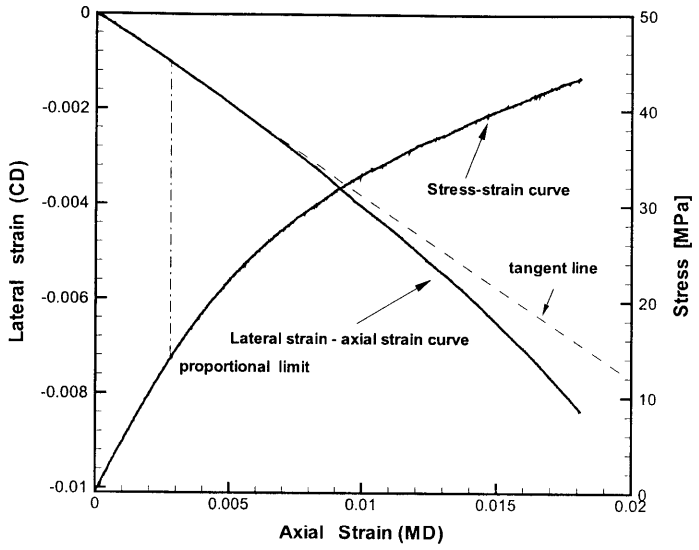

Figure 2-2: Lateral strain *vs.* axial strain curve for tensile loading in the MD direction. (Stenberg [31])

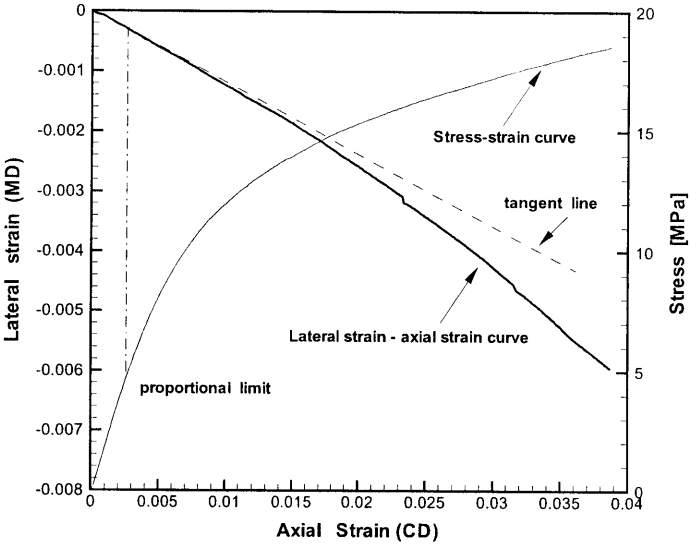

Figure 2-3: Lateral strain *vs.* axial strain curve for tensile loading in the CD direction. (Stenberg [31])

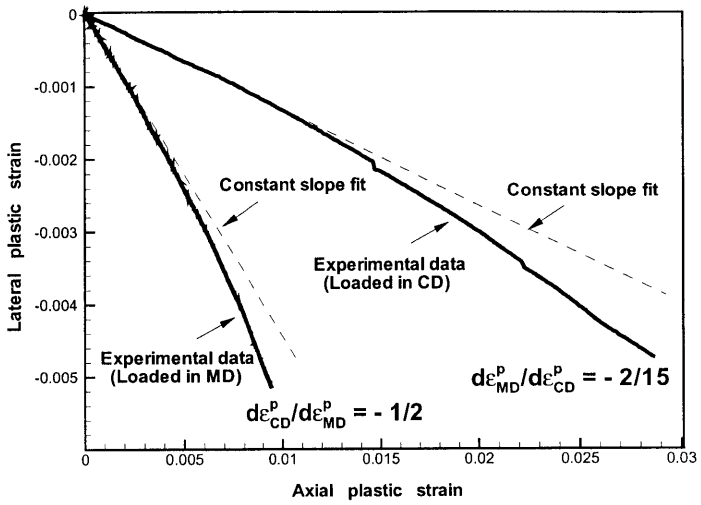

Figure 2-4: Lateral plastic strain *vs.* axial plastic strain curve for tensile loading in the MD and CD directions. (Stenberg [31])

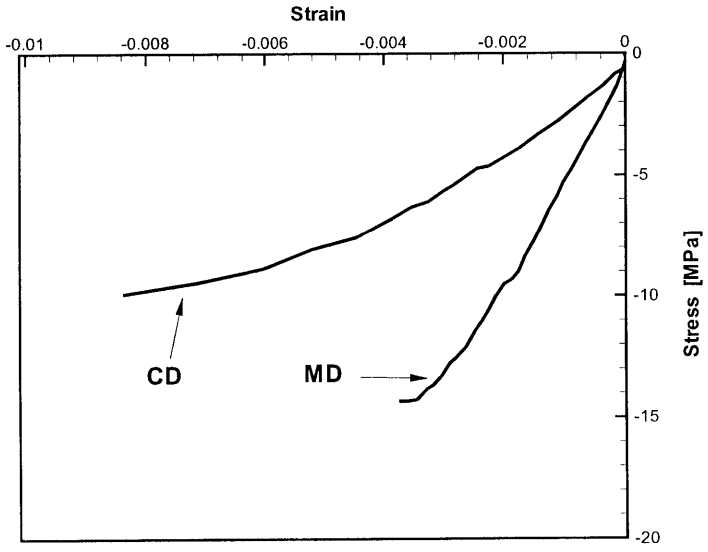

Figure 2-5: In-plane compression stress-strain curves for MD and CD directions. (Stenberg, *et al.* [32])

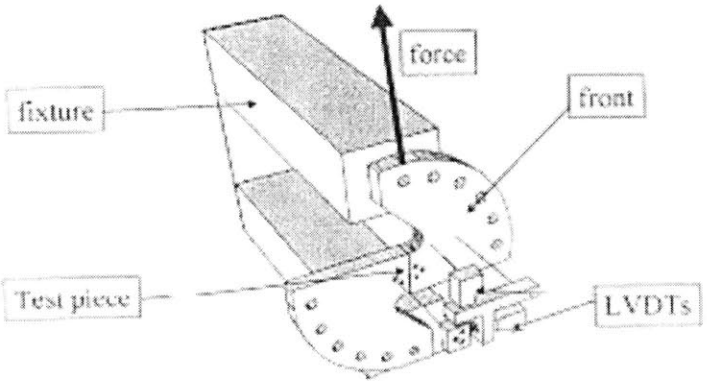

Figure 2-6: Illustration of the new Arcan design. [32]

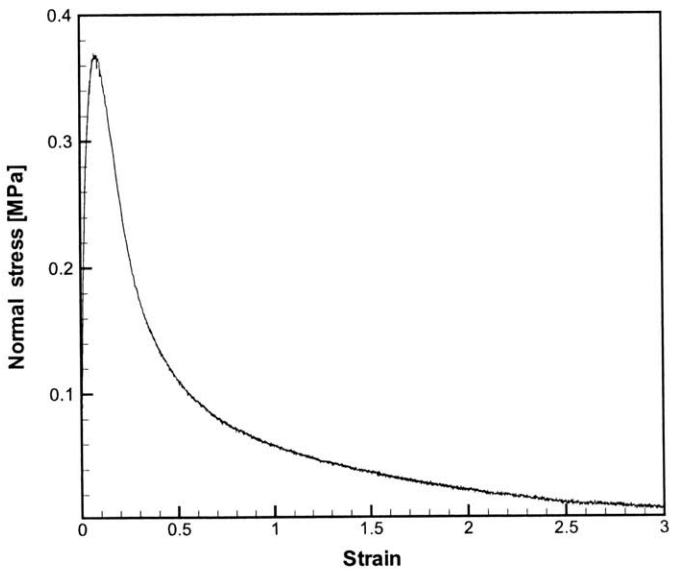

Figure 2-7: Through-thickness ZD tension stress-strain curve. (Stenberg, *et al.* [32],[33])

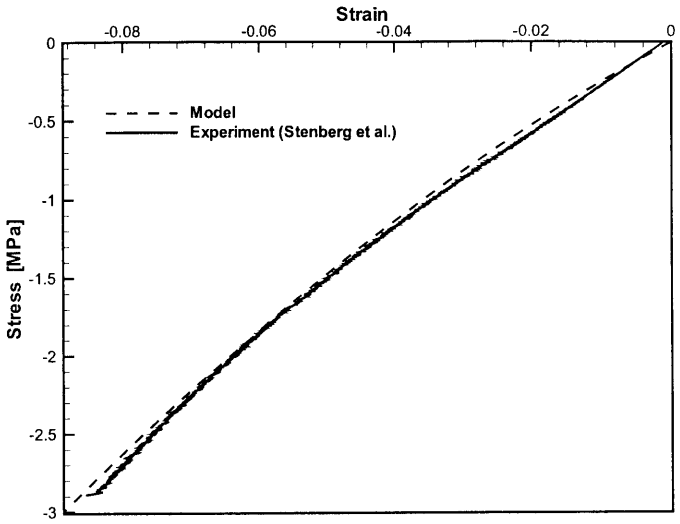

Figure 2-8: Through-thickness compressive stress-strain curve.

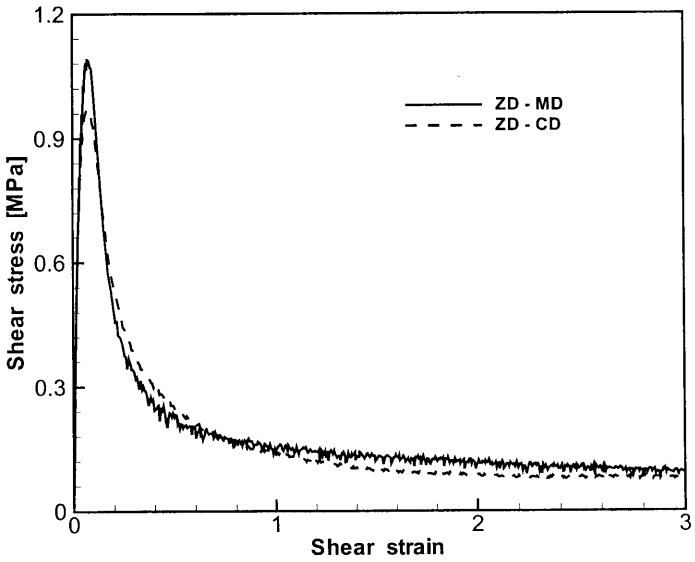

Figure 2-9: Through-thickness MD-ZD and CD-ZD shear stress-strain curves. (Stenberg, *et al.* [32],[33])

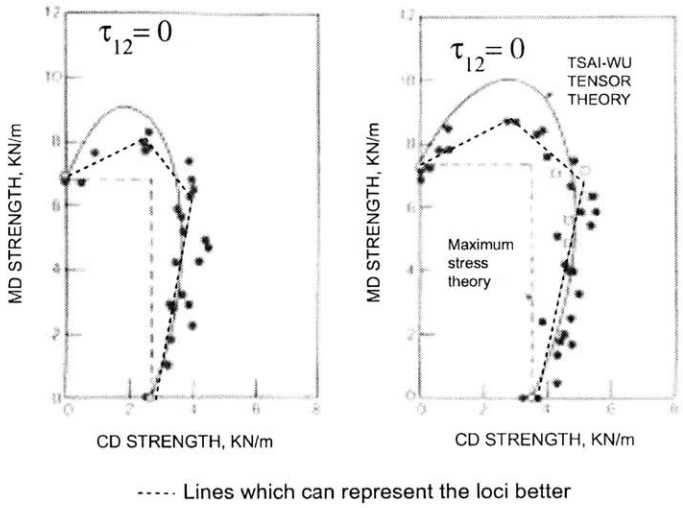

Figure 2-10: Biaxial failure surfaces (deRuvo, *et al.* (1980)). Note: here τ_{12} indicates the in-plane shear stress.

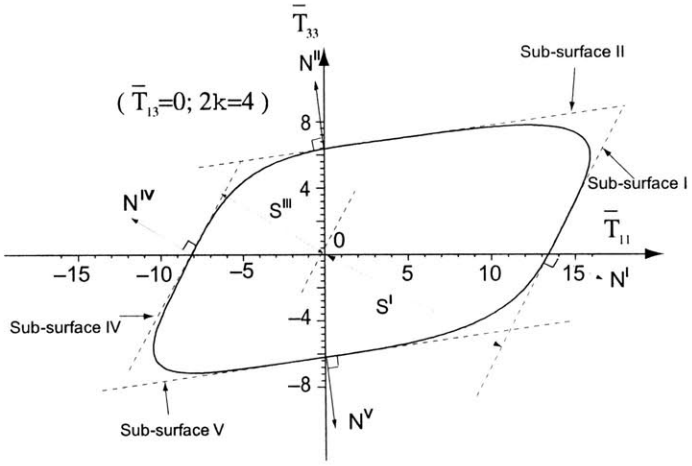

Figure 2-11: Initial yield surface for biaxial normal stress loadings, showing its four sub-surfaces. ($2k = 4$)

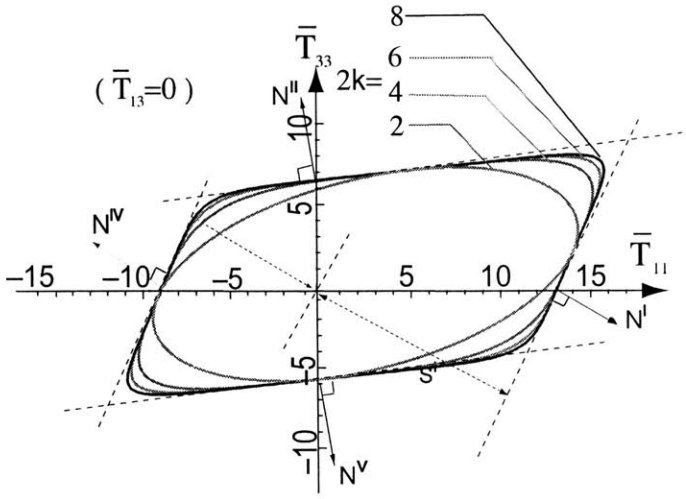

Figure 2-12: Effect of constant $2k$ on the shape of yield surface.

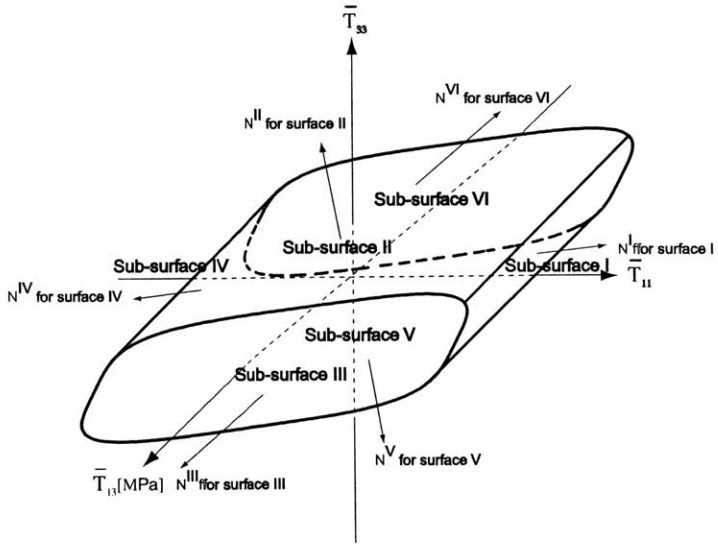

Figure 2-13: Schematic of yield surface for general in-plane loading, showing six sub-surfaces.

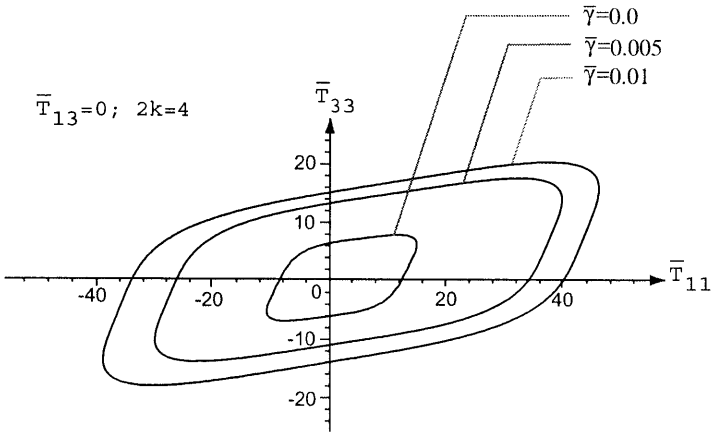

Figure 2-14: Hardening of yield surface. ($2k = 4$)

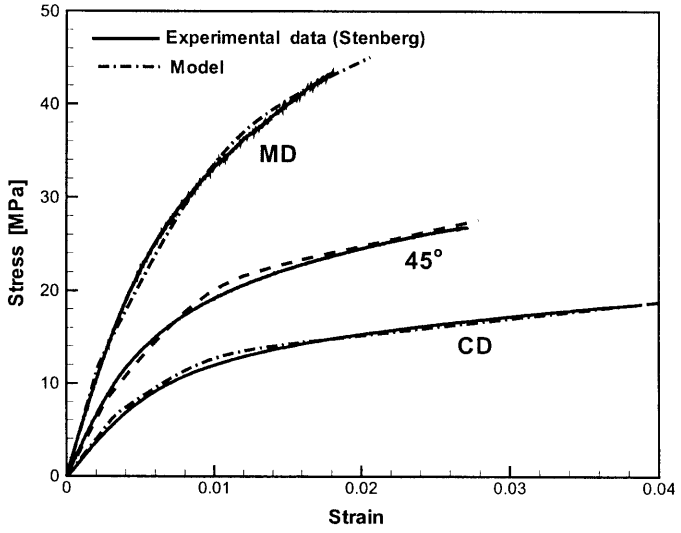

Figure 2-15: Comparison of experimental and simulated stress-strain curves for uniaxial MD, CD and 45° tension.

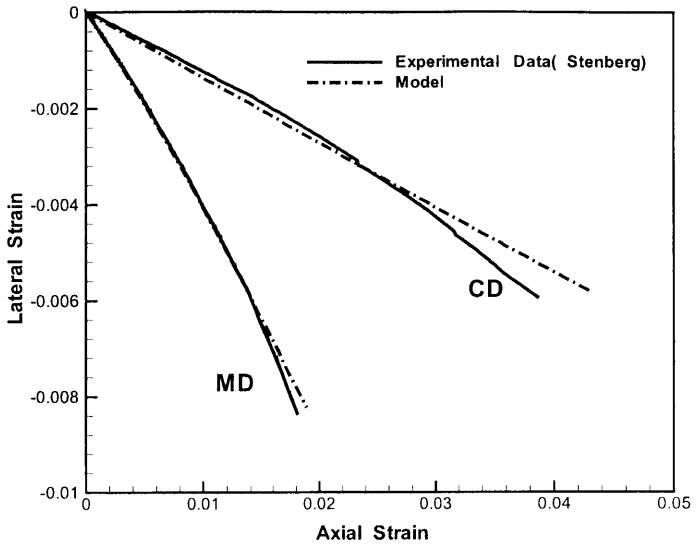

Figure 2-16: Comparison of experimental and simulated lateral strain *vs.* axial strain curves for uniaxial MD and CD tension.

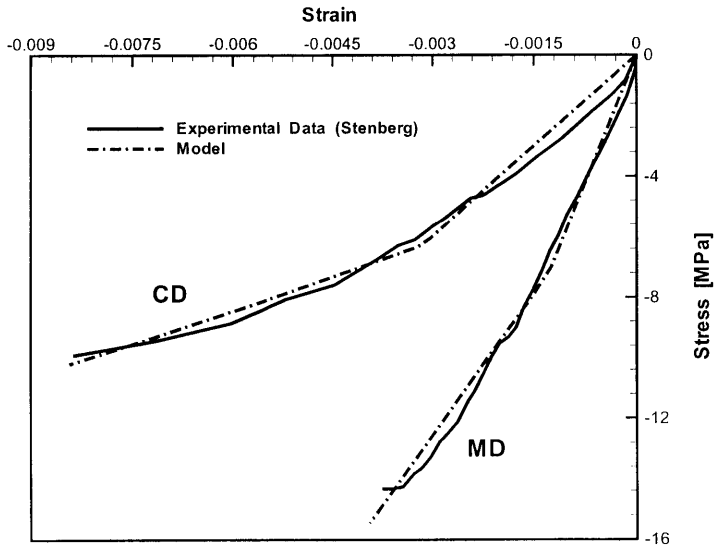

Figure 2-17: Comparison of experimental and simulated stress-strain curves for uniaxial MD and CD compression.

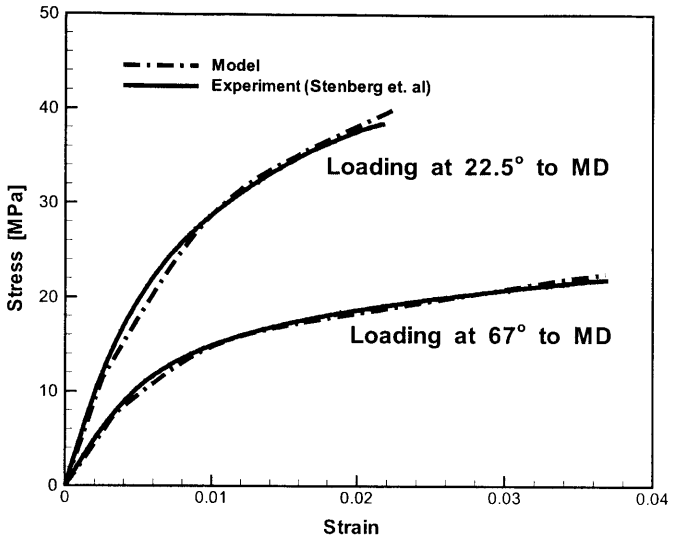

Figure 2-18: Comparison of experimental and simulated stress-strain curves for tensile loading in off-axis directions 22.5° and 67° from the MD direction.

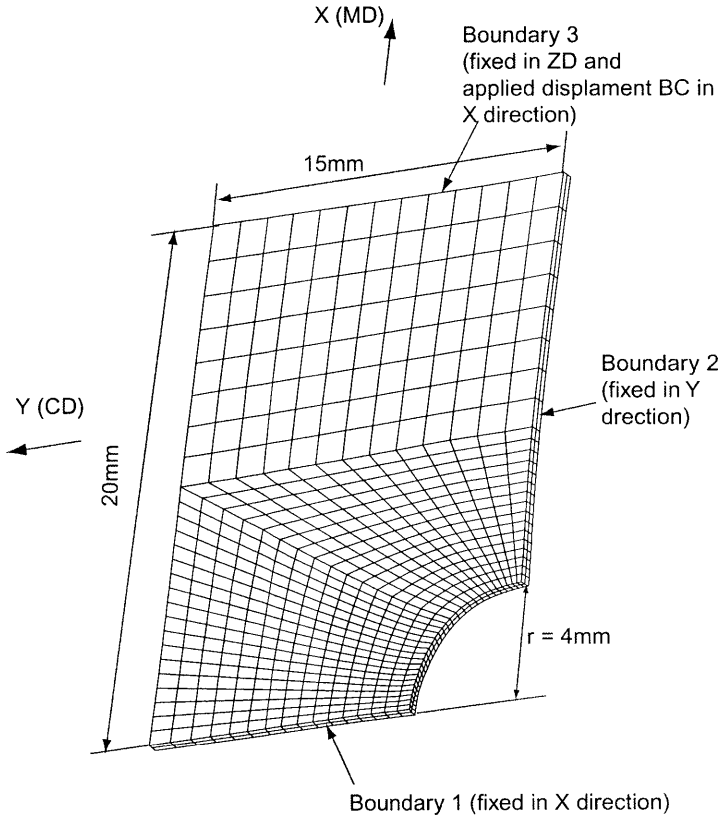

Figure 2-19: Mesh of simulation of straining of TRIPLEX^{TM} rectangular board ($40mm$ long; $30mm$ wide) with central hole.

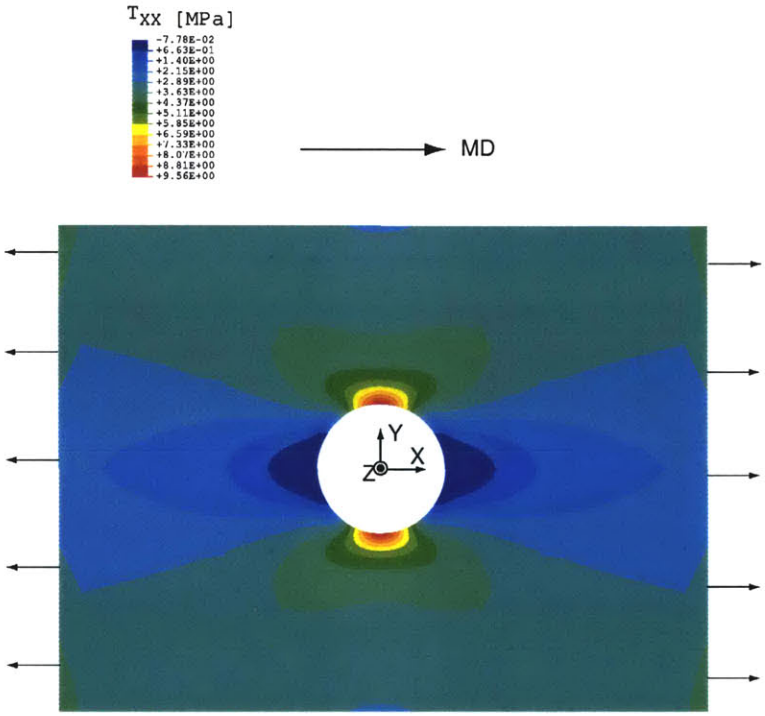

Figure 2-20: Contour plot of the in-plane normal stress component T_{XX} before any plasticity developed (Stage A on the corresponding macroscopic stress-strain curve) from simulation of straining of TRIPLEX^{TM} rectangular board ($40mm$ long; $30mm$ wide) with central hole.

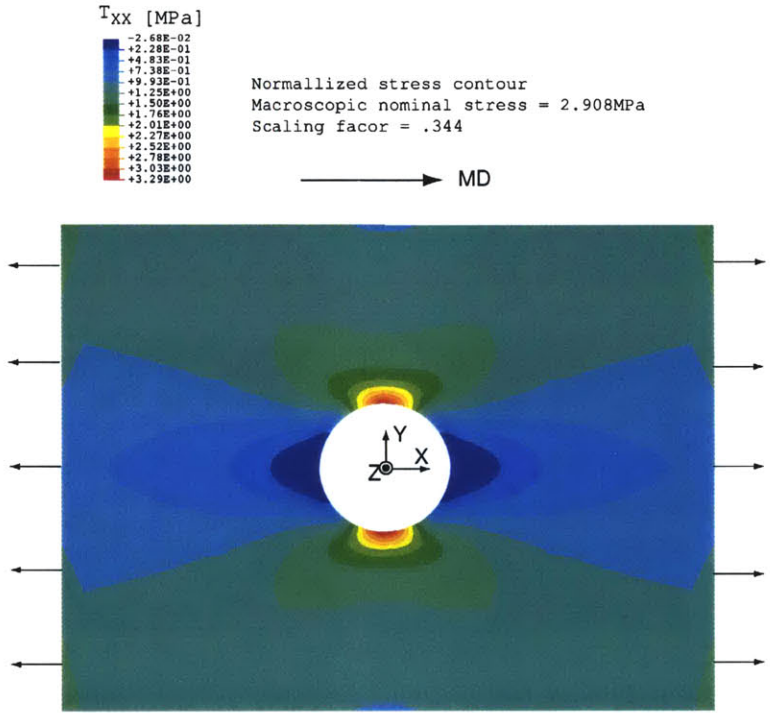

Figure 2-21: Contour plot of the normalized in-plane normal stress component T_{XX} before any plasticity developed from simulation of straining of TRIPLEX^{TM} rectangular board ($40mm$ long; $30mm$ wide) with central hole.

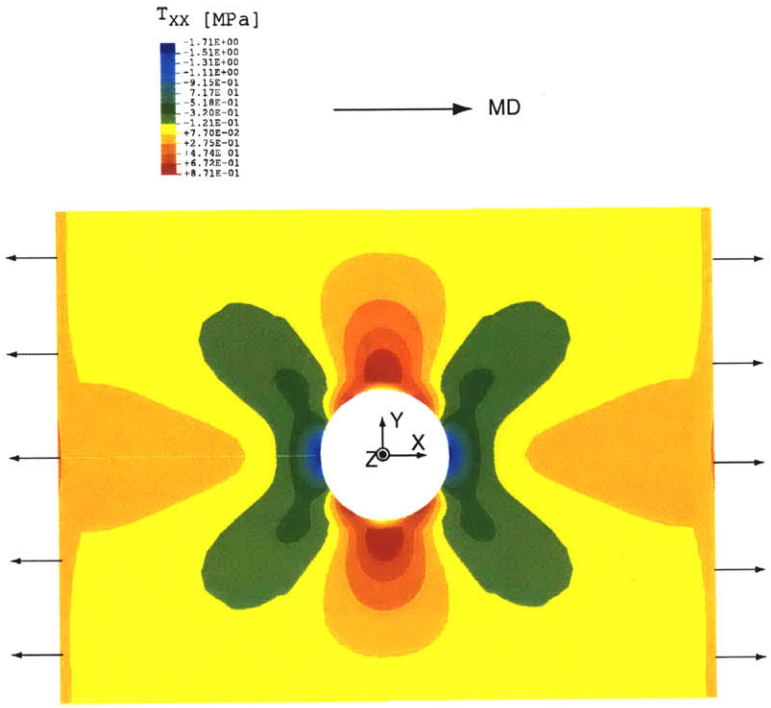

Figure 2-22: Contour plot of the in-plane normal stress component T_{YY} before any plasticity developed from simulation of straining of TRIPLEX^{TM} rectangular board ($40mm$ long; $30mm$ wide) with central hole.

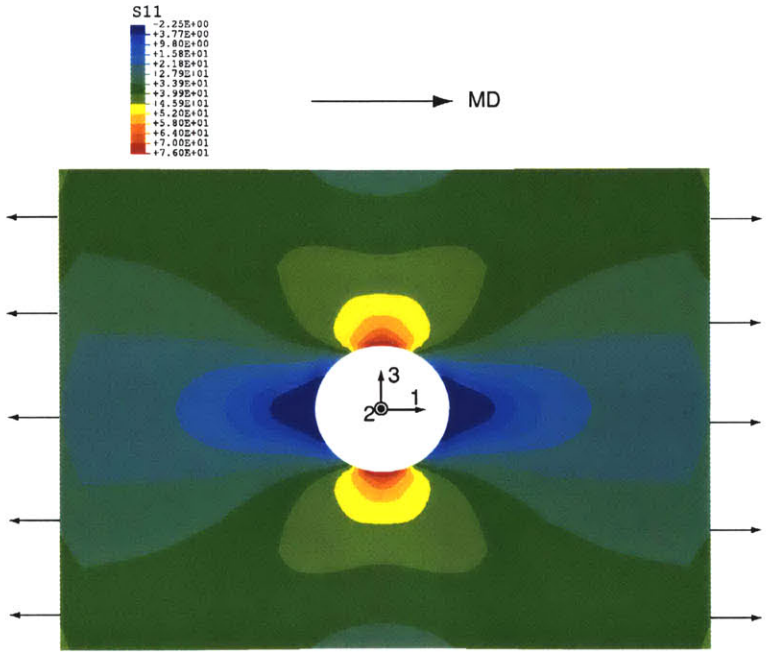

Figure 2-23: Contour plot of the in-plane normal stress component T_{XX} from simulation of straining of TRIPLEX^{TM} rectangular board ($40mm$ long; $30mm$ wide) with central hole.

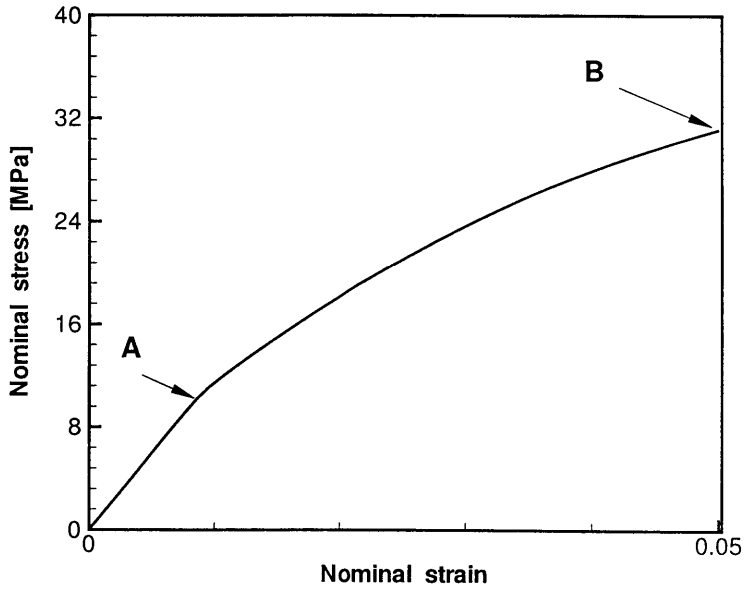

Figure 2-24: Macroscopic nominal stress *vs.* nominal strain curve for normal stress component T_{XX} from simulation of straining of TRIPLEX^{TM} rectangular board ($40mm$ long; $30mm$ wide) with central hole.

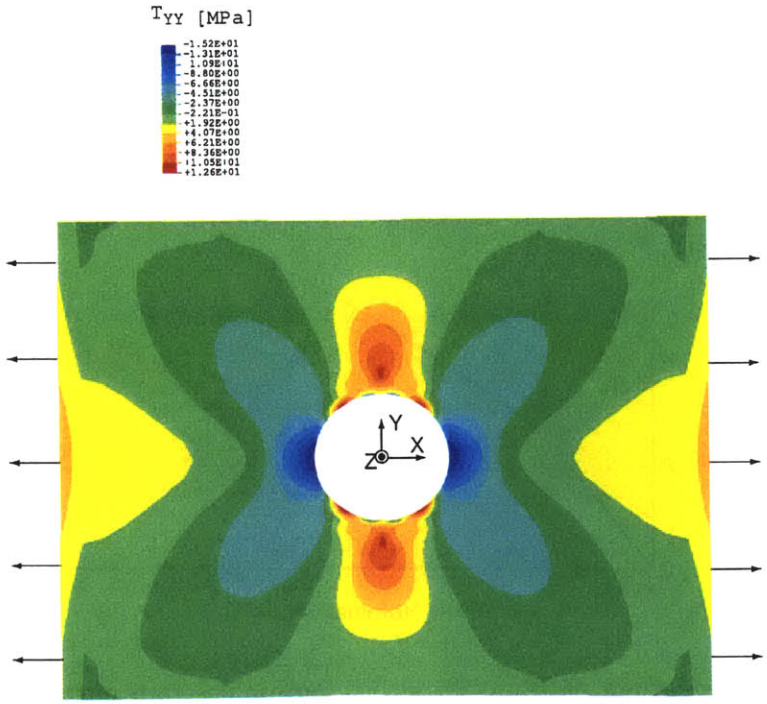

Figure 2-25: Contour plot of the in-plane normal stress component T_{YY} from simulation of straining of TRIPLEX^{TM} rectangular board ($40mm$ long; $30mm$ wide) with central hole.

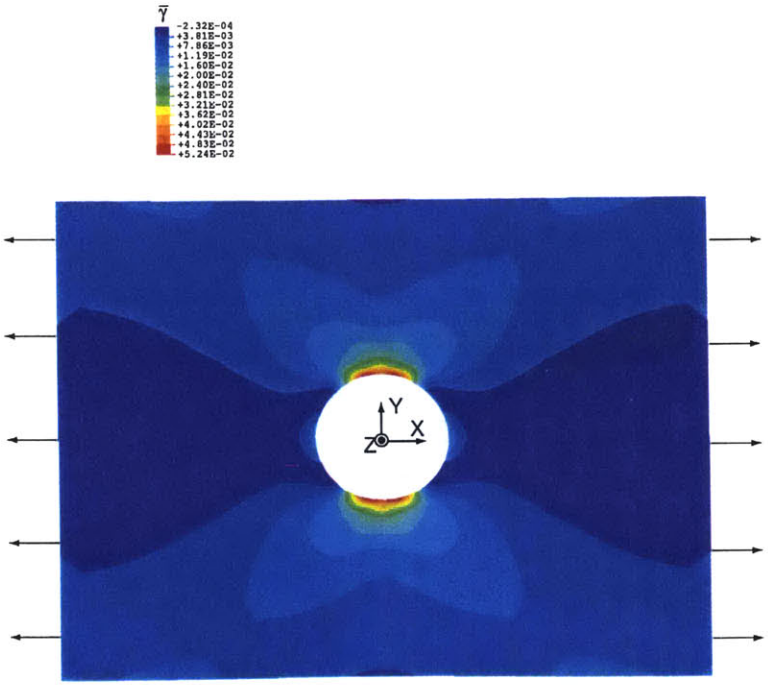

Figure 2-26: Contour plot of the equivalent plastic strain, $\bar{\gamma}$, from simulation of straining of TRIPLEX^{TM} rectangular board ($40mm$ long; $30mm$ wide) with central hole at nominal strain of 5%.

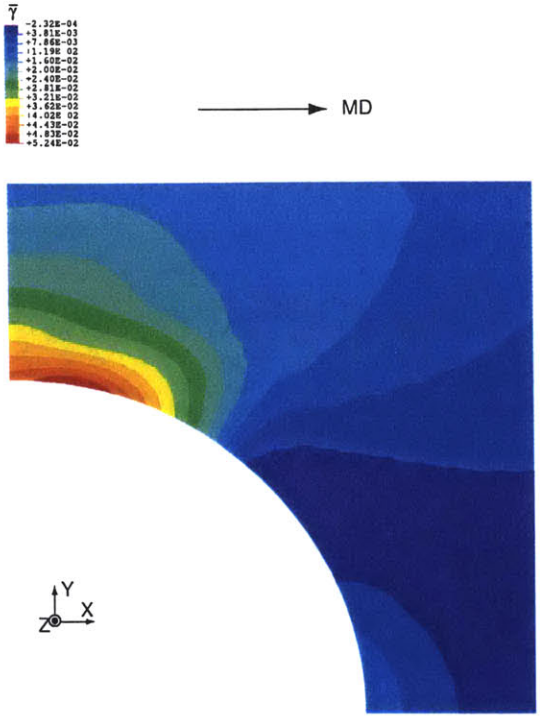

Figure 2-27: Magnified upper right corner (around the hole) of the contour plot of the equivalent plastic strain, $\bar{\gamma}$, shown in Fig. 2-26.

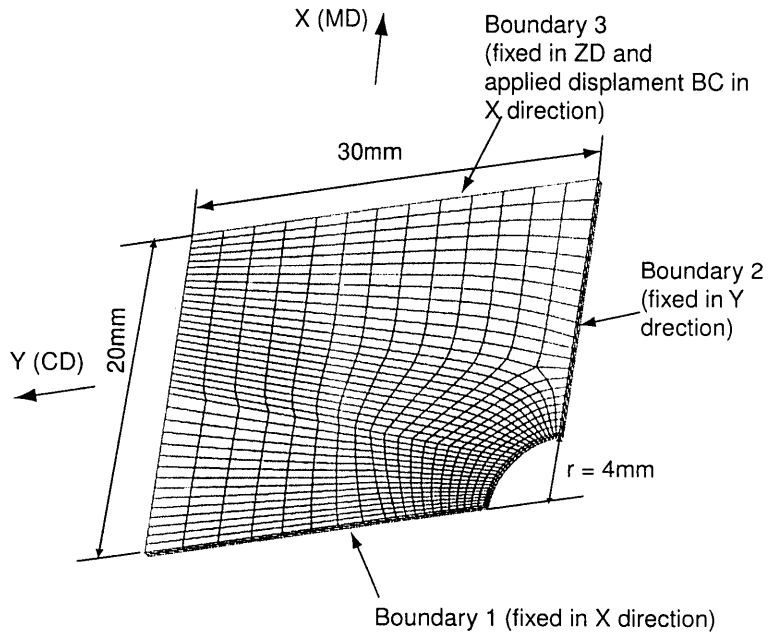

Figure 2-28: Mesh of simulation of straining of TRIPLEX^{TM} rectangular board ($40mm$ long; $60mm$ wide) with central hole.

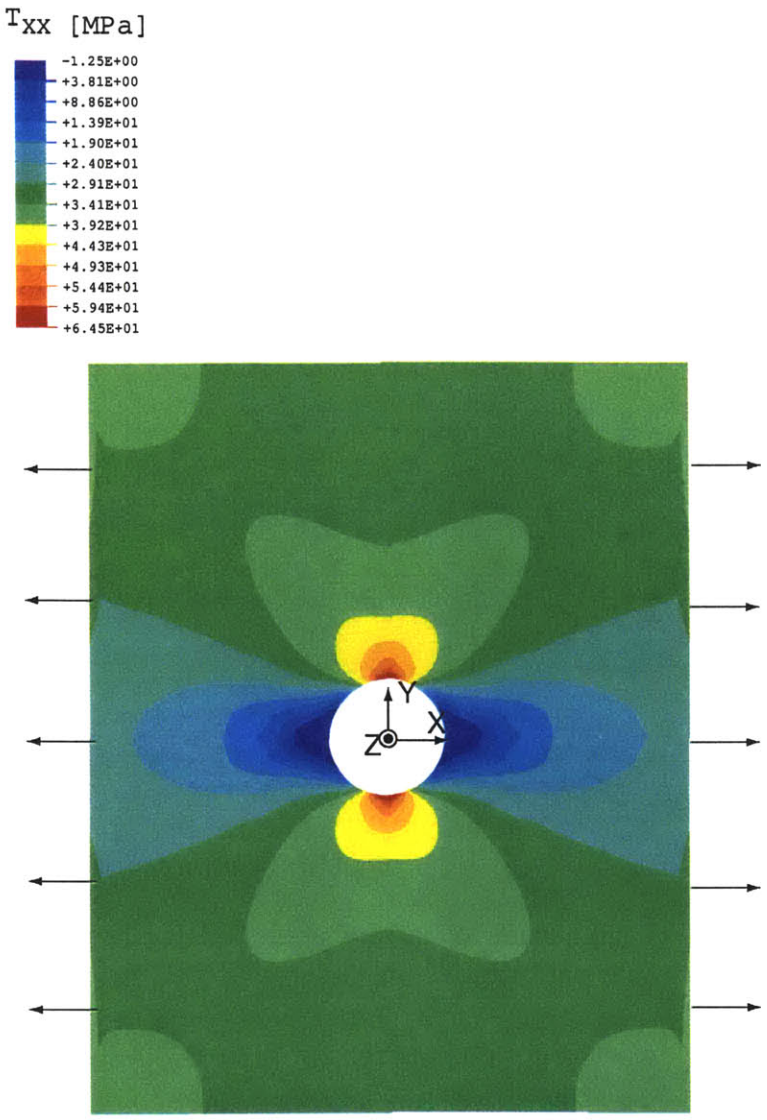

Figure 2-29: Contour plot of the in-plane normal stress component T_{XX} from simulation of straining of TRIPLEX^{TM} rectangular board ($40mm$ long; $60mm$ wide) with central hole.

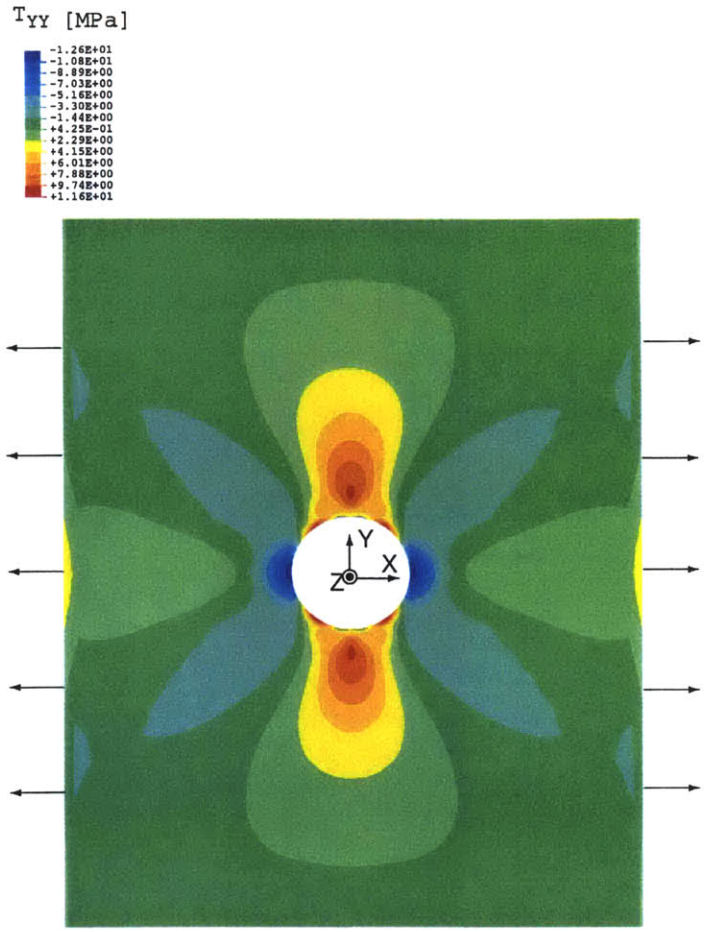

Figure 2-30: Contour plot of the in-plane normal stress component T_{YY} from simulation of straining of TRIPLEX^{TM} rectangular board ($40mm$ long; $60mm$ wide) with central hole.

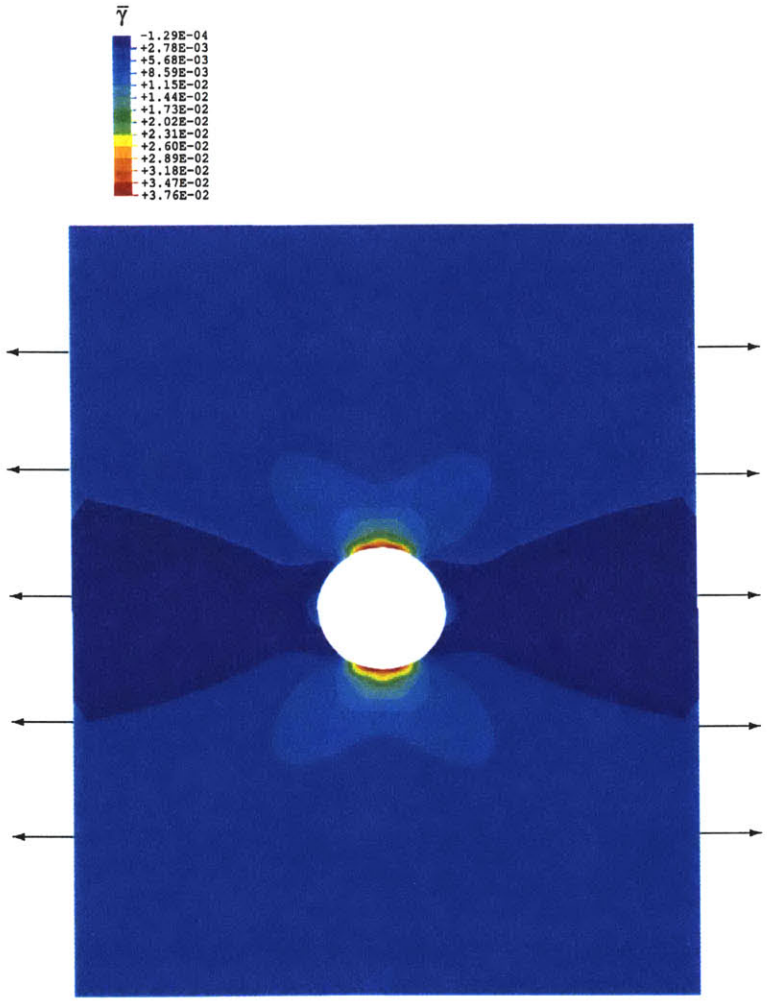

Figure 2-31: Contour plot of the equivalent plastic strain, $\bar{\gamma}$, from simulation of straining of TRIPLEX^{TM} rectangular board ($40mm$ long; $60mm$ wide) with central hole.

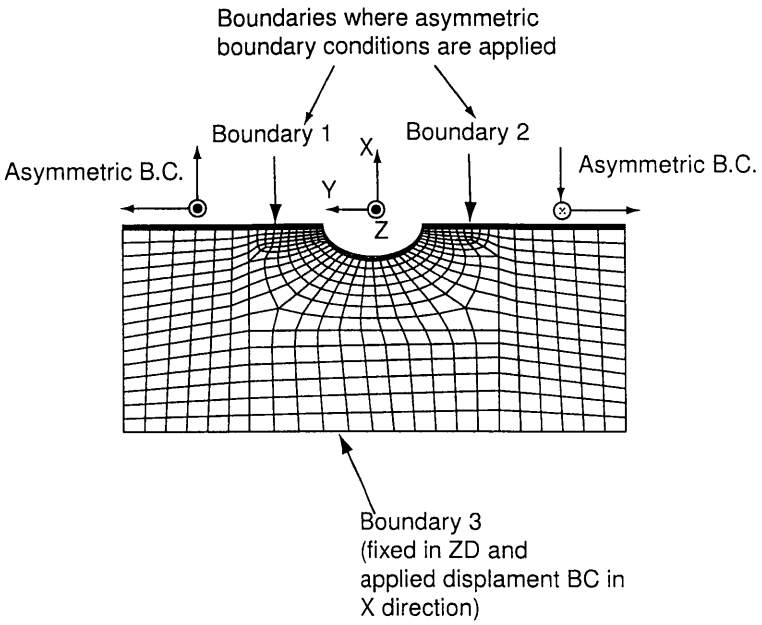

Figure 2-32: Mesh of simulation of off-axis straining of TRIPLEX^{TM} rectangular board ($40mm$ long; $30mm$ wide) with central hole.

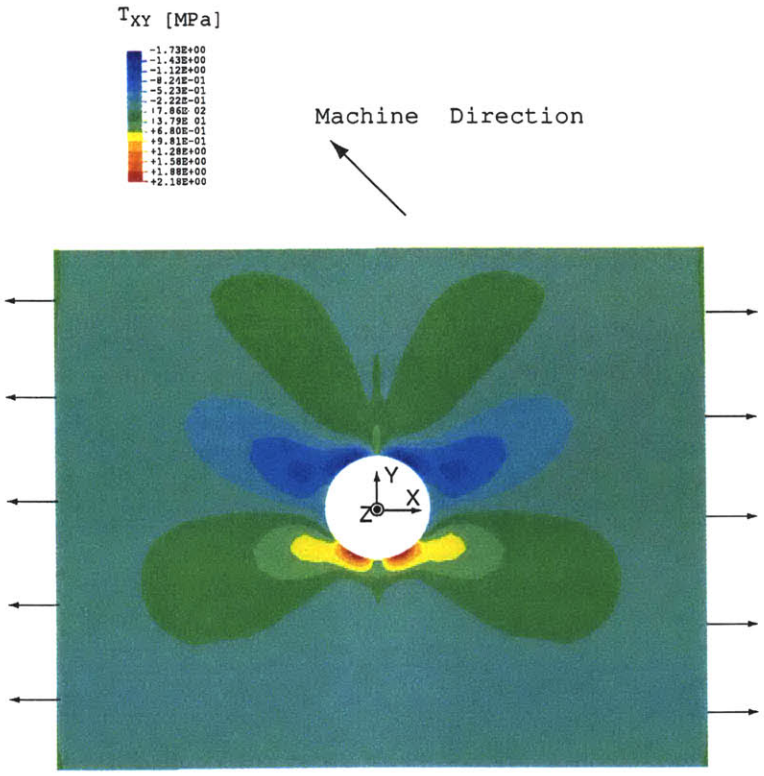

Figure 2-33: Contour plot of the in-plane normal stress component T_{XY} before any plasticity developed from simulation of off-axis straining of TRIPLEX^{TM} rectangular board ($40mm$ long; $30mm$ wide) with central hole.

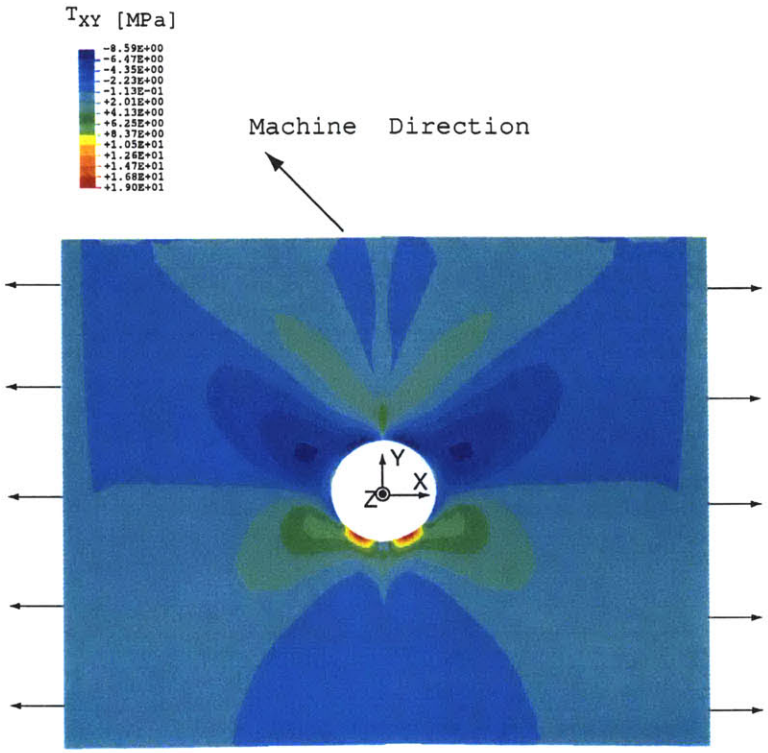

Figure 2-34: Contour plot of the in-plane normal stress component T_{XY} from simulation of off-axis straining of TRIPLEX^{TM} rectangular board ($40mm$ long; $30mm$ wide) with central hole.

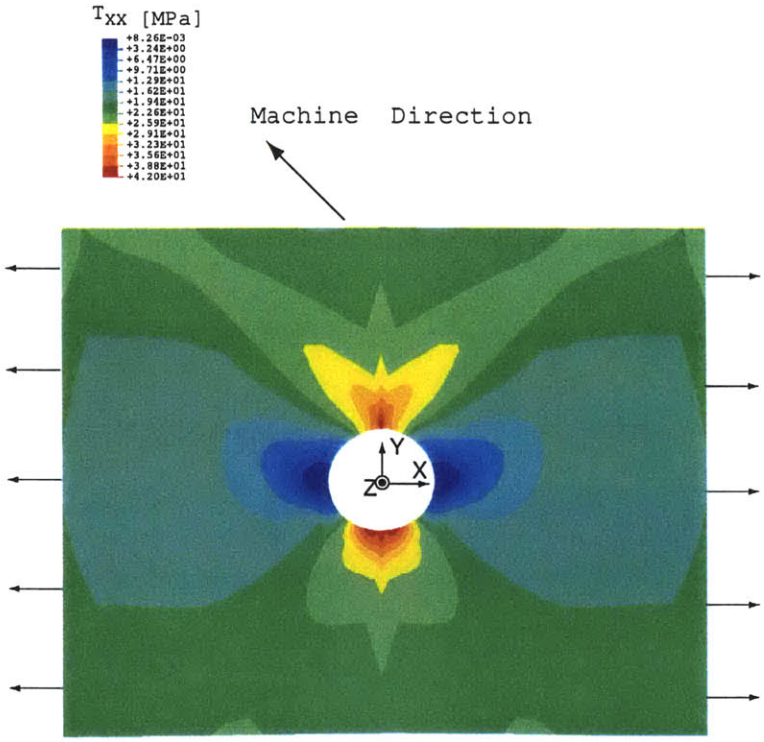

Figure 2-35: Contour plot of the in-plane normal stress component T_{XX} from simulation of off-axis straining of TRIPLEX^{TM} rectangular board ($40mm$ long; $30mm$ wide) with central hole.

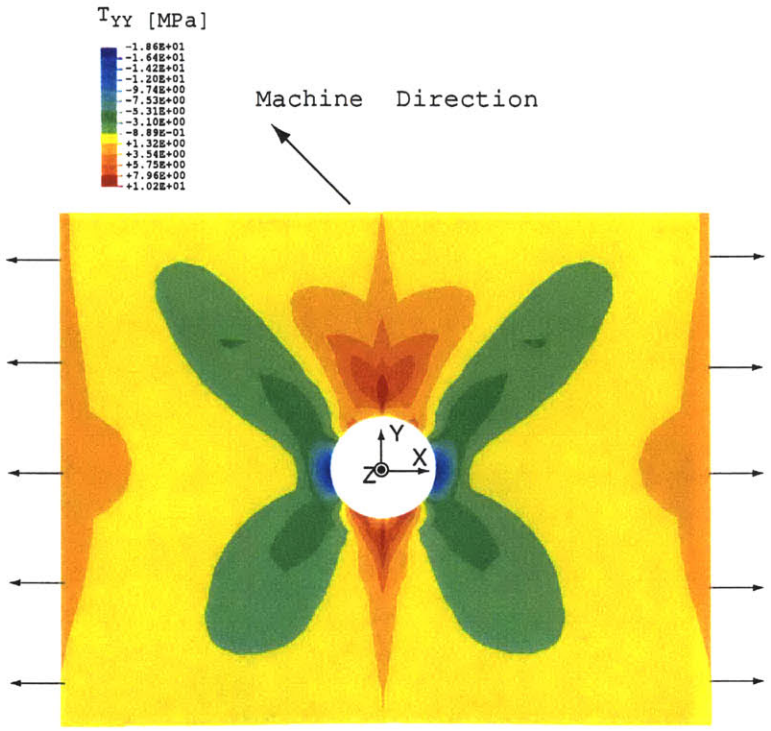

Figure 2-36: Contour plot of the in-plane normal stress component T_{YY} from simulation of off-axis straining of TRIPLEX^{TM} rectangular board ($40mm$ long; $30mm$ wide) with central hole.

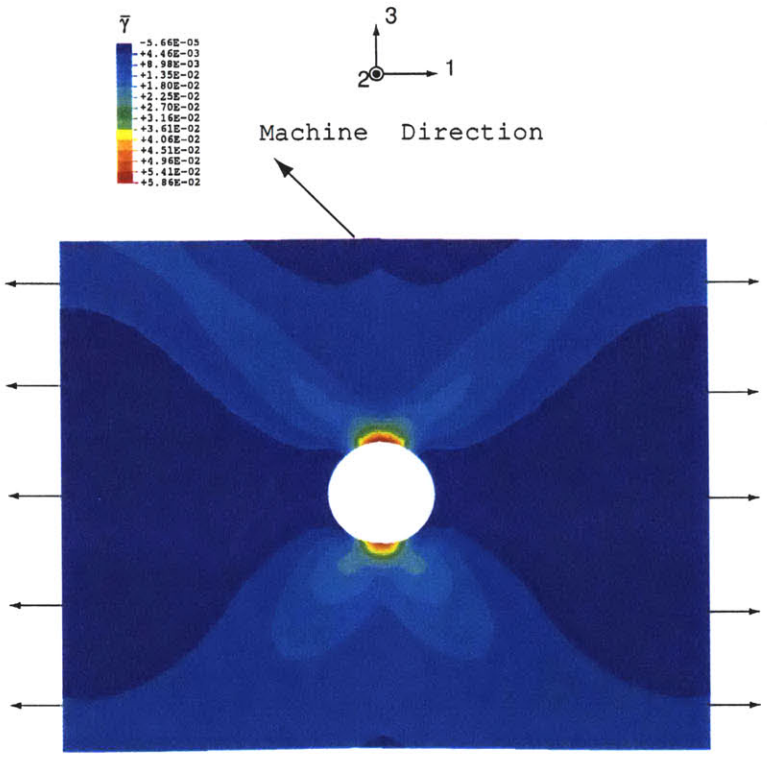

Figure 2-37: Contour plot of the equivalent plastic strain, $\bar{\gamma}$, from simulation of off-axis straining of TRIPLEX^{TM} rectangular board ($40mm$ long; $30mm$ wide) with central hole.

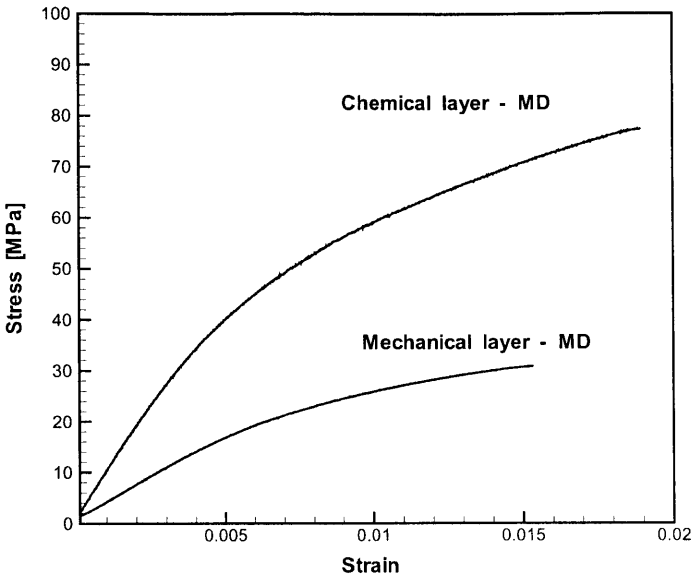

Figure 2-38: Comparison of MD tensile stress-strain curve for mechanical and chemical pulp layers (Stenberg [31])

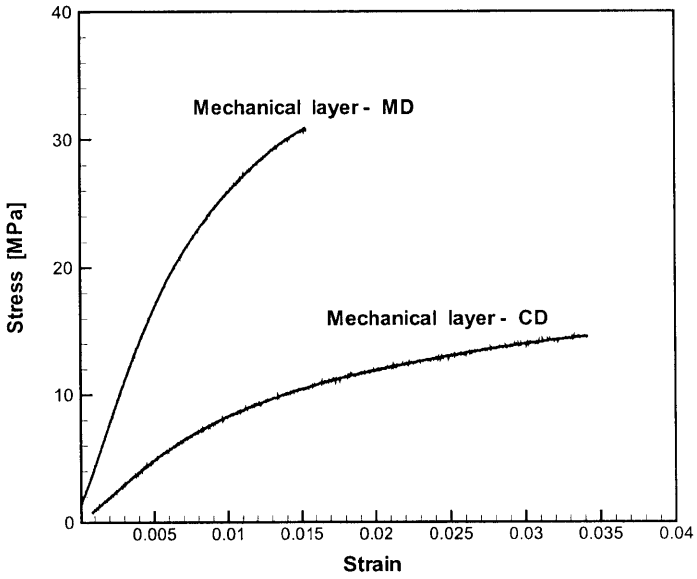

Figure 2-39: Comparison of MD and CD tensile stress-strain curve for mechanical pulp layer (Stenberg [31])

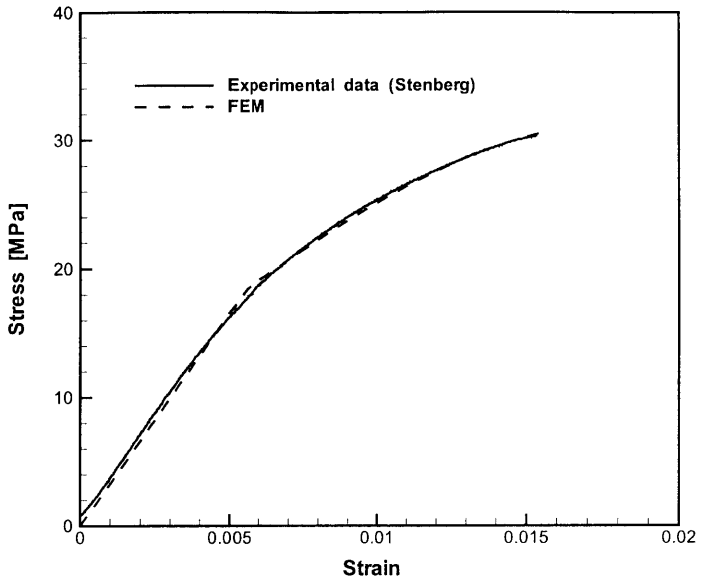

Figure 2-40: Comparison of experimental and simulated stress-strain curves for MD tensile loading for mechanical pulp layer.

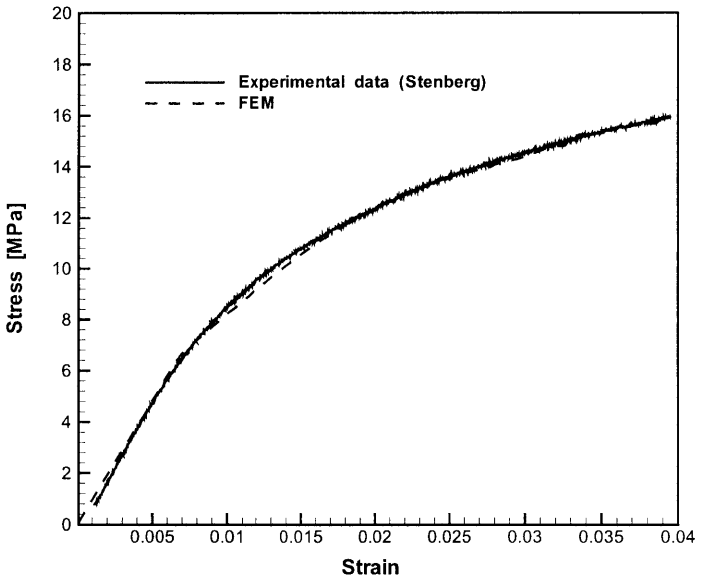

Figure 2-41: Comparison of experimental and simulated stress-strain curves for CD tensile loading for mechanical pulp layer.

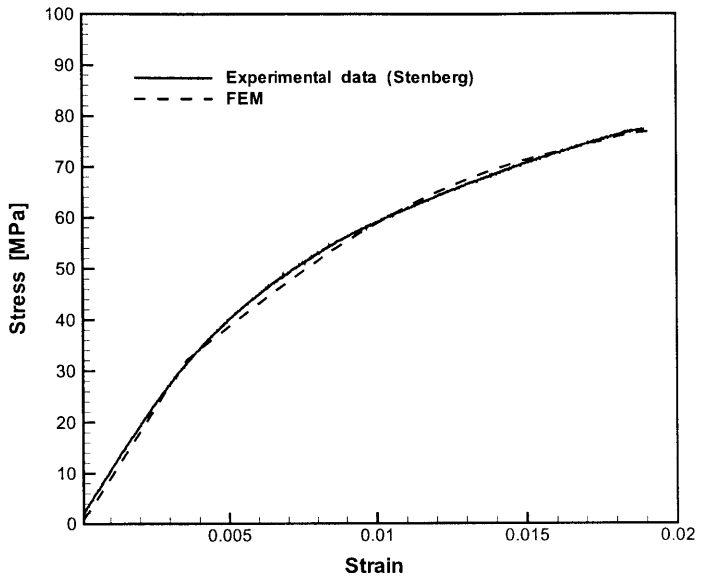

Figure 2-42: Comparison of experimental and simulated stress-strain curves for MD tensile loading for chemical pulp layer.

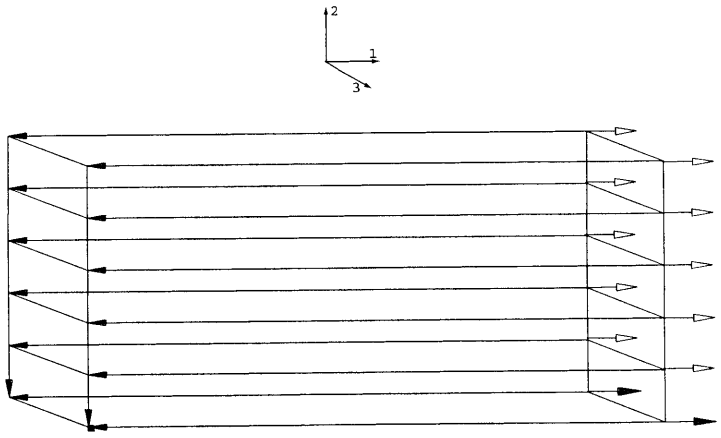

Figure 2-43: Mesh used to reproduce the MD tensile stress-strain curve for TRIPLEX^{TM} using fitted parameters for each of the individual layers.

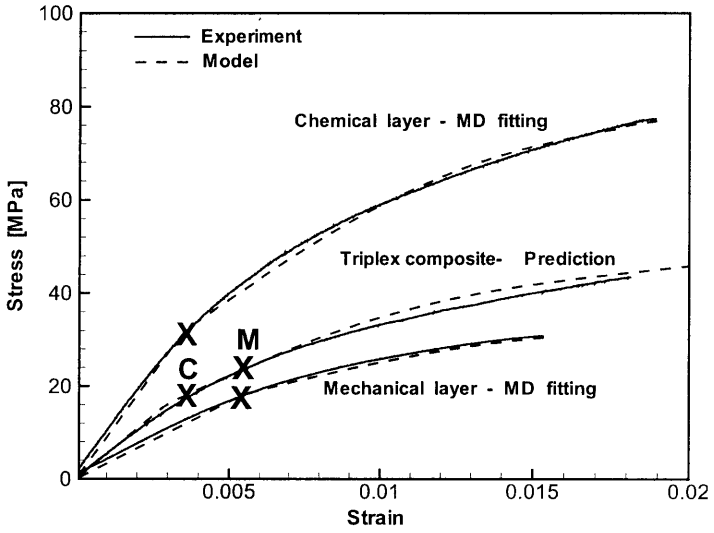

Figure 2-44: Comparison of model-reproduced and experimental MD tensile stress-strain curve for TRIPLEX^{TM}.

Chapter 3

Interface Constitutive Model

During certain converting processes (processes whereby paperboard is converted into a product such as a milk carton) and in-service applications, paperboard is often subjected to combined loadings which include out-of-plane deformations. The out-of-plane loadings can cause interfacial delamination to separate the paperboard layers. In some instances delamination is desirable, as in the case of creasing, whereby a punching process locally damages the interface in a controlled manner to enable accurate formation of corners during the subsequent folding of paperboard. In other instances, however, delamination is undesirable, such as during in-service loading, where, for example, a box may be dropped or subjected to bending (Carlsson, *et al.*[21], Donner and Backer[10])

In work by Dunn [18], the deformation mechanisms operative during through-thickness loading of paperboard were experimentally investigated. Scanning electron microscopy was used to monitor the evolution in microstructure during through-thickness tensile and shear loading. Results revealed that the initiation, interaction and propagation of delamination along interfaces between paperboard laminae play a crucial role in the damage and failure of the laminated structure under out-of-plane loading. In work by Stenberg, *et al.* [32][33], a series of modified ARCAN[6] testing systems were used to obtain nominal stress-strain curves of paperboard under various combined out-of-plane loading conditions. Based on these experimental results, we

propose a 3D interface traction *vs.* relative-displacement separation model where a limiting separation surface (analogous to a yield surface) in the normal-shear traction space evolves with a monotonically-increasing measure of the inelastic part of the relative interface displacement following an internal state variable approach. The model is implemented into finite element software (here, the commercial ABAQUS[19] program is used) on a plane strain basis to analyze the out-of-plane behavior of multi-layer paperboard structures.

3.1 EXPERIMENTAL OBSERVATIONS

To study the out-of-plane mechanical behavior of paperboard, macroscopic tests were conducted on specially-designed test fixtures at STFI (Swedish Pulp and Paper Research Institute) by Stenberg, *et al.* [32][33] using the ARCAN[6] design. Nominal stress-strain curves were obtained for a multi-layer paperboard under various through-thickness loading conditions. To investigate the micro-mechanisms behind the macro-level behaviors observed, microscopic tests were conducted using in situ SEM by Dunn[18].

3.1.1 Macroscopic experiments

Three types of macroscopic through-thickness experiments were conducted by Stenberg, *et al.* [32][33]: ZD pure extension; shear without normal constraint (ZD-MD or ZD-CD); and combined normal (tensile or compressive load in ZD) and shear (MD or CD) tests. Specimens were constructed from TRIPLEX^{TM} paperboard. It should be noted that some important differences exist between paperboard and conventionally-defined laminated composites. It is customary for layers of conventional laminated composites to be distinct, separate entities with relatively clearly-defined interfaces between such layers. For the paperboard structure, since it is continuously formed by laying one wet mat over another, the individual layers are not particularly distinct from one another. Instead, there exists a small amount of weaving and entanglement

of fibers across the interfaces, in addition to the sprayed bonding agent. Therefore, a relatively weak mechanical coupling exists between layers due to both the fiber entanglement and bonding along the interfaces. Procedures such as controlling the amount of starch applied during different stages of processing enables the interfaces between the core mechanical layers to be designed to be weaker than the interfaces between the mechanical core and outer chemical layers.

A ZD tensile stress-strain curve obtained by Stenberg, *et al.* [32][33] is shown in Fig. 2-7. The stress measure is force per initial cross-sectional area; the nominal strain is calculated by dividing relative opening displacement of the loading platens by the initial board thickness. At the earliest stage of deformation, the stress increases linearly with displacement. The stress-strain relation shows a small amount of pre-peak nonlinearity before reaching a peak stress value. After the peak, the stress-strain curve exhibits pronounced softening. This result is similar to data from Persson[28].

A through-thickness shear (ZD-MD) stress-strain curve obtained by Stenberg, *et al.* [32][33], is shown in Fig. 2-9. Features similar to those of the tensile curve are observed, except that the stress transmitted through the paperboard does not drop to zero even when a very large amount of relative motion is applied to top and bottom loading surfaces. Instead, it asymptotically approaches a value (about 12% of the peak strength) that cannot be ignored in general. Another important feature of the shear test is that normal dilation is observed during the test; *i.e.*, ZD thickening is observed when out-of-plane shear load is applied under conditions of zero net ZD tension/compression, as shown in Fig. 3-1. According to SEM tests by Dunn[18], this can be explained by the interface shear failure mechanisms, which produces dilation due to fiber disentangling, interlocking and rotation.

A series of combined normal (ZD) loading and shear loading tests (MD or CD) were also conducted by Stenberg, *et al.* [32][33]. In these experiments, a fixed normal force, either tensile or compressive, was applied, together with increasing shear displacement. Shear stress-strain curves were obtained for each of these tests. Several shear stress-strain curves in MD-ZD are plotted in Fig. 3-2 for different normal force

conditions. The applied normal stresses and the corresponding peak shear stresses are plotted in the normal-shear stress space as shown in Fig. 3-3. As can be seen, the shear strength of the paperboard is "pressure" dependent. These stress loci form a separation surface in the through-thickness normal and shear traction space. Details about using this surface as the interface separation criterion will be discussed later in this chapter.

In summary, macroscopic data reveal the following important features of the out-of-plane behavior of paperboard:

- For through-thickness tension, the stress-strain curve starts linearly, showing a modulus of $18MPa$. The curve shows a small amount of non-linearity prior to the peak load. For through-thickness shear, the stress linearly increases with the strain with an initial moduli of $34MPa$ (ZD-MD) and $26MPa$ (ZD-CD). Similar to the tensile behavior, only a small amount of non-linearity is shown before reaching the peak shear stress.

- A peak stress of approximately $0.4MPa$ is reached for ZD tension, followed by pronounced softening behavior after the peak. The peak shear stresses achieved are approximately $1.1MPa$ (ZD-MD) and $0.9MPa$(ZD-CD).

- The shear strength of the paperboard increases with compressive normal stress and decreases with tensile normal stress; *i.e.*, the shear strength of paperboard is normal-stress-dependent.

- The stress drops dramatically after the peak stress is reached for both through-thickness tension and shear. The tensile stress decreases to zero at large tensile strain. However, residual shear-load carrying capability remains even for more than 200% out-of-plane nominal shear strain.

- Paperboard tends to dilate in the through-thickness direction when out-of-plane shear is applied.

- As discussed in Chapter 2, TRIPLEX^{TM} exhibits nonlinear elastic stress-strain behavior under ZD compression up to large strains of more than 20%. This behavior is modeled by the in-plane model. (Interfaces do not fail under ZD compression alone.)

3.1.2 Microscopic experiments

Microscopic tests were conducted by Dunn[18] at MIT using a scanning electron microscope (SEM) testing system to investigate the micro-level physical mechanisms underlying the through-thickness paperboard behavior observed in macroscopic tests. Through-thickness extension, shear, shear without normal constraint, combined normal load and shear tests, and bending tests were conducted on five-layer TRIPLEX^{TM} paperboards, the same material used in the macroscopic tests of Stenberg, *et al.* [32][33]. SEM micrographs were taken at different stages of deformation, concurrently with the stress-strain curves, to monitor the micro-level events occurring during the deformation.

Fig. 3-4 shows an example of a ZD tensile stress-strain curve correlated with microscope images of the ZD-MD cross section, as shown in Fig. 3-5 - Fig. 3-14. Positions on the curve where SEM pictures were taken are marked by step numbers. By inspecting the *in situ* SEM micrographs corresponding to each of the points on the stress-strain curve, Dunn[18] found that no noticeable microcracking can be observed prior to the peak stress. At stage 4, which is immediately post-peak, microcrack formation is apparent inside the cross-section, indicating that the peak in stress-strain curve correlates with the beginning of microcrack formation. Furthermore, the microcracks are observed primarily along the weaker mechanical/mechanical interfaces. After peak step 4, the stress drops as the coalescence of microcracks forms several major delaminations, as can be seen in the micrograph at step 5. As the imposed displacement increases, the load continues to drop, major delaminations become dominant, and small local delaminated regions start to unload, as shown in micrographs of steps $6-7$. At step 8, fiber bridging between separated interfaces is obvious, and

at step 9, a second major delamination re-opens. Beyond step 10, stress drops slowly as fibers bridging the delaminated gap are disengaged. At very large strains, the specimen splits into two separate parts, and the stress goes to zero.

In summary, there is no significant change in material structure prior to the peak in stress. At the peak stress, microcracks initiate primarily along the relatively weaker mechanical/mechanical interfaces inside the core. The formation of microcracks and their subsequent coalescence decreases the internal load-carrying area of the specimen at the elevation of the interface, leading to the dramatic drop of the nominal stress level. After a dominant delamination spreads across the entire cross section of the specimen, the rate of decrease in nominal stress with additional strain is reduced. Fiber bridging and fiber pull-out are now the dominant deformation mechanisms, providing residual load-carrying capability until final separation of the specimen.

Fig. 3-15 shows an example of a ZD-MD shear stress-strain curve correlated with microscope images, as shown in Fig. 3-16 - Fig. 3-21. The first figure shows the specimen at no load. In Fig. 3-17, the specimen has been loaded into the nonlinear region. By comparing with the previous picture, no appreciable deformation is developed in this stage. The third image was taken immediately after the peak stress is achieved. It can be clearly seen that at this stage, most of the damage was concentrated along one of the mechanical/mechanical interfaces in the form of a single delamination spanning the entire viewing frame. This is obviously different from what was observed in the ZD tension test. In the subsequent images, it can be seen that the major delamination continues to open in the Z-direction. Because of extensive fiber-fiber interactions along the shearing interface, observable in the form of fiber bending as well as fiber interlocking and friction, the stress plateaus instead of dropping to zero. These fiber-fiber interactions are also responsible for the normal (through-thickness) dilation associated with interface shearing.

In summary, the following major observations were made from the microscopic tests:

- Corresponding to the peak on the stress-strain curve, one or several micro cracks

were first observed, and the propagation and coalescence of the cracks leads to the softening behavior.

- The major separations or delaminations of the laminated paperboard occur primarily at the interfaces between different pulp layers. Furthermore, the delaminations are more likely to develop along the weaker mechanical/mechanical interfaces than along the stronger mechanical/chemical interfaces.

- Delamination of the paperboards under pure through-thickness shear tests is more homogeneous (both along an interface and over the set of interfaces) than that under through-thickness pure tension tests.

- The mechanisms observed in SEM videos and image analysis from the microscopic tests are also operative at the macro-level.

- General features of the microscopic stress-strain tests are similar to those obtained from macro-level tests.

3.1.3 Summary

Based on these observations, it is clear that the behavior of the interfaces between different paper pulp layers plays a crucial role in the damage and failure of the paperboard laminates when out-of-plane loading is applied. This leads us to propose an interface model which can capture important features of the through-thickness behavior of paperboards: *e.g.*, the peak stress, the post-peak strain-softening, the shear-induced dilation and the normal-stress-dependence of the shear strength. Further, the observation that interface cracking occurs around the peak point of the stress-strain curve indicates that we can construct a separation surface using the data points of peak shear stress and applied normal stress in normal-shear traction space as an interface separation criterion. Such a surface, based on data by Stenberg [32],[33],[31], has been previously shown in Fig. 3-3. Furthermore, the interface

constitutive law can be implemented into FEM models to explicitly simulate the interface separation process, thus providing the capabilities to provide more insights to the design and manufacturing of paperboards.

3.2 Interface modeling and formulation

To explicitly model the delamination of an interface, some researchers have developed cohesive zone models to describe the interface between two materials. A cohesive zone type of model was first developed by Dugdale[14] and Barenblatt[8] and further developed by Comninou [12], Needleman[24] and Ortiz and Blume[26] to analyze interface separation between different materials. Needleman first incorporated this method into finite element analysis simulations of void nucleation by inclusion debonding [25]. Later Xu and Needleman[35] used the model in other applications. Several other researchers (*e.g.*, Socrate[29]; Biner[9]; Williams and Addessio[34]; Lissenden[22]) utilized similar types of models to simulate interface behavior under different conditions.

In most models, the cohesive surface constitutive relation relates the traction and relative displacement across the separating surfaces by introducing an interface potential. These previous interface traction-displacement models have many advantages. However, in these prior research works, the interface constitutive relation is derived from an interface potential and so is not history-dependent; *i.e.*, the cohesive traction-displacement relationship is fully reversible. Therefore, the irreversible damage accumulated at the interface is not taken into account, and these models cannot be accurately applied to situations where the interface is subject to unloading and subsequent reloading. Such histories are common in many manufacturing processes of paperboard products, *e.g.*, the creasing and subsequent folding of paperboard. Needleman[25] and Ortiz and Pandolfi[27] have proposed irreversible cohesive laws to overcome this problem by introducing an evolution in either the effective peak stress or effective peak opening displacement of their potential-based models. However, these new approaches solve the problem numerically without explicitly addressing the physics behind the history-dependent behavior of the interface. Also, the potential-based nature of these methods limits the general flexibility to handle different types of traction-displacement relations.

In this research, an interface decohesion model is constructed based upon a sep-

aration surface in the normal-shear traction space that enables inelastic separation following an internal state variable approach. The model has the benefits of the potential-based cohesive interface models. For example, there are no prior restrictions on the size, location, distribution, or direction of growth of the interface cracks; no restrictions on the size of plastic zone ahead of the crack tips; no restrictions on the constitutive behavior of the bulk of material; and interactions between developing microcracks or major delaminations at different locations within the structure will be taken care of naturally as a result of calculation. Furthermore, the proposed model addresses the history-dependent nature of interface separation in a physically-based manner. Instead of using an interface energy potential as the basis of the cohesive models, a separation criterion is formulated in a manner analogous to that of a yield surface in plasticity, as discussed previously. The separation criterion is constructed in the normal-shear traction space and is introduced to control the initiation and evolution of interface cracks. A non-associated flow rule enables the model to simulate normal dilatation due to shearing of the separated surfaces. A history-dependent state variable, the interface damage, is also introduced in the model. With the evolution of the state variable, the history-dependent behavior of the interface is accurately captured. Furthermore, through-thickness shear, pure tension and combined normal and shear loading experiments provide enough information to determine the material properties needed for model implementation.

3.2.1 Kinematics

Consider a body as shown in Fig. 3-22, with initial undeformed configuration B_0 partitioned by an interface S_0 into two parts, ${B_0}^+$ and ${B_0}^-$, lying on the plus and minus sides of S_0, respectively. The respective boundary portions, ${S_0}^+$ of ${B_0}^+$ and ${S_0}^-$ of ${B_0}^-$ initially coincide with S_0 in the undeformed configuration. On S_0 there are corresponding points ${P_0}^+ \subset {S_0}^+$ and ${P_0}^- \subset {S_0}^-$, which also coincide in the undeformed configuration. The position of any point P on the interface surface in the undeformed configuration is denoted by $\boldsymbol{X}$, and we assume parametric coordinates

ξ_1 and ξ_2 in surface S_0. The two tangent vectors of the reference interface then can be written as

$$\boldsymbol{t}_{i_0} = \frac{\partial \boldsymbol{X}}{\partial \xi_i}, \qquad i = 1, 2 \tag{3.1}$$

and the initial normal direction of interface S_0 can be obtained as

$$\boldsymbol{n_0} = \frac{\boldsymbol{t}_{1_0} \times \boldsymbol{t}_{2_0}}{| \boldsymbol{t}_{1_0} \times \boldsymbol{t}_{2_0} |}, \tag{3.2}$$

with the understanding that coordinates have been chosen such that $\boldsymbol{n_0}$ points from ${S_0}^-$ to ${S_0}^+$. Upon deformation mapping $\boldsymbol{x}$, the initially-coincident surfaces of the interface, ${S_0}^+$ and ${S_0}^-$, are separated into the deformed positions S^+ and S^-, respectively. To describe this discontinuous behavior of the deformation mapping, a mean deformation mapping can be defined over the initial surface S_0 to identify a unique deformed configuration of the interface, S, by defining

$$\bar{\boldsymbol{x}} = \frac{1}{2}(\boldsymbol{x}^+ + \boldsymbol{x}^-) \tag{3.3}$$

and setting

$$S = \bar{\boldsymbol{x}}(S_0). \tag{3.4}$$

The initially-coincident points ${P_0}^+$ and ${P_0}^-$ are now located at $P^+ = \boldsymbol{x}^+({P_0}^+)$ and $P^- = \boldsymbol{x}^-({P_0}^-)$, and we can define the interface relative displacement as

$$\boldsymbol{\Delta} = \boldsymbol{x}^+({P_0}^+) - \boldsymbol{x}^-({P_0}^-) \tag{3.5}$$

Furthermore, a co-rotational coordinate system for the interface can be defined by two tangential vectors

$$\boldsymbol{t}_i^* = \frac{\partial \bar{\boldsymbol{x}}}{\partial \xi_i} \qquad i = 1, 2 \tag{3.6}$$

and a normal vector

$$\boldsymbol{n} = \frac{\boldsymbol{t}_1^* \times \boldsymbol{t}_2^*}{| \boldsymbol{t}_1^* \times \boldsymbol{t}_2^* |}. \tag{3.7}$$

To make the two tangent vectors have unit length are perpendicular to each other, we further define

$$\boldsymbol{t_1} = \frac{\boldsymbol{t_1^*}}{|\ \boldsymbol{t_1^*}\ |}, \tag{3.8}$$

and

$$\boldsymbol{t_2} = \frac{\boldsymbol{n} \times \boldsymbol{t}_1}{|\ \boldsymbol{n} \times \boldsymbol{t}_1\ |}. \tag{3.9}$$

This co-rotational coordinate system $(\boldsymbol{t}_1, \boldsymbol{t}_2, \boldsymbol{n})$ will rotate with the body under rigid body rotation and translation, as shown in Fig. 3-22. Use of such co-rotational coordinate system is convenient for implementation of a frame-indifferent description of the traction-displacement law.

The traction vector $\boldsymbol{T}$ and relative displacement across the interface, $\boldsymbol{\Delta}$, can be expressed in component form as

$$\begin{aligned} \boldsymbol{T} &= T_n \boldsymbol{n} + T_{t_1} \boldsymbol{t_1} + T_{t_2} \boldsymbol{t_2} \\ &= (\boldsymbol{T} \cdot \boldsymbol{n})\boldsymbol{n} + (\boldsymbol{T} \cdot \boldsymbol{t_1})\boldsymbol{t_1} + (\boldsymbol{T} \cdot \boldsymbol{t_2})\boldsymbol{t_2}; \end{aligned} \tag{3.10}$$

and

$$\begin{aligned} \boldsymbol{\Delta} &= \Delta_n \boldsymbol{n} + \Delta_{t_1} \boldsymbol{t_1} + \Delta_{t_2} \boldsymbol{t_2} \\ &= (\boldsymbol{\Delta} \cdot \boldsymbol{n})\boldsymbol{n} + (\boldsymbol{\Delta} \cdot \boldsymbol{t_1})\boldsymbol{t_1} + (\boldsymbol{\Delta} \cdot \boldsymbol{t_2})\boldsymbol{t_2}. \end{aligned} \tag{3.11}$$

In the following parts of this section, the subscripts 'n', 't_1' and 't_2' will always indicate components in the normal, the first and the second tangential directions along the interface surfaces, respectively in the current configuration.

In applications to interfaces in paperboard, the reference configuration will be essentially planar, so that generalized coordinates ξ_i are most conveniently taken to be cartesian in the MD and CD, respectively.

3.2.2 Decomposition of Displacement Jump

Through-thickness load-unload tests indicate that unloading prior to the peak stress does not result in significant permanent deformation; whereas, upon unloading after the peak stress, a significant permanent deformation is observed along with continuously diminishing elastic unloading stiffness. Therefore, the relative interface incremental displacement, $d\boldsymbol{\Delta} = \boldsymbol{\Delta}(t + dt) - \boldsymbol{\Delta}(t)$, where t is a monotonically-increasing (time) parameter, can be additively decomposed into elastic ($d\boldsymbol{\Delta}^{\boldsymbol{e}}$) and plastic ($d\boldsymbol{\Delta}^{\boldsymbol{p}}$) parts:

$$\boldsymbol{d\Delta} = d\boldsymbol{\Delta}^{\boldsymbol{e}} + d\boldsymbol{\Delta}^{\boldsymbol{p}}. \tag{3.12}$$

In component form, the relations can be written as

$$\begin{aligned} d\Delta_n &= d\Delta_n^e + d\Delta_n^p \\ d\Delta_{t_1} &= d\Delta_{t_1}^e + d\Delta_{t_1}^p \\ d\Delta_{t_2} &= d\Delta_{t_2}^e + d\Delta_{t_2}^p. \end{aligned} \tag{3.13}$$

3.2.3 Interface Constitutive Law

The interface constitutive law relates the co-rotational incremental traction components with the incremental displacement components through the interface stiffness as follows in component form

$$\begin{aligned} dT_n &= K_n(d\Delta_n - d\Delta_n^p) \\ dT_{t_1} &= K_{t_1}(d\Delta_{t_1} - d\Delta_{t_1}^p) \\ dT_{t_2} &= K_{t_2}(d\Delta_{t_2} - d\Delta_{t_2}^p), \end{aligned} \tag{3.14}$$

where K_n, K_{t_1} and K_{t_2} are the components of the instantaneous interface stiffness, evaluated in the co-rotational coordinate system, shown in Fig. 3-22. This incremental interface traction-displacement law is expressed in co-rotational coordinates because rigid body rotation introduces neither relative interface separation nor traction force.

Also note that the components of the interface stiffness are, in general, functions of the state of the interface. In other words, the stiffness may evolve with the evolution of interface damage, which will be discussed in detail later.

3.2.4 Interface separation criterion

As discussed in section 3.1, the experimental data by Stenberg [32][33] indicates that a peak stress exists in through-thickness shear, tension and combined normal-shear stress-strain curves. From the stress-strain curves it can also be seen that the pre-peak inelastic or nonlinear portion is relatively insignificant. Microscopic tests by Dunn [18] show that these peak stresses coincide with the formation of interface delamination in the form of microcracks, which then propagate and coalesce with ongoing deformation, producing the post-peak softening. Thus, if we plot the peak shear stress values together with the amount of ZD normal stress applied in the stress space, we obtain a separation surface in the shear-normal traction space that is analogous to a yield surface. This surface is a physically descriptive representation of the criterion for the onset of permanent interface separation. An experimental separation surface has been shown previously in Fig. 3-3, together with a functional form chosen to match it.

Based on the experimental data for TRIPLEX^{TM} paperboard, a specific form for the criterion was determined:

$$f(T_n, T_{t_1}, T_{t_2}, S_n, S_{t_1}, S_{t_2}) = a_1 {T_{t_1}}^{2k} + a_2 {T_{t_2}}^{2k} + T_n - c = 0 \tag{3.15}$$

where T_n, T_{t_1} and T_{t_2} are the components of the traction vector defined previously; k is an integer which determines the curvature of the surface. The parameters a_1, a_2 and c are defined as follows:

$$c = S_n(D); \qquad a_1 = \frac{S_n(D)}{S_{t_1}(D)^{2k}}; \qquad a_2 = \frac{S_n(D)}{S_{t_2}(D)^{2k}}. \tag{3.16}$$

where $S_n(D)$, $S_{t_1}(D)$ and $S_{t_3}(D)$ are the instantaneous ZD tensile strength, the shear strength in MD, and the shear strength in CD of the interface, respectively. To simplify the model further, we assume that there is only one state variable, which controls the state of separation of the interface, the accumulated damage in the interface, D. Definition of the damage state variable will be given later in this chapter. The strengths are then assumed to take initial values of S_{n0}, $S_{t_{1_0}}$ and $S_{t_{2_0}}$ and are taken to evolve with the dimensionless interface damage variable D, which monitors the level of interface damage.

As a simplification, the numerical simulations in this thesis will be based on a 2-D framework. (This is a good approximation as long as there is no off-axis (MD/CD) in-plane loading.) In 2-D, Equation 3.15 can be simplified to:

$$f(T_n, T_t, S_n, S_t) = a_t T_t^{2k} + T_n - c = 0 \tag{3.17}$$

where S_t can be either S_{t_1} or S_{t_2} and $a_t = \frac{S_n(D)}{S_t(D)^{2k}}$, as defined in Equation 3.15; T_t can be either T_{t_1} or T_{t_2} defined in Equation 3.16, depending on which 2-D stress space is being probed. The exponent $2k$ is taken to be 2 in this work since this was found to best fit the available data. The shape of this function in the traction space is shown in Fig. 3-3. It can be seen that this functional form provides a very good approximation to the experimental surface. The tension, S_n, and the shear, S_{t_1}, strengths of the interface are the respective intersections of the locus with the axes.

The proposed interface separation criterion has the following features:

- The shear strength of the interface is dependent on the normal pressure. The shear strength increases with increasing compressive normal stress and decreases with increasing tensile normal stress.

- The shear behavior is symmetric with respect to the normal traction axis. In other words, the behavior of the interface under shear is the same if the direction of shear traction is reversed. This appears to be generally true for paperboard.

- The separation criterion is not closed on the compressive side of the normal traction axis because interface failure does not develop under purely normal compressive load.

- With a certain $2k$ value (*e.g.*, $2k = 2$), the 2-D interface separation criterion is determined if the two parameters a and c are determined. In other words, the criterion can be fully determined by conducting a shear and a tension test on the paperboard laminates. If a series of combined out-of-plane normal and shear loading tests could be done, more accurate mathematical forms of the criterion could be obtained by data-fitting the experimentally-obtained surface in the traction space, perhaps leading to other values for the curve-shaping exponent $2k$.

3.2.5 Flow rule

The flow rule determines the inelastic components of the relative displacement increment once inelastic separation across the interface starts. In general, a flow rule can be written as

$$d\boldsymbol{\Delta}^p = \chi \boldsymbol{M} d\bar{\Delta}^p, \tag{3.18}$$

where

$$\chi = \begin{cases} 1; & \text{if } f = 0 \text{ and } \boldsymbol{dT}^* \cdot \frac{\partial f}{\partial \boldsymbol{T}} > 0 \\ 0; & f < 0 \text{ or } f = 0 \text{ and } \boldsymbol{dT}^* \cdot \frac{\partial f}{\partial \boldsymbol{T}} < 0 \ . \end{cases} \tag{3.19}$$

Here $d\bar{\Delta}^p = \sqrt{d\boldsymbol{\Delta}^p \cdot d\boldsymbol{\Delta}^p}$ is the magnitude of the equivalent plastic displacement increment, $\boldsymbol{dT}^*$ is the incremental trial traction vector (defined as $\sum K_i d\Delta_i \boldsymbol{e}_i$, $i = t_1, t_2, n$), $\frac{\partial f}{\partial \boldsymbol{T}}$ is the normal direction on the separation surface, and $\boldsymbol{M}$ is the unit flow direction, expressed in the co-rotational normal and tangential interface coordinate system as

$$\boldsymbol{M} = \hat{\boldsymbol{M}} / \parallel \hat{\boldsymbol{M}}, \parallel \tag{3.20}$$

where

$$\hat{\boldsymbol{M}} = \hat{M}_n \boldsymbol{n} + \hat{M}_{t_1} \boldsymbol{t_1} + \hat{M}_{t_2} \boldsymbol{t_2}. \tag{3.21}$$

For an associated flow rule, the flow direction is the normal to the interface separation surface, and we may take

$$\hat{\boldsymbol{M}} = \frac{\partial f}{\partial \boldsymbol{T}}, \tag{3.22}$$

where f is the interface separation function defined in Eqn. 3.15, and $\boldsymbol{T}$ is the traction vector. This equation can be expressed in component form as

$$\hat{M}_n = \frac{\partial f}{\partial T_n}, \quad \hat{M}_{t_1} = \frac{\partial f}{\partial T_{t_1}}, \quad \hat{M}_{t_2} = \frac{\partial f}{\partial T_{t_2}}. \tag{3.23}$$

The associated flow rule acting on the f of equation 3.15 will result in some amount of normal dilation under the action of only shear stress. However, the experimentally-observed dilation exceeds the amount produced assuming an associated flow rule and $2k$-values that fit adjacent points on the separation surface. Therefore, a non-associated flow rule is followed to better capture the observed behavior. For a normal/shear non-associated flow rule, the components of the flow direction $\hat{\boldsymbol{M}}$ can be constructed as

$$\hat{M}_n = \mu \frac{\partial f}{\partial T_n}, \quad \hat{M}_{t_1} = \frac{\partial f}{\partial T_{t_1}}, \quad \hat{M}_{t_2} = \frac{\partial f}{\partial T_{t_2}}, \tag{3.24}$$

where μ is a dimensionless frictional function which is dependent on the state variable, interface damage, *i.e.*, $\mu = \mu(D)$. For example, the μ-function could be a function of the equivalent inelastic separation. The function μ will be determined by matching the experimental curve of ZD dilation *vs.* MD/CD shear strain. In this research the μ function is taken to be

$$\mu = A(1 - BD) \tag{3.25}$$

where A and B are constants determined by matching the experimental dilation curve and D is the internal state variable monitoring the damage, which will be defined later.

For the particular form of interface separation criterion considered in Eqn. 3.17,

an associated flow rule gives the direction of the normal to the interface separation surface as

$$\boldsymbol{N} = 2a_t T_t \boldsymbol{t} + \boldsymbol{n}; \tag{3.26}$$

for the case of a non-associated flow rule, the direction of the inelastic displacement increment is given by

$$\hat{\boldsymbol{M}} = 2a_t T_t \boldsymbol{t} + \mu \boldsymbol{n} \tag{3.27}$$

where $\boldsymbol{t}$ can be either $\boldsymbol{t}_1$ or $\boldsymbol{t}_2$; T_t can be either T_{t_1} or T_{t_2} defined in Equation 3.16, depending on which 2-D stress space is being probed.

The magnitude of the inelastic displacement jump, $d\bar{\Delta}^p$, is determined by the consistency condition, which requires the interface separation criterion to be satisfied at any time once the criterion is reached under any monotonic loading, *i.e.*, $f(t+dt) = 0$, where f is defined in Equation 3.15.

3.2.6 Evolution of State Variable

As discussed previously in the experimental work review, microscopically, the physical mechanism behind the mechanical behavior of the paperboard under out-of-plane loading is the same for different loading situations; namely the breaking and slippage of bonds between fibers. In other words, it is the damage of these fiber bonds which gives rise to the initiation of permanent interface separation. Therefore in this research, a single dimensionless scalar state variable, the interface damage D, is used. The interface damage can be interpreted as the fraction of interface area debonded *vs.* the initial interface bonding area. Since the interface damage is directly related to the permanent separation of the interface, it is further assumed to be a function of the equivalent inelastic displacement, which is determined by the consistency condition. Therefore, for the damage state variable, we have

$$D = h_D(\bar{\Delta}^p) \tag{3.28}$$

where h_D is a mathematical function which makes D evolve from 0 to 1 when $\bar{\Delta}^p$ increases from 0 to a sufficiently large value, *e.g.*, about the average fiber length.

In this research, h_D is taken to be the following form

$$h_D = tanh(\bar{\Delta}^p/b) \tag{3.29}$$

where b is a constant with units of length. It is usually of the order of the fiber diameter, say $30 - 80\mu m$. The interface strength and stiffness are in turn assumed to evolve with the damage state variable as follows:

$$S_n = S_{n_0}(1 - R_n D); \quad S_{t_1} = S_{t_{1_0}}(1 - R_{t_1} D); \quad S_{t_2} = S_{t_{2_0}}(1 - R_{t_2} D), \tag{3.30}$$

where S_{n_0}, $S_{t_{1_0}}$ and $S_{t_{2_0}}$ are the initial (undamaged) interface strengths, and R_n, R_{t_1} R_{t_2} are constants controlling the residual strengths of the interface, as will be discussed later.

For the interface stiffness, unloading tests by Stenberg [31] show continuously diminishing elastic stiffness once inelastic separation has begun (*i.e.*, post-peak). In this research we take

$$K_n = K_{n_0}(1 - R_n D); \quad K_{t_1} = K_{t_{1_0}}(1 - R_{t_1} D); \quad K_{t_2} = K_{t_{2_0}}(1 - R_{t_2} D), \tag{3.31}$$

where K_{n_0}, $K_{t_{1_0}}$ and $K_{t_{2_0}}$ are the initial interface stiffness in the normal and shear directions, respectively; R_n, R_{t_1} and R_{t_2} are constants controlling the asymptote values of the elastic stiffness.

3.2.7 Residual shear resistance

The Stenberg[32],[33] through-thickness shear test results show non-negligible shear load-carrying capability remaining after the shear deformation is very large(*e.g.*, more than 100% nominal strain) as shown in Fig. 3-41. Due to the nature of the fiber network structure of paperboard, some fibers protrude from the separated interface and

are dragged during the shearing. These protruding fibers interact with each other and give rise to the residual shear resistance phenomenon observed. This interesting phenomenon can be captured within this interface model framework by letting the two interface shear strengths S_{t_1} and S_{t_2} asymptote towards the residual strengths observed in the out-of-plane shear tests under zero ZD load, as shown in Equation 3.30. Theoretically, there should be no ZD normal tension strength after the interface is completely separated under large shear straining, as any protruding fibers would become disengaged. However, in order to avoid numerical problems when implementing the model and to keep the overall shape of the yield surface without significant change, we assume there would also be a very small amount of normal tensile strength remaining when the interface is fully damaged, such as one to two percent of the initial normal tensile strength. Mathematically, this idea of capturing the residual shear strength behavior is to evolve the shear strengths between their undamaged values to their residual values

$$\begin{aligned} R_n S_{n_0} \leq S_n(D) \leq S_{n_0}; \\ R_{t1} S_{t_{10}} \leq S_{t_1}(D) \leq S_{t_{10}}; \\ R_{t2} S_{t_{20}} \leq S_{t_3}(D) \leq S_{t_{20}}, \end{aligned} \tag{3.32}$$

where R_n, R_{t_1} and R_{t_2} are constants controlling the asymptote value of the normal tensile strength and the two shear strength values relative to their initial values. R_{t_1} and R_{t_2} are first determined by matching the asymptotic value of the experimental residual shear strength and R_n, is then determined such that the overall shape of the limiting surface will not change significantly, as will be discussed later in this chapter. (The same R_n, R_{t_1} and R_{t_2} have been previously introduced in Equation 3.31 for the de-stiffening of the elastic constants. These two groups of constants can take different values.)

3.2.8 Finite element implementation

One of the advantages of the interface constitutive law is that it can be naturally incorporated into conventional finite element software by directly applying the constitutive relation into surface-like finite elements, *i.e.*, interface elements. The user-defined element capability (UEL) of the commercial FEM software ABAQUS is used in this case to fulfill the task.

For the 2-D plane strain case, an interface element with four nodes and two degrees of freedom at each node is designed to carry out the kinematics, as shown in Fig. 3-24. These four nodes form two pairs of nodes whose reference locations initially coincide on surface S_0 in the undeformed configuration. A co-rotational coordinate system can be defined on the mean surface S (in the 2-D case, it becomes a line), as introduced in the preceding section, as η_1 and η_2. By using the standard shape function, $N_i(\eta_1, \eta_2)$, $i = 1, ..n$, where n is the number of nodes on each side of the surfaces, we can express the relative displacement across the interface as

$$\boldsymbol{\Delta}(\eta_1, \eta_2) = \sum_{i=1}^{n} \boldsymbol{x_i} N_i(\eta_1, \eta_2), \tag{3.33}$$

where

$$\boldsymbol{x_i} = \boldsymbol{x_i}^+ - \boldsymbol{x_i}^- \tag{3.34}$$

are the relative displacement at the corresponding nodes on the surface. For a 2-D case, relative displacement across the line of interface can be expressed as

$$\boldsymbol{\Delta}(\eta) = \sum_{i=1}^{n} \boldsymbol{x_i} N_i(\eta), \tag{3.35}$$

where η can be either η_1 or η_2 in Equation 3.33. Under this definition, $\boldsymbol{\Delta}$ remains invariant upon rigid rotation and translation of the element.

The nodal forces are derived from the principal of virtual work

$$\delta V = \delta W, \tag{3.36}$$

where δV and δW are the virtual variations of internal strain energy and external work, and are calculated over the surface S respectively as

$$\delta V = \int_S \boldsymbol{T} \cdot \delta \boldsymbol{\Delta}(\eta_1, \eta_2) dS = \int_S \boldsymbol{T} \cdot \delta \boldsymbol{x_i} N_i(\eta_1, \eta_2) dS \tag{3.37}$$

and

$$\delta W = \sum_{i=1}^{n} F_i \delta \boldsymbol{x_i}, \tag{3.38}$$

where F_i are nodal forces.

The interface elements are compatible with conventional FEM elements, which can be used to model the bulk materials.

3.3 Evaluation of properties of interfaces

As discussed previously, most of the experimental work was conducted on TRIPLEX^{TM} paperboard, which is a five-layered structure containing four interfaces of two types: two between the mechanical core and the outer chemical pulp layers (the outer interfaces) and two between the mechanical pulp layers inside the mechanical core (the inner interfaces). The outer interfaces are stronger than the inner ones. For this reason, the testing results of Stenberg, *et al.*[32],[33],[31] shown in the previous sections represent the behavior of the whole composite. Nevertheless, because the pulp layers and the interfaces are essentially in series when loaded out-of-plane, the load carried by the interfaces is the same as that applied. Furthermore, because the mechanical/mechanical interface is weaker than the mechanical/chemical interface, the peak and post-peak softening behavior observed in the stress-strain curve are due to delaminations taking place primarily along the mechanical/mechanical interfaces, as observed from the SEM tests. Thus, out-of-plane data on the entire TRIPLEX^{TM} more or less gives the behavior of the mechanical/mechanical layer. To obtain the behavior of the mechanical/chemical interface, some further experiments are necessary.

To fulfill this purpose, Stenberg[31] conducted ZD tensile tests on the outer interface only. A representative stress-strain curve for the outer interface is shown together with a stress-strain curve for the entire composite in Fig. 3-25. The "outer interface" is obtained by carefully grinding out the rest of the material from the TRIPLEX^{TM} composite using a flat grinder. Because the five pulp layers and the four interfaces are in series with each other under out-of-plane loading, the force carried by each of them is the same. Furthermore, Dunn's [18] work shows that before the peak stress is achieved, the majority of the through-thickness deformation comes from the pulp layers, not from the interfaces. Based on the first observation, we can infer the initial interface strengths S_{n_0}, $S_{t_{1_0}}$ and $S_{t_{2_0}}$ of the weaker mechanical-mechanical interfaces directly from the peak stresses on the stress-strain curves for the composite. With

this information, we can obtain the initial strength of the two interfaces based on the information shown in Fig. 3-25. Based on Dunn's observation [18], we assume that the stiffness of the interface is much larger than those of the pulp layers, so that the majority of the elastic out-of-plane deformation would come from the pulp layers. With this assumption, the initial slope of the through-thickness tensile and shear stress-strain curves can be taken as the average through-thickness stiffness of the pulp layers. For the interface stiffness, we take them to be approximately ten times larger than those of the pulp layers. The method to obtain the out-of-plane elastic constants for the pulp layers has been discussed in the previous chapter.

The interface stiffness can be backed out by considering the individual pulp layers and the interfaces as springs in series, since we know the stiffness of the laminate and those of the individual pulp layers.

Since there is no experimental data available on out-of-plane shear stress-strain behavior of the mechanical/chemical interface in this research (Note: as discussed before, we can more-or-less interpret the data on TRIPLEX^{TM} as a good approximation to represent strength behavior of the weaker mechanical/mechanical interface), we assume the ratio between shear stiffness and strength of the inner and outer interfaces is the same as that between their tensile stiffness. With this assumption and shear behavior of the entire composite as an approximation to the behavior of the weaker inner interface, we can deduce the shear parameters needed by the model for the outer interface also.

It is also worth noting that with the ground laid down by this research work and the experimental work done by Stenberg, *et al.* [32],[33],[31], it should be relatively easy to conduct further tests to obtain more accurate properties of the interfaces.

The interface properties used in this research will be summarized in the simulation results section.

3.4 Verification of interface model

A series of general one-interface-element simulations are conducted to verify the implementation of the interface model.

First, a ZD tension simulation is conducted. The corresponding stress-strain curve is shown in Fig. 3-26. The figure shows that the typical softening behavior of the interfaces is represented by the model. Before peak, the interface behaves elastically until the separation criterion is satisfied. The pre-peak hardening is neglected because it is relatively insignificant in the overall deformation behavior being modelled, and our attention is focused on the peak and post-peak behavior. At peak, the interfaces start to undergo permanent separation, causing softening behavior. Under large strain, the ZD tensile strength approaches zero.

A shear test without normal constraint simulation is also simulated. The corresponding stress-strain curve is shown in Fig. 3-27. Again, the typical softening behavior of the interfaces is represented. At large strain, the interface shear strength approaches the asymptote value we assigned, capturing the residual shear strength behavior of the interface as discussed in the previous section. Fig. 3-28 shows the ZD normal dilation versus applied shearing displacement curve for this simulation, capturing the shear dilation behavior of the interface.

Fig. 3-29 shows the normal stress *vs.* shear displacement curve from a simple shear simulation with ZD normal deformation constrained. Under shearing, once the separation criterion is satisfied, shear sliding attempts to dilate the interface, which is not permitted by the boundary condition, so a compressive normal stress is generated, as shown in the figure. The shear stress-strain curve will be shown later with other curves in Fig. 3-30.

To show the normal-stress sensitivities of the model, four more simulations are conducted. In the first two simulations, different fixed ZD normal tensile stress are applied, along with monotonically increasing shear displacement. In the other two simulations, different fixed normal compressive stress levels are applied, along with

increasing shear displacement. The obtained shear stress versus applied shear displacement curves are plotted in Fig. 3-30, together with the curves from the "pure shear" and "shear" with normal constraint simulations. This figure clearly shows that the shear strength of the interface increases under compressive normal stress and decreases under tensile normal stress, a typical pressure sensitivity behavior for this material.

To illustrate the history-dependence of the model, a loading-unloading simulation is conducted. First the element is loaded by through-thickness ZD tension until some amount of damage has been accumulated in the interface element. Then the load is reduced before it is finally increased again for further loading. The through-thickness normal tensile traction-displacement curve is plotted in Fig. 3-31. The figure shows that upon unloading and reloading, the interface element correctly keeps track of the remaining strength of the interface as well as the evolution in the stiffness of the interface due to accumulation of interface damage.

Two simulations are conducted to verify the response of the interface element in the traction space. In both simulations the interface element is loaded in combined through-thickness shear and tension. For the first simulation, the separation criterion for the interface is fixed without evolving, *i.e.*, no softening ($h_D = 0$). The theoretical separation criterion for the interface is plotted, along with the response of the interface element obtained from FEM simulation in the traction plane in Fig. 3-32. Initially, the interface behaves linear elastically until the separation criterion is satisfied. Once the separation surface is reached, the traction response of the interface from FEM remains on the separation surface, and moves around the separation surface to satisfy the flow rule. For the second simulation, the interface softens, so the separation surface shrinks in the traction plane. Fig. 3-33 shows the separation surfaces at different stages of the deformation, associated with different levels of interface damage accumulated. These separation surfaces are compared to the FEM traction response of the interface. In this case, after reaching the initial separation surface, the FEM response follows the softening evolution of the separation surfaces with the damage

state variable evolving. These two figures verified that the separation criterion, the evolution of the criterion and the flow rule are working correctly.

3.5 Simulation of out-of-plane tests on paperboard

Finally we present numerical results obtained from the simulation of out-of-plane tests as conducted by Stenberg, *et al.* [32],[33],[31] and Dunn[18]. The numerical simulations effectively test the capability of the interface model to capture the macroscopic behavior and the underlying micromechanical mechanisms behind the mechanical behavior of paperboard during out-of-plane loading.

The FEM model is composed of two parts, the continuum pulp layers and the interfaces between pulp layers, as shown in Fig. 1-1. The length of the board (in MD or CD) is $40mm$, and the thickness is $0.45mm$. Because the out-of-plane inelastic behavior is primarily controlled by the interfaces, instead of using the in-plane elastic-plastic material model described in the previous chapter, an orthotropic elasticity constitutive relation is used for the paperboard pulp layers to simplify the simulations. In fact, as will be discussed later in the section, the in-plane stress-levels achieved in the out-of-plane test simulations are relatively low compared to the initial yield strength of the pulp layers. Thus, assuming orthotropic linear elastic behavior for the pulp layers in these simulation will not change the important features of the simulations. The proposed interface model is used for the interfaces. As discussed previously, TRIPLEX^{TM} is comprised of five pulp layers with four interfaces, as shown in Fig. 1-1. One thousand first-order continuum plane strain elements are used for the pulp layers in the FEM model, with 100 elements in the length direction and 2 elements in the thickness direction for each layer. An orthotropic elastic model is assigned to these plane-strain elements. The nine orthotropic elastic constants used for the chemical pulp layers are summarized in Table 2.6, and those used for the mechanical pulp layers are in Table 2.7. These constants for chemical and mechanical pulp layers are calculated from stress-strain curves from tests on these individual layers by Stenberg, *et al.*[31], as discussed in the previous chapter.

As discussed previously, the initial strength and the elastic constants needed for each interface can be backed out from the stress-strain curves for the individual

Stiffness	
K_{n_0} (MPa/mm)	400
K_{t1_0} (MPa/mm)	800
Initial interface strength	
S_{n_0} (MPa)	0.45
S_{t1_0} (MPa)	1.45
Strength/Stiffness residual	
R_n	0.97
R_{t_1}	0.87
Damage Evolution and flow rule	
A	0.28
B	0.99
b (mm)	0.085

Table 3.1: Parameters used for the outer interfaces (MD-ZD plane)

interface, pulp layer and the TRIPLEX^{TM} composites. The constant b used in the evolution function of damage can be determined by matching the post-peak stress-strain curves. The constants used in the friction function μ can be determined by matching the experimental dilation curve. The values of these parameters used in the interface model are summarized in Table 3.1 for MD-ZD loading of the outer interfaces and in Table 3.2 for the inner interfaces.

Due to the nature of the material structure and its manufacturing, there are always heterogeneous defects distributed along the interfaces. In the case of paperboard, such defect areas could be those over which there is less concentration of starch and/or lower density of inter-fiber bonds. These relatively weaker areas are usually the locations where the micro-cracks initiate and later on develop into major interface delaminations. To simulate this important physical phenomenon, spatial distributions of the strength of the interfaces are needed. With the interface element model, incorporation of such spatial distribution is easily achieved by assigning an initial distribution of strengths to the interface elements on the four interfaces in the paperboard laminate. There are two main issues in finding a good representative defect distribution model for the real interfaces. First, we must consider the location

Stiffness	
K_{n_0} (MPa/mm)	320
K_{t1_0} (MPa/mm)	640
Initial interface strength	
S_{n_0} (MPa)	0.35
S_{t1_0} (MPa)	1.18
Strength/Stiffness residual	
R_n	0.97
R_{t_1}	0.87
Damage Evolution and flow rule	
A	0.28
B	0.99
b (mm)	0.085

Table 3.2: Parameters used for the inner interfaces (MD-ZD plane)

and the length scale of the defect area. The distribution is assumed to be random due to the nature of paper manufacturing. Thus the location of the defect area is really of random nature. The length scale of the defect area involves both the macroscopic fiber density and the length scale of the microstructure of paperboard, *i.e.*, size of inter-fiber bonds, fiber length etc. Second, we must determine the magnitude of the interface strength heterogeneity over these weaker areas. It is non-trivial to develop rigorous answers for these classes of questions, and the procedure requires intensive statistical testing. As a simple expedient, a step-type of random distribution is used in this research, as shown in Fig. 3-34 and Fig. 3-35 for MD axial distribution. In 3-D, the real interface strength distribution should cover the area of interface. In our plane-strain idealization, it is simplified into a line distribution. The assumed relative interface strength, normalized by the maximum interface strength, is plotted as the y axis, and the normalized location of the interface elements in the MD/CD-direction is plotted as the x axis. Such a distribution is somewhat coarse but sufficient to demonstrate the capabilities of the model. In fact, the relatively easy process of generation and usage of such interface strength distributions is one of the advantages of this type of interface model. It also should be noted that this idealization is used for

simulations in the MD-ZD plane. We further note that since we are idealizing the area defects as line defects (for plane strain simulation), simulations in CD-ZD plane may require a different line distribution.

With the distributions of interface strength shown in Fig. 3-34 and Fig. 3-35, respectively, for the four interfaces, two simulations of ZD tension were conducted, where the bottom surface of the paperboard was fixed and the top surface was displaced in ZD. The through-thickness average normal stress *vs.* applied displacement curves as obtained in the experiment and as computed by the models are compared in Fig. 3-36. The FEM results and experimental results match very well. Also, the two defect distributions give very similar macroscopic outputs. Contour plots of through-thickness normal stress component for the first defect distribution case, at different loading stages, are plotted in Fig. 3-37 and Fig. 3-38. These stages are also marked on the overall stress *vs.* applied displacement curve in Fig. 3-36, as A, B, C ...H. At the beginning of the deformation, *e.g.*, stage A, all the composite deforms elastically. With increasing tensile loading, the locations on the interfaces with lowest assigned interface strength start to undergo plastic separation, as indicated by arrows shown in stage B, which is near the peak on the stress-applied displacement curve. With further loading applied, the initiated small cracks start to propagate until several major cracks start to dominate the deformation, as can been in stages C and D. At these two stages, we can also see stress concentration near the crack tips and much lower stress levels along the separating surfaces. At later stages, the propagation of the major cracks finally causes the delamination of the laminates. By comparing the distribution of the interface strength as shown in Fig. 3-34 with the locations where the initial cracks start and the final major cracks develop in the contour plots, we can clearly see that the defects are instrumental in initiating the delamination process. The propagation and interactions between cracks are also taken care of as a natural outcome of the calculation. To further compare the FEM deformed configuration with those obtained by Dunn[18], a central portion of the contours (relative position $0.3 \leq x \leq 0.65$, $x = 0$ at the left end of the specimen and $x = 1$ at the right end of

the specimen) from Fig. 3-37 and Fig. 3-38 are magnified and shown in Fig. 3-39 and Fig. 3-40. Comparison of these deformed configurations with the SEM micrographs obtained by Dunn[18] shows that the FEM model accurately captures the structural feature of the deformation of the paperboard. The highest in-plane normal stress component at each step is checked to make sure it is appropriate to use the elastic material model for the pulp layers. The results show that it is near stage F, which is far beyond peak stage, that stress levels higher than the in-plane initial yield strength are achieved, and then only at local areas of the pulp layers. This indicates that using linear elastic behavior for the pulp layers in this simulation is appropriate.

Fig. 3-41 shows a comparison of through-thickness shear stress *vs.* applied shear displacement curves obtained from ZD-MD shearing of paperboard without normal constraint. In this simulation the bottom surface of the paperboard was fixed, and the top surface was subjected to a shear displacement, but was free to expand in the ZD. The FEM results and experimental results again match very well, and the two defect distributions again give very similar results. The comparison of through-thickness dilation *vs.* applied shear displacement curves is shown in Fig. 3-42. Contours of the out-of-plane shear stress component are plotted in Fig. 3-43 and Fig. 3-44. At the beginning of deformation, there is no inelastic interface separation. Once the separation criterion is satisfied at some of the weaker spots, small cracks initiate in shear and pop open in the thickness direction, due to the shear-induced dilation. Stress concentration around the crack tips and stress relaxation on the fractured interface surfaces can be seen during the delamination process. At the final stages of deformation, one major de-bonding separates the paperboard into two pieces. By comparing the deformed shapes of paperboard under pure extension and pure shear, we can also see that the deformation of TRIPLEX^{TM} under shear without normal constraint is more homogeneous than that of the paperboard under pure tension, as also observed in the microscopic experiments by Dunn [18]. As in the last simulation, to further compare the FEM deformed configuration with those obtained by Dunn[18], central portion of the contours (relative position $0.3 \leq x \leq 0.65$) from Fig. 3-43 and

Fig. 3-44 are magnified and shown in Fig. 3-45 and Fig. 3-46. Once more, one can see that comparison of these deformed configurations with the SEM micrographs obtained by Dunn[18] indicates that the FEM model accurately captures the structural features of the deformation of the paperboard under out-of-plane shear. The highest level of in-plane stress is checked for each stage of deformation and is less than $10MPa$ in this simulation, which is less than the initial MD yield strength of the pulp layers. Again, this justifies the usage of linear elastic in-plane behavior.

To show the ability of the model to capture the sensitivity of through-thickness shear resistance on the through-thickness normal pressure, simulations are conducted by fixing the bottom surface and first applying on the top surface different constant values of ZD normal compressive stress, followed by increasing imposed shear displacement. The resulting through-thickness shear stress versus applied shear displacement curves are plotted in Fig. 3-47, together with the curves from the corresponding simulations. The numerical results agree very well with the tests.

Fig. 3-48 shows contours of the through-thickness normal stress from another simulation with interface strength distribution 1. In this simulation, increasing shearing displacement is first applied until the laminate started to exhibit permanent separation at the weak spots; then the shear displacement is held at this fixed value ($0.07mm$); and through-thickness tensile displacement is applied to further delaminate the system. History of the applied boundary condition is shown in Fig. 3-49. The corresponding macroscopic shear stress-strain curve for the first stage and normal stress-strain for the second stage are shown in Fig. 3-50 and Fig. 3-51, respectively. During the shearing period, small cracks initiate and pop open in the thickness direction, due to the shear-induced dilation. Again, the initial small cracks develop along the locations of the pre-assigned defects. In the second loading stage, the interfaces continue to delaminate along the cracks caused by the first stage shearing until several major cracks become dominant and the final delamination of the laminate occurs. Another important observation is that the peak overall tensile stress achieved in the second stage of deformation of the laminate is about $0.14MPa$, as shown in Fig. 3-

51, lower than the peak stress achieved in the pure ZD extension case, $0.35MPa$, as shown in Fig. 3-36. Explanation for this behavior is that during the first shearing stage, some interface damage has been developed which leads to the decreased tensile strength.

3.6 Simulation of local buckling of paperboard under in-plane compression

The interface model represented interfaces as an integral part of the paperboard structure. The model can be applied to simulate mechanical behavior of paperboard in many other applications other than simple out-of-plane loading scenarios. In this section, we apply the interface model to simulate the in-plane compression of TRIPLEX^{TM} paperboard which results in local layer kinking and buckling.

The 2-D plane strain mesh during different stages of the compressive deformation is shown in Fig. 3-52. The length of the entire paperboard is $1.75mm$ and the thickness is $0.45mm$. Orthotropic linear elastic behavior is used for the pulp layers and the interface element is used along the four interfaces. As shown in the figure, a mesh density difference is used as the source of inhomogeneity to trigger the buckling. The board is fixed at one end, and a uniform in-plane compressive displacement boundary condition is applied on the other end. At step 1, the board started to kink near the location where mesh density changes. At step 2, the interface starts to delaminate primarily near locations where the kinks were developed. A major delamination formed at step 3. In step 4, this major delamination takes over, causing the whole structure to fail by buckling.

The corresponding compressive stress *vs.* the applied compressive displacement curve is shown in Fig. 3-53. The peak stress obtained is around $28MPa$. The average MD compressive strength obtained by Stenberg[31], is around $20MPa$. Considering the fact that, first, linear elastic behavior is used for the in-plane behavior of the pulp

layers and second, the length of the specimen here is shorter than those of Sternberg, the result obtained is very good. Furthermore, the fact that such good prediction of peak compressive strength is obtained with only linear elastic in-plane behavior indicates that the interface model is capable of representing a very important part of structural behavior of the composite.

3.7 Discussion

Based on microscopic and macroscopic through-thickness experimental results, a general 3-D elastic-plastic internal state variable theory interface constitutive relation is presented to model the out-of-plane behavior of laminated paperboard. The initiation of the permanent interface separation is controlled by a pressure-dependent traction-based separation criterion. The behavior of the fractured interface is controlled by the evolution of the separation criterion and frictional separation flow rule. The constitutive relation is verified by simplifying it into a 2-D plane-strain interface model and implemented kinematically into a 2-D interface element through the user defined element (UEL) of the commercial software ABAQUS. (In the latest versions of ABAQUS, the constitutive model can be more easily implemented with a newly available user-defined interface behavior module (UINTER/VUINTER), which exempts the users from implementing the kinematics portion of the interface element as in UEL.) The interface element is compatible with conventional continuum finite element discretization of the continuum pulp material. The interface elements are used to simulate the delamination of paperboard laminates under through-thickness loading. Numerical results show that the model can represent the following important features of the mechanical behavior of interfaces in paperboard as well as many other laminated composite materials:

- Shear strength dependence on normal stress
- Post-peak softening interface traction-displacement jump relation

- Coupling between through-thickness normal and shear behavior; *i.e.*, shear deformation introduces dilation in the normal direction due to the interaction of fiber entanglement and the fractured interface surfaces

- History-dependent interfacial behavior

- Reduction of interface stiffness with interface damage

The proposed interface constitutive law can explicitly simulate the delamination and fracture of interfaces. It imposes no explicit restrictions on the size, location, distribution, or direction of the growth of cracks. This enables the model to be able to naturally predict the initiation of microcracks and their growth into major delamination at any location.

This interface constitutive relation can be relatively easily modified and applied to many different type of interfaces ranging from interfaces in classical composite materials to brittle materials. The simplified 2-D model shows that even with only a single state variable, the interface damage D, very good numerical results can be obtained. The interface damage can be interpreted as a fraction of interface area debonded *vs.* the initial bonding area. The post-peak softening behavior can be adjusted by tuning the evolution function of the state variables. The frictional pressure sensitivity behavior can be adjusted by adopting different forms of separation or delamination criterion. The coupling effect between normal and tangential shear behavior can be adjusted by using non-associated flow rule to control the ratio between normal plastic flow and tangential plastic flow.

Functionals and parameters needed in the constitutive relation can be relatively easily obtained by conducting pure tension, pure shear and combined normal and shear loading experiments.

Simulations show that with a distribution of interface strength to simulate the distributed interface defects, the delamination process of the laminated paperboard can be explicitly simulated. In the absence of localized external loadings, small cracks

first initiate at these defects and later propagate into dominant major cracks which lead to the final delamination of the laminates.

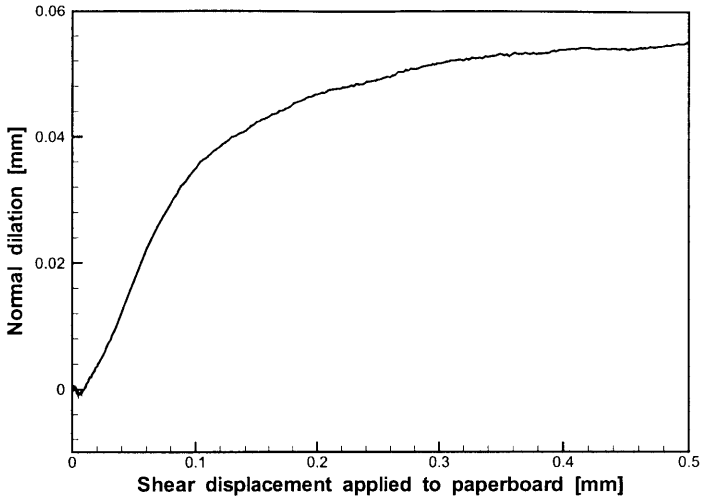

Figure 3-1: ZD dilation - shear displacement curve under unconstrained ZD-MD shear(Stenberg, *et al.* [32], [33]).

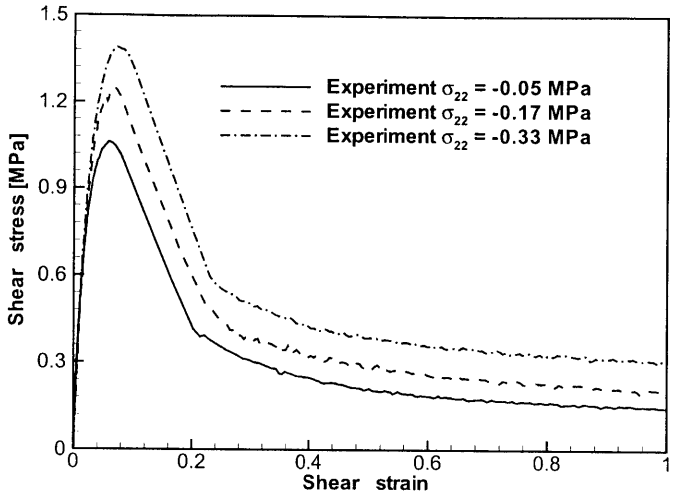

Figure 3-2: Normal stress sensitivity of shear strength: MD-ZD experimental shear stress-strain curves with different fixed normal stress values.

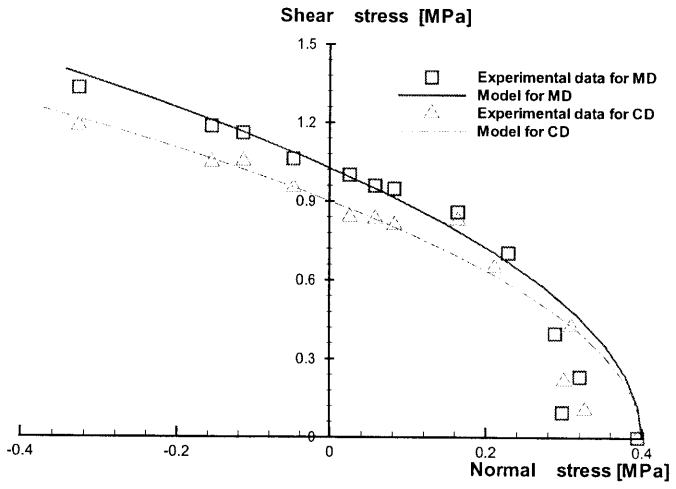

Figure 3-3: Experimental peak strength locus and theoretical initial separation surfaces.

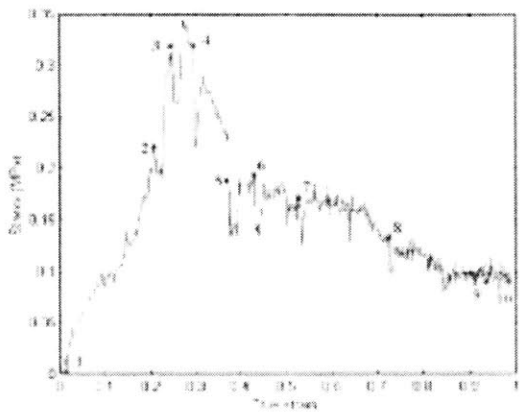

Figure 3-4: Micro-level ZD normal stress-strain curve obtained by Dunn [18] from SEM.

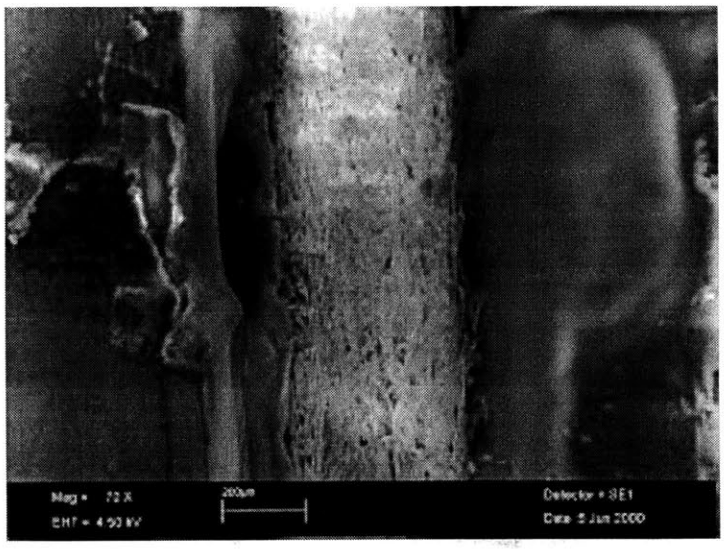

Figure 3-5: Triplex MD through-thickness SEM tension image correlated with stress-strain data obtained by Dunn [18](Step 1).

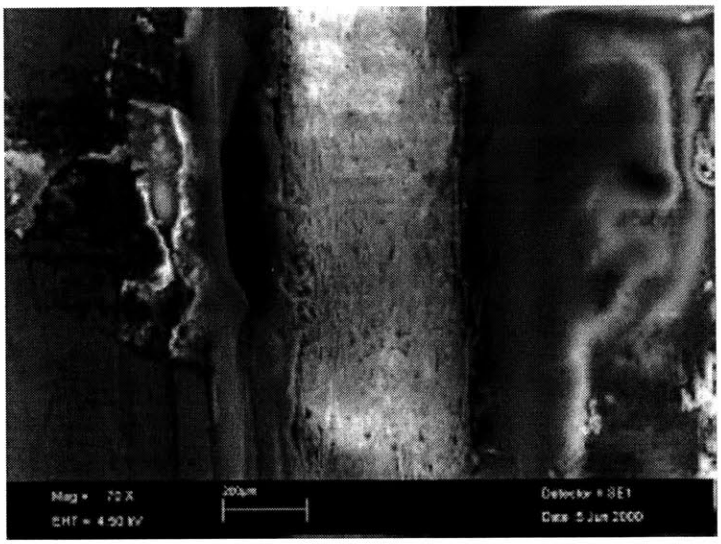

Figure 3-6: Triplex MD through-thickness SEM tension image correlated with stress-strain data obtained by Dunn [18] (Step 2).

Figure 3-7: Triplex MD through-thickness SEM tension image correlated with stress-strain data obtained by Dunn [18] (Step 3).

Figure 3-8: Triplex MD through-thickness SEM tension image correlated with stress-strain data obtained by Dunn [18] (Step 4).

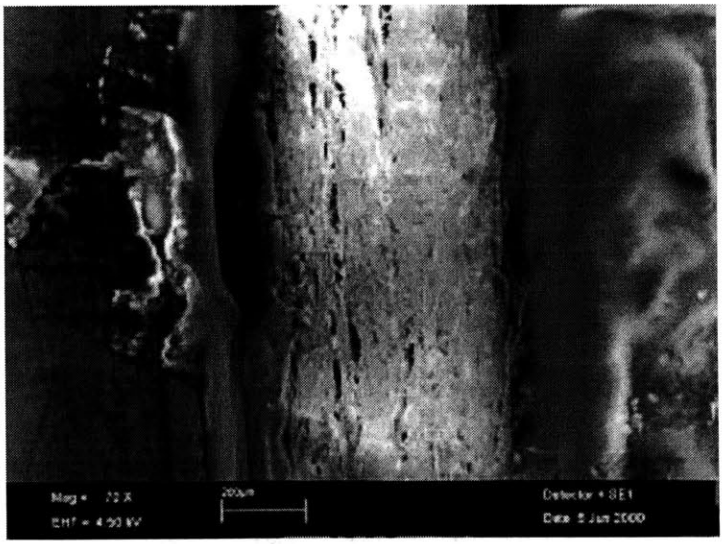

Figure 3-9: Triplex MD through-thickness SEM tension image correlated with stress-strain data obtained by Dunn [18] (Step 5).

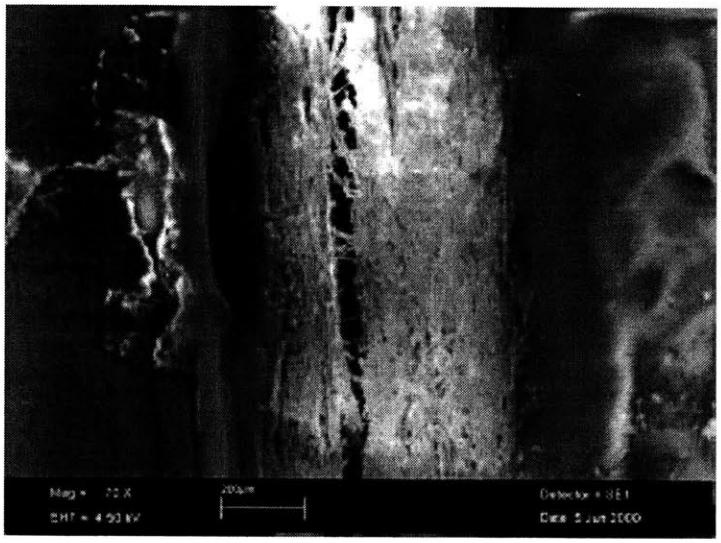

Figure 3-10: Triplex MD through-thickness SEM tension image correlated with stress-strain data obtained by Dunn [18] (Step 6).

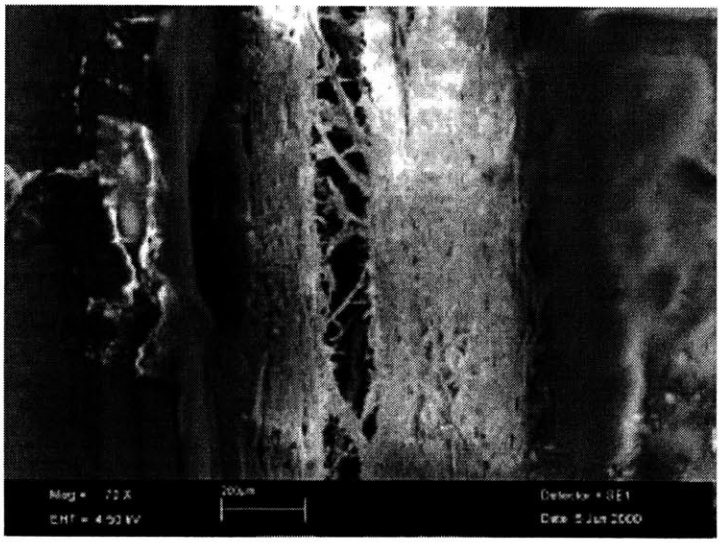

Figure 3-11: Triplex MD through-thickness SEM tension image correlated with stress-strain data obtained by Dunn [18] (Step 7).

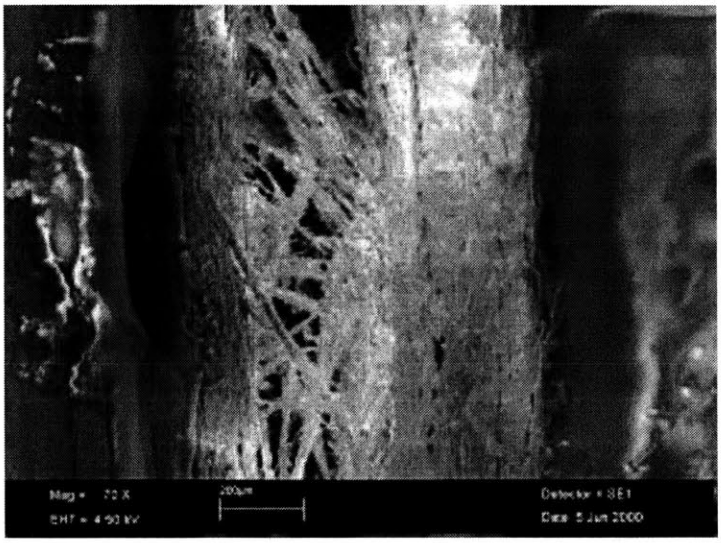

Figure 3-12: Triplex MD through-thickness SEM tension image correlated with stress-strain data obtained by Dunn [18] (Step 8).

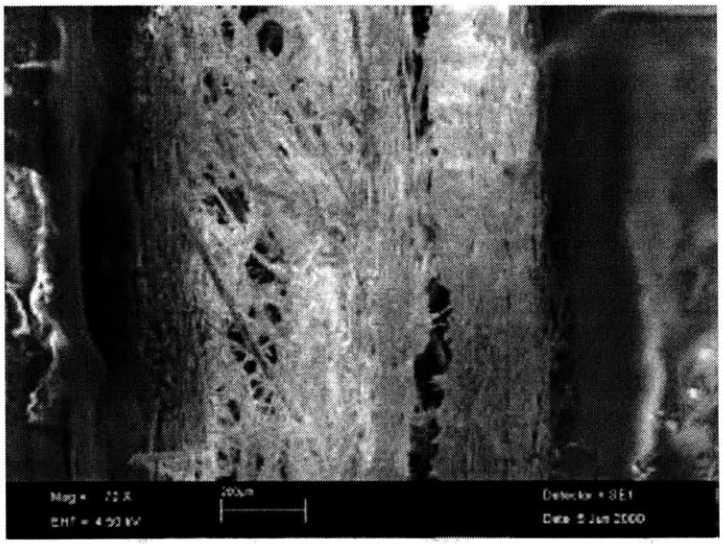

Figure 3-13: Triplex MD through-thickness SEM tension image correlated with stress-strain data obtained by Dunn [18] (Step 9).

Figure 3-14: Triplex MD through-thickness SEM tension image correlated with stress-strain data obtained by Dunn [18] (Step 10).

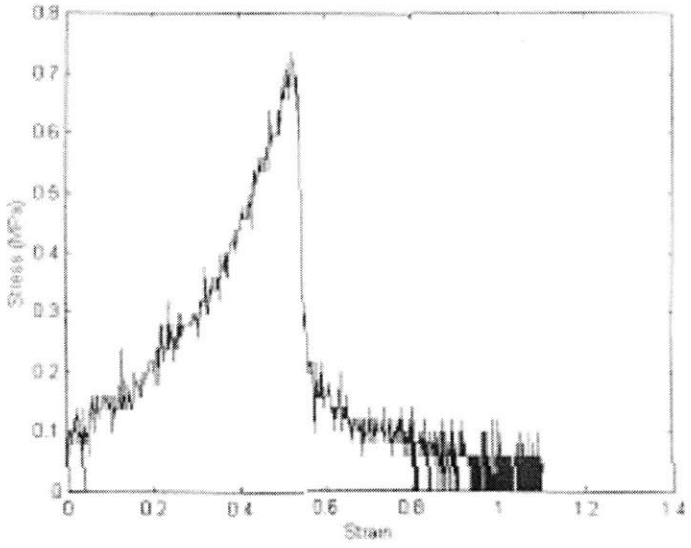

Figure 3-15: Micro-level stress ZD-MD shear strain curve curve obtained by Dunn [18] from SEM.

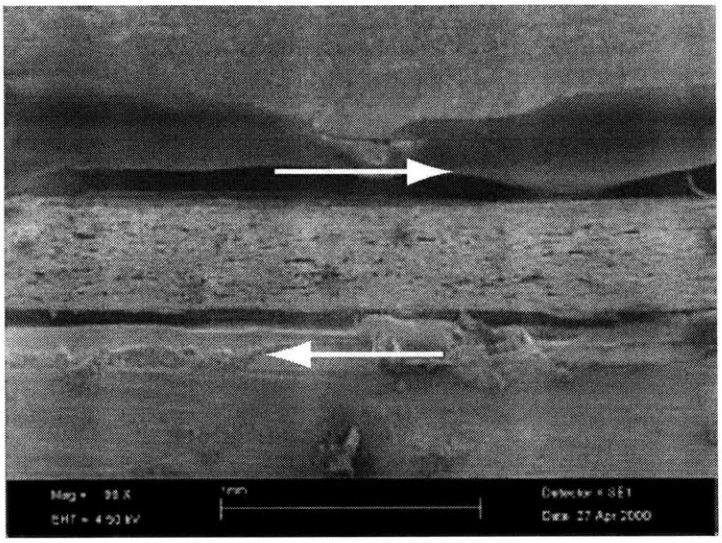

Figure 3-16: Triplex MD through-thickness SEM shear image correlated with stress-strain data obtained by Dunn [18] (Step 1).

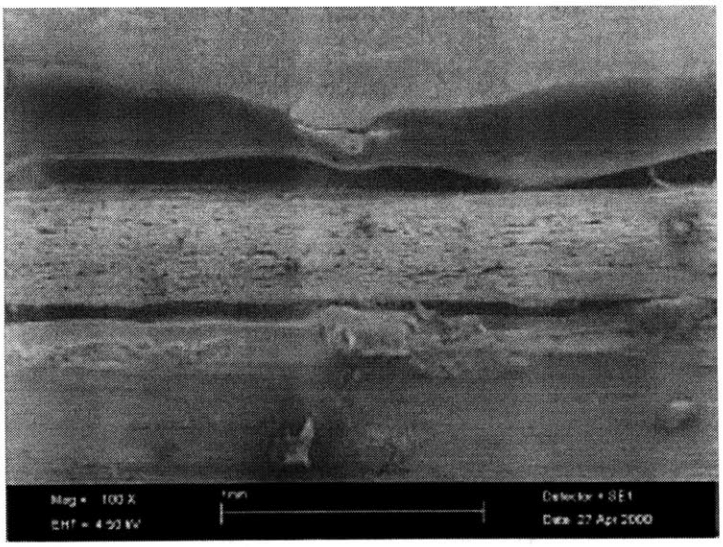

Figure 3-17: Triplex MD through-thickness SEM shear image correlated with stress-strain data obtained by Dunn [18] (Step 2).

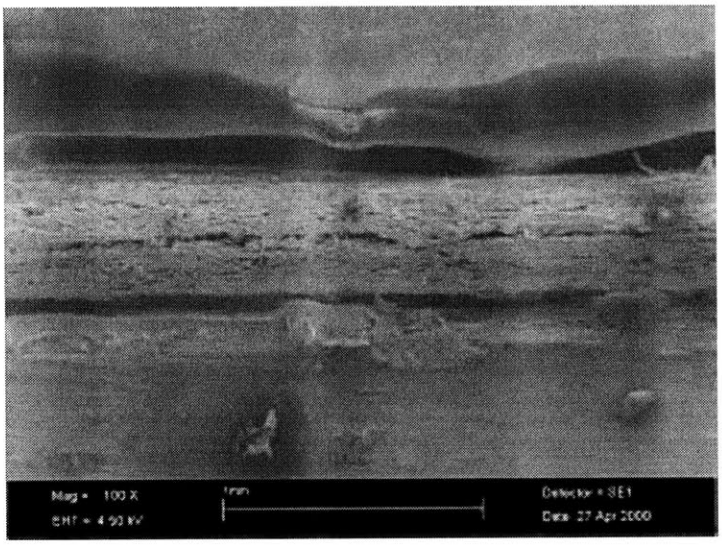

Figure 3-18: Triplex MD through-thickness SEM shear image correlated with stress-strain data obtained by Dunn [18] (Step 3).

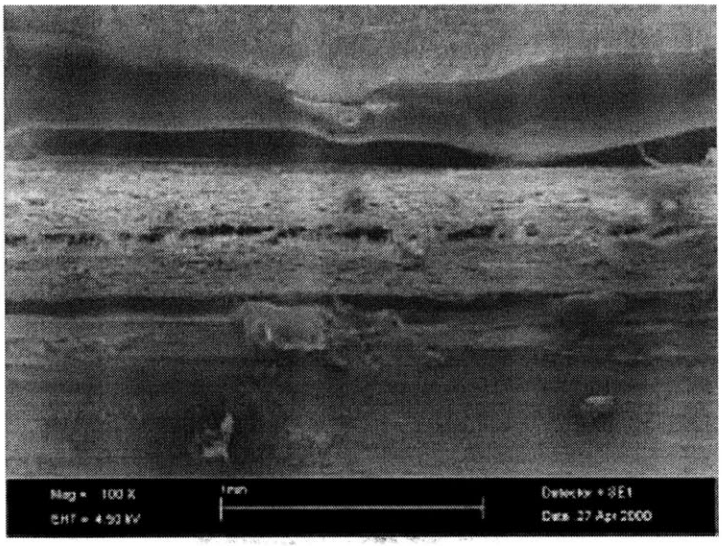

Figure 3-19: Triplex MD through-thickness SEM shear image correlated with stress-strain data obtained by Dunn [18] (Step 4).

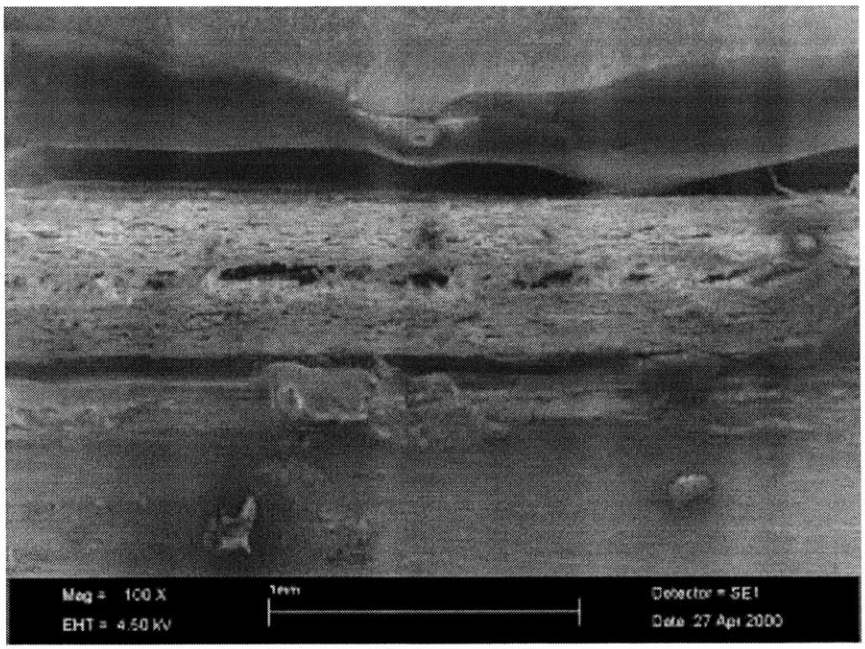

Figure 3-20: Triplex MD through-thickness SEM shear image correlated with stress-strain data obtained by Dunn [18] (Step 5).

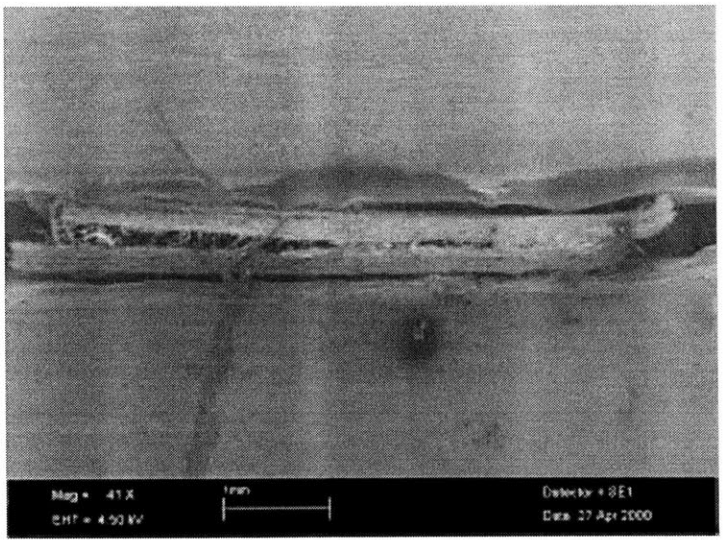

Figure 3-21: Triplex MD through-thickness SEM shear image correlated with stress-strain data obtained by Dunn [18] (Step 6).

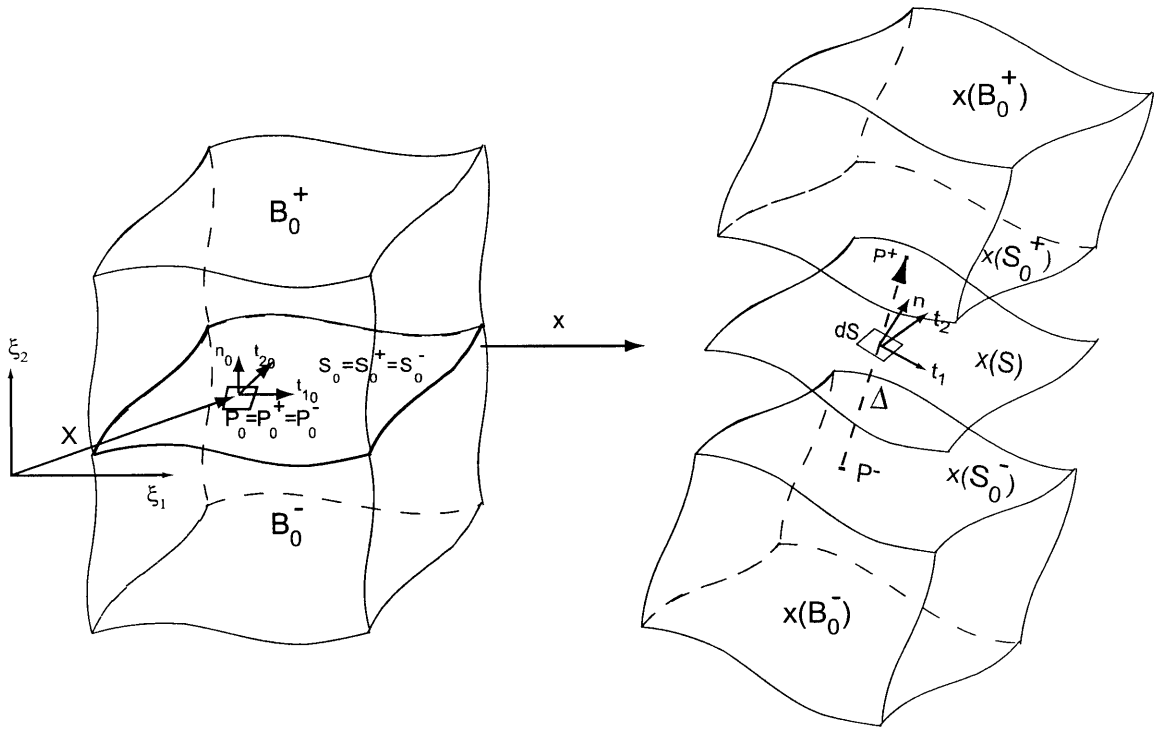

Figure 3-22: Illustration of 3-D interface between two solids.

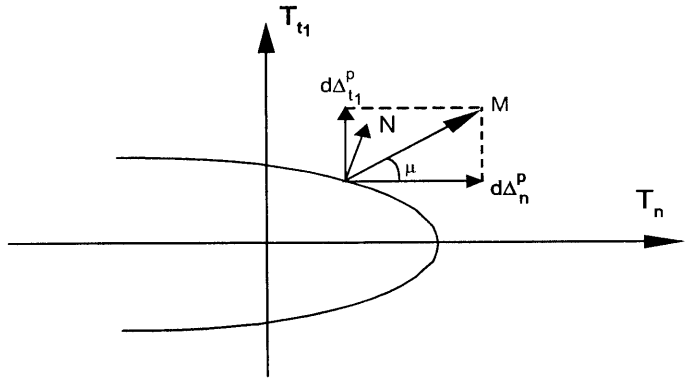

Figure 3-23: Flow directions on the yield surface.

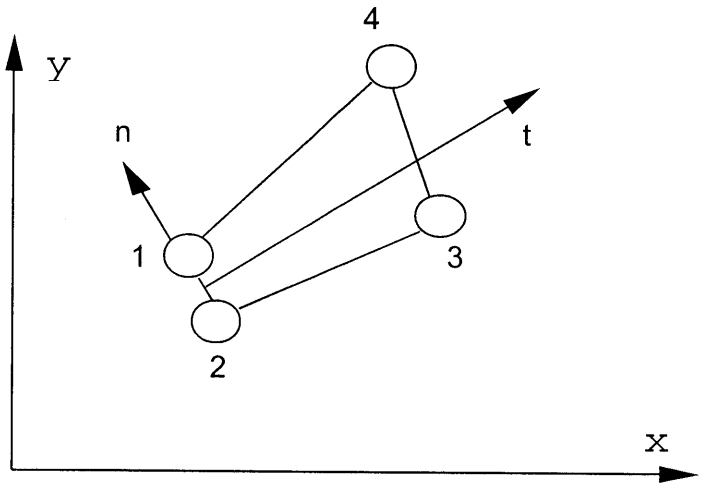

Figure 3-24: Kinematics: 2-D interface element.

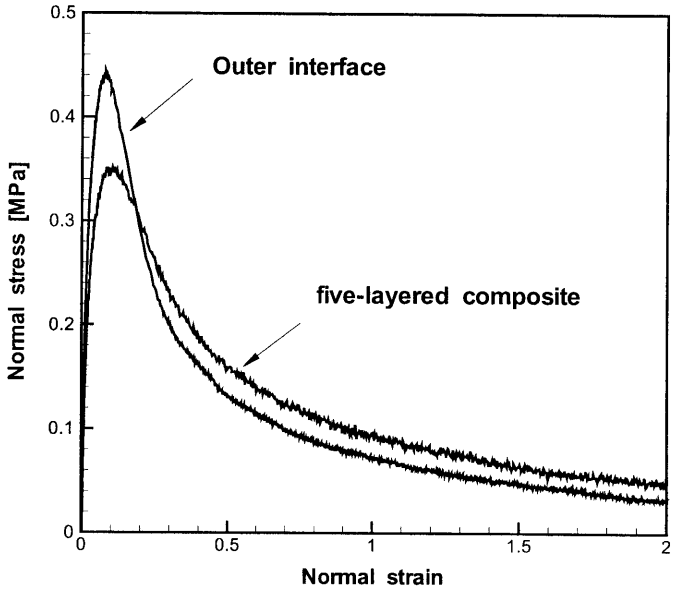

Figure 3-25: Comparison of ZD tensile stress-strain curve of the outer interface and the TRIPLEX^{TM} composite laminate.

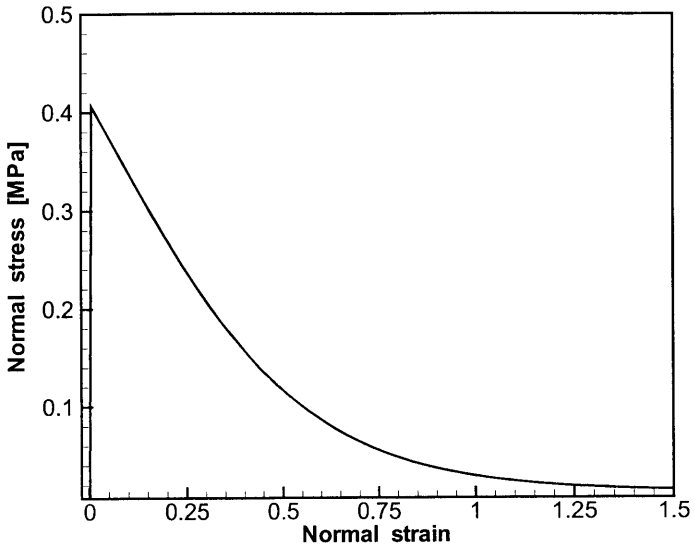

Figure 3-26: Through-thickness tensile stress-strain curve from one-element FEM simulation

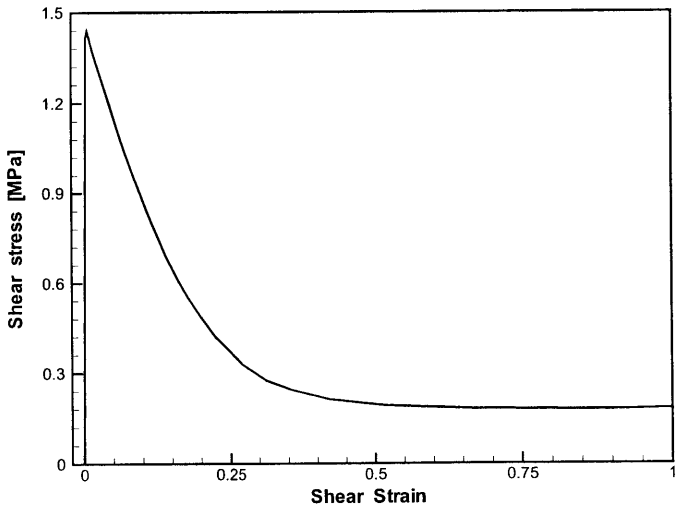

Figure 3-27: Through-thickness MD-ZD shear stress-strain curve from one-element FEM simulation.

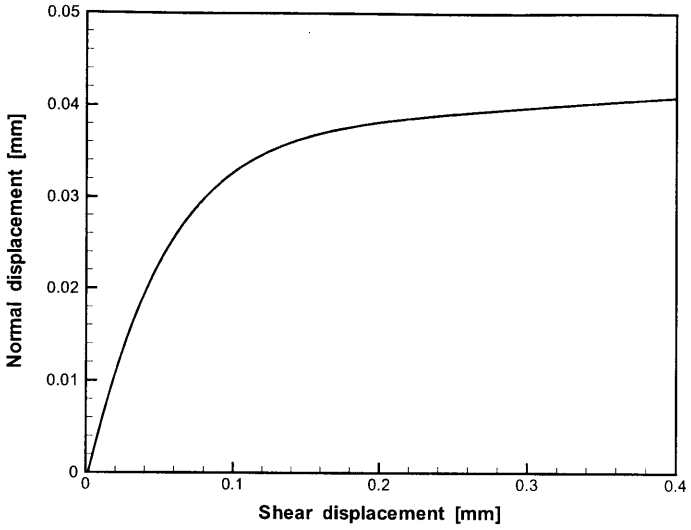

Figure 3-28: Through-thickness dilation *vs.* shear displacement (MD-ZD) curve from one-element FEM simulation.

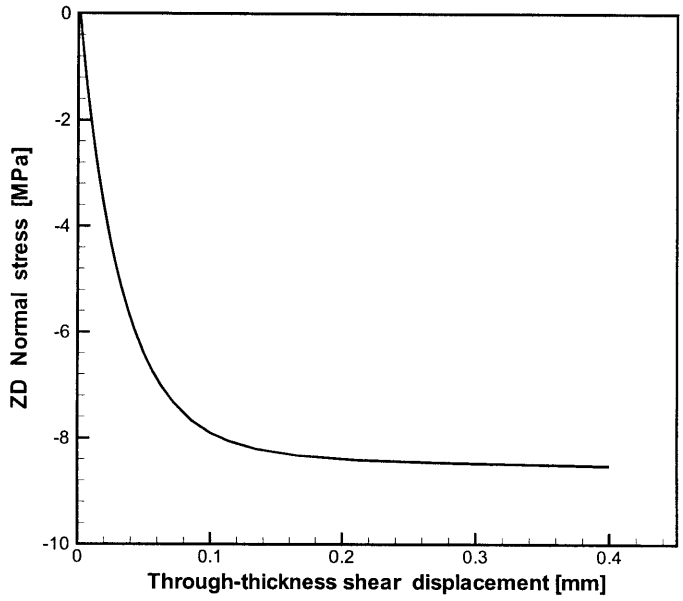

Figure 3-29: Through-thickness normal stress *vs.* shear displacement (MD-ZD) curve from one-element FEM simulation with zero through-thickness normal displacement ($\Delta_n = 0$).

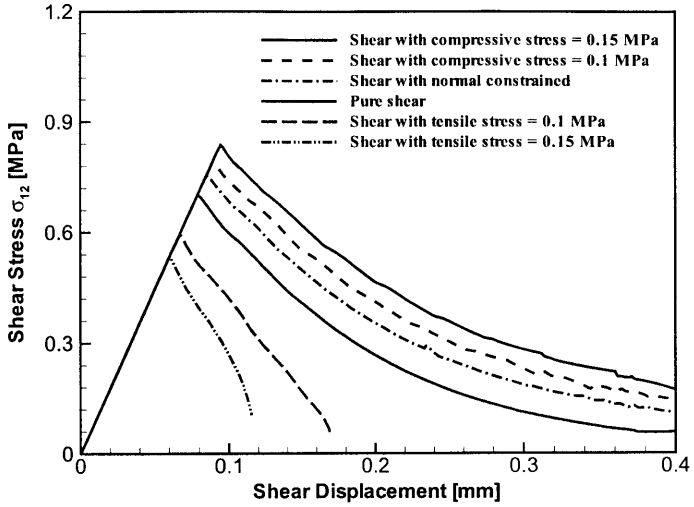

Figure 3-30: Normal stress sensitivity curve of through-thickness shear stress-strain behavior (MD-ZD) from one-element FEM simulations.

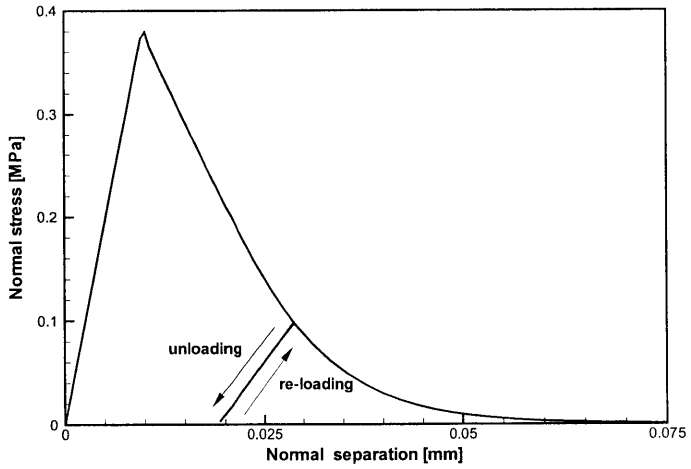

Figure 3-31: Loading/unloading stress-strain curve from one-element FEM simulation

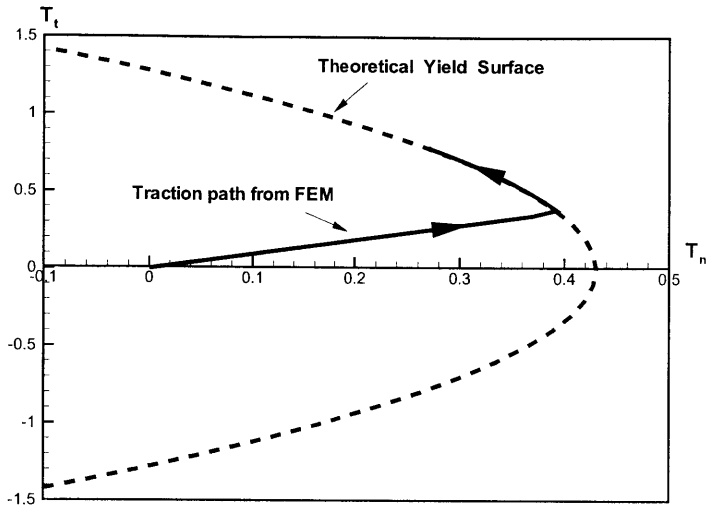

Figure 3-32: Response of non-softening interface element in the traction space under combined through-thickness loading of monotonically increasing proportional relative separation and sliding. ($d\Delta_t/d\Delta_n = 1.0$)

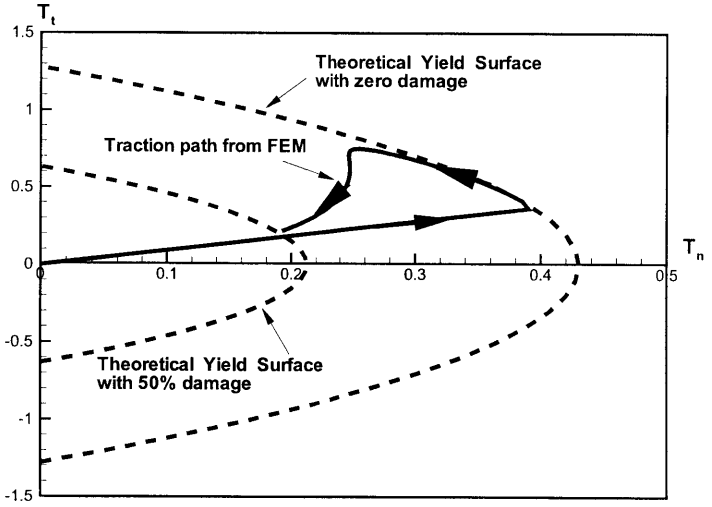

Figure 3-33: Response of softening interface element in the traction space under combined through-thickness loading of monotonically increasing proportional relative separation and sliding. ($d\Delta_t/d\Delta_n = 1.0$)

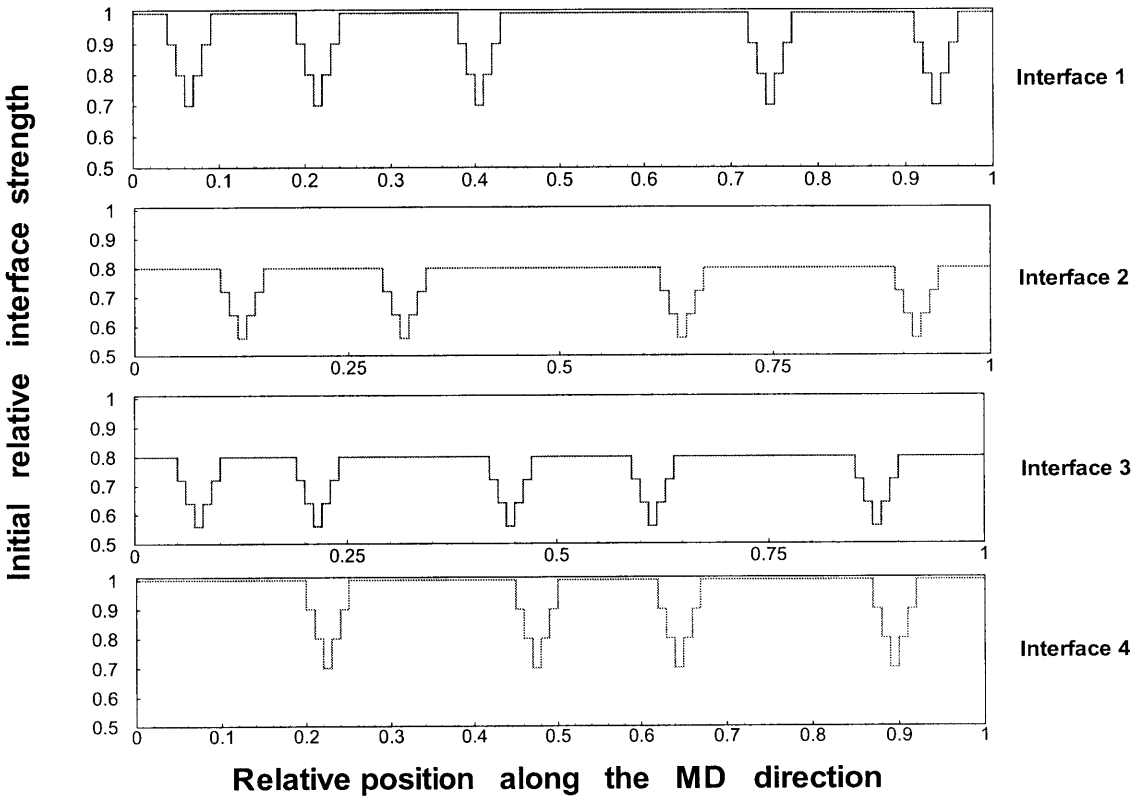

Figure 3-34: Initial defect distribution 1.

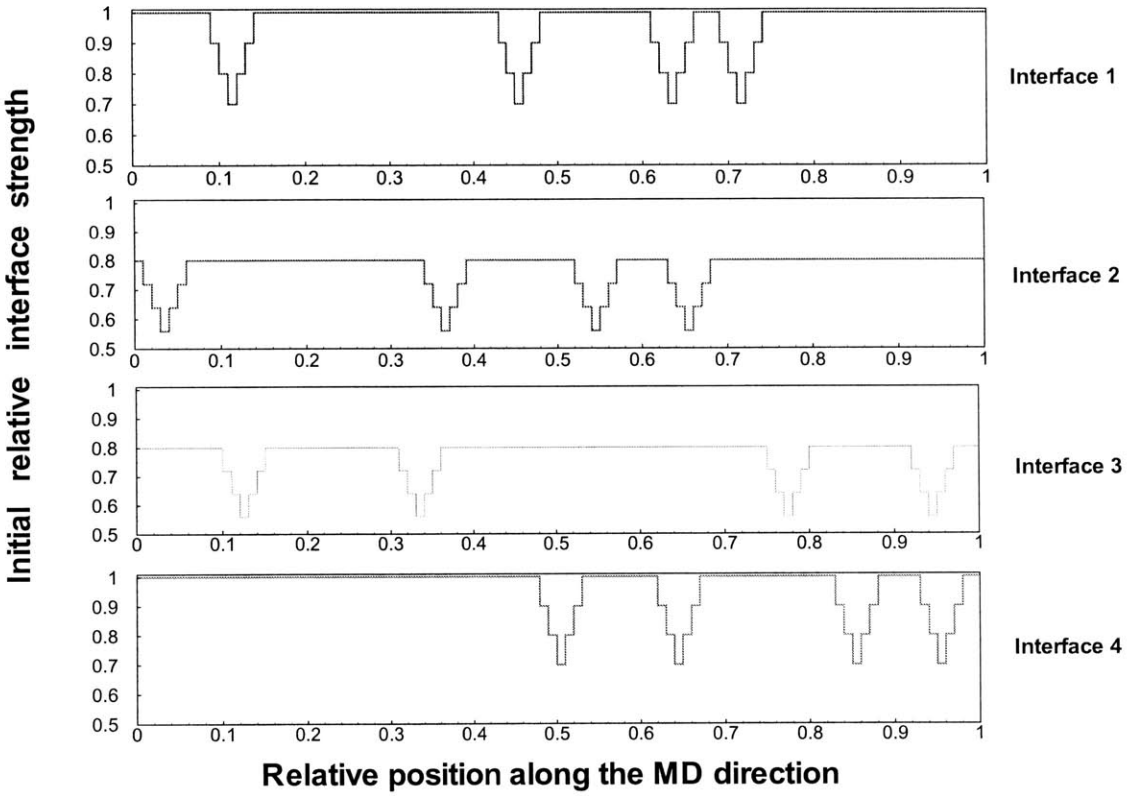

Figure 3-35: Initial defect distribution 2.

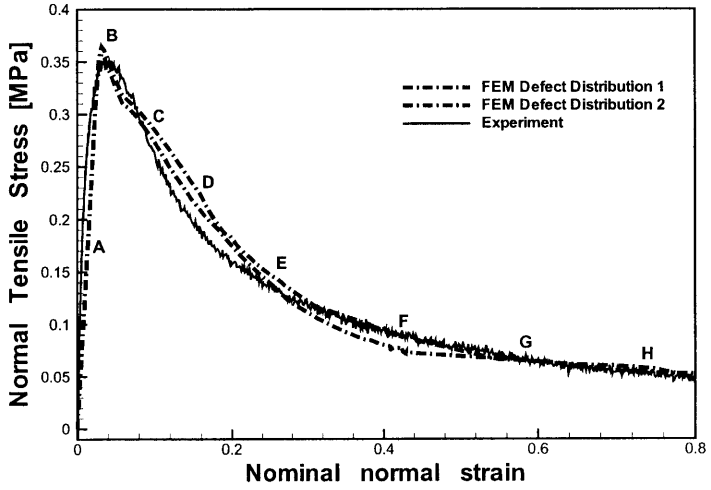

Figure 3-36: Comparison of ZD tension stress-strain curves from experiment and FEM.

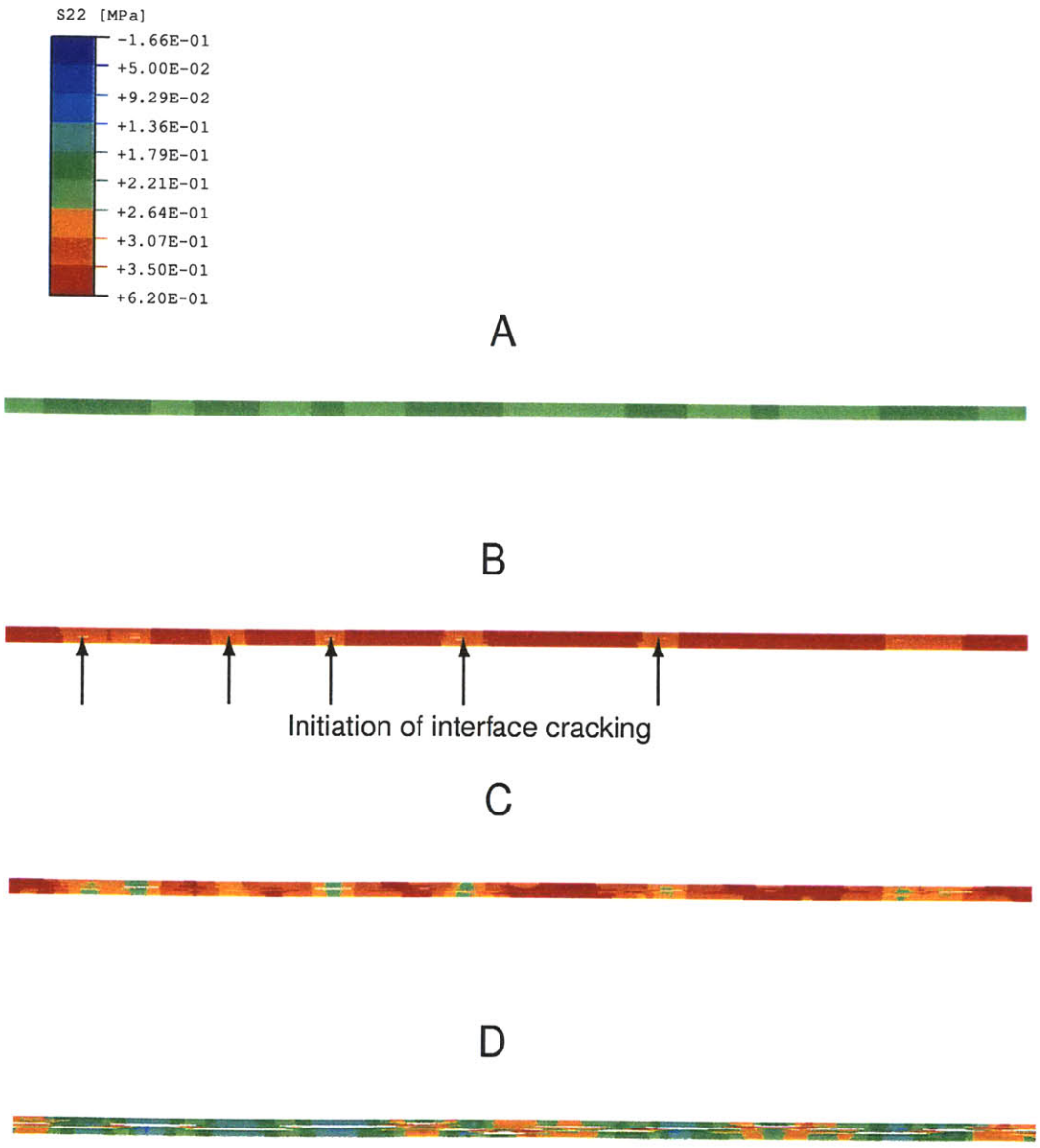

Figure 3-37: Contour of local normal stress component in ZD from pure tension simulations using defect distribution 1 (Fig. 3-34). A-D, respectively, denote contours at load levels of the correspondingly named points on the stress-strain curves shown in Fig. 3-36

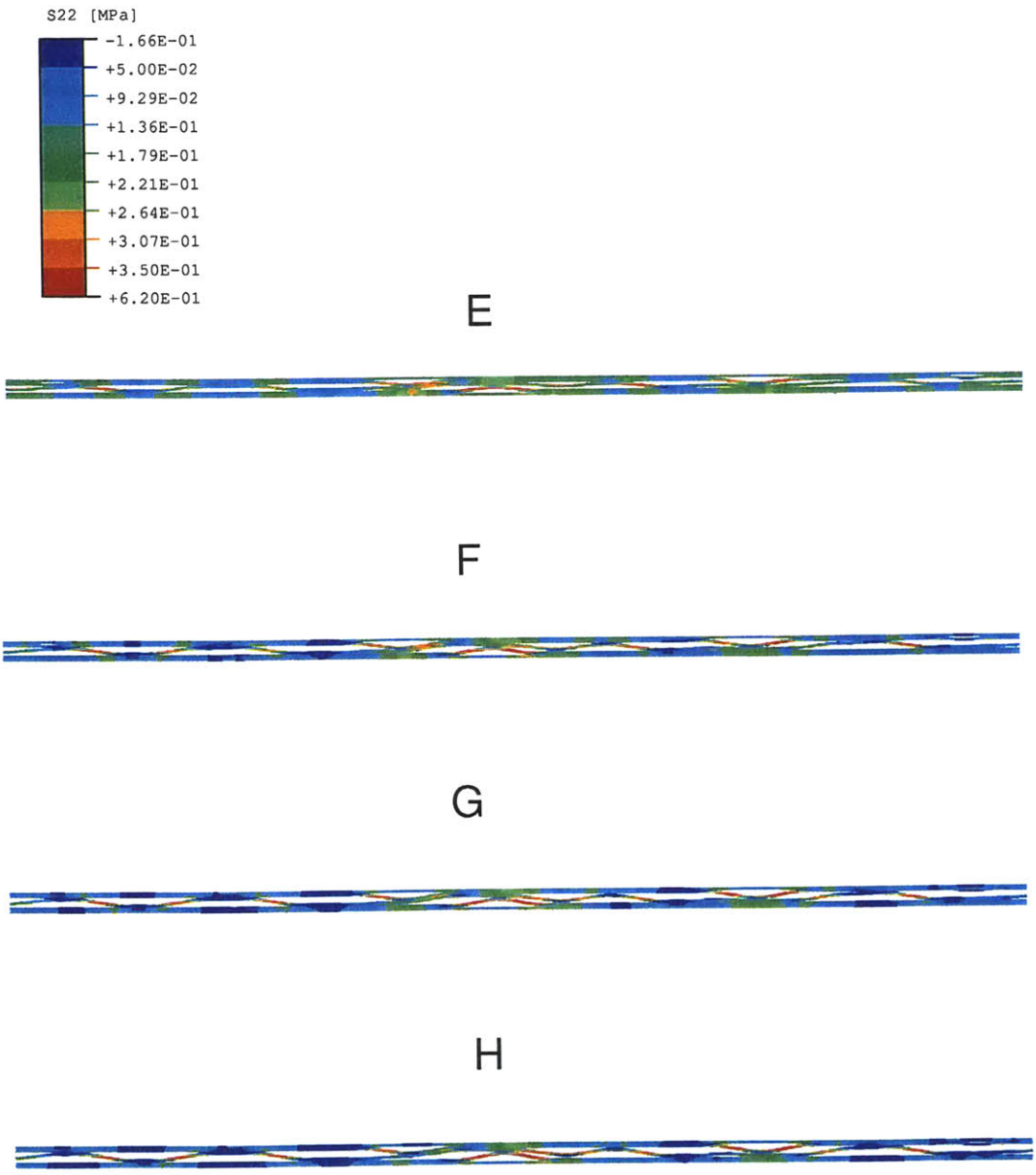

Figure 3-38: Contour of normal stress component in ZD from pure tension simulations using defect distribution 1 (Fig. 3-34) (continued). E-H, respectively, denote contours at load levels of the correspondingly named points on the stress-strain curves shown in Fig. 3-36

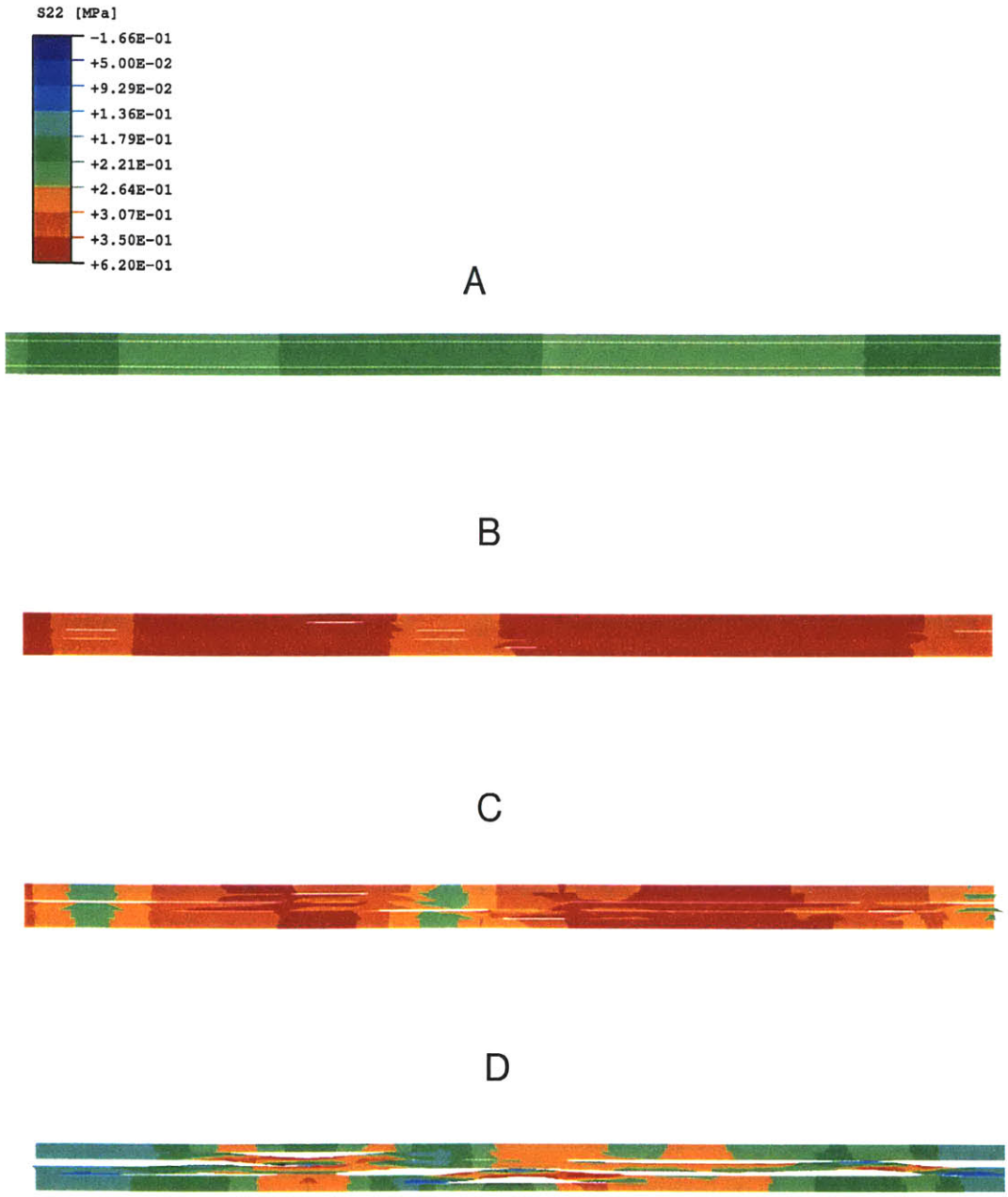

Figure 3-39: Magnified view of central part of contour of normal stress component in ZD from pure tension simulation using defect distribution 1 (Fig. 3-34). Relative position $0.3 \leq x \leq 0.65$.

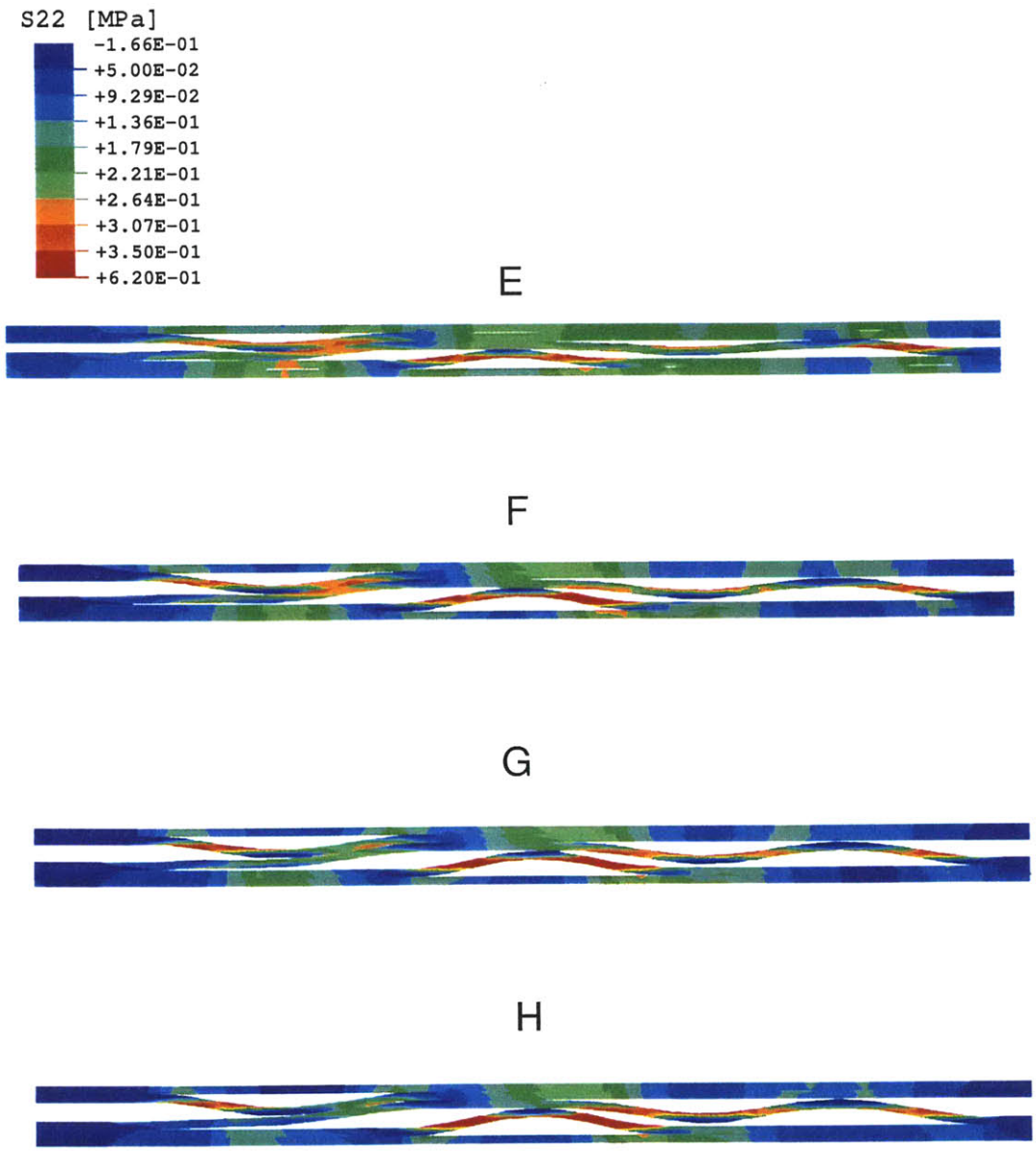

Figure 3-40: Magnified view of central part of contour of normal stress component in ZD from pure tension simulation using defect distribution 1 (Fig. 3-34) (continued). Relative position $0.3 \leq x \leq 0.65$.

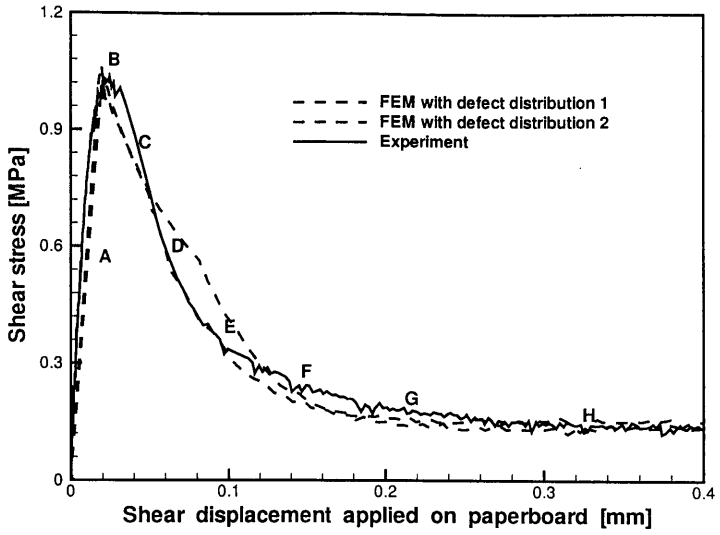

Figure 3-41: Comparison of MD-ZD pure shear stress applied shear displacement curves from experiment and FEM.

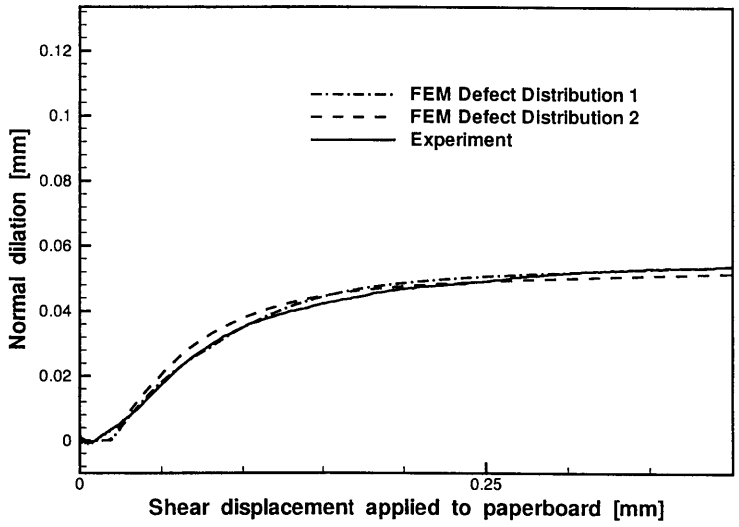

Figure 3-42: Comparison of dilation curves under pure shear from experiment and FEM.

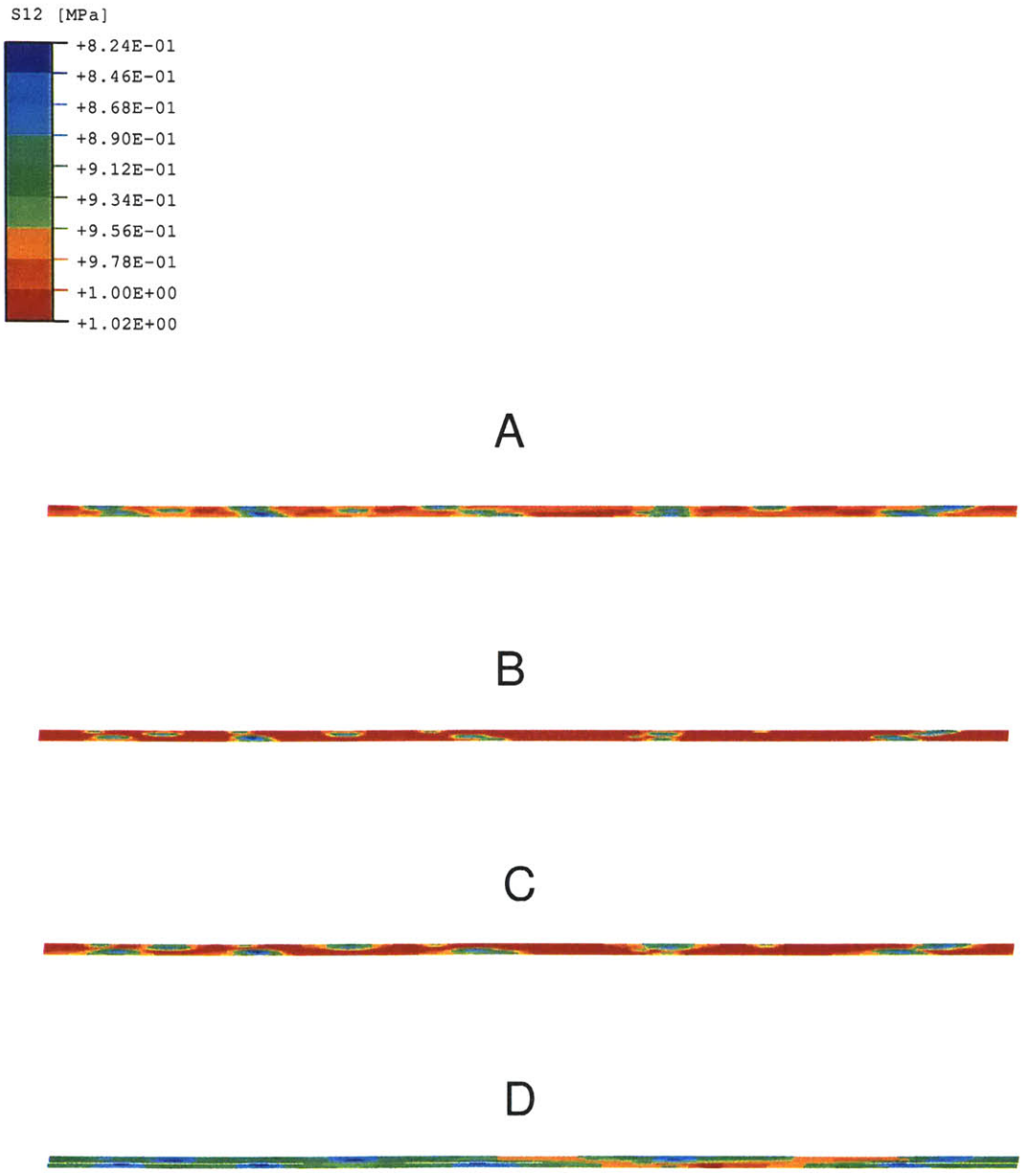

Figure 3-43: Contour of through-thickness shear stress component from pure shear simulation using defect distribution 1 (Fig. 3-34). A-D, respectively, denote contours at load levels of the correspondingly named points on the stress-strain curves shown in Fig. 3-41.

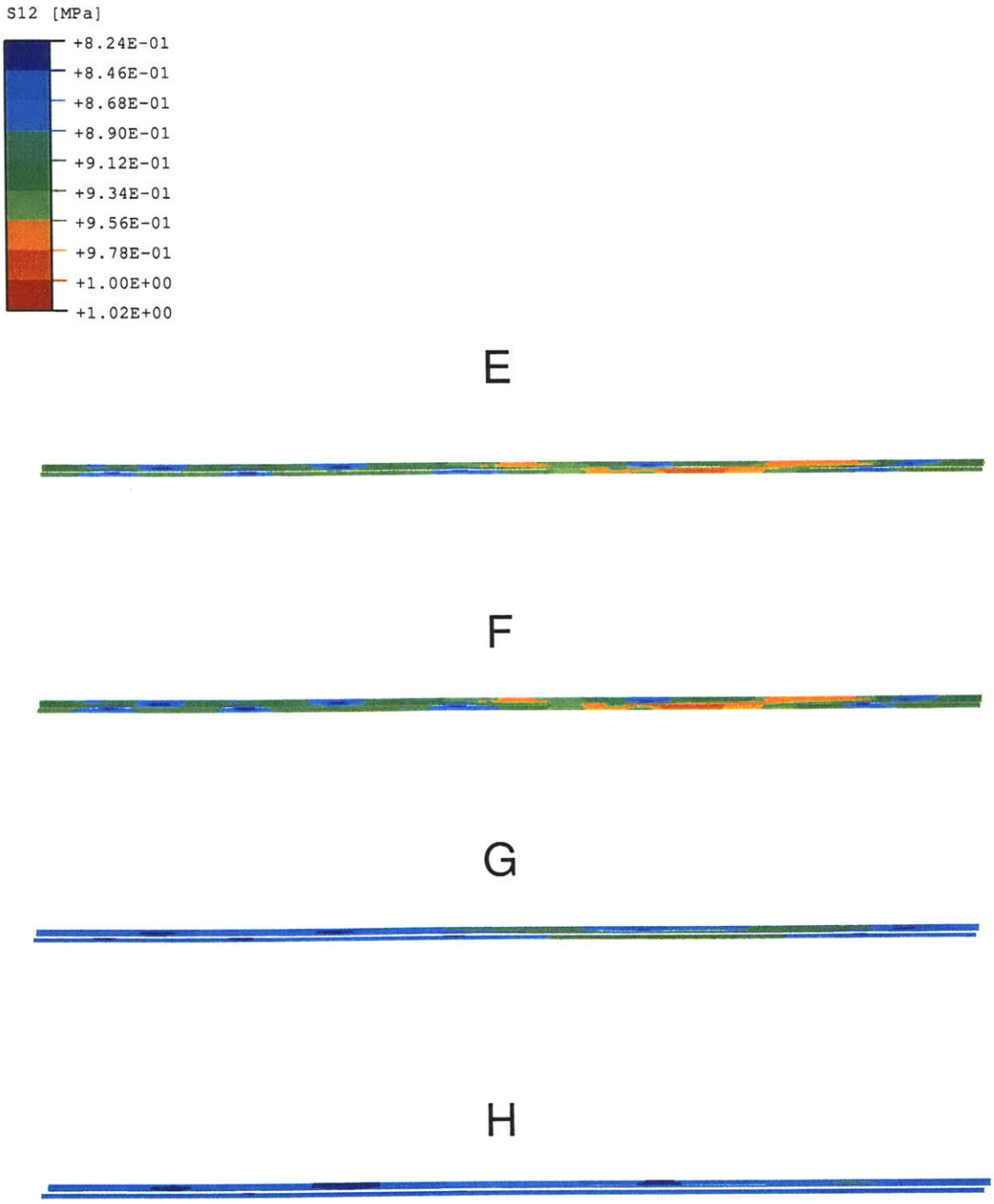

Figure 3-44: Contour of through-thickness shear stress component from pure shear simulation using defect distribution 1 (Fig. 3-34) (continued). E-H, respectively, denote contours at load levels of the correspondingly named points on the stress-strain curves shown in Fig. 3-41.

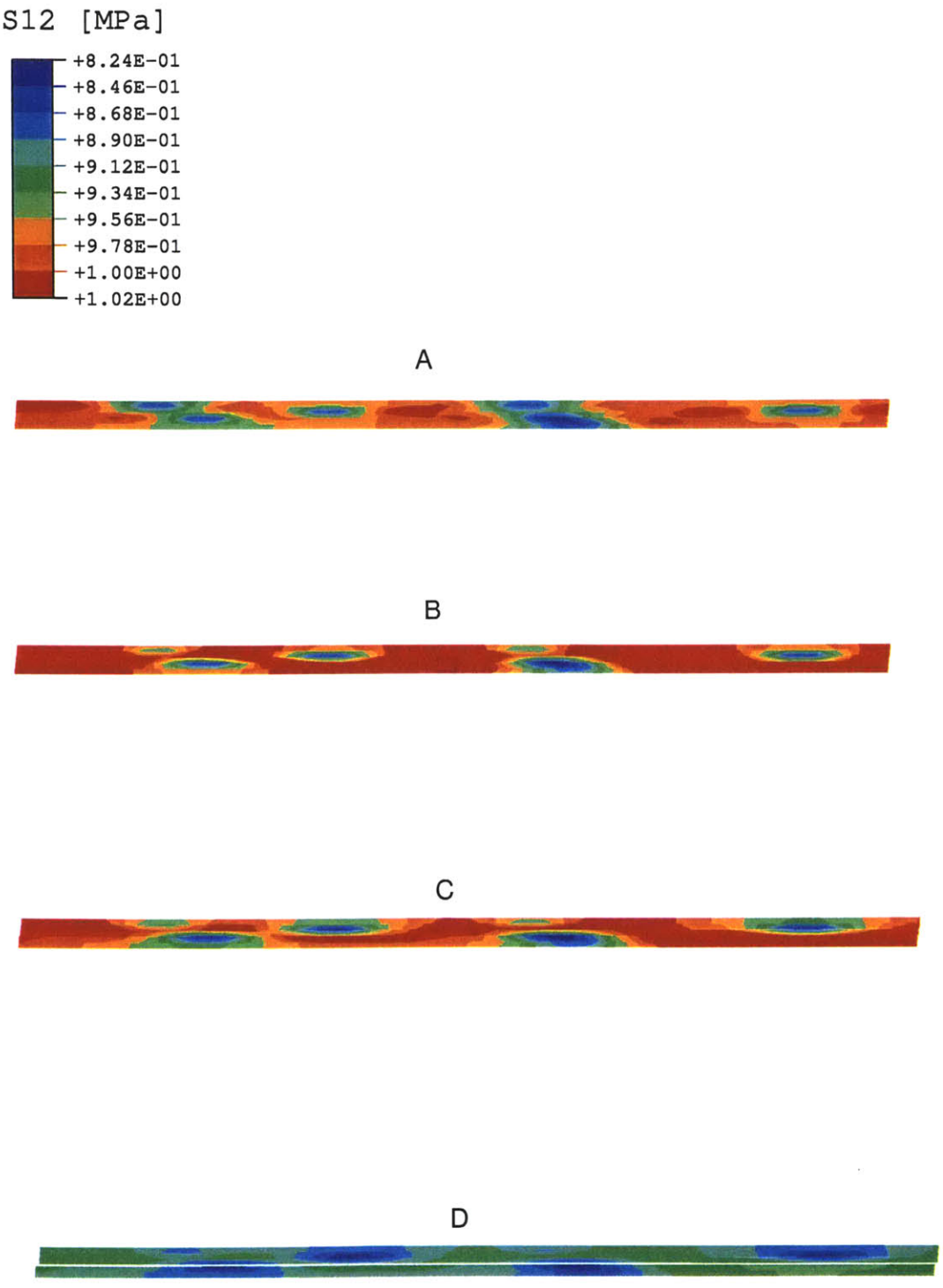

Figure 3-45: Magnified view of central part of contour of normal stress component in ZD from pure shear simulation using defect distribution 1 (Fig. 3-34). Relative position $0.3 \leq x \leq 0.65$.

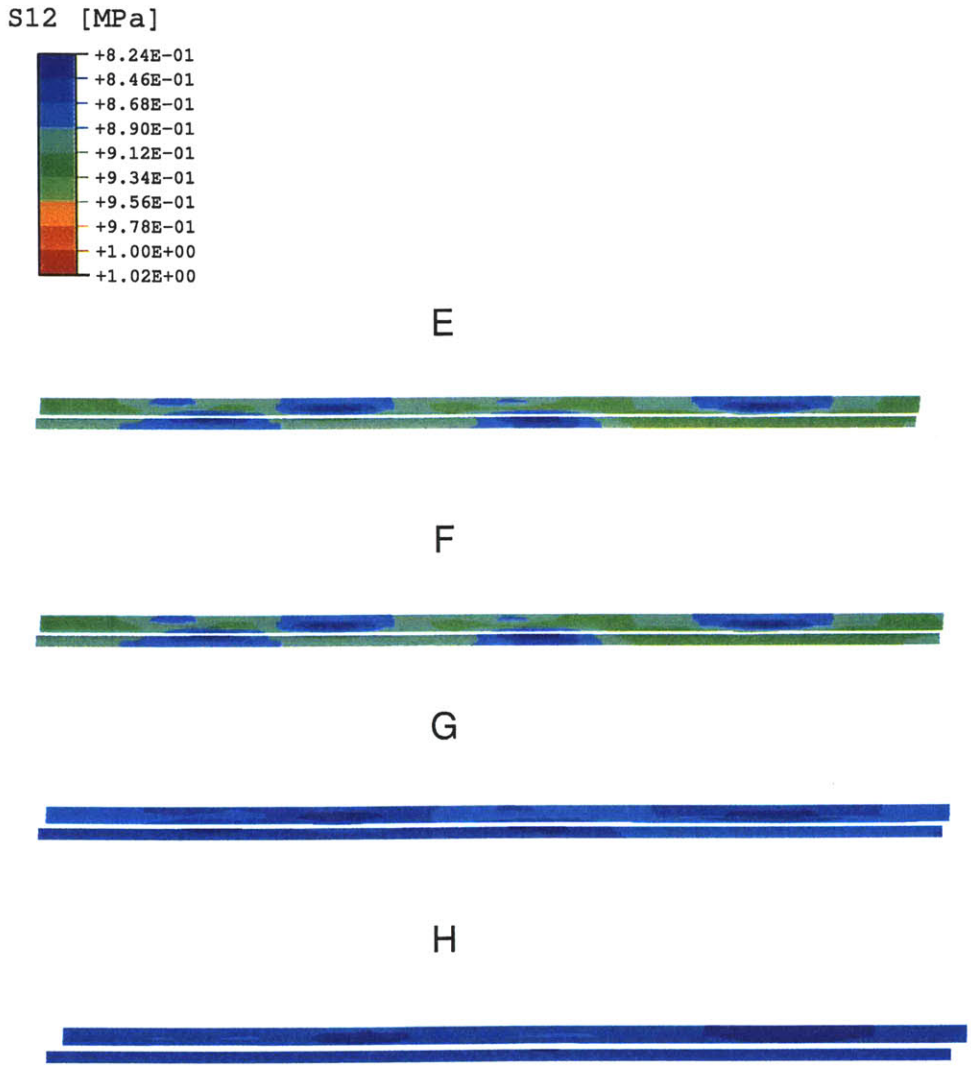

Figure 3-46: Magnified view of central part of contour of normal stress component in ZD from pure shear simulation using defect distribution 1 (Fig. 3-34) (continued). Relative position $0.3 \leq x \leq 0.65$.

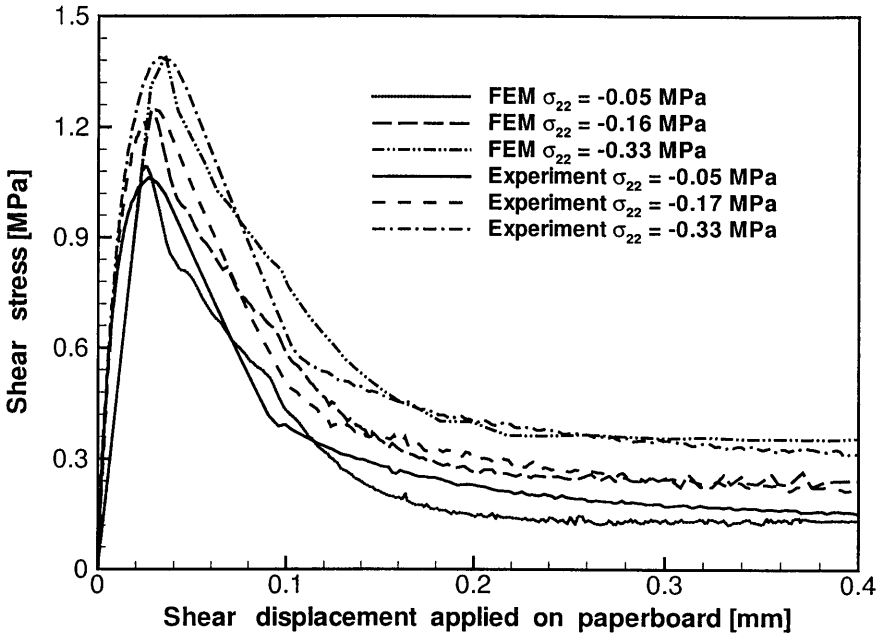

Figure 3-47: Pressure sensitivity of shear strength: Comparison of experimental and numerical results in MD-ZD.

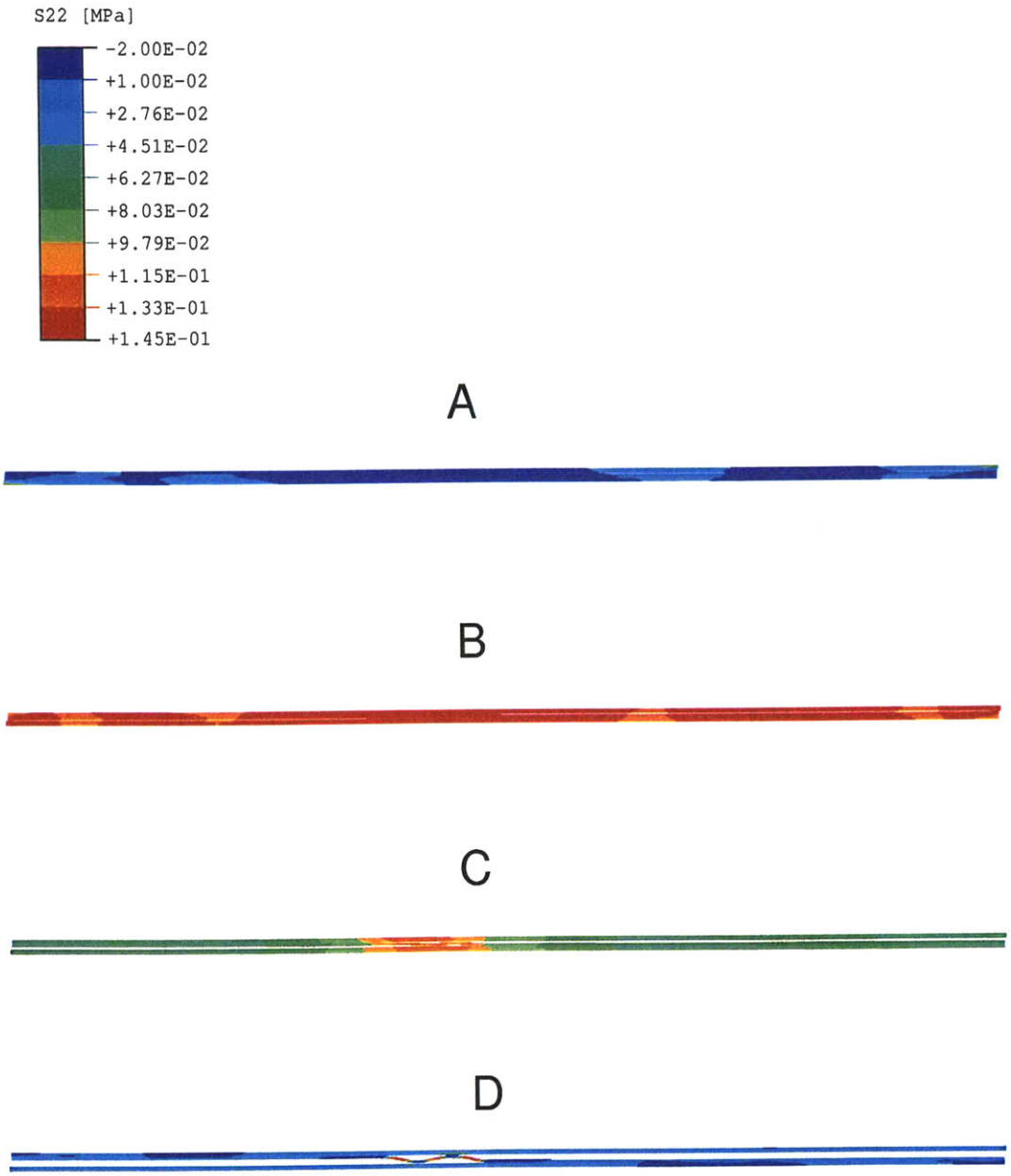

Figure 3-48: Contour of through-thickness normal stress component from combined through-thickness shear and tension simulation using defect distribution 1 (Fig. 3-34) (MD-ZD).

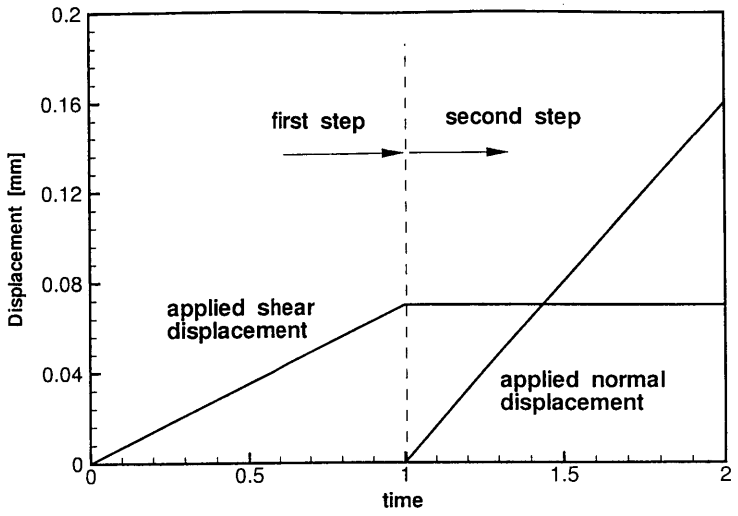

Figure 3-49: History of applied boundary conditions for from FEM simulation using defect distribution 1 (Fig. 3-34)

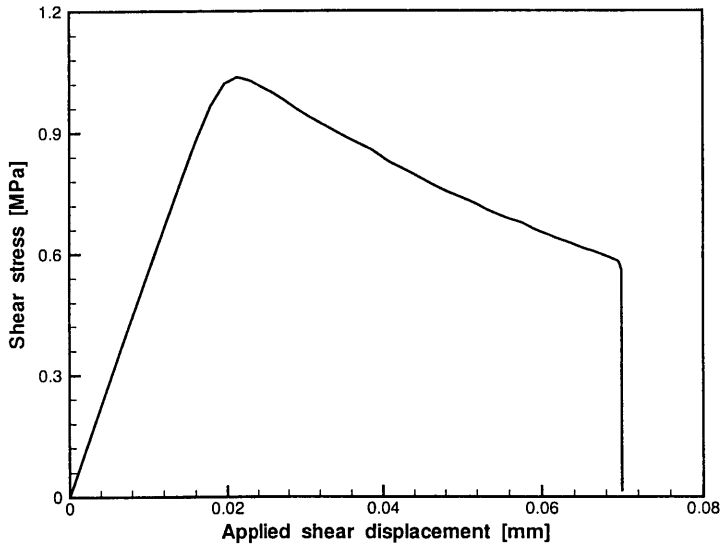

Figure 3-50: MD-ZD pure shear stress applied shear displacement curves from FEM using defect distribution 1 (Fig. 3-34) (first stage of deformation).

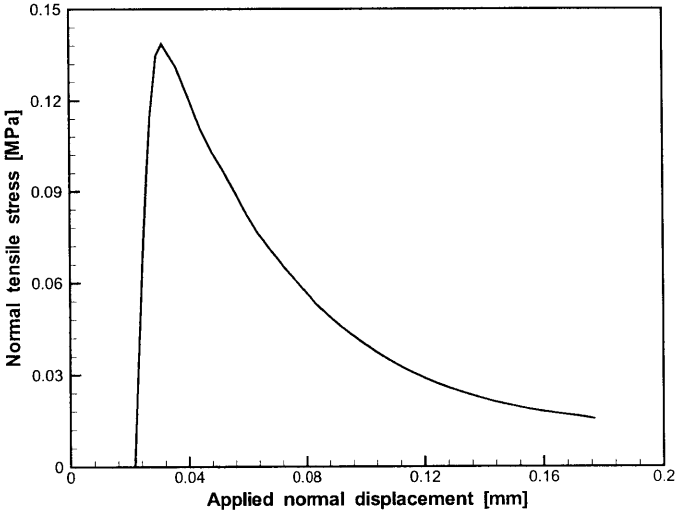

Figure 3-51: ZD normal stress *vs.* applied normal displacement curves from FEM using defect distribution 1 (Fig. 3-34) (second stage of deformation).

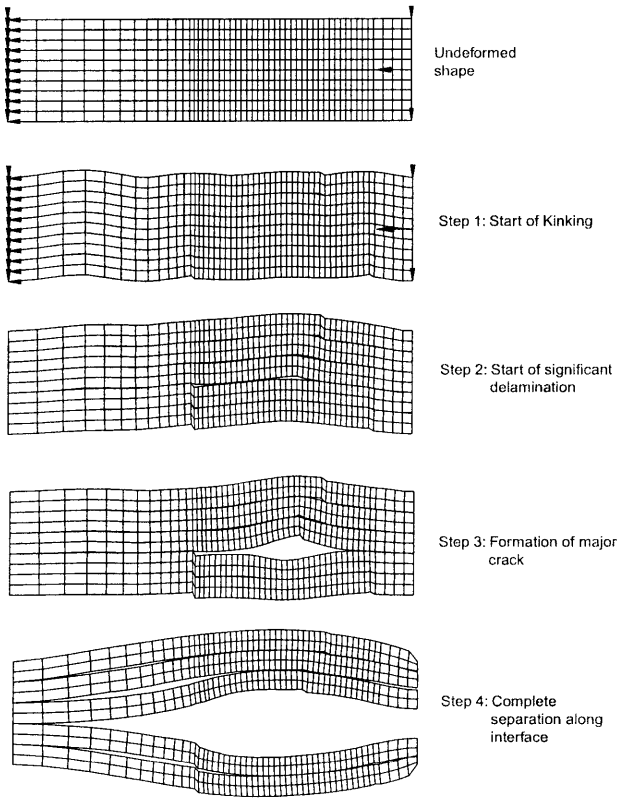

Figure 3-52: Mesh of the paperboard at different stages of deformation from the in-plane buckling simulation of TRIPLEX^{TM}.

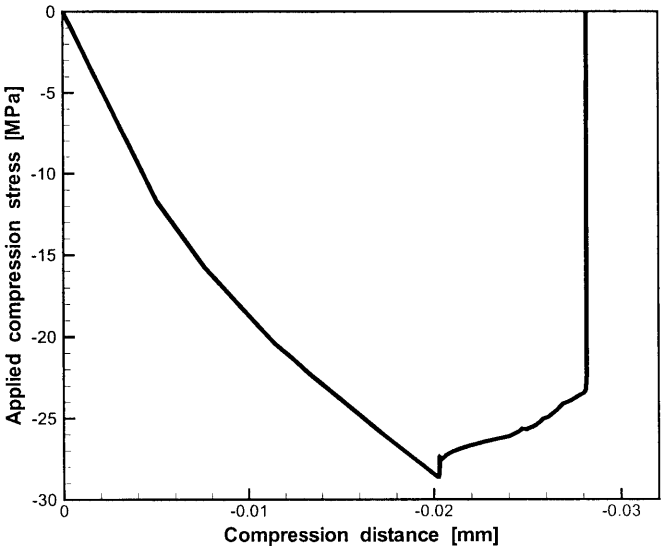

Figure 3-53: Compressive stress *vs.* applied compressive displacement curve obtained from in-plane buckling simulation of TRIPLEX^{TM}.

Chapter 4

Simulation of an exemplar converting process: creasing and folding

Converting process converts flat paperboard into a final shape through a series of sub-processes, *e.g.*, the creasing and subsequent folding of paperboard; the gluing of the paperboard; printing or coating on the paperboard surface, etc. The entire converting process involves dozens of different control variables. For example, during the creasing process, many parameters can influence the processing results. Some of the parameters have been previously shown in Fig. 1-13, such as the punching depth, the width of the male and female die, the shape of the male die, etc.

It is very desirable for the paperboard industry to be able to simulate the process because the high number of design parameters involved in the process makes it expensive to conduct experimental parametric studies on all of the variables for so many different types of paperboards. With the implementation of the interface model and the in-plane model into a finite element package, simulation of the process is made possible.

In this chapter, two types of simulations are conducted. First, simulations of a creasing/folding processes performed in a SEM are conducted. Then industrial

creasability tests are simulated. The primary difference between these two types of simulations lies in the way the pre-punched paperboard is folded. Both of these simulations are conducted within a 2-D plane-strain framework.

4.1 Simulation of SEM creasing/folding process

Dunn [18] conducted tests to investigate the micro-mechanisms underlying the deformation behavior of paperboard during creasing and folding. Photographs of the testing apparatus used to conduct the creasing and that used to perform folding are shown in Fig. 4-1 and Fig. 4-2, respectively. The FEM simulations of the creasing and folding processes are illustrated in Fig. 4-3 and Fig. 4-4. The first step is to apply a fixed normal in-plane stress at the ends of the paperboard before placing it between a male die and a female die, with two stoppers on each side of the male die above the top surface of the paperboard. The fixed stress is applied to simulate the web-tension that paperboard experiences during the actual punching process that occurs on a roller. The second step is the punching (or creasing) of the paperboard by a male die into the female die, followed by unloading of the male die in step 3. In step 4, the web tension stress is removed, as well as the two dies and the two stoppers. The creased paperboard is then clamped on its left side (see Fig. 4-4). The top clamp starts some distance beyond the far left tip of the specimen and ends near the center of the creased region. The bottom clamp starts at the same place as the top clamp, but ends at a distance about the thickness of the specimen to the left end of the creased region. In the next step (step 7), the clamped paperboard is rotated approximately 20 degrees, as done in the SEM tests. Step 7 also moves in the load cell which will fold the creased specimen. In Step 8, the load cell displaces vertically and the paperboard is folded to form the designed corners. In the last step, the folding load cell is unloaded.

As discussed earlier, the creasing process involves a large number of design variables which influence the end quality of the paperboard products. Dunn [18] con-

ducted SEM tests to investigate the effect of the width of the male and the female die on the quality of the crease. In this section, two tests are simulated. In the FEM models, the material parameters obtained for the mechanical and chemical layers, as well as those obtained for the inner and outer interfaces in the previous chapters are used to represent the TRIPLEX^{TM} paperboard. Because the in-plane model doesn't include mechanisms to fracture or fail the material when the in-plane strain is large enough, the in-plane hardening equations expressed in Eqn. 2.22 are modified such that the flow strength of the sub-surfaces would flatten out after reaching the corresponding fracture strength, instead of continuing to increase with increasing plastic strain. These new hardening constants are summarized in Table 4.1 and Table 4.2, respectively. As will be shown later in the SEM pictures taken by Dunn [18], in-plane fracture does not occur until the very end of the test and only in very localized areas.

$A_1(MPa)$	$A_2(MPa)$	$A_3(MPa)$	$A_4(MPa)$	$A_5(MPa)$
70.0	28.0	12.5	12.0	12.0
B_1	B_2	B_3	B_4	B_5
80.0	80.0	30.0	60.0	30.0
$C_1(MPa)$	$C_2(MPa)$	$C_3(MPa)$	$C_4(MPa)$	$C_5(MPa)$
10.0	10.0	25.0	10.0	10.0

Table 4.1: Modified in-plane yielding and hardening parameters used by model for mechanical pulp layers in TRIPLEX^{TM}.

$A_1(MPa)$	$A_2(MPa)$	$A_3(MPa)$	$A_4(MPa)$	$A_5(MPa)$
35.0	18.0	10.5	10.0	10.0
B_1	B_2	B_3	B_4	B_5
80.0	80.0	30.0	60.0	30.0
$C_1(MPa)$	$C_2(MPa)$	$C_3(MPa)$	$C_4(MPa)$	$C_5(MPa)$
10.0	10.0	25.0	10.0	10.0

Table 4.2: Modified in-plane yielding and hardening parameters used by model for chemical pulp layers in the TRIPLEX^{TM} composite laminate.

In the first simulation, the width of the male die is $0.5mm$ and and that of the

female die is $1.56mm$. The length of the specimen is $24mm$. The paperboard specimen is punched to a depth of about $0.6mm$ and then taken out and folded at a moment arm of about $20mm$. SEM micrographs of the MD-ZD cross section are taken during the process, and these images are compared with corresponding FEM contour plots from simulation of the test as follows.

Fig. 4-5 shows the micrograph taken when the male die just came into contact with the specimen. Contours of the MD normal stress component at the corresponding stage in the FEM simulation is plotted in Fig. 4-6. In Fig. 4-7 and Fig. 4-8, experimental and numerical results are compared when the punching begins. At this stage, material directly beneath the male die undergoes both through-thickness and in-plane compression. At the bottom surface of the specimen under the male die, the material is under in-plane tension. Material in the gap between the male die and the female die is primarily under out-of-plane shear. At this stage, no obvious delaminations are apparent in either the SEM or the FEM images. Fig. 4-9 and Fig. 4-10 show results when the male die is about to penetrate into the female die. At this stage, as depicted in both the SEM and FEM images, material in the gap between the male and female die starts to delaminate due to out-of-plane shear. Both images also show the specimen thickness to increase in these sections because of the shear-induced interface dilation. The final stage of punching (creasing) is depicted in Fig. 4-11 and Fig. 4-12. Up to this point, the intended shear damage is imparted to the material being punched through between the male and female die. Delaminations are more apparent and are distributed along the sheared sections of the specimen. Note that, as shown by the contours from the FEM simulation, the maximum MD normal stress achieved in the chemical layers exceeds both the experimental uniaxial MD tensile and the compressive failure strength. (approximately $90MPa$ and $40MPa$, respectively). However, these stress values are only reached at small localized areas under significant amount of ZD compression.

After the maximum punching depth is reached, the male die is retracted. Fig. 4-13 and Fig. 4-14 show the results at some intermediate stage. It can be seen from

both numerical and experimental results that the specimen during the retraction step follows the retraction of the male die at this stage, indicating elastic unloading. In Fig. 4-15 and Fig. 4-16, however, the male die pulls away from the specimen, showing plastic deformation accumulated inside the specimen. Arrows in Fig. 4-15 indicate some of the damage locations. It should be noted that, due to the fibrous nature of paperboard and the effect of a 2-D SEM image, the delaminations in the SEM images are not as obvious as those shown by the FEM results. However, the very fact that the SEM images show significant thickening of the specimen on each side of the male die clearly indicates the existence of delaminations inside the creased region. Another observation is that both FEM and SEM results show distinct regions of compression and shear. Material at the ZD compressed center under the male die is much denser that the surrounding shear-dilated regions. The punching force *vs.* punching distance curve for the male die is plotted in Fig. 4-17.

For the folding process, the SEM images of the specimen prior to folding are shown in Fig. 4-18. The corresponding contour plot of the equivalent plastic strain from the FEM simulation is shown in Fig. 4-19. Some of the very obvious delaminations created during the punching process are marked by arrows in Fig. 4-18. In addition to the cracks near the creased region, cracks are also observed outside of the region as indicated by the arrows. During folding (Fig. 4-19), we can see obvious delaminations and in-plane plasticity at localized regions where the male and female die had contacted the specimen during the punching step. In Fig. 4-20 and Fig. 4-21, the pre-delaminated interfaces continue to open up, primarily because of the in-plane compressive stress produced by the bending moment, as indicated by the FEM MD normal stress contour. Fig. 4-22 and Fig. 4-23 show the final shape of the specimen at the end of the test after the load is removed. The FEM simulation captures the main features of the folded region very well, *i.e.*, one major delamination along the outer interface on the outside of the crease and another long delamination along one of the inner interfaces inside the mechanical core. The bending moment (vertical reaction force times the corresponding moment arm) from the FEM simulation is also plotted

in Fig. 4-24. This curve is similar to curves obtained from industrial creasability test results, as will be shown later. (The maximum bending angle achieved by the FEM simulation is about 60 degrees before the elements became too distorted for the simulation to continue. The exact bending angle was not measured in the SEM test. A reasonable estimation will be between 60 to 90 degrees.)

To further study the underlying mechanics of the creasing/folding process. The behavior of one representative interface element during the entire simulation is studied. The representative element is located in the region between the male and female die, as indicated in Fig. 4-25. Fig. 4-26 plots the time history of the relative normal and shear displacement of the interface element across the entire process history. Step time 0 to 2 corresponds to the period when web-tension is applied and the male die just started touching the specimen. Step time 2 to 4 corresponds to the punching period, and step time between 4 to 9 represents the intermediate steps between the punching step and the folding step. Time 10 and after corresponds to the folding step. From Fig. 4-26 we can see that the representative interface element is subjected to negative shearing separation which in turn created ZD normal tensile separation during the punching step. The two relative displacements plateau after the punching step before increasing again in the final folding step. The corresponding accumulated interface damage is plotted in Fig. 4-27. This figures show the essential idea of the creasing/folding process: interface damages are created during the punching step (around a value of 0.6 in this case, on a scale of 1.0) so that later on, this intended damage will make it easier for the ideal crease shape be created in the folding process, where the interfaces delaminate further. (In this case, a final damage of around 0.8 was achieved)

The crease created in this test is considered to be a "good" crease because it is more or less symmetric about its center. Dunn [18] also produced a crease of poorer quality by using larger dies. In particular, the male die width is increased to $0.86mm$ and the female die width to $2.03mm$. The larger gap between the male and female die generates lower out-of-plane shear strain in the material in the gap, which means

less interface damage will be created. Meanwhile, a larger male die creates a wider punched region, which in turn increases the difference in moment arm length between the two ends of the punched region. These two effects together generally result in an unsymmetrical crease.

Simulation of this test is conducted to further test the predictive capability of the models. As in the last simulation, contours from the FEM simulation are compared with the corresponding SEM pictures. Fig. 4-28 shows the picture taken when the male die just came into contact with the specimen. Contours of the MD normal stress component at the corresponding stage in the simulation is plotted in Fig. 4-29. A similar comparison is made for the last step of the punching process in Fig. 4-30 and Fig. 4-31. As in the last simulation, the FEM results capture the general characteristics of the punch process. The punching force *vs.* punching distance curve for the male die is plotted in Fig. 4-17 as the dashed line. Comparing to the solid line shown for the previous simulation in the same figure, a bit lower punch force is required to punch the specimen to the same depth into the female die because the gap between male die and female is larger in the second simulation, which makes it easier for the male die to punch the board into the female die. The same information at the end of the subsequent unloading step is shown in Fig. 4-32 and Fig. 4-33. Note that the radius of the corner of the male die used in the simulation is larger than that of the male die in the SEM test, for the purpose of better numerical convergence. This results in lower stress level in material in the regions around the male die corners in the FEM simulation compared to that generated in the test. For the folding process, the SEM image with no folding moment applied is shown in Fig. 4-34. The corresponding contour plot of the equivalent plastic strain at the same stage from the FEM simulation is shown in Fig. 4-35. Fig. 4-36 and Fig. 4-37 show the comparison of the experimental and numerical results at the stage when a major delamination has developed along one of the inner interfaces. With further increase in the bending moment applied, more delaminations develop under in-plane compression stress in the creased region as shown in Fig. 4-39. The corresponding SEM image is shown in Fig. 4-

38. By comparing these two figures, it is obvious that the FEM simulation captures the main features of the deformation of the creased region very well at this stage. Fig. 4-40 shows the SEM image at the end of the test. The crease became lopsided to some extent at this stage, indicating the formation of "bad" crease with more delaminations developed at end of the punched-damaged region closest to the clamps. The simulation started to have convergence problems before this stage is reached. The bending moment (vertical reaction force times the corresponding bending arm) from the FEM simulation is also plotted in Fig. 4-41. The peak bending moment required to fold the specimen in this simulation is about $14Nmm$, higher than that required in the last simulation. (A value of about $13Nmm$, as shown in Fig. 4-24). This is as expected since the larger gap between male die and female die creates less damage during the punching process which makes it harder to fold later on. In summary, comparison of the FEM simulation results with SEM creasing/folding tests show that, armed with the interface model and the in-plane model, the numerical simulations represent the entire process very well by capturing the micro-mechanical mechanisms underlying the creasing/folding process. Combinations of the SEM and FEM results provides a complete understanding of the mechanics behind the process. In particular, the stress contours and information about the interface available from the FEM simulation (such as those shown in Fig. 4-26 and Fig. 4-27) provides additional insights to the entire process. This information can be utilized to optimize the design of the process.

4.2 Simulation of an industrial creasability test

Simulations were also conducted to simulate the industrial standard creasability test (Swedish standard test number SE 015). A schematic of the test is showne in Fig. 4-42. The creasability test is different from the SEM creasing/folding test of the last section in that the folding of the creased paperboard is done by clamping one side of the un-punched portion of the board and rotating this portion with respect to a fixed point, instead of by vertical translational movement of a loadcell against the

specimen. This procedure is performed on a creasability tester, which is an instrument used to measure the bending resistance of paperboard as a function of the bending angle. As shown in Fig. 4-42, a creasability tester consists of a clamping device with one fixed clamp and one movable clamp. The paperboard sample is pivoted about a rotational center located at the front edge of the fixed clamp. The loadcell is a blunted knife-edge mounted near the other end of the specimen. A force transducer is used to measure the reaction force at the knife tip.

The steps of the FEM simulations are illustrated in Fig. 4-43 and Fig. 4-44. Five simulations were conducted to investigate the effect of die size and punch depth on the bending resistance of the creased paperboard. Since the punching step is more or less the same as that in the previously discussed punching process, here we concentrate our attention on the folding process and the corresponding bending moment *vs.* bending angle curve. A schematic of the folding process of the creasability test simulated is shown in Fig. 4-45, and the parameters studied are depicted in Fig. 4-46. The length of the rotating portion of the specimen is $10mm$ and the width of the specimen is $20mm$. The control parameters of the simulated creasability tests are listed in Table 4.3.

test#	Male width $[mm]$	Male type	Female width $[mm]$	Crease depth $[\mu m]$
1	0.7	Square	1.5	-50
2	0.7	Square	1.5	150
3	0.9	Round	1.5	50
4	0.9	Square	1.7	-50
5	0.9	Square	1.7	150

Table 4.3: Control parameters used for the creasability tests.

Comparison of the numerical and experimental bending moments *vs.* bending angle curves are shown in Fig. 4-47 to Fig. 4-51 (The tests were conducted at Tetra Pak, Sweden). From these curves, we can see that the FEM simulations predict the peak moment of the test quite well. The numerical results also predict the trend of the effects of the test parameters accurately, *i.e.*, (1) the peak bending moment decreases

with increasing punch depth (shown by comparison of tests 1 and 2, 4 and 5); (2) with the same punch depth, a larger gap between male die and female die width, or in other words, a larger distance between male and female die, decreases the peak bending moment (shown by comparison of tests 1 and 4, 2 and 5); (3) There is a lower peak bending moment when a square-shaped male die is used instead of a round-shaped one (shown indirectly by comparison of test 3 and 5). The peak bending moments of these simulated tests are listed together with values from corresponding experiments in Table 4.4. The numerical predictions of the bending angle corresponding to the peak bending moment are larger than the experimental values in all of the cases. This is primarily because in the FEM simulations, a rounded plate (attached to a load cell) with finite width was used, which causes some sliding between the plate and the specimen; while in the creasability tests, a sharp knife is used, which prevents the specimen from finite sliding at the contact point at the beginning of the rotation of the clamped portion. Another issue encountered in the FEM simulation is that, when the rotation of the clamps reaches about 40 - 50 degrees, mesh distortion at the far end of the crease (with respect to the clamps) becomes too large for the simulation to continue. This is why, in the FEM simulations, the maximum bending angle that can be reached is around 50 degrees. However, since the peak bending moment is the most important indicator of the bending resistance of the specimen, this issue is less significant.

test#	Experimental peak moment $[Nmm]$	Numerical peak moment $[Nmm]$
1	22	20
2	14	13.5
3	24	21
4	22	19
5	15	15

Table 4.4: Comparison of peak bending moment for the creasability tests.

Contour plots of the MD normal stress component at the final stage of the FEM simulation is plotted in Fig. 4-52, and that of the equivalent plastic strain is shown in

in Fig. 4-53. From Fig. 4-52, we can see that the individual layers are under bending and each layer is subject to both tension and compression. At this stage, most of the plastic strain is concentrated in regions that had made contact with the male and female dies during the punch process.

With the good predictive capability shown, the combined interface and in-plane model can be used to make the design of the creasing/folding process for different types of paperboards more efficient by running computer simulations which complement a much-reduced amount of testing.

4.3 Discussion

Although the simulations are found to be predictive of the corresponding experimental observations, there are still aspects of the simulations that need to be further explored in order to make the simulations better representative of the real process. Some of these possible future improvement are listed below:

- In these simulations, a uniform distribution of the interface strength is used. As discussed and investigated in the interface model chapter, the real paperboards have a nonuniform distribution of interface strength, and the strength distribution changes the properties of the paperboard. So in future simulations, defect distributions should be introduced.

- Extension of the simulation to three dimension.

- Further investigation in numerical techniques is needed to improve the severe discontinuity issue during contact and localized mesh distortion. For example, an explicit finite element package (*e.g.*, ABAQUS EXPLICIT) can be used which will improve the contact simulation, with data transferred back to implicit package for unloading. Also remeshing techniques can be used to prevent severe element distortion.

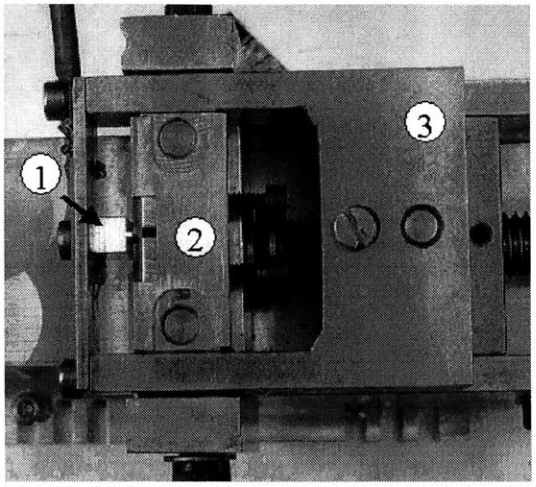

Figure 4-1: Experimental apparatus for conducting the punching test [18].

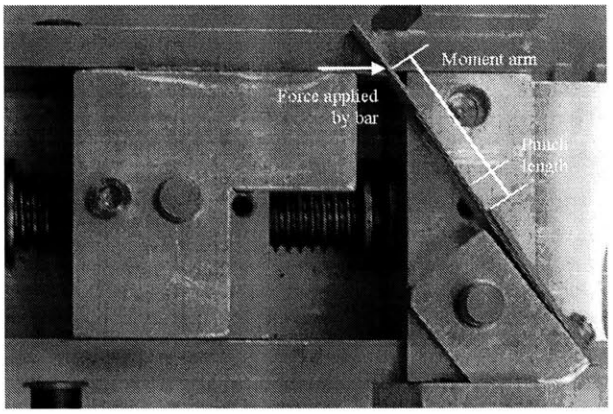

Figure 4-2: Experimental apparatus for conducting the folding test [18].

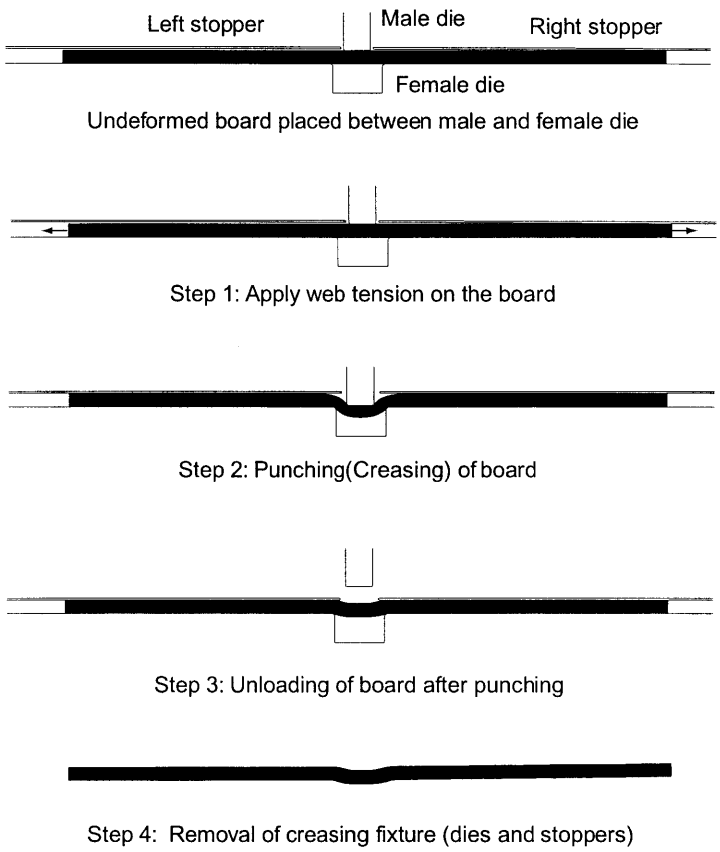

Figure 4-3: Illustration of the creasing/folding process; part (a), creasing.

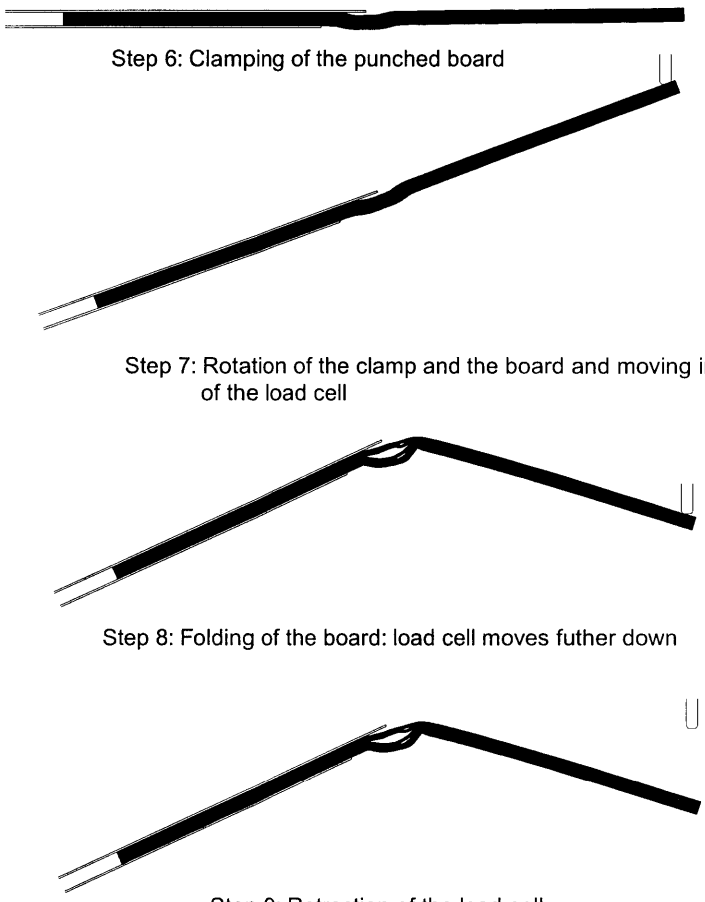

Figure 4-4: Illustration of the creasing/folding process; part (b), bending.

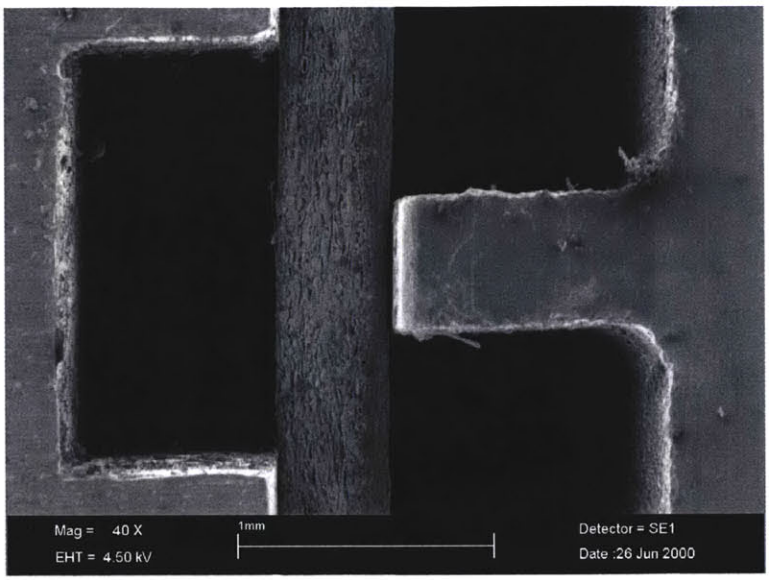

Figure 4-5: SEM image of TRIPLEX^{TM} MD punching process (step 1) [18]

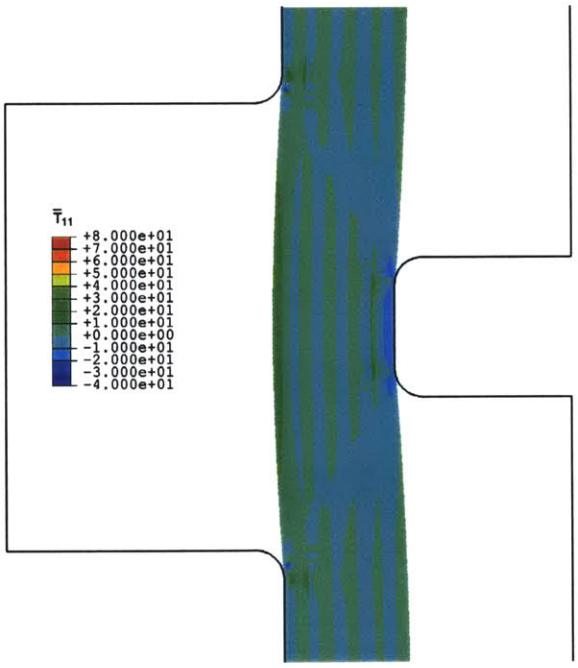

Figure 4-6: Contour plot of MD normal stress from simulation of SEM TRIPLEX^{TM} MD punching process corresponding to that shown in Fig. 4-5.

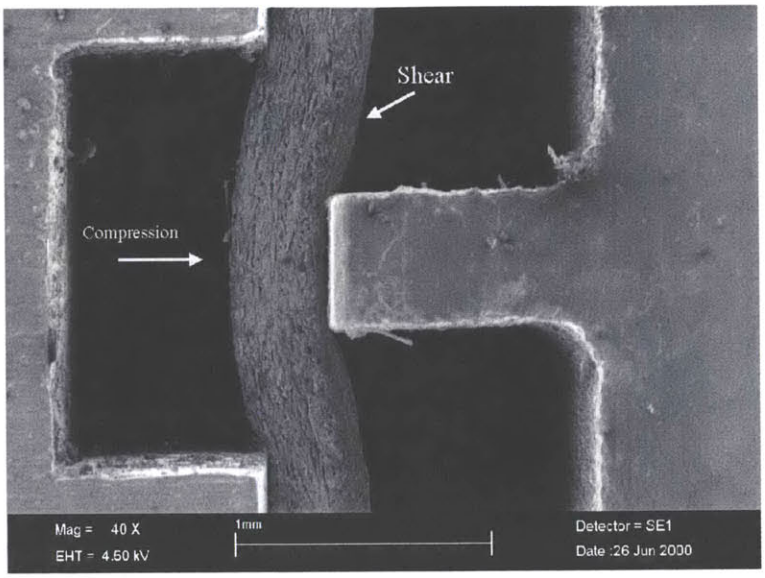

Figure 4-7: SEM image of TRIPLEX^{TM} MD punching process (step 2) [18].

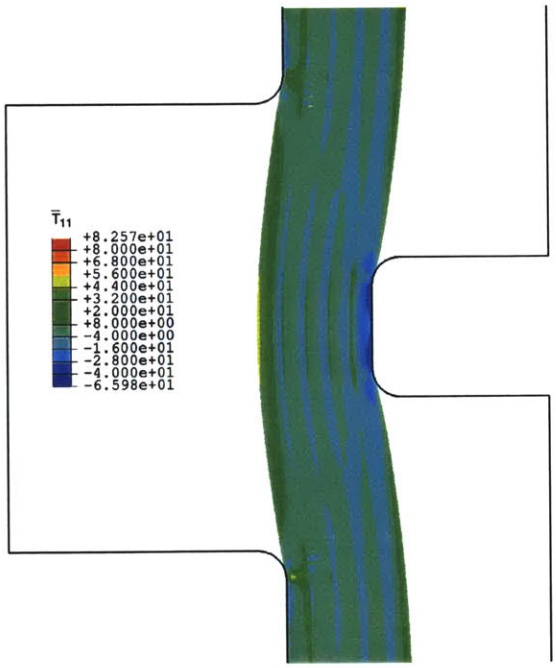

Figure 4-8: Contour plot of MD normal stress from simulation of SEM TRIPLEX^{TM} MD punching process corresponding to that shown in Fig. 4-7.

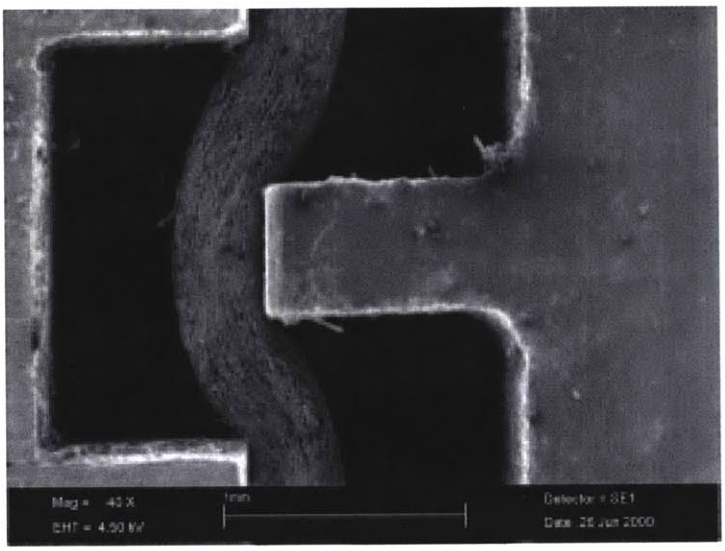

Figure 4-9: SEM image of TRIPLEX^{TM} MD punching process (step 4) [18].

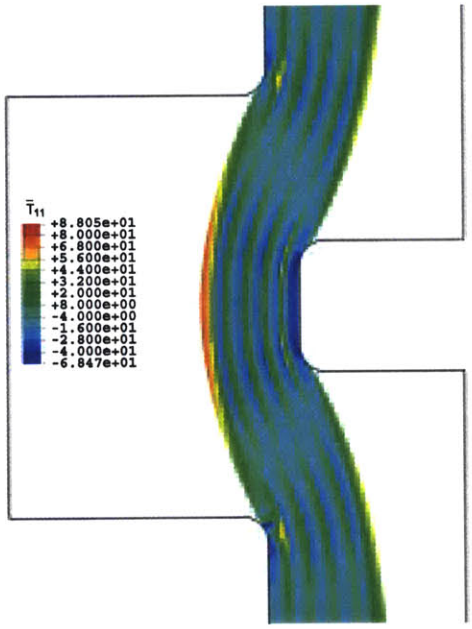

Figure 4-10: Contour plot of MD normal stress from simulation of SEM TRIPLEX^{TM} MD punching process corresponding to that shown in Fig. 4-9.

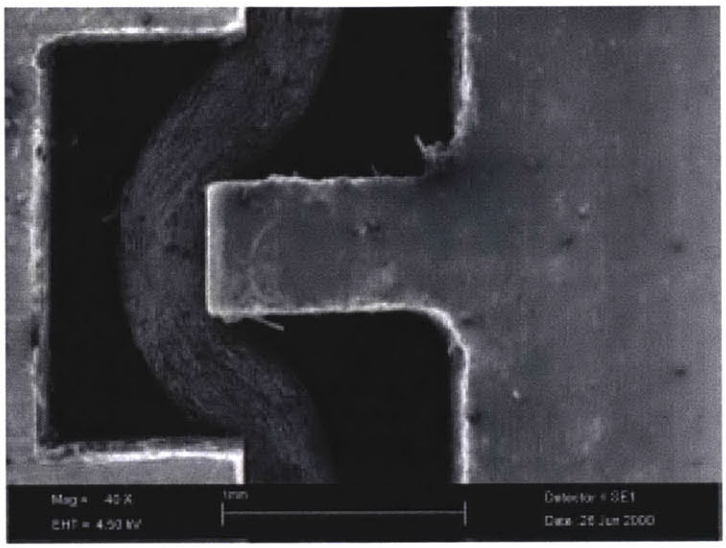

Figure 4-11: SEM image of TRIPLEX^{TM} MD punching process (step 6) [18].

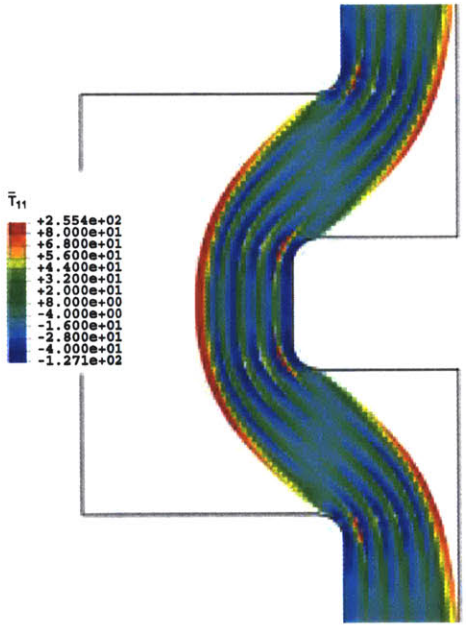

Figure 4-12: Contour plot of MD normal stress from simulation of SEM TRIPLEX^{TM} MD punching process corresponding to that shown in Fig. 4-11.

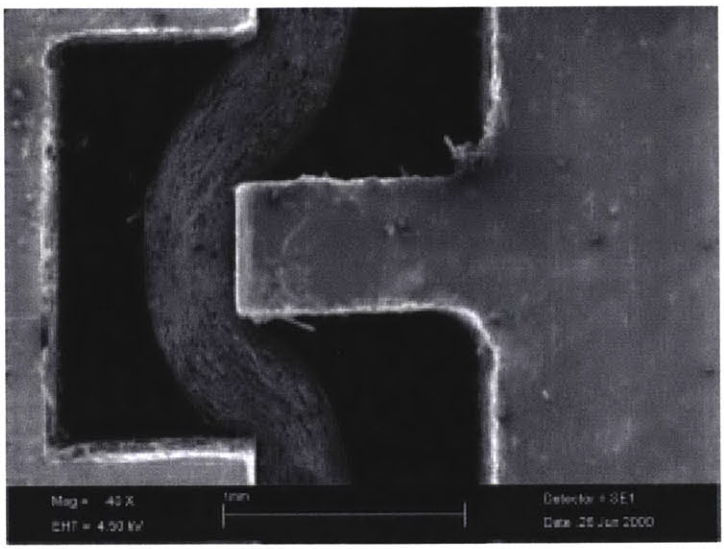

Figure 4-13: SEM image of TRIPLEX^{TM} MD punching process (step 7) [18].

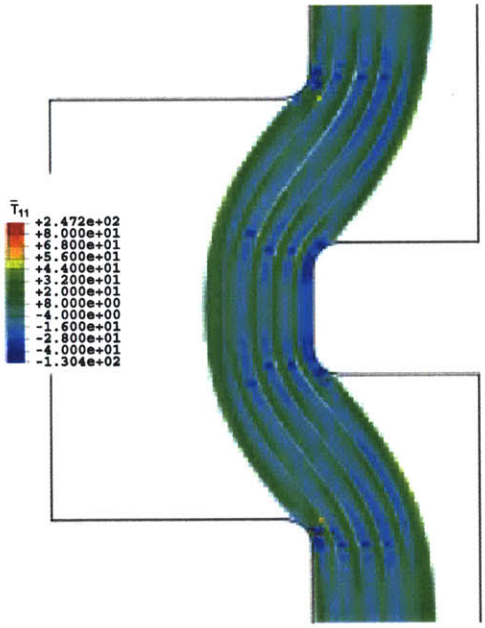

Figure 4-14: Contour plot of MD normal stress from simulation of SEM TRIPLEX^{TM} MD punching process corresponding to that shown in Fig. 4-13.

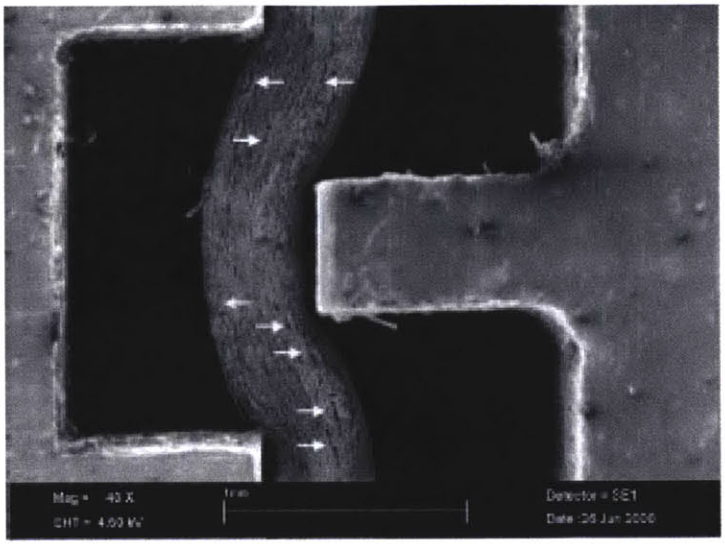

Figure 4-15: SEM image of TRIPLEX^{TM} MD punching process (step 8) [18].

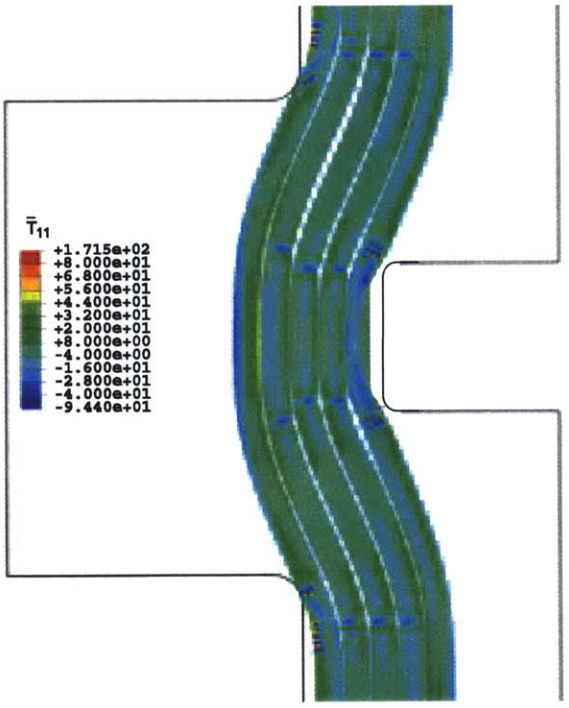

Figure 4-16: Contour plot of MD normal stress from simulation of SEM TRIPLEX^{TM} MD punching process corresponding to that shown in Fig. 4-15.

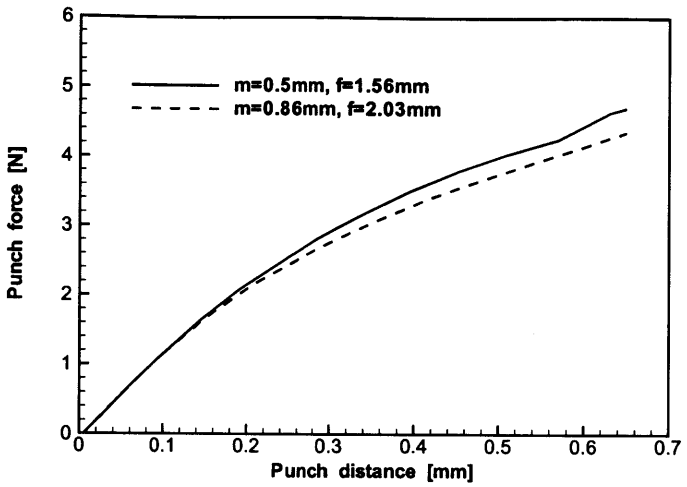

Figure 4-17: Punching force *vs.* punching distance curve for the male die obtained from FEM simulation of the punching process as first step of a converting process.

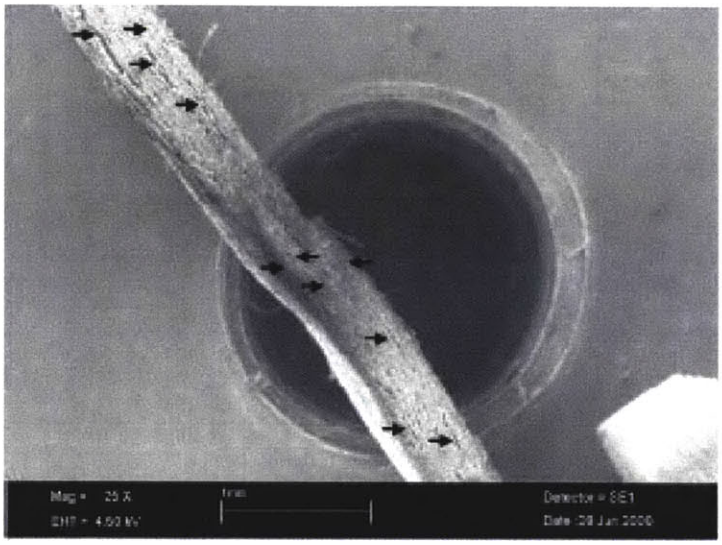

Figure 4-18: SEM image of TRIPLEX^{TM} MD folding process (step 1) [18].

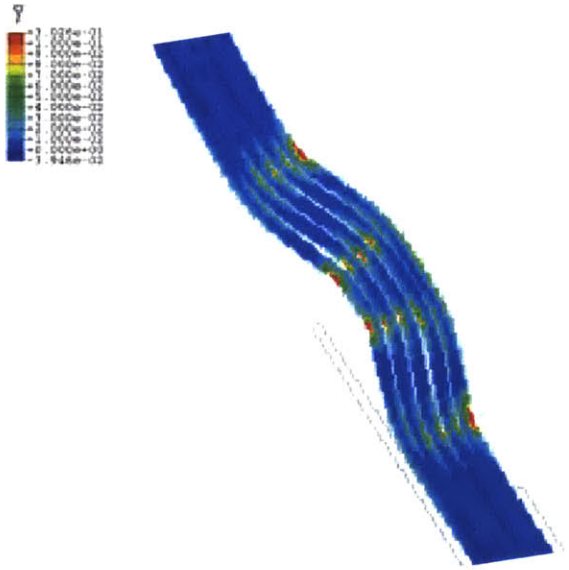

Figure 4-19: Contour plot of initial equivalent plastic strain from simulation of SEM TRIPLEX^{TM} prior to MD folding process corresponding to that shown in Fig. 4-18.

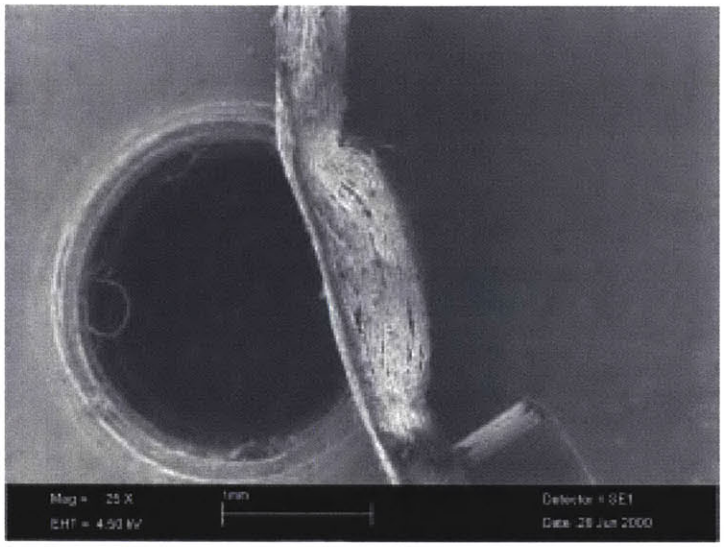

Figure 4-20: SEM image of TRIPLEX^{TM} MD folding process (step 3) [18].

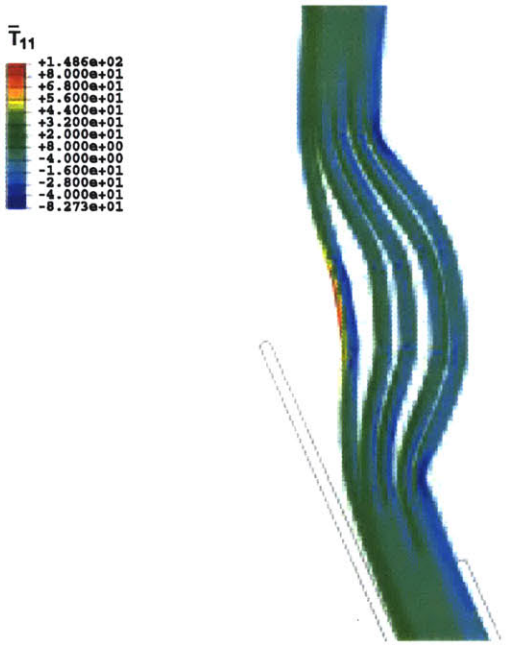

Figure 4-21: Contour plot of MD normal stress from simulation of SEM TRIPLEX^{TM} MD folding process corresponding to that shown in Fig. 4-20.

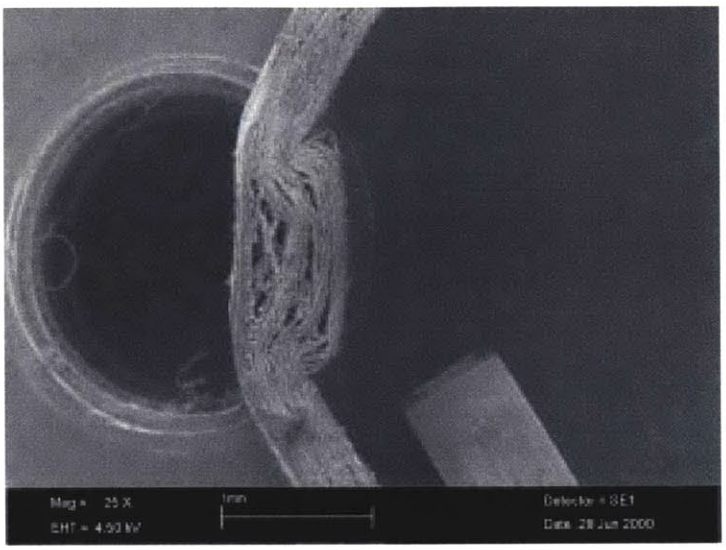

Figure 4-22: SEM image of TRIPLEX^{TM} MD folding process (step 6) [18].

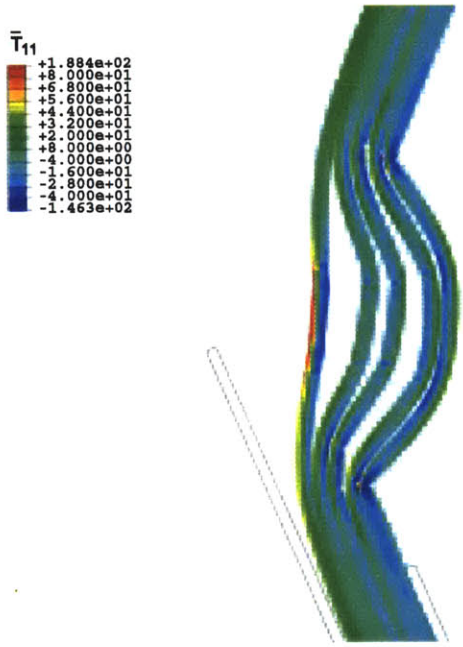

Figure 4-23: Contour plot of MD normal stress from simulation of SEM TRIPLEX^{TM} MD folding process corresponding to that shown in Fig. 4-22.

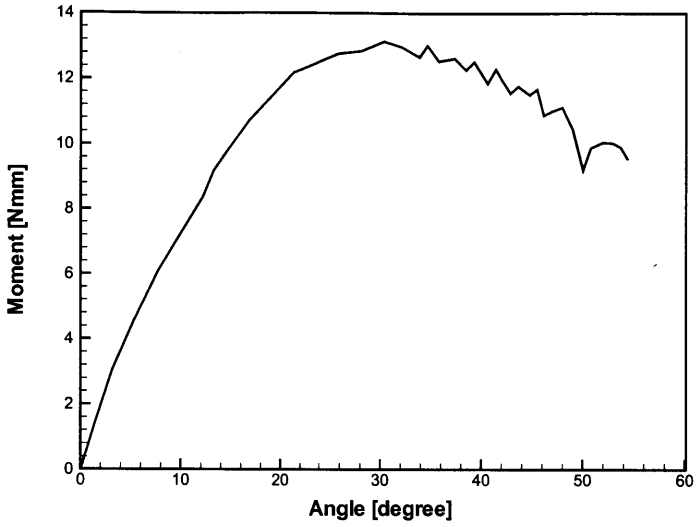

Figure 4-24: Bending moment *vs.* bending angle curve obtained from FEM simulation of the folding process as last step of a converting process.

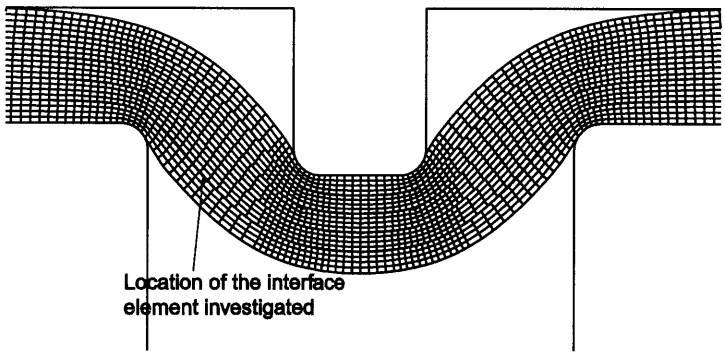

Figure 4-25: Illustration of location of a representative interface element used to investigate behavior of the interface during converting process.

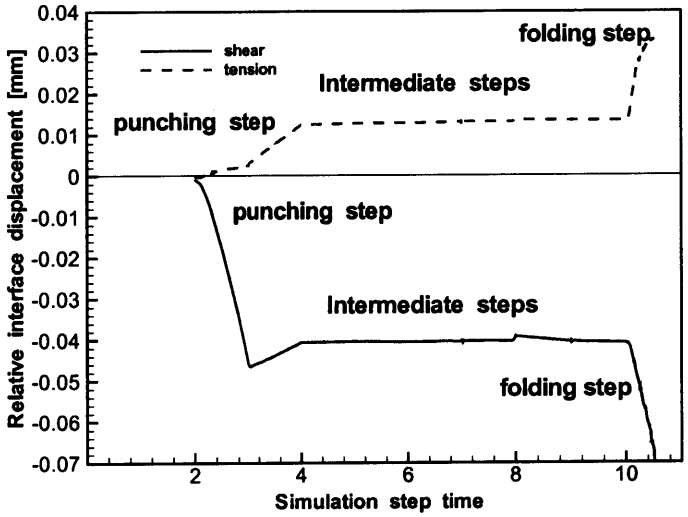

Figure 4-26: Time history of the relative interface normal and tangential separation of the representative interface element shown in Fig. 4-25 during the entire converting process.

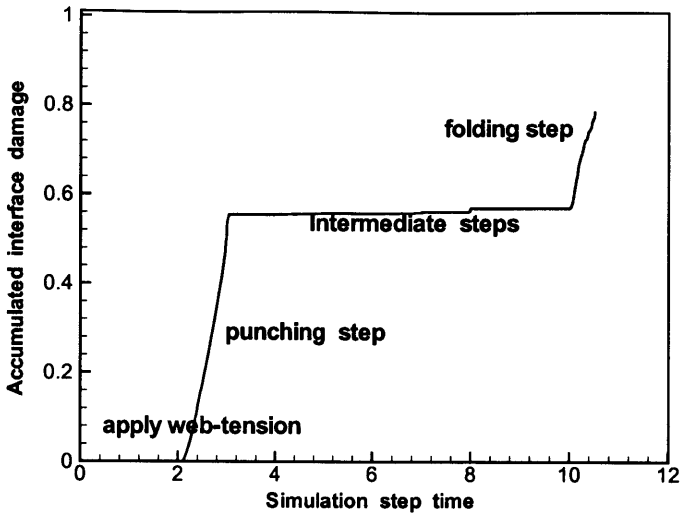

Figure 4-27: Time history of the accumulated damage inside the representative interface element shown in Fig. 4-25 during the entire converting process.

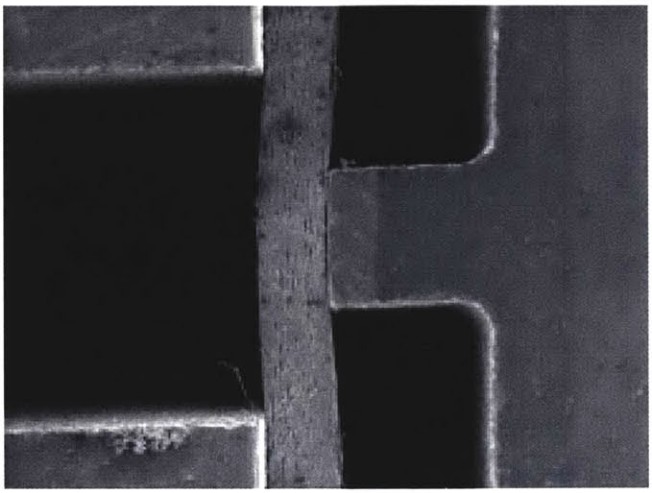

Figure 4-28: SEM image of TRIPLEX^{TM} MD punching process (step 1, male die width $0.84mm$ and female die width $2.03mm$) [18].

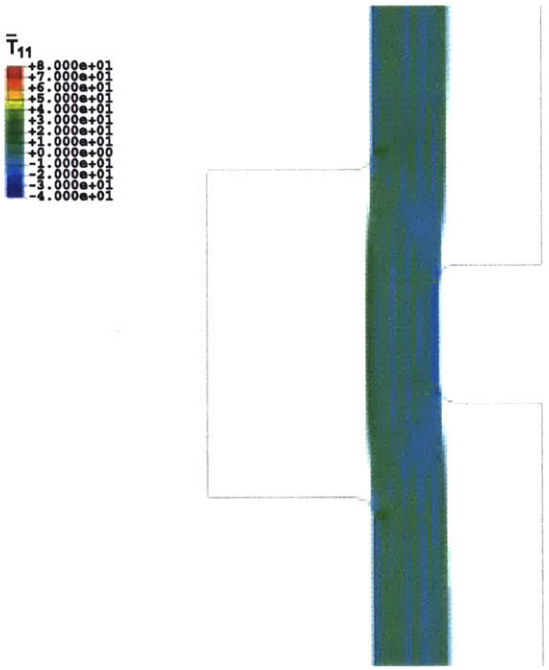

Figure 4-29: Contour plot of MD normal stress from simulation of SEM TRIPLEX^{TM} MD punching process corresponding to that shown in Fig. 4-28.

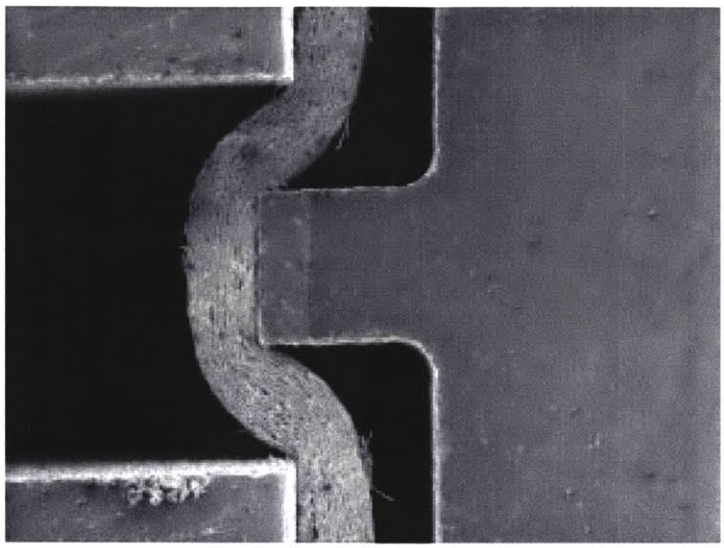

Figure 4-30: SEM image of TRIPLEX^{TM} MD punching process at the last step (male die width $0.84mm$ and female die width $2.03mm$) [18].

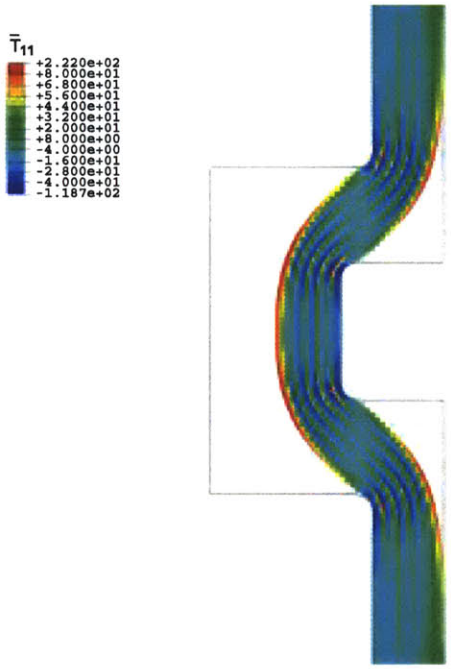

Figure 4-31: Contour plot of MD normal stress from simulation of SEM TRIPLEX^{TM} MD punching process corresponding to that shown in Fig. 4-30.

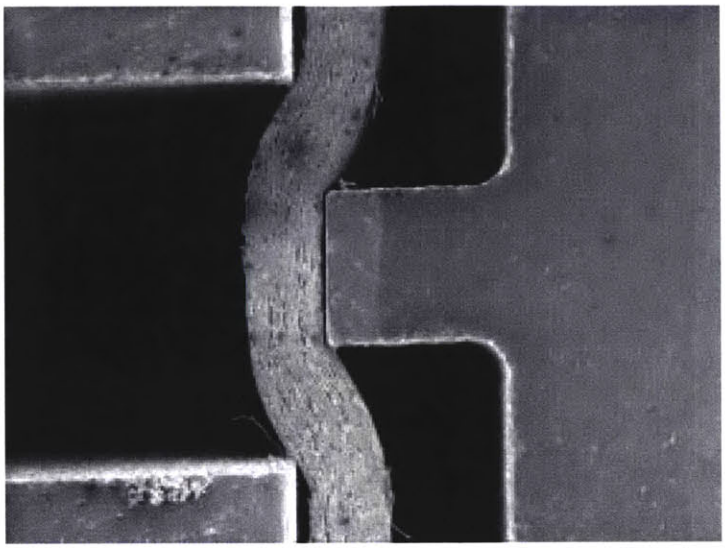

Figure 4-32: SEM image of TRIPLEX^{TM} MD punching process at the last step of unloading (male die width $0.84mm$ and female die width $2.03mm$) [18].

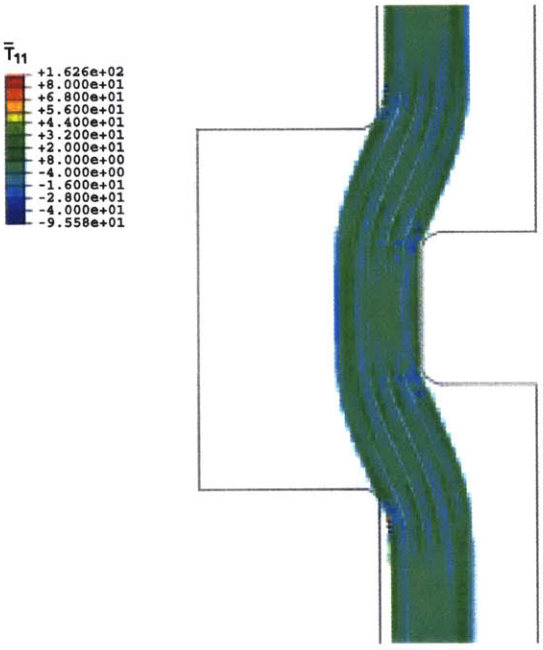

Figure 4-33: Contour plot of MD normal stress from simulation of SEM TRIPLEX^{TM} MD punching process corresponding to that shown in Fig. 4-32.

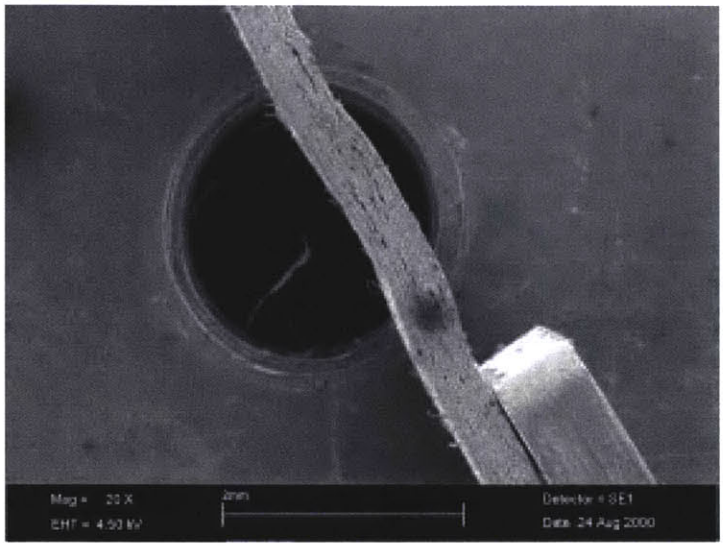

Figure 4-34: SEM image of TRIPLEX^{TM} MD punching process at the first step of folding (male die width $0.84mm$ and female die width $2.03mm$) [18].

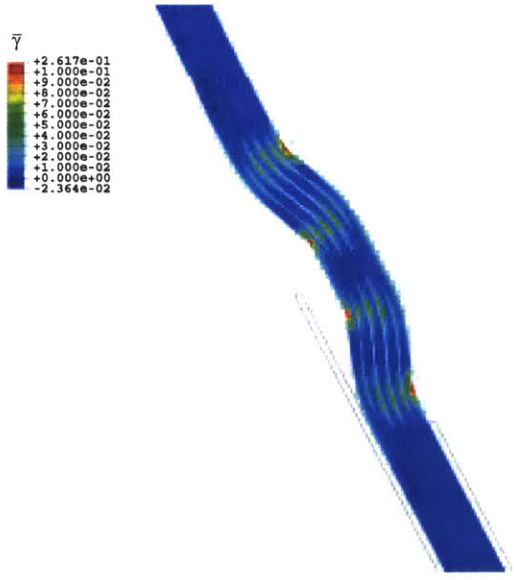

Figure 4-35: Contour plot of MD normal stress from simulation of SEM TRIPLEX^{TM} MD punching process corresponding to that shown in Fig. 4-34.

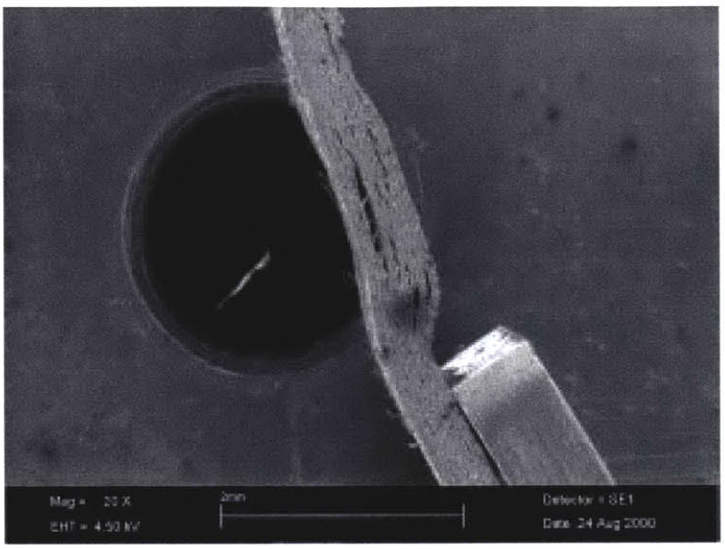

Figure 4-36: SEM image of TRIPLEX^{TM} MD punching process at step 2 of folding (male die width $0.84mm$ and female die width $2.03mm$) [18].

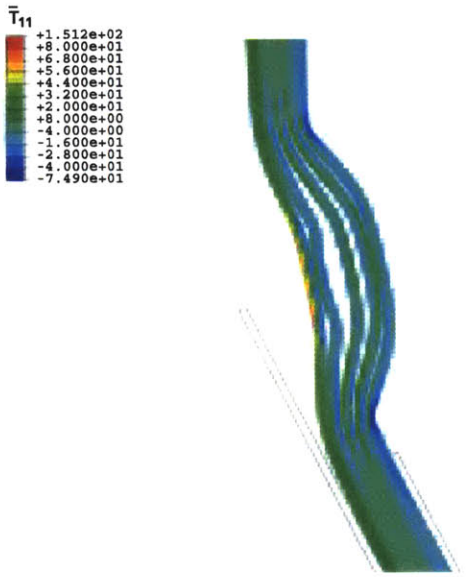

Figure 4-37: Contour plot of MD normal stress from simulation of SEM TRIPLEX^{TM} MD punching process corresponding to that shown in Fig. 4-36.

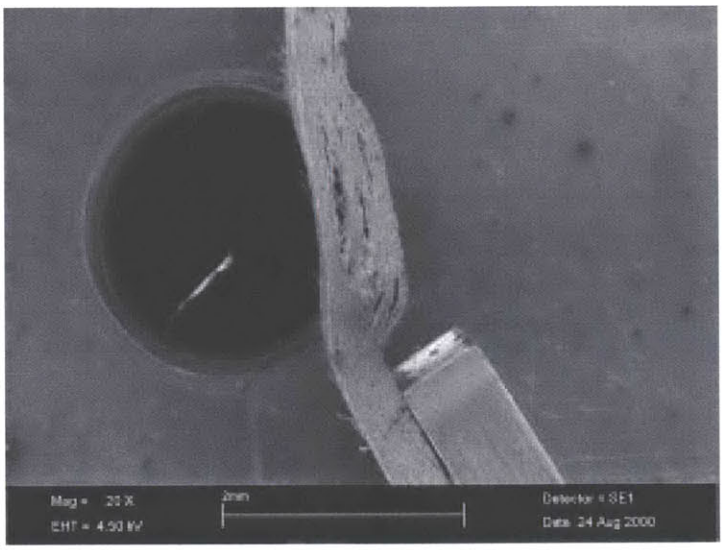

Figure 4-38: SEM image of TRIPLEX^{TM} MD punching process at step 3 of folding (male die width $0.84mm$ and female die width $2.03mm$) [18].

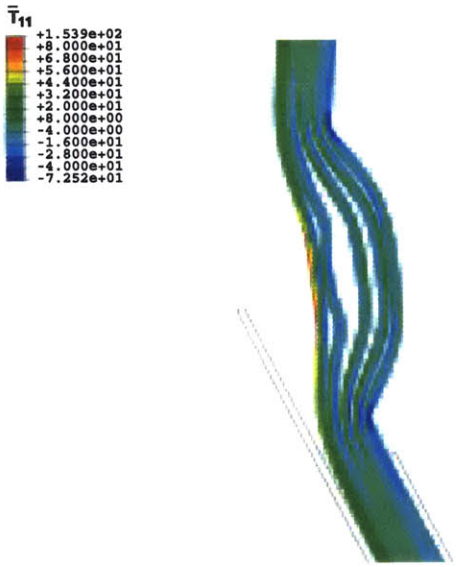

Figure 4-39: Contour plot of MD normal stress from simulation of SEM TRIPLEX^{TM} MD punching process corresponding to that shown in Fig. 4-38.

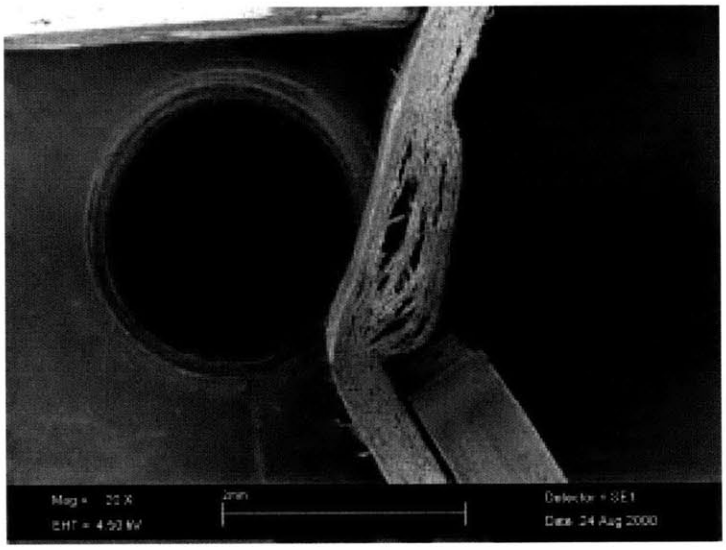

Figure 4-40: SEM image of TRIPLEX^{TM} MD punching process at the final step of folding (male die width $0.84mm$ and female die width $2.03mm$) [18].

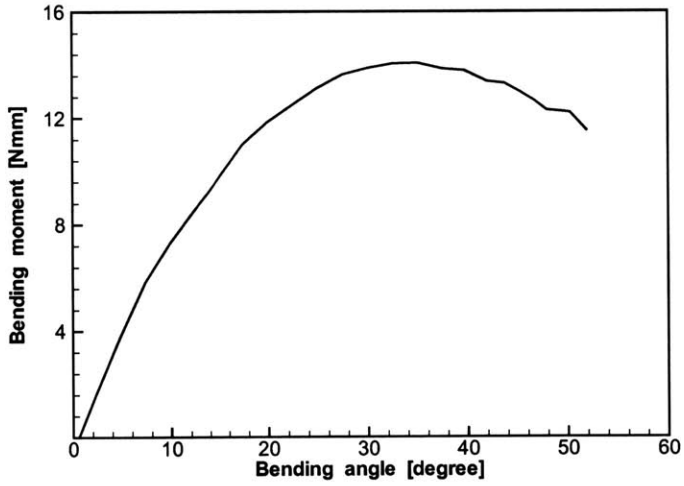

Figure 4-41: Bending moment *vs.* bending angle curve obtained from FEM simulation of the folding process as last step of a converting process. (male die width $0.84mm$ and female die width $2.03mm$)

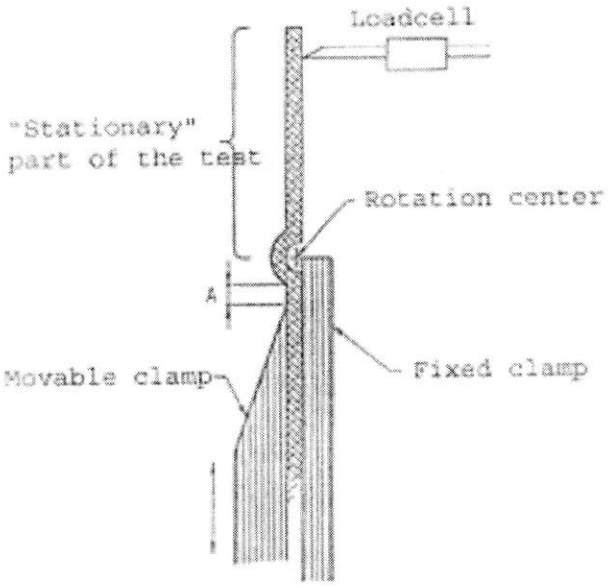

Figure 4-42: Schematics of the creasability test apparatus. (Swedish standard test number SE 015)

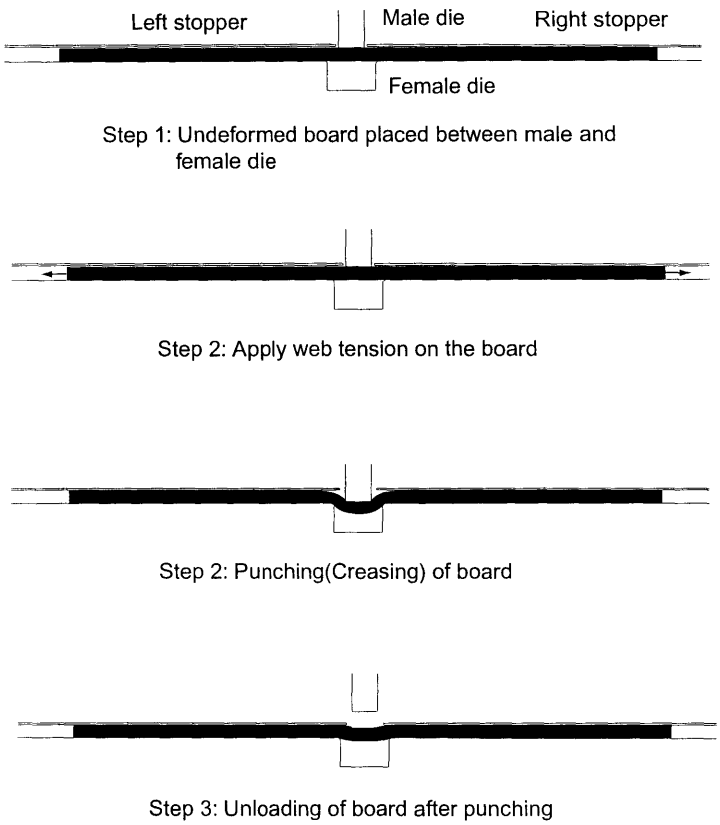

Figure 4-43: Illustration of the creasability test; part (a), creasing.

Step 5: Removal of creasing fixture (dies and stoppers)

Step 6: Clamping of the punched board

Step 7: Move in the folding load cell

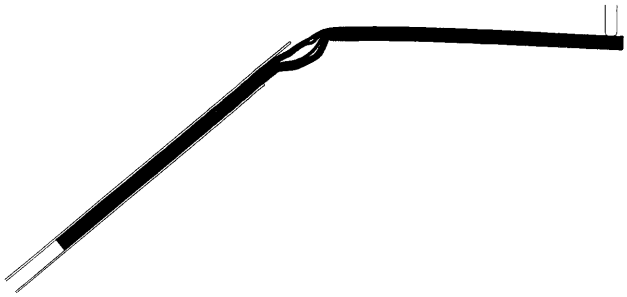

Step 8: Folding of the board: rotation of the the clamps
with load cell fixed

Figure 4-44: Illustration of the creasability test; part (b), folding.

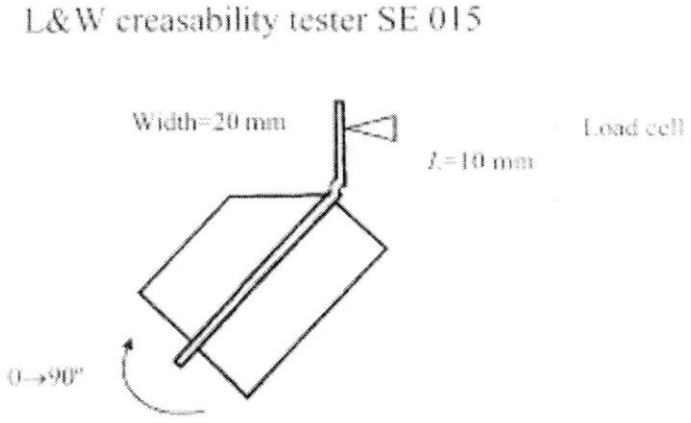

Figure 4-45: Geometry of the creasability test.

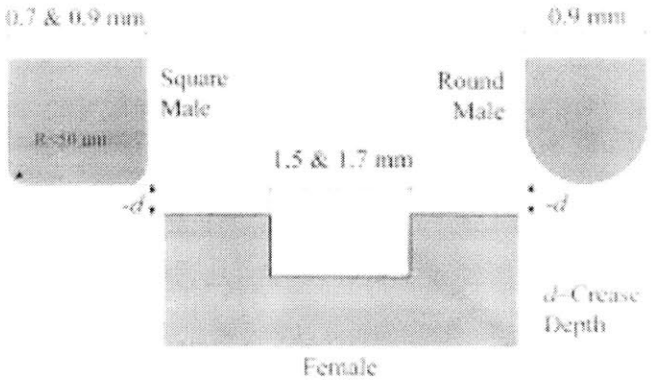

Figure 4-46: Illustration of parameters whose effect is investigated in the creasability test.

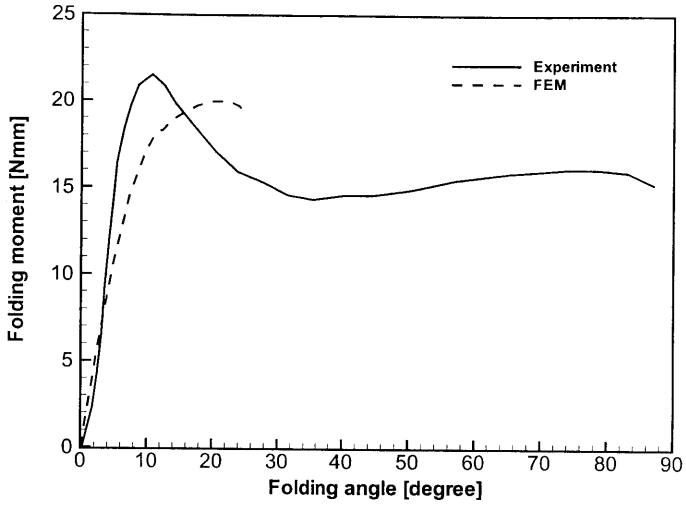

Figure 4-47: Comparison of numerical and experimental bending moment *vs.* bending angle curve for creasability test 1.

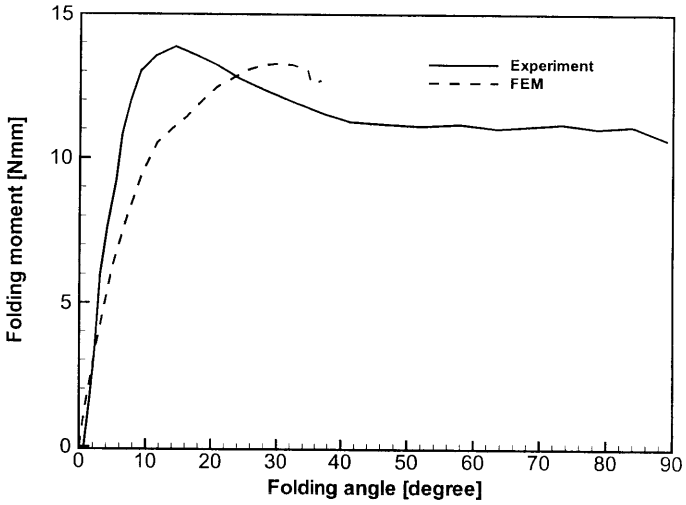

Figure 4-48: Comparison of numerical and experimental bending moment *vs.* bending angle curve for creasability test 2.

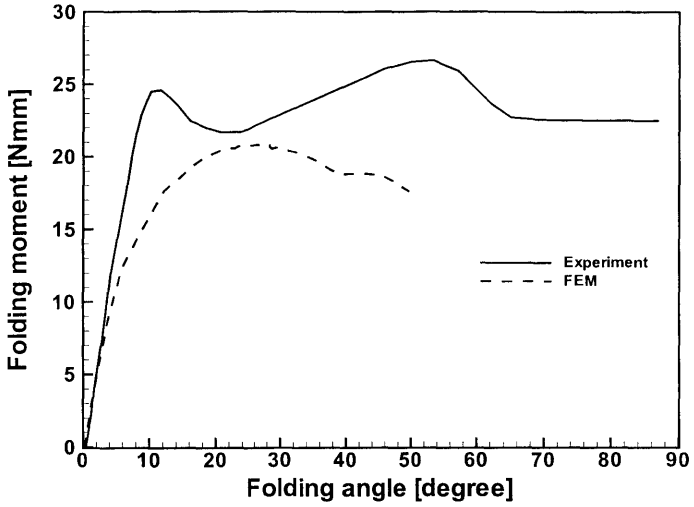

Figure 4-49: Comparison of numerical and experimental bending moment *vs.* bending angle curve for creasability test 3.

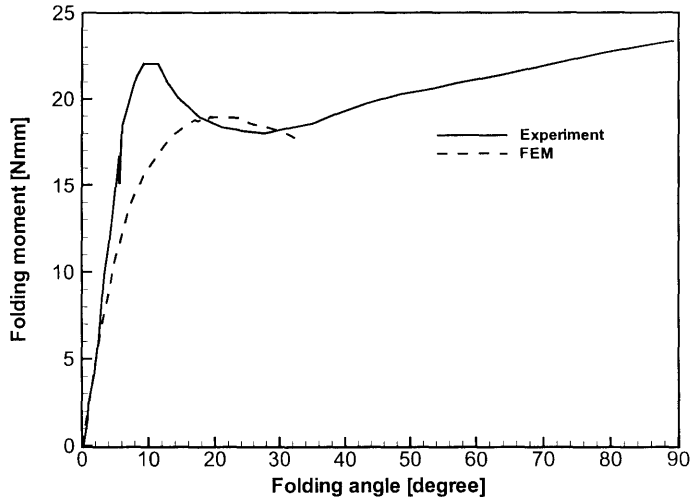

Figure 4-50: Comparison of numerical and experimental bending moment *vs.* bending angle curve for creasability test 4.

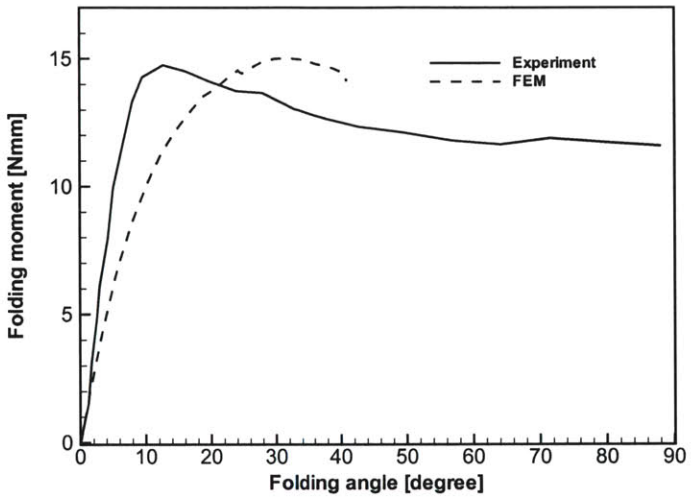

Figure 4-51: Comparison of numerical and experimental bending moment *vs.* bending angle curve for creasability test 5.

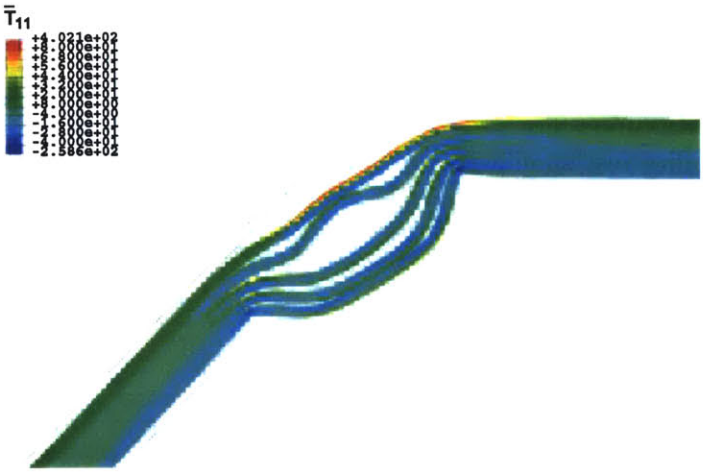

Figure 4-52: Contour plot of MD normal stress component at the final stage of the FEM creasability test simulation.

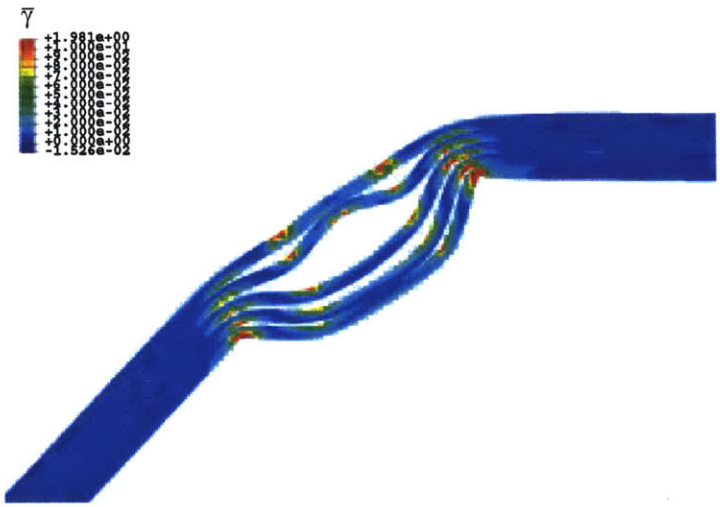

Figure 4-53: Contour plot of the equivalent plastic strain at the final stage of the FEM creasability test simulation.

Chapter 5

Summary and Future Work

5.1 Summary

Two constitutive models are developed to model the behavior of paperboard under finite, combined in- and out-of-plane deformations:

1. A three-dimensional elastic-plastic interface constitutive model is presented to model the out-of-plane delamination behavior of paperboard. The onset of interface separation is controlled by an evolving limit surface in the normal-shear traction space. The limit surface is taken to evolve with the inelastic component of relative interface displacement via a state-variable approach. The constitutive relation is implemented into finite element software to enable simulation of the delamination of paperboard under complex through-thickness loading conditions. The functional forms and material properties needed by this model can be experimentally determined by conducting through-thickness shear, pure extension and combined shear and normal loading tests. Simulations of combined loading conditions are conducted and compared with experimental data, demonstrating the capability of the proposed model to capture the delamination behavior of paperboard and, potentially, other laminated composite materials. The proposed interface constitutive law imposes no explicit restrictions on the

size, location, distribution, or direction of the growth of cracks. This enables the model to be able to naturally predict the initiation of microcracks and their growth into major delamination at any location.

2. A three-dimensional, anisotropic continuum constitutive model is developed to model the in-plane elastic-plastic deformation of paper and paperboard. The proposed initial yield surface is directly constructed from the yield strengths measured in various loading directions and the corresponding ratios of plastic strain components. An associated flow rule is used to model the plastic flow of the material. Anisotropic strain-hardening of yield strengths is introduced to model the evolution in the yield surface with strain. The constitutive model is found to capture major features of the highly anisotropic elastic-plastic behavior of paper and paperboard. Furthermore, with material properties fitted to experimental data in one set of loading directions, the model predicts the behavior of other loading states well.

The implementation of each constitutive models is tested extensively before being applied to simulate two of the key manufacturing processes of paperboard products: creasing and subsequent folding. Two types of simulations were conducted: simulations of the SEM creasing/folding process and simulations of the industrial creasability test. The simulations are found to be predictive of the corresponding experimental observations. In particular, the underlying micromechanisms of damage and delamination developed during creasing and subsequent folding are predicted well; the numerical macroscopic response of bending moment *vs.* bending angle curves under different sets of creasability testing parameters also agree with experimental data. Parametric study of numerical macroscopic response also predicted the trend well. These simulations show the proposed physically-based material models of the three-dimensional anisotropic, elastic-plastic behavior of paperboard enable the computational design of paperboard processing and product design.

5.2 Future work

First, the interface constitutive relation can be relatively easily modified and applied to many different types of interfaces ranging from interfaces in classical composite materials to brittle materials. Although very good numerical results were obtained with only a single state variable (the scalar interface damage D), it might be worthwhile to introduce more state variables which will better represent the process of interface damage. For example, if experiments can be conducted such that the interface is loaded first in tension till some damage is created before unloading and subsequently being loaded in shear, the extra information can then facilitate improvement of the evolution of the interface damage as multi-factor controlled process. Further work can also be done to refine the separation criterion and softening functions. More refined distribution functions of the interface strength and their effects on the macroscopic behavior of the structure will be another set of interesting topics to investigate. Work can also be done to implement the model into three dimension and conduct simulations of creasing at angles to MD/CD.

For the in-plane constitutive model, with more experimental information (*e.g.*, off-axis stress-strain curves with corresponding lateral strain *vs.* axial strain curves), the yield surface and, in turn, the flow rule can be easily refined to provide even more accurate modeling of the behavior of paper or paperboard layer by incorporating more sub-surfaces. Further work can also be done to address the issue of cross-hardening (*e.g.*, how material behave when loaded in CD before being loaded in MD till some amount of plasticity and unloaded.) by making the strain hardening function depend on more state variables, instead of just the equivalent plastic strain. As indicated in the creasing/folding simulation discussions, failure mechanisms need to be introduced into the model to capture in-plane fracture or fiber-pull-out behavior such that the stress carrying capability of the paper or paperboard will drop down when the in-plane strain is large enough. (An interesting idea will be modifying the interface model and apply it to model the in-plane fracture.)

In addition to the creasing/folding process, the combined models can be applied to aid other aspects of paperboard processing and product design.

Appendix A

Method to determine the model parameters from experiments

In this appendix, we summarize the definition of the material properties and the method to obtain them from experimental data. The yield surface is comprised of six sub-surfaces as shown in Fig. 2-13.

A.1 Definition of properties

The elastic properties used for TRIPLEX^{TM} were listed in Table 2.1 and Table 2.2. The yield and post-yield properties are listed here in Table 2.5. The yield surface normals were listed in Table 2.3.

A.2 Methodology for identifying material properties from data

The properties needed by the model can be obtained from relatively simple uniaxial experimental data on paper or paperboard pulp material.

Notes	Properties	Definition
Elasticity (see Table 2.1 and Table 2.2)	E_{MD}	Young's modulus in MD direction
	E_{CD}	Young's modulus in CD direction
	E_{ZD_0}	Young's modulus in ZD direction
	ν_{12}	Poisson's ratio between MD and ZD directions
	ν_{13}	Poisson's ratio between MD and CD directions
	ν_{23}	Poisson's ratio between ZD and CD directions
	G_{12}	Shear modulus in the MD-ZD plane
	G_{13}	Shear modulus in the MD-CD plane
	G_{23}	Shear modulus in the CD-ZD plane
Initial value of sub-surface strengths (Table 2.5)	S_0^I	Initial equivalent yield strength of sub-surface I
	S_0^{II}	Initial equivalent yield strength of sub-surface II
	S_0^{III}	Initial equivalent yield strength of sub-surface III
	S_0^{IV}	Initial equivalent yield strength of sub-surface IV
	S_0^V	Initial equivalent yield strength of sub-surface V
	S_0^{VI}	Initial equivalent yield strength of sub-surface VI
Flow strength of sub-surfaces (Eqn. 2.22)	S^I	Flow strength of sub-surface I
	S^{II}	Flow strength of sub-surface II
	S^{III}	Flow strength of sub-surface III
	S^{IV}	Flow strength of sub-surface IV
	S^V	Flow strength of sub-surface V
	S^{VI}	Flow strength of sub-surface VI
Hardening constants (Table 2.5)	$A_i, i = 1...5$	Hardening constants in Equation 2.22
	$B_i, i = 1...5$	Hardening constants in Equation 2.22
	$C_i, i = 1...5$	Hardening constants in Equation 2.22
Stiffening constant (Table 2.2)	a	constant determing stiffening of ZD elastic modulus under compression (Eqn. 2.5)

Table A.1: Definition of properties

A.2.1 Elastic constants

The initial elastic behavior is taken to be orthotropic in this model. A total of ten elastic constants are needed to define the orthotropic elasticity: the Young's moduli in MD, CD and ZD, the shear moduli G_{12}, G_{13}, G_{23} and the Poisson's ratio ν_{21}, ν_{13}, ν_{23} and the ZD stiffening constant, a. These data can be obtained by standard uniaxial stress-strain and corresponding lateral strain *vs.* axial strain curves.

A.2.2 Initial yield and subsequent strain hardening

As discussed in the text, for the yield surface, the sub-surface strengths, S^i, are directly related to the uniaxial in-plane yield strengths of the material and the corresponding plastic strain ratios.

To obtain the material properties, consider the case where the uniaxial stress-strain curves for tension in the MD and tension in the CD, compression in the MD and compression in the CD have been obtained. Let X^t denote the yield strength for MD uniaxial tension. For this case, the yield condition expressed in equation 3.14 is reduced to:

$$\sum_{i=I}^{N} [\frac{\chi_i X^t {N^i}_{11}}{S^i}]^{2k} - 1 = 0. \tag{A.1}$$

Furthermore, for uniaxial MD tension, the only non-zero contributions, due to the switching controller, are those for the sub-surfaces I and V, which gives

$$[\frac{X^t {N^I}_{11}}{S^I}]^{2k} + [\frac{X^t {N^V}_{11}}{S^V}]^{2k} - 1 = 0. \tag{A.2}$$

Similarly, for the case of uniaxial tension in CD, the yield criterion reduces to:

$$[\frac{Y^t {N^{II}}_{33}}{S^{II}}]^{2k} + [\frac{Y^t {N^{IV}}_{33}}{S^{IV}}]^{2k} - 1 = 0, \tag{A.3}$$

where Y^t denotes the CD tensile yield strength. For the case of MD compression, the yield condition becomes:

$$[\frac{-X^c N^{II}{}_{11}}{S^{II}}]^{2k} + [\frac{-X^c N^{IV}{}_{11}}{S^{IV}}]^{2k} - 1 = 0 \tag{A.4}$$

where $X^c > 0$ is the MD compression yield strength. For the case of CD compression:

$$[\frac{-Y^c N^{I}{}_{33}}{S^{I}}]^{2k} + [\frac{-Y^c N^{V}{}_{33}}{S^{V}}]^{2k} - 1 = 0 \tag{A.5}$$

where $Y^c > 0$ is the CD compression yield strength. Thus, by solving equations (A.2) to (A.5) with four equations for four unknows, $S^i, i = I, II, IV$ and V, direct relations between the $S^i, i = I, II, IV$ and V and uniaxial tensile and compressive yield strengths are obtained as follows:

$$S^I = (\frac{\Omega_2}{\Omega_1})^{\frac{1}{2k}} \quad ; \tag{A.6}$$

$$S^{II} = (\frac{\Omega_4}{\Omega_3})^{\frac{1}{2k}} \quad ; \tag{A.7}$$

$$S^{IV} = Y^t N_{33}^{IV}[1 - (Y^t N_{33}^{II})^{2k}(\frac{\Omega_3}{\Omega_4})]^{-\frac{1}{2k}} \quad ; \tag{A.8}$$

and

$$S^V = X^t N_{11}^{V}[1 - (X^t N_{11}^{I})^{2k}(\frac{\Omega_2}{\Omega_1})]^{-\frac{1}{2k}}, \tag{A.9}$$

where

$$\Omega_1 = [-Y^c N_{33}^{V}]^{2k} - [X^t N_{11}^{V}]^{2k} \quad , \tag{A.10}$$

$$\Omega_2 = (X^t Y^c)^{2k}[(N_{11}^{I} N_{33}^{V})^{2k} - (N_{33}^{I} N_{11}^{V})^{2k}] \quad , \tag{A.11}$$

$$\Omega_3 = [-X^c N_{11}^{IV}]^{2k} - [Y^t N_{33}^{IV}]^{2k} \quad , \tag{A.12}$$

and

$$\Omega_4 = (X^c Y^t)^{2k}[(N_{11}^{IV} N_{33}^{II})^{2k} - (N_{33}^{IV} N_{11}^{II})^{2k}] \quad . \tag{A.13}$$

The equivalent yield strengths for the two shear sub-surfaces are taken to be equal, $S^{III} = S^{VI}$. With one additional experimental stress-strain curve, for example, the in-plane shear MD-CD stress-strain curve which gives the shear strength Z^t, S^{III} and S^{VI} can be expressed as a function of X^t, Y^t, X^c, Y^c and Z^t by applying the same method. However, a shear stress-strain curve may be difficult to obtain for paper material. Instead, an off-axis tensile stress-strain curve can be used to calculate S^{III} and S^{VI}. Here, the uniaxial stress-strain curve in the off-axis direction 45° to the MD direction is used. The uniaxial stress state in the off-axis direction can be transformed to the material directions by a simple tensor rotation which gives the following non-zero stress components instead:

$$\bar{\boldsymbol{T}} = \frac{V^{45}}{2} \begin{bmatrix} 1 & 1 & 0 \\ 1 & 1 & 0 \\ 0 & 0 & 0 \end{bmatrix} \tag{A.14}$$

where V^{45} is the yield stress obtained from the 45° off-axis stress-strain curve. Substitution of $\bar{\boldsymbol{T}}$ into the yield condition and utilizing the values of $S^i, i = I, II, IV$ and V already obtained, S^{III} and S^{VI} are related to the in-plane experimental data by:

$$S^{III} = S^{VI} = V^{45} N_{13}^{III} [1 - (\frac{\frac{V^{45}}{2} N_{11}^{I} + \frac{V^{45}}{2} N_{33}^{I}}{S^I})^{2k} - (\frac{\frac{V^{45}}{2} N_{11}^{II} + \frac{V^{45}}{2} N_{33}^{II}}{S^{II}})^{2k}]^{-\frac{1}{2k}}. \tag{A.15}$$

Bibliography

[1] *Perkins, R. and Sinha, S. A micromechanics plasticity model for the uniaxial loading of paper materials*, number 135 in Plastic flow and creep, New York, 1992. ASME Applied Mechanics Division.

[2] *Schulgasser, K. and Page, D. The influence of transverse fiber properties on the in-plane elastic behavior of paper*, number 96 in ESPRI, 1993.

[3] *Sinha, S. and Perkins, R. A micromechanics constitutive model for use in finite element analysis*, number 209 in Mechanics of Cellulosic Materials, New York, 1995. ASME Applied Mechanics Dvision.

[4] Koubaa A. and Koran Z. Measure of the internal bond strength of paper/board. *TAPPI*, 78(3):103–111, March 1995.

[5] Smith A. Micromechanics of the through-thickness deformation of paperboard. Master's thesis, Department of Mechanical Engineering, Massachusetts Institute of Technology, 1999.

[6] M. Arcan, Z. Hashin, and A. Voloshin. A method to produce uniform plane-stress states with applications to fiber-reinforced materials. *Experimental Mechanics*, 18(4):141–146, 1978.

[7] Y. P. Arramon, M. M. Mehrahadi, D. W. Martin, and S. C. Cowin. A multi-dimensional anisotropic strength criterion based on kelvin modes. *International Journal of Solids and Structures*, 37:2915–2935, 2000.

[8] G. I. Barenblatt. The mathematical theory of equilibrium cracks in brittle fracture. *Advances in Applied Mechanics*, 7:55–129, 1962.

[9] S. B. Biner. Role of interfaces on the ductile fracture of discontinuous fiber reinforced composites. *Advanced Composites'93: International Conference on Advanced Composite Materials*, pages 1309 –1315, February 1993.

[10] Donner B. C. and Backer S. The role of continuum instabilities in compression and bending failure of paper and paperboard. *International Paper Physics Conference*, pages 231–236, 1989.

[11] Mark R.E. Castegnade B. and Seo Y.B. New concepts and experimental implications in the description of the 3-d elasticity of paper. *Journal of Pulp Paper Science*, 15(6):151–159, 1989.

[12] M. Comninou. The interface crack. *J. Appl. Mech.*, 44:631–636, 1977.

[13] A. deRuvo, L. Carlsson, and C. Fellers. The biaxial strength of paper. *TAPPI*, 63(5):133–136, 1980.

[14] D. S. Dugdale. Yielding of steel sheets containing slits. *Journal of the Mechanics and Physics of Solids*, 8:100 – 108, 1960.

[15] C. Fellers, B. Westerlind, and A. deRuvo. An investigation of the biaxial failure envelope of paper. *Proceedings of 7th Fundamental Research Symposium: The Role of Fundamental Research in Papermaking*, pages 527–556, 1981.

[16] D. E. Gunderson. Determining paperboard strength. *International Paper Physics Conference*, pages 253–263, 1983.

[17] D. E. Gunderson, L. A. Bendtsen, and R. E. Rowlands. Mechanistic perspective of the biaxial strength of paperboard. *Journal of Engineering Materials and Technology*, 108:135–140, 1986.

[18] Dunn H. Micromechanisms of paperboard deformation. Master's thesis, Department of Mechanical Engineering, Massachusetts Institute of Technology, 2000.

[19] HKS Inc. *ABAQUS Reference Manuals.* Pawtucket, R.I., 5.8 and 6.2 edition, 2001.

[20] A. P. Karafillis and M. C. Boyce. A general ansiotropic yield criterion using bounds and a transformation weighting tensor. *Journal of the Mechanics and Physics of Solids*, 41(12):1895–1886, 1993.

[21] Carlsson L., Fellers C., and deRuvo A. The mechanisms of failure in bending of paperboard. *Journal of Materials Science*, 15:2636–2642, 1980.

[22] C. J. Lissenden. Fiber-matrix interfacial constitutive relations for metal matrix composites. *Composites part B: Engineering(UK)*, 30(3):267 – 278, 1999.

[23] Baum G. A. Mann R. W. and Habeger C. C. Orthotropic elastic constants of paper. *TAPPI*, 64(8):97 – 106, 1981.

[24] A. Needleman. A continuum model for void nucleation by inclusion debonding. *Journal of Applied Mechanics*, 54:525 – 531, 1987.

[25] A. Needleman. Micromechanical modeling of interfacial decohesion. *Ultramicroscopy*, 40:203 – 214, 1992.

[26] M. Ortiz and J. A. Blume. An analysis of tensile decohesion along an interface. *International Journal of Fracture*, 42:117–128, 1990.

[27] M. Ortiz and A. Pandolfi. Finite deformation irreversible cohesive elements for three-dimentional crack-propagation analysis. *International Journal for Numerical Methods in Engineering*, 44:1267–1282, 1999.

[28] K. Persson. Material model for paper. Master's thesis, Diplomat report, Lund Institute of Technology, Lund, Sweden, 1991.

[29] S. Socrate. *Mechanics of microvoid nucleation and growth in high-strength metastable austenitic steels.* PhD dissertation, Massachusetts Institute of Technology, Department of Mechanical Engineering, 1995.

[30] D. C. Stahl and S. M. Cramer. A three-dimensional network model for a low density fibrous composites. *Journal of Engineering Materials and Technology*, 120:126–130, 1998.

[31] N. Stenberg, 2001. Communication between Stenberg and Xia.

[32] N. Stenberg, C. Fellers, and S. Östlund. Measuring the stress-strain properties of paperboard in the thickness direction. *Journal of Pulp and Paper Science*, 27(6):213–221, June 2001.

[33] N. Stenberg, C. Fellers, and S. Östlund. Plasticity in the thickness direction of paperboard under combined shear and normal loading. *ASME Journal of Engineering Material and Technology*, 123:184–190, April 2001.

[34] T. O. Williams and F. L. Addessi. A general theory for laminated plates with delaminations. *International Journal of Solids and Structures*, 34(16):2003–2024, 1997.

[35] X. P. Xu and A. Needleman. Numerical simulations of dynamic crack growth along an interface. *International Journal of Fracture*, 74:289 – 324, 1996.